PLACE IN RETURN BOX
to remove this checkout from your record.
TO AVOID FINES return on or before date due.

DATE DUE	DATE DUE	DATE DUE

MOLTEN SALT SYNTHESIS OF QUATERNARY

CHALCOANTIMONATES AND THIOPHOSPHATES

By

Jason A. Hanko

A DISSERTATION

Submitted to

Michigan State University

in partial fulfillment of the requirements

for the degree of

DOCTOR OF PHILOSOPHY

Department of Chemistry

1998

ABSTRACT

MOLTEN SALT SYNTHESIS OF QUATERNARY CHALCOANTIMONATES AND THIOPHOSPHATES

By

Jason A. Hanko

We used the now proven molten alkali polychalcogenide flux method to synthesize new quaternary chalcoantimonate and thiophosphate materials. The chalcoantimonate and thiophosphate fluxes are formed by the *in situ* fusion of $A_2Q/Sb/Q$ (A = alkali metal; Q = S, Se) or $A_2S/P_2S_5/S$ (A = alkali metal) forming highly reactive $[Sb_xQ_y]^{n-}$ and $[P_xS_y]^{n-}$ units solubilized in the excess polychalcogenide flux. These molecular building blocks coordinate to metal ions in a multitude of ways, building extended lattices stabilized by alkali cations. By examining the coordination chemistry of these systems, we discovered that the thiophosphate system is best thought of as completely different than the corresponding selenophosphate systems and different materials are formed under similar experimental conditions. In the thiophosphate system the P^{5+} species appears to be stable under a variety of conditions, and increasing the binary P_2S_5 concentration stabilized higher nuclearity $[P_xS_y]^{n-}$ units. While the Sb^{5+} species is readily observed in the chalcoantimonate systems, it is exclusively observed as the discrete tetrahedral unit. The enhanced stability of the Sb^{3+} species increases the diversity of the coordination chemistry displayed by the chalcoantimonate system due to the complicated equilibrium stabilizing higher nuclearity $[Sb_xS_y]^{n-}$ units. Changing the Lewis basicity in of the chalcoantimonate fluxes resulted in the stabilization of recognizable $[Sb_xS_y]^{n-}$ structural fragments that could be used as building blocks forming compounds with several potential applications. Several

new $[P_xS_y]^{n-}$ and $[Sb_xQ_y]^{n-}$ units have been synthesized and their coordination chemistry examined.

In this dissertation, the synthesis, and characterization and properties of several new silver chalcoantimonates A_2AgSbS_4 (A = K, Rb, Cs), $Cs_3Ag_2Sb_3Q_8$ (Q = S, Se), α,β-$RbAg_2SbS_4$, and three new silver-rich gold thioantimonate compounds α,β-$Rb_2Ag_{20}Sb_4S_{19}$ and $Cs_2Ag_{20}Sb_4S_{19}$ will be discussed. Extending this methodology to gold, three new compounds, A_2AuSbS_4 (A = Rb, Cs) and $Rb_2Au_6Sb_4S_{10}$ were synthesized, further proving the generality of the method at accommodate a variety of metals. Utilizing the corresponding thiophosphate flux a number of new quaternary compounds $A_2CuP_3S_9$ (A = K, Rb, Cs), $K_3CuP_2S_7$, $Cs_2Cu_2P_2S_6$, A_2AuPS_4 (A = K, Rb, Cs), and $AAuP_2S_7$ (A = Rb, Cs), were discovered. The synthetic work performed here provides the ground work for systematic synthesis, and further exploration into these and other systems.

DEDICATION

To my wife, Pauline for her patience and understanding.

ACKNOWLEDGMENTS

TABLE OF CONTENTS

CHAPTER 3

Thioantimonate Flux Synthesis of α,β-Rb Ag_2SbS_4: Two New

Three-Dimensional Compounds With Acentric Structures.

CHAPTER 4

Synthesis and Characterization of the Novel Mixed Valent Quaternary

Silver-Rich Thioantimonates A$_2$Ag$_{20}$Sb$_4$S$_{19}$ (A = Rb, Cs) and

β-Rb$_2$Ag$_{20}$Sb$_4$S$_{19}$. A Thioantimonate with a Large Supercell.

CHAPTER 5

The Chemistry of Au in Molten Polythioantimonate Fluxes. Synthesis and Characterization of the New Multinary Gold Thioantimonates A_2AuSbS_4 (A = Rb, Cs) and $Rb_2Au_6Sb_4S_{10}$. A Novel Compound with a Binary and Ternary Interconnected Framework.

CHAPTER 6

$A_2CuP_3S_9$ (A = K, Rb), $Cs_2Cu_2P_2S_6$, and $K_3CuP_2S_7$: New Phases from the Dissolution of Copper in Molten Polythiophosphate Fluxes.

CHAPTER 7

Chemistry of Gold in Molten Alkali Metal Polychalcogeno-phosphate Fluxes.

Synthesis and characterization of the low dimensional Compounds A_2AuPS_4

(A = K, Rb, Cs) and $AAuP_2S_7$ (A = K, Rb)

LIST OF TABLES

LIST OF FIGURES

xvii

CHAPTER 1

1. Introduction

Solid-state chemistry is the cornerstone on which numerous aspects of our present and future technologies will be built. Several commercial applications now entrenched as "essential" to modern life owe their conception to solid state chemistry. Semiconducting chalcogenide compounds are viable candidates for a variety of applications such as solar cells[1], IR radiation detection[2], electroluminescent displays[3], thermoelectric[4] and nonlinear optical[5] devices, second generation high density storage batteries[6], and catalysis.[7] These technologies rely on the refinement of existing solid-state materials or the synthesis of novel materials with enhanced properties to advance current and future applications. Therefore, exploratory solid-state synthesis continues to be a highly active area of research.

This field accurately deserves the term "exploratory" because the methods available to solid-state chemists lack the same level of predictability that synthetic chemists in the other disciplines sometimes take for granted. The lack of predictability is largely due to the high reaction temperatures (>800 ºC) required by solid-state "heat & beat" syntheses. The majority of the starting materials are typically solids; very high temperatures are necessary to ensure sufficient diffusion between the reactants. In most cases, the high reaction temperatures alone are not enough to ensure a complete reaction. For a reaction to proceed to completion, the material must be cooled to room temperature, thoroughly ground to expose fresh surface area, and the subsequently reheated to allow the reaction to proceed. The elevated temperatures drive the products to the most thermodynamically stable products, usually binary or ternary compounds. As a result, quaternary compounds are difficult to form, the preference lying with the more stable binary and ternary compounds.

Motivated by the desire to move way from the high temperatures of classical solid state synthesis, new low temperature methods such as chemical vapor deposition (CVD),[8]

1

solventothermal[9] and the relatively new supercritical solvent[10] synthesis were developed to address the problems of diffusion. Of these, the solventothermal method proved to be conducive to the low temperature synthesis of zeolites[11] and a variety of other materials[12-13]. While direct combination and solventothermal methods are an excellent choice for the synthesis of new materials, they left an intermediate temperature range, between 200 - 800°C, largely unexplored. To explore this regime, the use of a low-melting alkali polychalcogenide A_2Q_x flux (A = alkali metal; Q = S, Se, Te) was developed as a new synthetic method.[14] By utilizing this method, a staggering number of A/M/Q (A = alkali metal; M = transition, main group, or rare earth metal; Q = S, Se, Te) compounds have been prepared.[15] Several of these compounds display interesting structural,[16] thermal,[17] and optical properties.[18,19] The molten polychalcogenide synthetic method proved to be highly accommodating, allowing the coordination chemistry of transition[19], main group[19-20], and rare earth metals[21] to be investigated without the formation of undesirable competing phases. This approach can stabilize kinetically stable phases that cannot be formed by other methods.

While investigating the ternary A/M/Q systems, certain molecular fragments were found to be stable in this molten reaction medium. This observation resulted in the utilization of discrete molecular building blocks or recognizable structural fragments to synthesize new multinary compounds. These molecular units are formed by the *in situ* fusion of $A_2Q/E/Q$ and contain various $[E_xQ_y]^{n-}$ units (E = main group element) in a molten polychalcogenide solvent. By this method, the polychalcogenide flux can act as a solvent by which the previously unexplored coordination chemistry of the highly basic $[E_xQ_y]^{n-}$ units can be investigated. To gain access to this area of chemistry, the polychalcogenide flux was modified by adding a second main group metal or binary chalcogenide to the starting $A_2Q/E/Q$ reactants, increasing the complexity of the reaction system, in the hopes of forming quaternary $A_wM_xE_yQ_z$ compounds. The lower reaction temperature increases the mobility of the reactants, favoring the probability of stabilizing metastable phases while

preventing the formation of the thermodynamically stable phases. Although thermodynamic influences cannot be totally avoided, it is clear that by enhancing the diffusion rate of the reactants, solid-state reactions can be performed at reduced reaction temperatures, favoring the formation of new multinary materials.

While this discussion has emphasizes the use of molten polychalcogenide fluxes as a conducive solvent to investigate the coordination chemistry of the various $[E_xQ_y]^{n-}$ units, they are far from "innocent" solvents. The alkali polychalcogenide fluxes allow for the easy incorporation of alkali metal cations into the anionic $[M_xE_yQ_z]^{n-}$ frameworks. The incorporation of alkali metal can lower the dimensionality of a compound or cause a structural transformation to a previously unknown structure. The use of these highly reactive solvents at intermediate temperatures has allowed the dismantling of stable compounds (i.e. Sb_2Q_3, and P_2Q_5) into reactive intermediates for the formation of new materials.

The multicomponent polychalcogenide flux method was first utilized by the incorporation of tin[19,22] into the polychalcogenide fluxes, followed by tellurium[23], the P_2Q_5 glasses (Q = S[24], Se[25]), and most recently germanium[26], all with remarkable results. The coordination chemistry of chalcometalates such as TeS_3^{2-}, $P_2Se_6^{4-}$, GeS_4^{4-} and SnS_4^{4-} have been largely ignored in favor of silicate, aluminate, and phosphate species that readily react in aqueous or other more traditional solvents. By utilizing the low melting alkali polychalcogenide salts as a reactive solvent the more non-classical chemistry of these various chalcometalates units can be explored. These non-classical chalcogenide ligands are more suitable for binding to "softer," chalcophilic metals, in contrast to the oxide-containing ligands, which prefer "hard," electropositive ions. The molten nature of the polychalcogenide flux allows rapid diffusion of reactants, promoting crystal growth. Since the major means of characterization of new solid-state materials is determining the single crystal X-ray structure, methods that routinely provide well crystallized products are necessary.

The growing importance of the chalcophosphate class of compounds prompted our lab to begin investigating this and other related systems via our developing polychalcometalate method. Although the preliminary investigation involved the coordination chemistry of both the polythiophosphate and polyselenophosphate systems, the emphasis quickly focused on further exploration of the selenophosphate system. The polyselenophosphate system blossomed into a rich coordination chemistry of the various $[P_xSe_y]^{n-}$ units with a variety of metal ions leading to a number of new materials whose structures vary from dense three-dimensional frameworks to molecular species[16]. We were interested in the continued exploration of the polythiophosphate system to develop this chemistry to a level of maturity similar to that observed in the polyselenophoshate system. During the course of our investigations, we discovered that the chemistry of the two systems was completely divergent, and they should be looked upon as two separate areas.

The first compounds reported from a $A_x[P_yQ_z]$ flux synthesis were $ABiP_2S_7$ (A = K, Rb)[27]. The structure consists of corrugated $[BiP_2S_7]^{n-}$ layers separated by A^+ ions. The layers are constructed from Bi^{3+} ions and multiply bonding $[P_2S_7]^{4-}$ units forming irregular eight-membered rings of alternating Bi-S-P atoms. The PS_4 tetrahedrons of the pyrothiophosphate unit coordinate in a bidendate chelation mode to Bi^{+3} ions and acts as a bridge to a second Bi^{+3} ion, forming the top side of the eight-membered ring. The Bi^{+3} ions are connected at the bottom of the ring by the PS_4 tetrahedron of a neighboring $[P_2S_7]^{4-}$ unit that acts as a bridge to the two Bi^{+3} ions, see Figure 1-1. The rings are linked in two dimensions by P-S-Bi bridges, forming the layer. The layers stack with the eight-membered rings in registry, forming channels that run along the a-axis. The Bi^{+3} ion is in a distorted monocapped trigonal prismatic coordination geometry. The distortion presumably arises from the stereochemically active $6s^2$ lone pair of the Bi^{+3} ion.
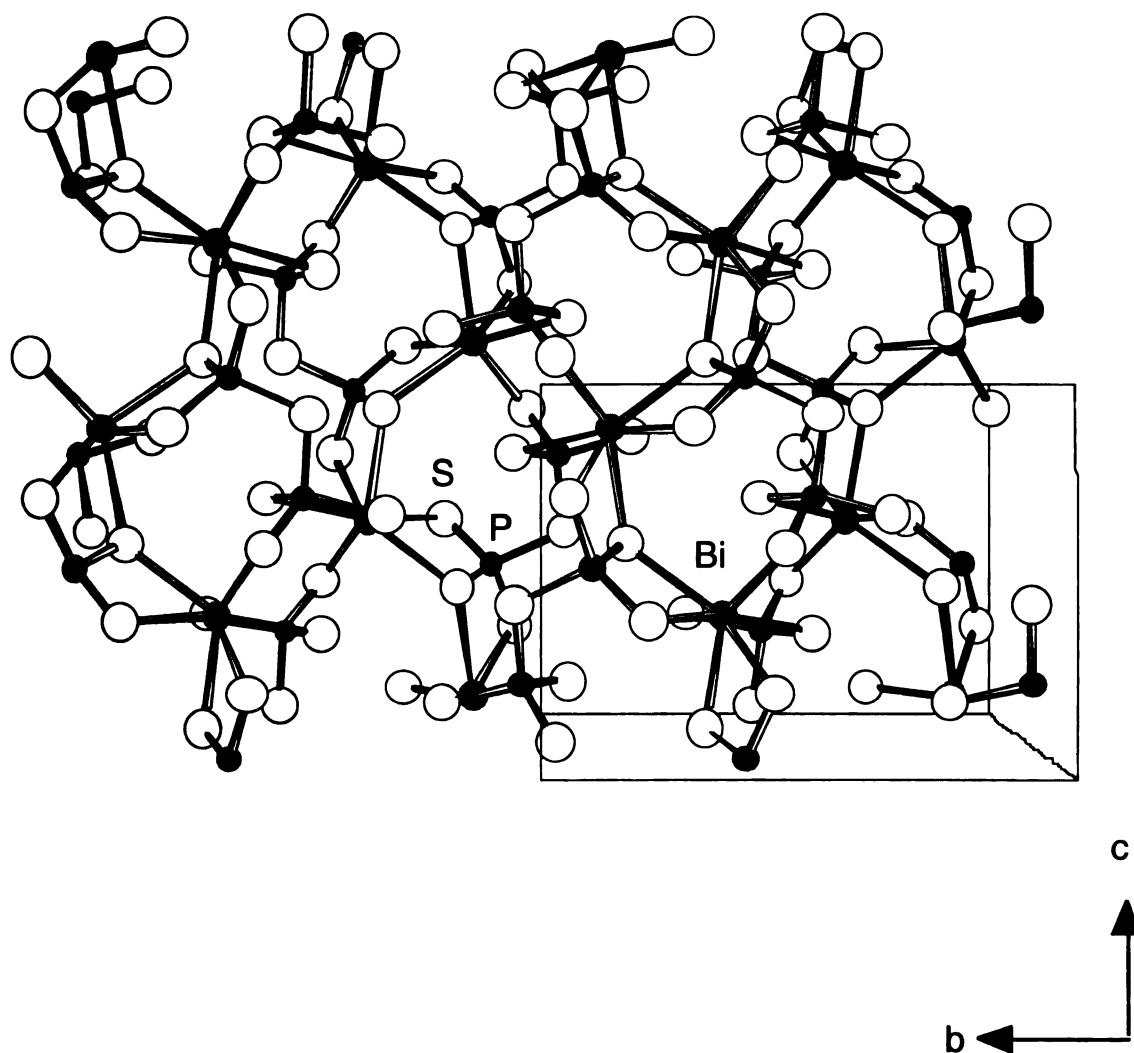
Figure 1-1:   Packing diagram of $ABiP_2S_7$ (A = K), as viewed down the a-axis. The alkali cations have been removed for clarity.

Under these proven conditions, we wished to explore the coordination chemistry of *polythiophosphate* and *polychalcoantimonate units* with transition metals. Because of sulfur's high affinity to form copper and silver antimony chalcogenide minerals, we focused our preliminary investigations on the group 11 transition metals in hopes of obtaining new quaternary alkali polychalcoantimonate compounds.

The exploration of the polychalcoantimonate fluxes looked very appealing because the vast majority of the known multinary antimony chalcogenide compounds are minerals,[28] containing Sb^{+3} species in $[Sb_xQ_y]^{n-}$ units neutralized primarily by silver and/or lead cations. The $[Sb_xQ_y]^{n-}$ frameworks containing the Sb^{+3} species exhibit a rich structural diversity due to the stereochemical effect of the inert lone pair and the tendency for the Sb^{+3} species to adopt three-[29] four-[30] or five-fold coordination.[31] Taking advantage of the thioantimonate units high affinity for coinage metals, we felt this was a convenient entry to the largely unexplored area of $[M_xSb_yQ_z]^{n-}$ frameworks stabilized by alkali metal cations.

A variety of synthetic routes have been reported to synthesize ternary alkali antimony (poly)chalcogenide compounds, with high temperature direct combination[32] and solventothermal synthesis[33] being the most successful. The compounds $Cs_2Sb_4S_8$ and $CsSbS_6$[34] represent the first examples of thioantimonate compounds synthesized using the polythioantimonate fluxes. The structure of $CsSbS_6$ is one-dimensional with Sb_2S_2 rhombic units linked into a chain by bridging $(S_5)^{2-}$ ligands, see Figure 1-2. Each Sb atom is bonded to four S atoms with distances that are typical for a four-coordinate SbS_4 species with a stereochemically active lone pair.
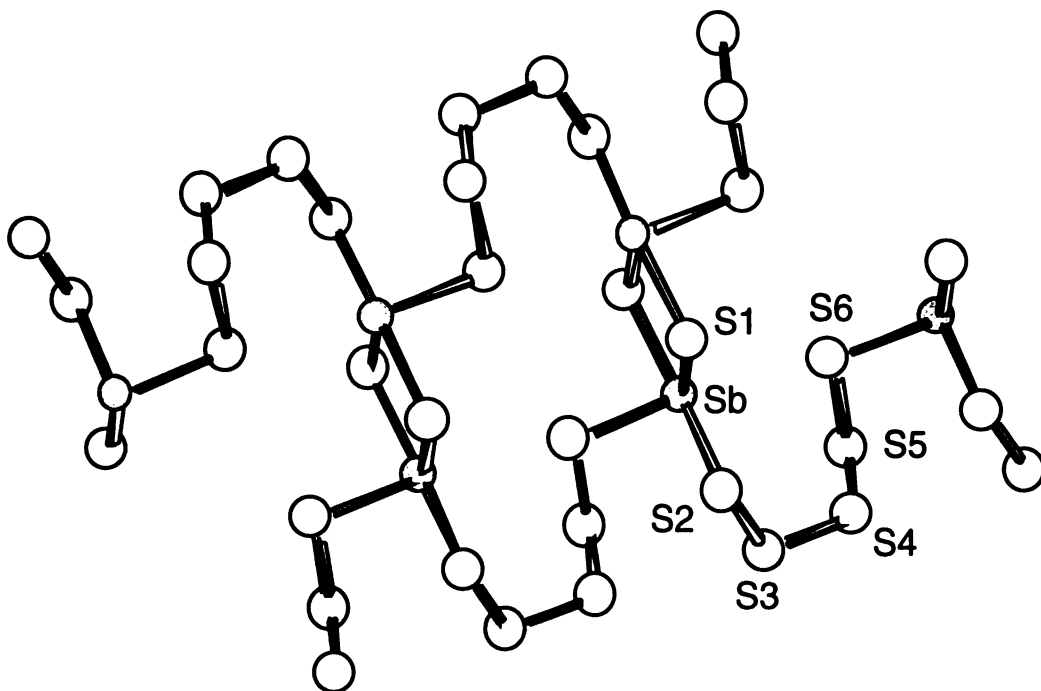
Figure 1-2:   The anionic chains of CsSbS$_6$. The alkali cations have been removed for
clarity. Large open balls; S, shaded balls; Sb.

The geometry about the Sb atoms is trigonal bipyramidal with the lone pair in an equatorial position exerting the expected distortions from an ideal trigonal bipyramidal coordination. The structure of $Cs_2Sb_4S_8$ is two dimensional containing of the same Sb_2S_2 rhombi observed in $CsSbS_6$, but now they are linked by trigonal pyramidal $[SbS_3]^{3-}$ units that connect the rhombi into chains running along the [110] direction. These chains are then linked into layers via $(S_2)^{2-}$ ligands that bridge $[SbS_3]^{3-}$ units from neighboring chains. The Sb atoms in both of the $[Sb_xS_y]^{n-}$ units have a mixture of long and short contacts to neighboring S atoms, see Figure 1-3. The Sb(1) atom has a square pyramidal geometry of S atoms with the lone pair presumably occupying the opposite axial site. The Sb(2) atom coordination is best described as distorted trigonal bipyramidal with three normal distances and one longer distance. Within the anionic layers of $Cs_2Sb_4S_8$ are 14-membered rings that stack in registry from layer to layer, forming tunnels that run along the c - axis.

The first reported quaternary alkali antimony sulfide compound was $KHgSbS_3$.[35] The structure consists of discrete pyramidal $[SbS_3]^{3-}$ units corner sharing to four-coordinate Hg^{+2} cations is a sea-saw geometry, forming a two - dimensional compound separated by K^+ cations, see Figure 1-4. The first examples of a quaternary alkali antimony chalcogenides incorporating the tetrahedral $[SbS_4]^{4-}$ unit, prepared in supercritical ammonia, were only recently reported[36].
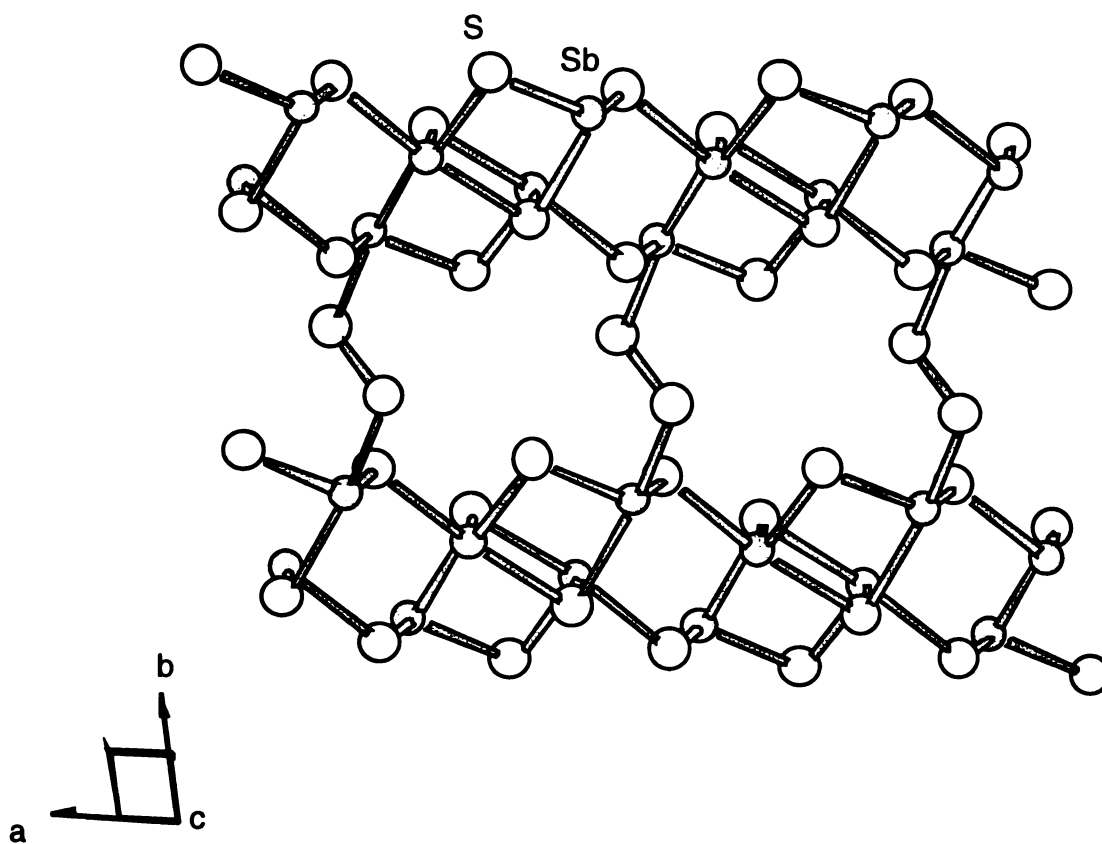
Figure 1-3:   A single anionic layer of $Cs_2Sb_4S_8$ as viewed down the c - axis. Large open balls; S, shaded balls; Sb. The alkali cations have been removed for clarity.
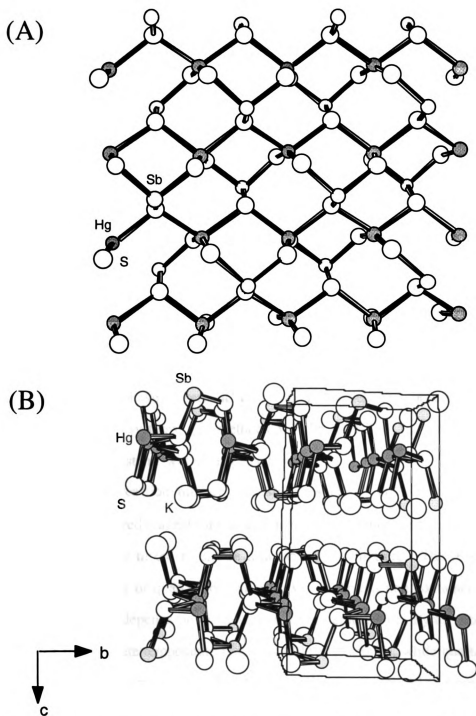
Figure 1-4:   (A) A view of a single [HgSbS$_3$]$^{n-}$ layer, with labeling. (B) Packing diagram of KHgSbS$_3$ as viewed down the a - axis, with labeling.

2. Nature of the Chalcophosphate Fluxes

A typical reaction involves the combination of $A_2Q/M/P_2Q_5/Q$ in various ratios. The reactants are elemental metal M, alkali chalcogenide A_2Q (A = alkali metal cation), the binary P_2Q_5 (Q = S, Se) and elemental chalcogen Q (Q = S, Se, Te). The flux formation is the result of the self-redox reaction of A_2Q reacting with n amounts of Q (Q = S, Se, Te) forming A_2Q_{n+1} ligands that act as a reactive solvent. Reactions between the metals and the molten Q_x^{2-} ligands are performed *in situ*. The most direct way to incorporate an additional main group metal into these systems is to add the elemental main group metal into the reaction mixture. For the chalcophosphate systems the binary P_2Q_5 compound was chosen to provide a preoxidized phosphorous source into the reaction mixture. Since the two systems have divergent chemical properties the polyselenophosphate and polythiophosphate systems; the methods will be described in general and differences between the two systems will be described as needed.

A typical reaction mixture consists of $A_2Q/M/P_2Q_5/Q$ in various stochoimetric ratios. The powdered reagents are loaded, in a dry box under inert atmosphere, into a glass vial and thoroughly mixed to ensure a homogeneous mixture. The resulting mixture is loaded into a Pyrex or quartz tube which serves as the reaction container. The choice of reaction container depends on the desired reaction temperature, Pyrex tubes are routinely used for intermediate temperature reactions (200°C - 550°C), while quartz tubes are used for high temperature reactions (≥ 550°C). The tubes are evacuated to a pressure of ~1×10^{-3} torr and flame sealed. The sealed tubes are loaded into a computer controlled furnace and then subjected to a preprogrammed heating profile. Upon heating, the $A_2Q/P_2Q_5/Q$ fuse together, forming a $A_x[P_yQ_z]$ flux in which the coordination chemistry of the various $[P_xQ_y]^{n-}$ units can be explored with a variety of metal ions. Although the redox chemistry that occurs is quite complex, and the exact composition of the resulting molten fluxes

remains unknown, one can gain insight by applying the basic principles learned from the polychalcogenide chemistry.

In molten polychalcogenide systems, the $(Q_x)^{2-}$ ligands exist in a variety of lengths by undergoing a complicated self-redox equilibrium as shown in Scheme 1.

Scheme 1

$$\left[\begin{array}{c} Q \\ \| \\ Q \end{array}\right]^{2-} + \left[\begin{array}{c} Q \\ / \\ Q \\ \| \\ Q \\ \backslash \\ Q \end{array}\right]^{2-} \rightleftharpoons \left[\begin{array}{c} Q \\ \| \\ Q \\ \backslash \\ Q \end{array}\right]^{2-} + \left[\begin{array}{c} Q \\ / \\ Q \\ \| \\ Q \end{array}\right]^{2-}$$
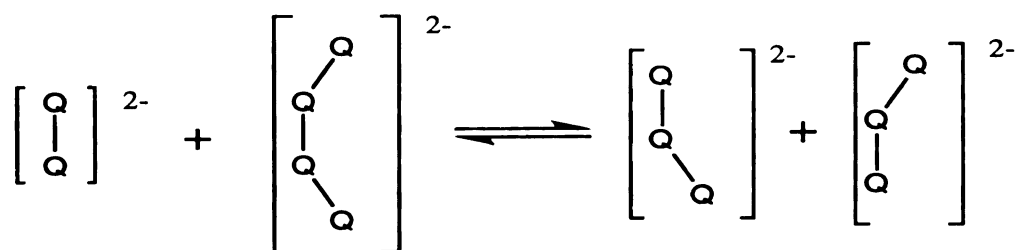
Scheme 1 shows an elementary example; another example is the initial flux formation reaction, where Q^{2-} reacts with n equivalents of Q forming the starting $Q_{(n+1)}^{2-}$ flux. The actual equilibrium is far more complicated than the examples presented here and is still not completely understood. The various $(Q_x)^{2-}$ ligands serve a dual purpose, the terminal chalcogenide atoms have a formal oxidation state of negative one, while the internal chalcogenide atoms are all formally neutral, keeping with the Zintl concept. This produces a basic, yet oxidizing media in which the metal is solubilized by a redox reaction with the internal chalcogenide atoms of the various polychalcogenide ligands in the flux, forming M^{n+} ions and breaking the $(Q_x)^{2-}$ ligands into smaller chalcogenide fragments by reducing a Q-Q bond.

The addition of P_2Q_5 renders the Lewis acid-base equlibria described above even more complex. The P_2Q_5 reacts with the molten polychalcogenide ligands to form various $A_x[P_yQ_z]$ units. The previously solvated metal cations are then coordinated by the basic

$[P_yQ_z]^{n-}$ units or $(Q_x)^{n-}$ ligands forming soluble intermediates; acting as potential nucleation sites for the growth of single crystals. These fluxes, being liquids, allow rapid diffusion of these intermediates, via a dissolution-reprecipitation process, promoting the growth of high-quality single crystals. This process of single crystal growth, commonly called a mineralizer effect, is particularly effective since the flux can redissolve small or poorly formed crystallites and redeposit the material onto larger well-formed crystallites or form new nucleation sites. Since the major means of characterization of new solid-state materials is determining the single crystal X-ray structure, methods that routinely provide well crystallized products are necessary.

The composition of the $A_2Q/M/P_2Q_5/Q$ mixture is a very important variable that can be easily manipulated. Changes in the $A_2Q/M/P_2Q_5/Q$ flux composition can alter the basicity of the flux, dramatically changing the coordination chemistry of the various $[P_xQ_y]^{n-}$ units with metal ions. The guiding principles for changing the Lewis basicity of the polychalcophosphate flux are:

(I) The elemental chalcogenide concentration is inversely proportional to the

Lewis basicity of the flux.

(II) The amount of A_2Q is directly proportional to the basicity of the flux. (III)

After extensive experimental observations, the amount of P_2Q_5 was determined to be critical in controlling the Lewis basictiy of the resulting flux, stabilizing various $[P_xQ_y]^{n-}$ units. Increasing the P_2Q_5 concentration (increasing the Lewis acidity) to the point where the elemental sulfur dilutant was removed, favoring the formation of nuclearity $[P_xS_y]^{n-}$ units, containing the P^{+5} species.

(IV) The size of the cation plays a significant role in the dimensionally of the resulting $[M_xP_yS_z]^{n-}$ framework. An example of the cation effect is observed in the structures of $A_2Ag_2P_2Se_6$ (A = K, Cs)[25b]. When the $[Ag_2P_2Se_6]^{2n-}$ framework is stabilized by Cs^+ cations, a chain structure of alternating ethane-like $[P_2Se_6]^{4-}$ units bound to Ag_2^{+2} dimers are observed, see Figure 1-5A. However, substitution of the larger Cs^+

cations by the smaller K^+ cations results in a dramatic structural change, stabilizing a three-dimensional $[Ag_2P_2Se_6]^{2n-}$ framework. This novel yet complicated three-dimensional tunnel framework consists of $AgSe_4$ tetrahedrons linked to $[P_2Se_6]^{4-}$ units forming K^+ filled channels that run along the crystallographic a - axis, see Figure 1-5B. The $[P_2Se_6]^{4-}$ units are assembled into layers that are connected by the $AgSe_4$ tetrahedrons into a dense three-dimensional network. The $[P_2Se_6]^{4-}$ units bridge four Ag^+ ions in two different binding modes, see Figure 1-5C. Surprisingly, no $Ag^+ \cdot \cdot \cdot Ag^+$ contacts were observed, which could not have been predicted based on the structure of $Cs_2Ag_2P_2Se_6$.

(A)

(B)

(C)
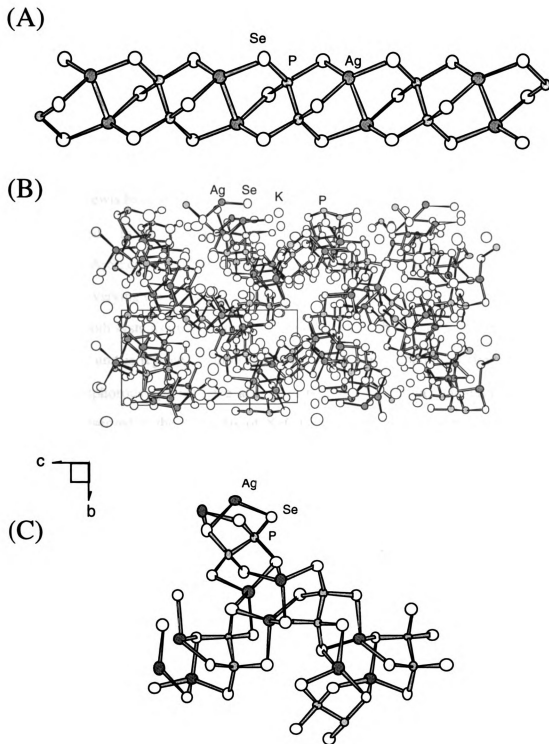
Figure 1-5:   (A) View of a single $[Ag_2P_2Se_6]^{2n-}$ chain, with labeling. (B) Unit cell of $K_2Ag_2P_2Se_6$ as viewed down the a - axis. (C) A Portion of the $[Ag_2P_2Se_6]^{2n-}$ framework, highlighting the $[P_2Se_6]^{2n-}$ binding modes.

Throughout our exploration of the chalcophosphate fluxes we have observed a significant difference between the selenophosphate and thiophosphate systems. While the thiophosphate flux appears to favor the P^{5+} species, the selenophosphate flux displays a tendency to favor the reduced P^{+4} species. The stability of the reduced P^{+4} species is consistent with the lower oxidizing power of the Se_x^{2-} ligands compared to S_x^{2-} ligands.

The Lewis basicity of the chalcophosphate flux controls the nature of the $[P_xQ_y]^{n-}$ units observed. In the selenophosphate system, the basicity is controlled primarily by changing the A_2Se concentration, while in the thiophosphate system, the Lewis basicity is controlled by varying the P_2S_5 concentration. The tetrahedral $[PQ_4]^{3-}$ (Q = S, Se) unit is observed in both systems under highly basic conditions (high A_2Q or low P_2S_5). Although the $[P_2Se_6]^{4-}$ unit is repeatedly observed under Lewis acidic conditions (low A_2Q), other reduced phosphorous species have also been reported.[37] Further increasing the Lewis acidity, as observed in the synthesis of $K_2Cu_2P_4Se_{10}$,[38] condenses two $[P_2Se_6]^{4-}$ units together via bridging selenides and forms a $[P_4Se_{10}]^{4-}$ unit containing a cyclohexane-like ring.

In the thiophosphate system, increasing the Lewis acidity of the flux (increasing the P_2S_5 concentration), favors the formation of higher nuclearity $[P_xS_y]^{n-}$ units. To further explore these phosphorous-rich conditions the elemental sulfur was removed from the reaction. A molten thiophosphate flux still forms by the combination of A_2S and P_2S_5, but the oxidative properties are different. With the lack of the elemental sulfur, a portion of the thiophosphate flux now must be sacrificial to oxidize the coinage metal. The exact influence of these phosphorous-rich conditions is not understood. Phosphorous-rich reactions produced $A_2CuP_3S_9$ (A = K, Rb)[39] and $Cs_2CuP_3S_9$[40] a one-dimensional compound with an unprecedented acentric helical packing arrangement of the anionic framework. Increasing both the P_2S_5 and Cs_2S concentrations lead to the synthesis of $Cs_2Cu_2P_2S_6$,[39] a thiophosphate compound containing a reduced P^{+4} species in the ethane-

like $[P_2S_6]^{4-}$ unit. This unprecedented observation suggests that slight changes in the Lewis acidity, via specific Cs_2S/P_2S_5 ratios, may stabilize the reduced P^{+4} species.

3. Nature of the polychalcoantimonate fluxes

The methodology of the polychalcoantimonate fluxes is very similar to the polychalcophosphate fluxes. A typical reaction involves the combination of $A_2Q/M/Sb/Q$ in various ratios, just as in the polychalcophosphate system, the only difference is the choice of antimony source. In the thioantimonate system, elemental Sb was experimentally observed to give the best results, while in the selenoantimonate system, the binary Sb_2Se_3 compound with a preoxidized Sb source is used. The reactions temperatures employed by the thioantimonate reactions (280 - 500°) were not sufficient to dismantle the Sb_2Se_3 framework. The elevated reaction temperatures utilized by the selenoantimonate system ($\geq$ 500°C) were required to dismantle the Sb_2Se_3 extended framework. Upon heating, the $A_2Q/Sb_2Q_3/Q$ fuse together, forming a $A_x[Sb_yQ_z]$ flux in which the coordination chemistry of the various $[Sb_xQ_y]^{n-}$ units can be explored with a variety of metal ions.

The addition of Sb or the binary Sb_2Se_3 renders the Lewis acid-base equlibria described above even more complex. The Sb or the binary Sb_2Se_3 reacts with the molten polychalcogenide ligands to form various $A_x[Sb_yQ_z]$ units, which can coordinate to the solvated metal cations forming a variety of $[M_xSb_yQ_z]^{n-}$ frameworks, stabilized by alkali cations.

The composition of the $A_2Q/M/Sb_2Q_3/Q$ mixture is a significant variable that can be easily manipulated. Changes in the $A_2Q/M/Sb_2Q_3/Q$ flux composition can alter the basicity of the flux resulting in dramatic changes in the coordination chemistry with metal ions.

A comparison of this system to the polychalcophosphate fluxes provides insight into the structural and chemical complexity of the two systems. The polychalcoantimonate system follows the experimentally observed trend of the polychalcophosphate system;[16] basic conditions (increase A_2Q) favor the tetrahedral $[EQ_4]^{3-}$ unit (E = P, Sb; Q = S, Se)

and acidic conditions (decrease A_2Q) favors a reduced species. In the basic system, the $[SbQ_4]^{3-}$ unit is observed as the discrete tetrahedral species, while the $[PQ_4]^{3-}$ unit (Q = S, Se), exhibits a complex condensation equilibrium. Examples include $[P_2S_7]^{4-}$ [24b], $[P_3S_9]^{3-}$ [39,40], $[P_2Se_8]^{4-}$ [24b], and $[P_2Se_9]^{4-}$.[25c]

For the polychalcophosphate system, Lewis acidic conditions (decreasing A_2Q or increasing the chalcogenide concentration) favor the stabilization of the reduced P^{+4} species which is readily observed in the ethane - like $[P_2Q_6]^{4-}$ unit (Q = S, Se). The stability of the reduced P^{+4} species is consistent with the lower oxidizing power of the Se_x^{2-} ligands compared to S_x^{2-} ligands. In the case of the Se_x^{2-} ligands, the lesser oxidative power of the Se atoms cannot oxidize the P atoms to the highly oxidized P^{5+} species, resulting in the stabilization of $[P_xQ_y]^{n-}$ units containing P^{4+} species due the excess of polychalcogenide ligands in the flux. Conceptually, stabilizing a $[Sb_xS_y]^{n-}$ unit containing the Sb^{4+} is possible but it has yet to be reported.

Under Lewis acidic conditions, the pyramidal Sb^{3+} species is the only variable oxidation state species observed. Although there is not enough experimental data to predict the exact nature of these $[Sb_xS_y]^{n-}$ units, Lewis acidic conditions can stabilize a variety of species, such as the tetrahedral $[SbQ_4]^{3-}$, pyramidal $[SbS_3]^{3-}$, and various oligomeric $[Sb_xS_y]^{n-}$ units. In the thioantimonate fluxes increasing the Sb concentration stabilizes oligomeric $[Sb_xS_y]^{n-}$ units, containing the Sb^{+3} species, increasing the repertoire of $[Sb_xS_y]^{n-}$ units available for the formation of new extended frameworks.

The advantages to the thiophosphate and chalcoantimonate flux methods over traditional high temperature reactions are:

(I) The use of intermediate reaction temperatures (280 - 550°C) allows the stabilization of metastable phases and the isolation of new $[P_xS_y]^{n-}$ and $[Sb_xQ_y]^{n-}$ units.

(II) The dual nature of the polychalcogenide fluxes, as an reactive solvent and a minrealizer, provides a mechanism for the formation of high quality crystalline materials, critical for the crystal structure determination and any potential applications.

(III) The tunable Lewis basicity of the fluxes allows for the stabilization of a specific $[P_xS_y]^{n-}$ and $[Sb_xQ_y]^{n-}$ unit, or a completely unexpected unit.

(IV) The $[P_xS_y]^{n-}$ and $[Sb_xQ_y]^{n-}$ units readily bind with a variety of metals with a ever increasing repertoire of bonding modes.

(V) The ease of isolation of highly pure materials due to the residual flux's high solubility in common organic solvents.

The $[P_xS_y]^{n-}$ and $[Sb_xQ_y]^{n-}$ units were thought to be the critical factor in determining the structure. They are typically thought of as molecular or ologomeric building blocks that bond to coinage metal cations in the polychalcogenide flux, building extended frameworks stabilized by alkali metal cations. The growing diversity of the phases synthesized owe their conception to the great diversity of the $[P_xS_y]^{n-}$ and $[Sb_xQ_y]^{n-}$ units observed and the staggering number of different binding modes displayed by these units. A unique feature of the thioantimonate system is the stabilization of novel $[M_xSb_yS_z]^{n-}$ frameworks that are dominated by the coinage metal chalcogen framework, not by the thioantimonate unit. This is a completely unexpected result, suggesting that an entirely new area of this chemistry can be explored. Even with this result, the thiophosphate and chalcoantimonate systems is critical for designing new materials since the $[P_xS_y]^{n-}$ and $[Sb_xQ_y]^{n-}$ units can be controlled by manipulating the Lewis basicity of the flux. To give a better indication of the great variety of binding modes of the $[Sb_xQ_y]^{n-}$ units we have constructed Tables 1-1 and 1-2. Table 1-1 summarizes the synthetic conditions that have stabilizes the various $[P_xS_y]^{n-}$ and $[Sb_xQ_y]^{n-}$ units discovered throughout the course of this dissertation. Table 1-2 lists the $[Sb_xQ_y]^{n-}$ units observed and an example of the binding mode displayed by these units. The vast majority of results shown in this table were unknown before the start of this research. Even more importantly, these two systems should be thought of as completely different systems, even when $[P_xS_y]^{n-}$ and $[Sb_xQ_y]^{n-}$ units are similar the resulting chemistry is rarely even closely related.

This dissertation focuses on the synthesis, characterization, and properties of several new thiophosphates and chalcoantimonates. The chemistry revolved around the coinage metals because of their highly chalcophilic nature and because the quaternary thiophosphate and chalcoantimonate chemistry was largely unexplored. The exploratory synthetic work performed here lays the ground work for the systematic synthesis and further exploration into this chemistry.

Table 1-1.   Synthetic conditions for the different $[P_yQ_z]^{n-}$ and $[Sb_yQ_z]^{n-}$units. (M = metal, A_2Q = alkali chalcogenide).

M / P_2Se_5 / A_2Se / Se	P^{n+} / ligands	References
1 / 1-3 / 1-2 / 10	P^{4+} / $[P_2Se_6]^{4-}$	16
1 / 1.5-2 / 3-4 / 10	P^{5+} / $[PSe_4]^{3-}$, $[PSe_5]^{3-}$, $[P_2Se_8]^{4-}$	16, 24b, 25c
1 / 2-3 / 2 / 10	P^{5+} / $[P_2Se_7]^{4-}$, $[P_2Se_9]^{4-}$	16, 25c
1 / 1 / 2 / 10	P^{3+} / $[P_3Se_9]^{4-}$	37

M / P_2S_5 / A_2S / S	P^{n+} / ligands	References
1 / 1.5-3 / 2-4 / 4-12	P^{5+} / $[PS_4]^{3-}$, $[P_2S_7]^{4-}$	24b
1 / 3 / 2 / 4	P^{4+} / $[P_2S_6]^{4-}$,	24a
1 / 2-3/ 2 / -	P^{5+} $[P_3S_9]^{3-}$	39,40
1 / 3 / 3 / -	P^{4+} / $[P_2S_6]^{4-}$,	39

M / Sb / A_2S / S	Sb^{n+} / ligands	References
1-2 / 1 / 2 / 8	Sb^{5+} / $[SbS_4]^{3-}$	36,43
1 / 1.5 / 1 / 8	Sb^{5+} / Sb^{3+} $[SbS_4]^{3-}$, $[Sb_2S_4]^{2-}$	36,43
3-4 / 1 / 2 / 8-16	Sb^{5+} / Sb^{3+} $[SbS_4]^{3-}$, $[SbS_3]^{3-}$	36,43
2 / 1 / 2 / 8	Sb^{3+} / $[Sb_4S_7]^{2-}$	49

M / Sb / A_2Se / Se	Sb^{n+} / ligands	References
4/1/1/16	Sb^{3+} / $[Sb_2Q_6]^{4-}$	48
2 / 1 / 2 / 8	Sb^{3+} / $[Sb_2Se_5]^{4-}$	50
1 / 3[a]	Sb^{3+} / $[SbSe_2]^-$, $\{[SbSe_2]\}_2^{2-}$	51

[a]The Sb and A_2Se_x source was the ternary compound Rb_3SbSe_3.

Table 1-2.   Structure and coordination examples of the various $[Sb_xQ_y]^{n-}$ units.
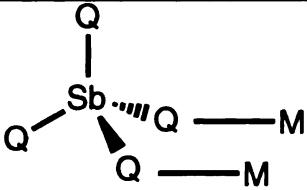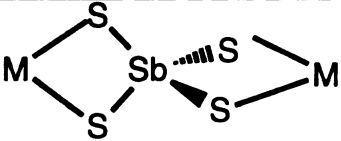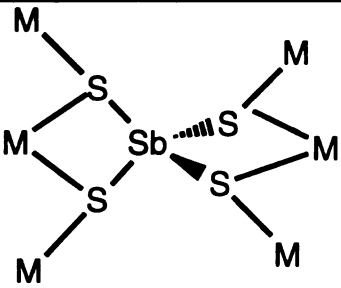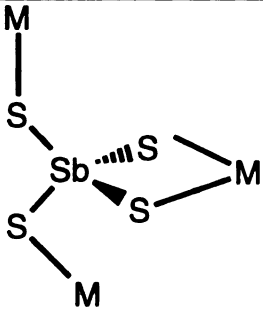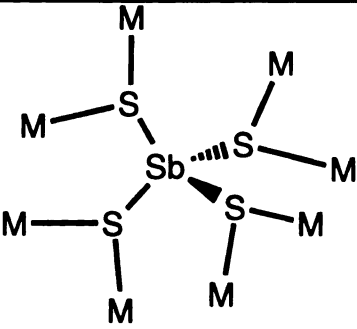
	$[SbS_4]^{3-}$ in A_2AuSbS_4 (A = Rb, Cs)[40] $[SbS_4]^{3-}$ in $Cs_3Ag_2Sb_3S_8$[36,43] $[SbSe_4]^{3-}$ in $Cs_3Ag_2Sb_3Se_8$[36,43]
	$[SbS_4]^{3-}$ in K_2AgSbS_4[36,43]
	$[SbS_4]^{3-}$ in KAg_2SbS_4[36]
	$[SbS_4]^{3-}$ in Rb_2AgSbS_4[36,43]
	$[SbS_4]^{3-}$ in $\alpha\text{-}RbAg_2SbS_4$[36,43]
	(Cont.)
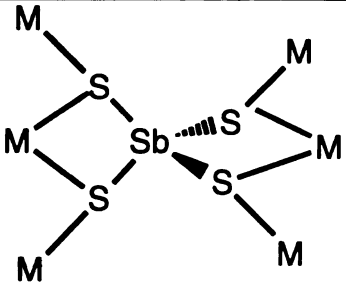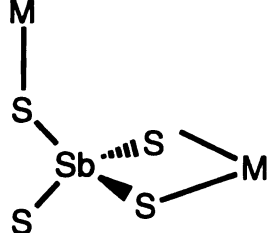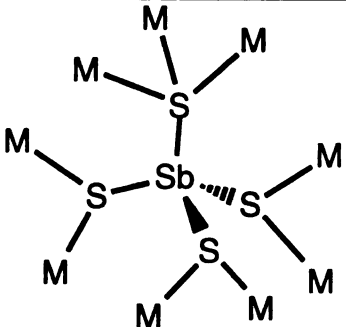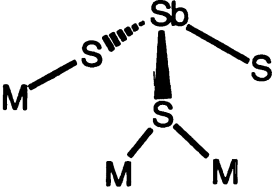
	Table 1-2. (Continued)
	$[SbS_4]^{3-}$ in β-RbAg$_2$SbS$_4$[45]
	$[SbS_4]^{3-}$ in α,β-Cs$_2$AgSbS$_4$[36,43]
	$[SbS_4]^{3-}$ in Cs$_2$Ag$_{20}$Sb$_4$S$_{19}$[46]
	$[SbS_3]^{3-}$ in Na$_2$CuSbS$_3$[44]
	(Cont.)
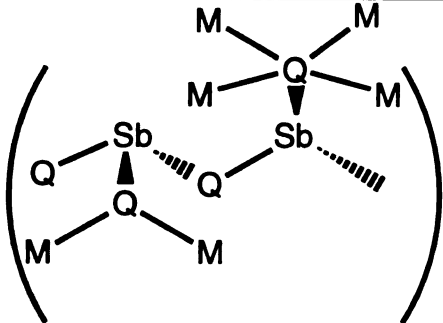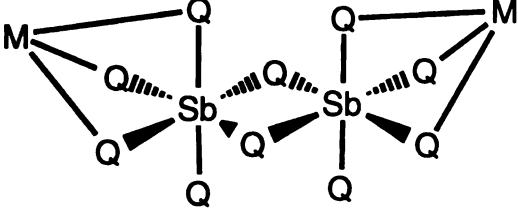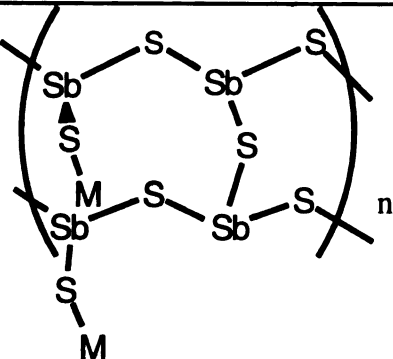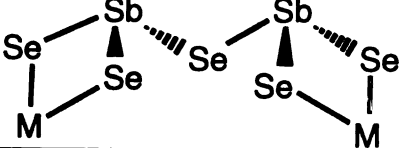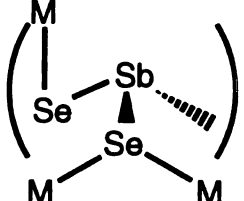
	Table 1-2. (Continued)
	$[Sb_2S_4]^{2-}$ in $Cs_3Ag_2Sb_3S_8$[36,43] $[Sb_2Se_4]^{2-}$ in $Cs_3Ag_2Sb_3Se_8$[43]
	$[Sb_2S_6]^{6-}$ in $K_2La_2Sb_2S_9$[48] $[Sb_2Se_6]^{6-}$ in $K_2Gd_2Sb_2Se_9$[48]
	$[Sb_4S_7]^{2-}$ in $Rb_2Au_6Sb_4S_{10}$[49]
	$[Sb_2Se_5]^{4-}$ in $KThSb_2Se_6$[50]
	$[SbSe_2]^{-}$ in $RbCuSb_2Se_4 \cdot H_2O$[51]
	(Cont.)
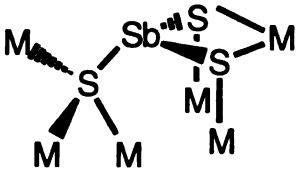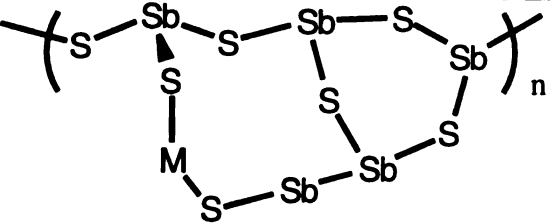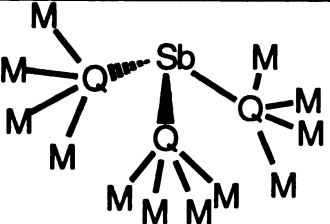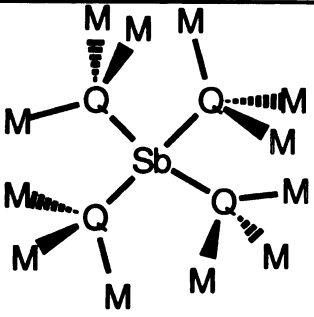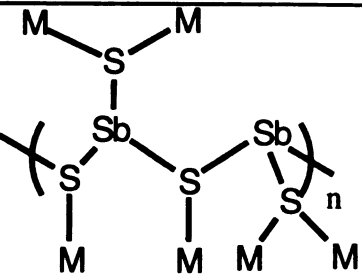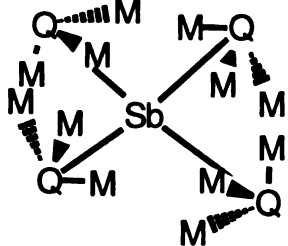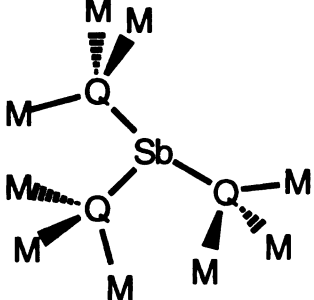
	Table 1-2. (Continued)
	$[SbS_3]^{3-}$ in $Cs_3Ag_2Sb_3S_7$[52]
	$[Sb_4S_7]^{2-}$ in $CsAgSb_4S_7$[52]
	$[SbSe_3]^{3-}$ in Cu_3SbSe_3[53] $[SbSe_3]^{3-}$ in Ag_3SbS_3[54]
	$[SbSe_4]^{3-}$ in Cu_3SbSe_4[55] $[SbS_4]^{3-}$ in Cu_3SbS_4[56]
	$[SbS_2]^{n-}$ in $AgSbS_2$[59]
	(Cont.)

27

	Table 1-2. (Continued)
	$[SbS_4]^{3-}$ in Cu_3SbS_4[60]
	$[SbS]^{3-}$ in Ag_3SbS_3[61] $[SbS]^{3-}$ in Ag_5SbS_4[62] $[SbS]^{3-}$ in Cu_3SbS_3[63] $[SbS]^{3-}$ in $Cu_{12}Sb_4S_{13}$[64]

List of References

1. Zweibel, K.; Michell, R. *CuInSe2 and CdTe: Scale-up for Manufacturing*, Solar Energy Research Institute, **Dec. 1989** and references therein. (b) Mickelsen, R.A.; Chen, W.S., *In Ternary and Multinary Compounds*, Eds. Deb, S.K.; Zunger, Z., Proceedings of the 7th Conference, Materials Research Society, **1987**, 39.

2. Smity, R.A. *Semiconductors*, Cambridge University Press, **1978**, 438. (b) Barlett, B.E. *Infared Phys.*, **1969**, *9*, 35.

3. Ballman, A.A.; Byer, R.L.; Eimerl, D,; Feigelson, R.S.; Feldman, B.J.; Goldberg, L.S.; Menyuk, N.; Tang, C.L. *Applied Optics*, **1987**, *26*, 224.

4. (a) Rowe, D. M.; Bhandari, C. M. *Modern Thermoelectrics*, Holt, Rinehart, and Winston, London, 1983, p. 103. (b) Borkowski, K.; Pyzyluski, J. *J. Mater. Res. Bull.*, **1987**, *22*, 381.

5. Ballman, A.A.; Byer, R.L.; Eimerl, D,; Feigelson, R.S.; Feldman, B.J.; Goldberg, L.S.; Menyuk, N.; Tang, C.L. *Applied Optics*, **1987**, *26*, 224.

6. (a) *The Sodium-Sulfur Battery*, Sudworth, J. L.; Tilley, A. R., Eds., Chapman and Hall, New York, 1985. (b) Fischer, W. *Mater Res. Soc Symp Proc.*, **1989**, *135*, 541. (c) Powers, R.W.; Karas, B.R. *J. Electrochem. Soc.*, **1989**, *136*, 2787.

7. (a) Chianelli, R. R.; Pecoraro, T. A.; Halbert, T. R.; Pan,W.-H.; Stiefel, E. I.*J. Catal.*, **1984**, *86*, 226. (b) Pecoraro, T. A.; Chianelli, R. R. *J. Catal.*, **1981**, *67*, 430. (c) Harris, S.; Chianelli, R. R. *J. Catal.*, **1984**,*86*, 400.

8. Steigerwald in *Inorganometallic Chemistry*, T.P. Fehlner, Ed., Plenum Press, New York, 1992, p.333.

9. Rabenau, A. *Angew. Chem., Int. Ed. Engl.*, **1985**, *24*, 1026.

10. Wood, P.T.; Pennington, W. T.; Kolis, J. W. *J. Am. Chem. Soc.*, **1992**, *114*, 9233.

11. Barrer, R.M. *Hydrothermal Chemistry of Zeolites*, Academic, New York, 1982.

12. (a) Morris, R.E.; Wikinson, A. P.; Cheetham, A. K. *Inorg. Chem.*, **1992**, *31*, 4774. (b) Harrison, W. T. A.; Stucky, G. D.; Morris, R.E.; Cheetham, A. K. *Acta Crystallogr.*, **1992**, *C48*, 1365. (c) Morris, R.E.; Harrison, W. T. A.; Stucky, G. D.; Cheetham, A. K. *J. Solid State Chem.*, **1991**, *94*, 227. (d) Harrison, W. T. A.; Morris, R.E.; Cheetham, A. K. *Acta Crystallogr.*, **1992**, *C48*, 1182. (e) Morris, R.E.; Hriljac, J. A.; Cheetham, A. K. *Acta Crystallogr.*, **1990**, *C46*, 2013, (1990). (f) Morris, R.E.; Cheetham, A. K. *Chem. Mater.*, **1994**,*6*, 67. (g) Harrison, W. T. A.; Stucky, G. D.; Cheetham, A. K. *Eur. J. Solid State Inorg. Chem.*, **1993**,*30*, 347.

13. (a) Liao, J.-H.; Kanatzidis, M.G. *Inorg. Chem.*, **1992**, *31*, 431. (b) Kim, K.-W.; Kanatzidis, M.G. *J. Am. Chem. Soc.*, **1992**, *114*, 4878. (c) Chou, J.-H.;

Kanatzidis, M.G. *Chem. Mater.*, **1995**, 7, 5. (d) Chou, J.-H.; Kanatzidis, M.G. *Inorg. Chem.*, **1994**, 33, 1001. (e) Stephan, H.-O.; Kanatzidis, M.G. *J. Am. Chem. Soc.*, **1996**, 118, 12226. (f) Chou, J.-H.; Hanko, J.A.; Kanatzidis, *Inorg. Chem.*, **1997**, 36, 4. (g) Bowes, C.L.; Ozin, G.A.; *Adv. Mater.*, **1996**, 8, 13.

14. Kanatzidis, M. G. *Chem. Mater.*, **1990**, 2, 353.

15. Sutorik, A.C.; Kanatzidis, M.G. *Prog. Inorg. Chem.*, **1995**, 43, 151.

16. Kanatzidis, M.G. *Curr.Opinion Solid State and Mater. Sci.*, **1997**, 2, 139.

17. (a) Dhingra, S.; Kanatzidis, M.G. *Science*, **1992**, 258, 1769. (b) Marking, G.A.; Hanko, J.A.; Kanatzidis, M.G. *Chem. Mater.*, **1998**, 10, 1191.

18. Marking, G.A.; Liao, J.-H.; Kanatzidis, M.G. manuscript in preparation. (b) Kanatzidis, M.G.; Liao, J.-H.; Marking, G.A., United States Patent 5,618,471. (c) Kanatzidis, M.G.; Liao, J.-H.; Marking, G.A., United States Patent 5,614,128.

19. Liao, J.-H., Ph.D. Thesis, Michigan State University, East Lansing, MI, **1993.**

20. Liao, J.-H.; Varotis, C.; Kanatzidis M.G. *Inorg, Chem.*, **1993**, 32, 2453.

21. Sutorik, A.C.; Kanatzidis, M.G. *Chem. Mater.*, **1997**, 9, 387.

22. Liao, J.-H.; Kanatzidis M.G. *Chem. Mater.*, **1993**, 5, 1561.

23. (a) Zhang, X.; Kanatzidis M.G. *J. Am. Chem. Soc.*, **1994** 116, 1890.
    (b) Zhang, X.; Kanatzidis M.G. *Inorg, Chem.*, **1994** 33, 1238.

24. (a) McCarthy, T.J.; Kanatzidis M.G. *Chem. Mater.*, **1993**, 5, 1061.
    (b) Chondroudis, K.; Hanko, J.A.; Kanatzidis, M.G. *Inorg. Chem.*, **1997**, 36, 2632. (c) McCarthy, T.J.; Kanatzidis M.G. *J. Alloy Comp.*, **1996**, 236, 70.

25. (a) McCarthy, T.J.; Kanatzidis M.G. *J. Chem. Soc. Chem. Commun.*, **1994**, 1089. (b) McCarthy, T.J.; Kanatzidis M.G. *Inorg. Chem.*, **1995**, 34, 1257. (c) Chondroudis, K.; Kanatzidis, M.G. *Inorg. Chem.*, **1995**, 34, 5401.

26. (a) Marking, G. A.; Kanatzidis, M.G.Abstract from 210th Fall ACS Meeting, Chicago Il. (b) Marking, G.A.; Hanko, J.A.; Kanatzidis, M.G. *Chem. Mater.*, **1998**, 10, 1191.

27. McCarthy, T.J.; Kanatzidis M.G. *J. Chem. Soc. Chem. Commun.*, **1994**, 1089.

28. Takeuchi, Y.; Sadanaga, R. *Z. Kistallogr.*, **1969**, 33, 1205.

29. Dittmar, V.G.; Schafer, H. *Z. Anorg. Allg. Chem.*, **1977**, 437, 183.

30. Cordier, G.; Schafer, H. *Z. Anorg. Allg. Chem.*, **1982**, 437, 519.

31. Cordier, G.; Schwidetzky, C.; Schafer, H. *Rev. Chem. Min.*, **1982**, 19, 179.

32.   (a) Olivier-Fourcade, E.; Phillippot, J.; M. Maurin Z. Anorg. Allg. Chem., **1978**, *446*, 159. (b) Graf, H.A.; Schafer, H. Z. Anorg. Allg. Chem., **1975**, *414*, 211. (c) Kanishcheva, A.S.; Kuznetsov, V.G.; Lazasrev, V.B.; Tarasova, T.G.; Zh. Strukt. Khim., **1977**, *18*, 1069. (d) Kanishcheva, A.S.; Mikhailov, Y.N.; Kuznetsov, V.G.; Batog, V.N. Dolk. Adad. Nauk SSSR, **1980**, *251*, 603. (e) Cordier, G.; Schafer, H. Rev. Chem. Min., **1981**, *18*, 218. (f) Dorrscheidt, W.; Schafer, H. Z. Naturforsch., **1981**, *36b*, 410.

33.   (a) Ko Y.H.; Tan K.M.; Parise J.B.; Darovsky A. Chem. Mater., **1996**, *8* , 493. (b) Parise J.B.; Ko Y.H. Chem. Mater., **1992**, *4* , 1446. (c) Parise J.B. J. Chem. Soc. Chem. Commun., **1990**, 1553. (d) Sheldrick, W.S.; Hausler, H.-J. Z. Anorg. Allg. Chem., **1988**, *561*, 149. (e) Dittmar, V.G.; Schafer, H. Z. Anorg. Allg. Chem., **1978**, *441*, 93. (f) Sheldrick, W.S.; Hausler, H.-J. Z. Anorg. Allg. Chem., **1988**, *557*, 105. (g) Eisenmann, B.; Schafer, H. Z. Narurforsch,. **1979**, *34b*, 383. (h) Graf, H.A.; Schafer, H. Z. Narurforsch., **1972**, *27b*, 735.

34.   McCarthy, T.J.; Kanatzidis M.G. Inorg. Chem., **1995**, *34*, 1257.

35.   Imafuku, M.; Nakai, I.; Nagashima, K. Mat. Res. Bull., **1986**, *21*, 493

36.   (a) Wood, P.T.; Schimek, G.L.; and Kolis J.W. Chem. Mater., **1996**, *8*,. (b) Schimek, G. L.; Jerome, J. E.; Pennington, W. T.; Kolis, J. W. J. Solid State Chem., **1996**, *123*, 277.

37.   Chondroudis, K.; Kanatzidis, M.G. Angew. Chem., **1997**, *36*, 1324.

38.   Chondroudis, K.; Kanatzidis, M.G. Submitted for publication.

39.   Hanko, J.A.; Sayettat, J.; Jobic, S.; Brec, R.; Kanatzidis, M.G. Submitted for publication.

40.   Hanko, J.A.; Kanatzidis, M.G. Submitted for publication.

41.   Hanko J.A.; Kanatzidis,M.G. J. Alloy and Comp., Accepted for publication.

42.   Drake, G.W.; Kolis, J.W. Coord. Chem. Rev. , **1994**, *137*, 131.

43.   Hanko, J. A.; Kanatzidis, M. G. Abstract #0413 from 210th Fall ACS Meeting, Chicago Il 1995.

44.   Jerome, J.E.; Schimek, G.L.; Drake, G.W.; Kolis, J.W. Eur. J. Solid State Chem., **1996**, *33*, 765.

45.   Hanko, J.A.; Kanatzidis, M.G. To be published.

46.   Hanko, J.A.; Kanatzidis, M.G. Submitted for publication.

47   Lee. J.; Chen, Z.; Wang, X.; Proserpio, D. M. J. Alloy and Comp., **1997**, *262-263*, 28.

48.   Choi, K.S.; Hanko, J.A.; Kanatzidis, M.G. Manuscript in preparation.

49.   Hanko, J.A.; Kanatzidis, M.G. J. Chem Soc. Chem Comm., **1998**,725.

50.   Choi, K.S.; Iordanidis, L. Chondroudis, K.; Kanatzidis, M.G. *Inorg. Chem.*, **1997**, *36*, 3804.

51.   Hanko, J.A.; Kanatzidis, M.G. *Angew. Chem. Int. Ed.,* **1998**, *37*, 342.

52.   Schimek, G.L.; Jerome, J.E.; Pennington, W.T.; Kolis, J.W. Submitted for publication.

53.   Pfitzner, A. *Z. Anorg. Allg. Chem.*, **1995**, *621*, 685.

54.   Harker, D. *J Chem. Phys.*, **1936**, *4*, 381.

55.   Pfitzner, A. *Z. Kistallogr.*, **1995**, *209*, 1205.

56.   Garin, J.; Parthe, E.; Oswald, H.R. *Acta Crystallogr.*, **1972**, *B28*, 3672.

57.   Imamov, R.M.; Pinsker, Z.G.; Ivchenko, A.I. *Krista.*, **1964**, *9*, 853.

58.   Hofmann, W. *Z. Kistallogr.*, **1932**, *84*, 177.

59.   Knowles, C.R.; *Acta Crystallogr.*, **1964**, *B17*, 847.

60.   Alieva, A.G.; Pinsker, Z.G. *Krista.*, **1961**, *6* , 204.

61.   Kutoglu, A. *Neues Jahrbuch Miner.*, **1968**, *5*, 145.

62.   Petrunina, A.A.; Maksimov, B.A.; Ilyukhin, V.V.; Belov, N.V. *Dolk. Adad. Nauk SSSR*, **1969**, *188*, 324.

63.   Machatschki, F. *Z. Kistallogr.*, **1928**, *68* , 204.

64.   Wuensch, B.J. *Z. Kistallogr.*, **1964**, *119*, 437.

CHAPTER 2

Chemistry of Silver in Molten Alkali Metal Polychalcoantimonate Fluxes. Synthesis and Characterization of the Quaternary Compounds A_2AgSbS_4 (A = K, Rb, Cs), and $Cs_3Ag_2Sb_3Q_8$ (Q = S, Se).

1. Introduction

Over the past several years, we have demonstrated that molten salt (poly)chalcogenide syntheses at intermediate temperatures (200-500°C) can produce a wide range of new multinary compounds.[1] During these investigations, it was discovered that certain molecular fragments are stable in this molten reaction medium. This observation led to an interesting twist to this chemistry, namely the utilization of molecular building blocks in the synthesis of new solid-state lattices. These building blocks are formed by the *in situ* fusion of $A_2Q/E/Q$ to form $A_xE_yQ_z$ species. (A = K, Rb, Cs; E = main group element, and Q = S, Se). By this method, the polychalcogenide flux can act as a solvent in which the coordination chemistry of the highly basic $[E_xQ_y]^{n-}$ ligands can be investigated. This approach was first explored in the tin system[2], followed by tellurium[3], the P_2Q_5 glasses (Q = S^4, Se^5), and most recently germanium[6], all with surprisingly good results. In this context, we explored the coordination chemistry of *polychalcoantimonate ligands* with transition metals, particularly group 11 metals .

During the past two decades, a number of solid-state ternary alkali metal antimony (poly)chalcogenide compounds have been synthesized by either high temperature direct combination reactions[7] or solventothermal synthesis.[8] Recently, $Cs_2Sb_4S_8$ and $CsSbS_6$[9] were synthesized by the now proven molten polysulfide flux method. The vast majority of the quaternary antimony chalcogenide compounds are minerals,[10] containing $[Sb_xQ_y]^{n-}$ framework neutralized primarily by silver and/or lead cations. In most of these mineral examples, the antimony exists as Sb^{+3} species in pyramidal coordination. The $[Sb_xQ_y]^{n-}$ frameworks containing the Sb^{+3} species exhibit a rich structural diversity due to the stereochemical effect of the inert lone pair and the tendency for Sb to adopt three[11]- four[12]- or five-fold coordination[7g]. The first reported

quaternary alkali antimony sulfide compound was $KHgSbS_3$.[13] The structure consists of discrete pyramidal $[SbS_3]^{3-}$ units linked together by distorted tetrahedral Hg^{2+} cations forming a two - dimensional compound separated by K^+ cations. The first examples of a quaternary alkali antimony chalcogenides incorporating the tetrahedral $[SbS_4]^{4-}$ unit, prepared in supercritical ammonia, were only recently reported[14]. Because of the high stability of copper and silver antimony chalcogenide minerals[15], we investigated the group 11 transition metals in hopes of obtaining new quaternary alkali polychalcoantimonate compounds.

Here we report the synthesis, structural characterization, optical, and thermal properties of the new solid-state alkali quaternary polychalcoantimonates, A_2AgSbS_4 (A = K, Rb, Cs) and $Cs_3Ag_2Sb_3Q_8$ (Q = S, Se). Complementing the small number of isostructural compounds, synthesized in supercritical ammonia, recently reported by Kolis, *et. al.*[14] The $Cs_3Ag_2Sb_3Q_8$ (Q = S, Se) represent a rare example of a mixed valence antimony compound with both Sb^{5+} and Sb^{3+} centers in the same structure.

2. Experimental Section

2.1. Reagents

The reagents mentioned in this study were used as obtained unless noted otherwise: (i) antimony powder 99.999% purity, -200 mesh, Cerac Inc., Milwaukee, WI; (ii) silver powder 99.95% purity, -325 mesh Alfa AESAR Group, Seabrook, NH; (iii) cesium metal, analytical reagent, Johnson Matthey/AESAR Group, Seabrook, NH; (iv) rubidium metal, analytical reagent, Johnson Matthey/AESAR Group, Seabrook, NH; (v) potassium metal, analytical reagent, Aldrich Chemical Co., Milwaukee, WI; (vi) sulfur powder, sublimed, J.T. Baker Chemical Co., Phillipsburg, NJ; (vii) N,N-

dimethylformamide (DMF) reagent grade, EM Science, Inc., Gibbstown, NJ; (viii)

diethyl ether, ACS anhydrous, EM Science, Inc., Gibbstown, NJ.

2.2 Syntheses.

A_2S (A = K, Rb, Cs) and Cs_2Se were prepared by reacting stoichiometric amounts

of the elements in liquid ammonia as described elsewhere.[16] All manipulations were

carried out under a dry nitrogen atmosphere in a Vacuum Atmosphere Dri-Lab glovebox.

Preparation of K_2AgSbS_4 (I). An amount of 0.164g (1.50 mmole) K_2S, 0.054g

(0.50 mmole) Ag, 0.092g (0.75 mmole) Sb, and 0.128g (4 mmole) S were thoroughly

mixed and transferred to a 6-ml Pyrex tube which was subsequently flame-sealed in

vacuo ($\sim 10^{-3}$ Torr). The reaction mixture was heated to 400°C over 12 hrs in a computer-

controlled furnace. It was isothermed at 400°C for 4 days, followed by cooling to 100°C

at a rate of 4°C/hr and then to room temperature in 1 hour. The air and moisture sensitive

product was isolated by dissolving the K_2S_x and any $K_x[Sb_yS_z]$ flux with DMF under

inert atmosphere to obtain orange-yellow crystals in 46% yield based on Sb. Quantitative

microprobe analysis on single crystals gave $K_{1.8}AgSbS_{4.5}$ (average of three acquisitions).

Preparation of Rb_2AgSbS_4 (II). An amount of 0.102g (0.50 mmole) Rb_2S,

0.027g (0.25 mmole) Ag, 0.031g (0.25 mmole) Sb, and 0.080g (2 mmole) S were

thoroughly mixed and transferred to a 6-ml Pyrex tube which was subsequently flame-

sealed in vacuo ($\sim 10^{-3}$ Torr). The reaction mixture was heated to 350°C over 12 hrs in a

computer-controlled furnace. It was isothermed at 350°C for 4 days, followed by cooling

to 110°C at a rate of 4°C/hr and then to room temperature in 1 hour. The product, which

is air and water stable, was isolated by removing the excess flux as in (I) to obtain yellow

to yellow-orange crystals in 52% yield based on Sb. Quantitative microprobe analysis of single crystals of the two crystals gave $Rb_{1.9}Ag_{1.1}SbS_{4.7}$ (average of three acquisitions).

Preparation of Cs_2AgSbS_4 (III). An amount of 0.298g (1 mmole) Cs_2S, 0.054g (0.50 mmole) Ag, 0.062g (0.50 mmole) Sb, and 0.128g (4 mmole) S were thoroughly mixed and transferred to a 6-ml Pyrex tube which was subsequently flame-sealed in vacuo ($\sim10^{-3}$ Torr) and heated as in (II). The product, which is air and water stable, was isolated by removing the excess flux as in (I) to obtain yellow crystals in 63% yield based on Sb. Quantitative microprobe analysis on single crystals gave $Cs_{1.5}AgSbS_{4.5}$ (average of three acquisitions).

Preparation of $Cs_3Ag_2Sb_3S_8$ (IV). An amount of 0.164g (0.55 mmole) Cs_2S, 0.054g (0.50 mmole) Ag, 0.092g (0.75 mmole) Sb, and 0.128g (4 mmole) S were thoroughly mixed and transferred to a 6-ml Pyrex tube which was subsequently flame-sealed in vacuo ($\sim10^{-3}$ Torr). The reaction mixture was heated to 280°C over 12 hrs in a computer-controlled furnace. It was isothermed at 280°C for 4 days, followed by cooling to 100°C at a rate of 2°C/hr and then to room temperature in 1 hour. The product, which is air and water stable, was isolated by removing the excess flux as in (I) to obtain red crystals in a 72% yield based on Sb. Quantitative microprobe analysis on single crystals gave a atomic ratio of $Cs_{1.2}AgSb_{1.5}S_{3.5}$ (average of three acquisitions). Reactions at 280°C were contaminated with a small amount, $\sim5\%$, of Ag_3SbS_3. Increasing the reaction temperature to 350°C produced (IV) in a pure form.

Preparation of $Cs_3Ag_2Sb_3Se_8$ (V). An amount of 0.104g (0.30 mmole) Cs_2Se, 0.032g (0.30 mmole) Ag, 0.055g (0.45 mmole) Sb, and 0.126g (1.60 mmole) Se were thoroughly mixed and transferred to a 6-ml Pyrex tube which was subsequently flame-sealed in vacuo ($\sim10^{-3}$ Torr). The reaction mixture was heated as in (IV). The product,

which is air and water stable, was isolated by dissolving the excess flux as in (I) to obtain black crystals in a 75% yield based on Sb. Quantitative microprobe analysis on single crystals gave an atomic ratio of $Cs_{1.3}Ag_{1.2}Sb_{1.3}Se_{4.45}$ (average of three acquisitions).

2.3 Physical Measurements

Powder X-ray Diffraction . Analyses were performed using a calibrated Rigaku-Denki/RW400F2 (Rotaflex) rotating anode powder diffractometer controlled by an IBM computer, operating at 45 kV/ 100 mA and with a 1°/min scan rate, employing Ni-filtered Cu radiation. The calculated powder patterns for (I) - (III) and (V) were prepared with the CERIUS[2] software.[17] Tables of calculated and observed XRD patterns are summarized in Tables 2-1 to 2-4, respectively.

Infrared Spectroscopy . Infrared spectra in the far-IR region (600-50 cm^{-1}), were recorded in 4 cm^{-1} resolution on a computer controlled Nicolet 750 Magna-IR Series II spectrophotometer equipped with a TGS/PE detector and a silicon beam splitter . The samples were ground with dry CsI into a fine powder and pressed into translucent pellets.

Raman Spectroscopy . Raman spectra were recorded with a BIO-RAD FT Raman spectrometer with a Spectra-Physics Topaz T10-106c 1.064 nm YAG laser running at 11 amps. The samples were ground into a fine powder and loaded into melting point capillary tubes.

Solid State UV/Vis/Near IR Spectroscopy. Optical diffuse reflectance measurements were performed at room temperature using a Shimadzu UV-3101PC double beam, double monochromator spectrophotometer. The instrument is equipped with integrating sphere and controlled by a personal computer. $BaSO_4$ was used as a 100% reflectance standard for all materials. Samples were prepared by grinding them to a fine powder and spreading them on a compacted surface of the powdered standard

material, preloaded into a sample holder. The reflectance versus wavelength data output can be used to estimate the band gap of the material by converting reflectance to absorption data as described earlier.[18]

Single crystal optical transmission spectroscopy. Room temperature single crystal optical transmission spectra were obtained on a Hitachi U-6000 Microscopic FT Spectrophotometer mounted on an Olympus BH2-UMA metallurgical microscope over a range of 900 to 380 nm. Crystals lying on a glass slide were positioned over the light source and the transmitted light was detected from above.

Differential Thermal Analysis (DTA). DTA experiments were performed on a computer-controlled Shimadzu DTA-50 thermal analyzer. Typically a sample (~ 20 mg) of ground crystalline material was sealed in quartz ampoules under vacuum. A quartz ampoule of equal mass filled with Al_2O_3 was sealed and placed on the reference side of the detector. The sample was heated to the desired temperature at 10 °C/min, isothermed for 10 minutes, and finally cooled to 50 °C at the same rate. Residue of the DTA experiment was examined by X-ray powder diffraction. To evaluate congruent melting we compared the X-ray powder diffraction patterns before and after the DTA experiments. The stability/reproducibility of the samples were monitored by running at multiple cycles.

Semiquantitative microprobe analyses. The analyses were performed using a JEOL JSM-6400V scanning electron microscope (SEM) equipped with a TN 5500 EDS detector. Data acquisition was performed with an accelerating voltage of 20kV and twenty second accumulation time.

Single crystal X-ray Crystallography. Intensity data for (I), (III) and (V) were collected on a Rigaku AFC6 diffractometer, using $\omega/2\theta$ scans. Intensity data for (II) was collected on a Nicolet p3 four circle diffractometer using θ scans. Data for (II), (III) and (V) were collected at -100° C while the data for (I) was collected at room temperature. In all cases, graphite-monochomatized radiation was used. The crystals showed no

significant intensity decay, monitored by three standard reflections measured every 150 reflections throughout the data collection. The space groups were determined from systematic absences and intensity statistics. The structures were solved by direct methods using SHELXS-86[19] and refined by full-matrix least-squares techniques of the TEXSAN package of crystallographic programs.[20] The secondary extinction coefficient was refined for all structures. An empirical absorption correction based on ψ scans was applied to each data set, followed by a DIFABS[21] correction to the isotropically refined structures. All atoms were eventually refined anisotropically. All calculations were performed on a VAX station 3100/76 computer. After full refinement the final R/Rw for (I) were 3.0/4.5%. Since the structure is non-centrosymmetric refinement was attempted on the other enantiomorph which converged with R/Rw = 3.2/4.8%. Therefore, the first solution was retained.

The complete data collection parameters and details of the structure solution and refinement for (I) - (II) and (V) are shown in Table 2-5. Tables 2-6 to 2-9 contain the coordinates of all atoms, average temperature factors, and their estimated standard deviations.

Table 2-1.   Calculated and Observed X-ray Powder Patterns for K_2AgSbS_4 (I).

hkl	d_{calc}, Å	d_{obsd}, Å	I/I_{max}(obsd)
011 101	6.32	6.29	26
111	5.38	5.38	54
210	4.62	4.62	12
121	4.03	4.00	14
220	3.67	3.67	100
112	3.48	3.48	34
130	3.32	3.31	4
022	3.16		
020	3.13	3.13	37
131	3.06	3.06	11
311	3.01	3.01	15
231	2.72		
222	2.69	2.69	34
040	2.63	2.62	35
400	2.57	2.57	27
132	2.54	2.54	16
312	2.51	5.51	16
141	2.42	2.42	4
411	2.38	2.38	4
232	2.33	2.33	4
123	2.29	2.92	4
241	2.24	2.24	2
042	2.19	2.19	4
402	2.15	2.16	5
412	2.11	2.11	4
332	2.08	2.08	11
051	2.03	2.03	6
242	2.015	2.015	6
422	1.994	1.997	12
323	1.941	1.946	8
114	1.907	1.913	3
251	1.892	1.891	3
521	1.862	1.868	5

440	1.839	1.841	23
152	1.829		
512 333	1.797	1.798	8
224	1.740	1.744	22
134	1.697	1.697	3
260	1.661	1.660	7
352	1.634	1.634	8
620	1.623	1.623	10
451	1.595	1.592	4
044	1.580	1.582	4
404	1.566	1.567	5

Table 2-2.   Calculated and Observed X-ray Powder Patterns for Rb_2AgSbS_4 (I).

hkl	d_{calc}, Å	d_{obsd}, Å	I/I_{max}(obsd)
011	7.47	7.48	6
110	6.52	6.54	8
101	6.32	6.34	19
11$\bar{1}$	5.58	5.59	11
111	5.45	5.47	8
012	4.66	4.66	10
11$\bar{2}$	4.11	4.11	9
210	3.83	3.84	19
022	3.73	3.74	100
21$\bar{1}$	3.62	3.63	18
211	3.55	3.57	24
12$\bar{2}$	3.43	3.43	6
122	3.37	3.37	8
20$\bar{2}$	3.25	3.26	10
10$\bar{3}$	3.21	3.21	16
21$\bar{2}$	3.11	3.12	15
212	3.03	3.04	32
023	2.904	2.912	3
13$\bar{2}$	2.797	2.799	4
230 040	2.705	2.712	39
21$\bar{3}$	2.597	2.586	27
213	2.522	2.516	7
11$\bar{4}$	2.421	2.424	6
232	2.762	2.386	6
233	2.338	2.338	2
14$\bar{2}$	2.308	2.313	4
		2.278	2
32$\bar{2}$	2.226	2.219	3
322	2.179	2.174	2
23$\bar{3}$	2.148	2.154	7
331	2.118	2.119	9
14$\bar{3}$	2.086	2.073	4
242	2.054	2.054	13

134	2.021	2.021	6
224	2.000	1.994	6
115	1.954	1.961	6
152	1.933	1.939	3
12$\overline{5}$	1.890	1.891	12
044	1.868	1.872	8
234	1.848	1.844	3
42$\overline{2}$	1.811	1.819	6
25$\overline{2}$	1.803	1.803	4
252	1.785	1.789	11
13$\overline{5}$	1.761	1.764	3
		1.743	2
062	1.702	1.706	7
33$\overline{4}$	1.684	1.688	3

Table 2-3.   Calculated and Observed X-ray Powder Patterns for Cs_2AgSbS_4

hkl	d_{calc}, Å	d_{obsd}, Å	$I/I_{max}(obsd)$
011	8.56	8.48	20
002	6.46	6.40	8
111	4.94	4.91	12
013	4.03	4.00	21
112	3.96	3.93	40
12$\overline{2}$	3.87	3.85	100
122	3.39	3.38	11
200	3.34	3.35	15
032 20$\overline{2}$	3.28	3.27	54
004	3.23	3.21	44
113	3.18	3.16	22
131	3.13	3.11	24
014	3.11	3.10	37
211	2.98	2.97	20
040	2.86	2.84	34
132	2.83	2.82	40
12$\overline{4}$	2.78	2.78	7
20$\overline{4}$	2.62	2.62	20
11$\overline{5}$	2.54	2.53	15
230	2.518	2.508	15
133	2.501	2.491	14
13$\overline{4}$	2.447	2.453	6
231	2.399	2.392	5
215 051	2.252	2.239	8
310	2.194	2.186	6
24$\overline{2}$ 13$\overline{5}$	2.152	2.146	18
204	2.109	2.104	11
214	2.075	2.068	6
20$\overline{6}$	2.021	2.015	12
33$\overline{1}$	1.962	1.955	14
32$\overline{4}$	1.936	1.929	20
250 061	1.890	1.894	6

322	1.875	1.881	7
054	1.866	1.869	8
251	1.841		
126	1.830	1.826	14
$16\bar{2}$	1.792	1.788	10
332	1.760	1.756	8
063	1.743	1.739	7
136	1.723	1.717	5
055	1.712	1.712	6
244	1.697	1.693	8
$41\bar{3}$	1.673	1.667	7
333	1.649	1.645	6
$26\bar{3}$	1.605	1.601	7
$34\bar{5}$	1.586	1.582	6

Table 2-4.   Calculated and Observed X-ray Powder Patterns for $Cs_3Ag_2Sb_3Se_8$

hkl	d_{calc}, Å	d_{obsd}, Å	I/I_{max}(obsd)
001	12.90	12.90	25
100	10.55	10.59	50
10$\bar{1}$	9.10	9.10	13
10$\bar{2}$	6.07	6.07	7
111 200	5.29	5.29	37
102	5.07	5.08	8
012	4.89	4.90	3
11$\bar{2}$	4.72	4.72	6
20$\bar{2}$	4.55	4.56	5
210	4.32	4.32	5
112	4.20	4.21	12
21$\bar{2}$	3.89	3.90	24
020	3.75	3.74	42
103 013	3.73	3.74	42
30$\bar{1}$	3.58	3.59	43
120	3.53	3.53	100
212 113	3.34	3.34	7
10$\bar{4}$	3.27	3.27	62
022	3.24	3.24	51
22$\bar{1}$	3.05	3.06	51
311	2.97	2.98	38
221 22$\bar{2}$	2.92	2.91	44
12$\bar{3}$	2.83	2.83	18
40$\bar{1}$	2.69	2.70	23
30$\bar{4}$	2.65	2.65	54
302	2.566	2.577	10
20$\bar{5}$	2.525	2.527	11
31$\bar{4}$	2.502	2.501	11
11$\bar{5}$	2.483	2.486	16
12$\bar{4}$	2.466	2.461	11
214	2.404	2.408	4
223	2.367	2.374	14
23$\bar{2}$	2.191	2.200	5

033	2.162	2.163	10
025	2.126	2.122	8
11$\bar{6}$	2.106	2.109	7
215	2.072	2.066	17
125	2.022	2.028	16
422	1.953	1.953	22
502	1.898	1.898	20
51$\bar{4}$	1.889	1.884	15
512	1.840	1.848	21
21$\bar{7}$	1.805	1.809	8
126	1.786	1.787	10
333	1.765	1.762	20
610	1.713	1.717	5
325	1.700	1.699	10
12$\bar{7}$	1.681	1.681	6

Table 2-5.   Crystallographic Data for K_2AgSbS_4, Rb_2AgSbS_4, Cs_2AgSbS_4, and $Cs_3Ag_2Sb_3Se_8$

	I	II	III	V
Formula	K_2AgSbS_4	Rb_2AgSbS_4	Cs_2AgSbS_4	$Cs_3Ag_2Sb_3Se_8$
fw	436.05	528.79	623.67	805.70
a,Å	10.287(4)	8.186(2)	6.8718(9)	10.791(4)
b,Å	10.537(3)	10.821(3)	11.442(2)	7.539(5)
c,Å	7.898(3)	10.331(2)	13.234(1)	13.177(3)
β, deg	90.000	91.81(2)	102.500(9)	101.40(4)
Z; V, Å^3	4; 856.1(4)	4; 914.7(7)	4; 1015.9(2)	4;1051(1)
λ, Å	0.71069	0.71069	0.71069	0.71069
space group	Pnn2 (#34)	P2$_1$/n (#14)	P2$_1$/c (#14)	P2$_1$/m (#11)
d_{calc}, g/cm^3	3.383	3.839	4.077	5.093
μ(Mo Kα), cm^{-1}	72.66	161.82	123.22	244.43
T, °C	23	-100	-100	-100
2Θ max, deg	50.0	50.0	50.0	50.0
no. data collected	918	1830	2060	2110
no. unique data	918	1719	1894	2002
no. data observed, $I > 3\sigma(I)$	776	1199	1398	1401
no. of variables	75	73	74	89
final R/R$_w$,[a]%	3.0/4.5	3.8/3.9	4.7/6.0	3.0/3.9
GOF	2.30	3.46	2.32	1.41

[a] $R = \Sigma(|F_o|-|F_c|)/\Sigma|F_o|$; $R_w = [\Sigma w(|F_o| - |F_c|)^2/\Sigma w|F_o|^2]^{1/2}$

Table 2-6. Fractional Atomic Coordinates and B(eq) Values for K_2AgSbS_4 (I) with Estimated Standard Deviations in Parentheses.

atom	x	y	z	$B_{eq}^{a}Å^2$
Ag1	0	1/2	0.5211(4)	2.61(7)
Ag2	1/2	1/2	0.7394(3)	1.94(7)
Sb1	0.22849(7)	0.27467(7)	0.5302	0. 82(3)
S1	0.2198(3)	0.0786(3)	0.3916(5)	1.2(1)
S2	0.0483(3)	0.2963(3)	0.7119(5)	1.2(1)
S3	0.2142(3)	0.4471(3)	0.3438(5)	1.2(1)
S4	0.4227(3)	0.2781(3)	0.6823(5)	1.4(1)
K1	0.2465(3)	0.2302(3)	0.0302(9)	1.7(1)
K2	0	1/2	0.0283(8)	1.3(1)
K3	1.0000	0	0.7009(7)	1. 7(2)

^{a} B values for anisotropically refined atoms are given in the form of the isotropic equivalent displacement parameter defined as $B_{eq} = (4/3)[a^2B(1, 1) + b^2B(2, 2) + c^2B(3, 3) + ab(\cos\gamma)B(1,2) + ac(\cos\beta)B(1,3) + bc(\cos\alpha)B(2, 3)$

Table 2-7.   Fractional Atomic Coordinates and B(eq) Values for Rb_2AgSbS_4 (II) with Estimated Standard Deviations in Parentheses.

atom	x	y	z	$B_{eq}{}^a\mathring{A}^2$
Ag1	0.1275(1)	-0.03136(7)	0.28040(7)	1.54(3)
Sb1	0.14243(7)	0.22640(5)	0.46172(6)	0.51(3)
S1	0.0164(3)	0.2279(2)	0.6611(2)	1.0(1)
S2	0.2574(3)	0.4242(2)	0.4428(2)	1.1(1)
S3	-0.0455(3)	0.1869(2)	0.2924(2)	0.9(1)
S4	0.3379(3)	0.0715(2)	0.4499(2)	0.9(1)
Rb1	0.1271(1)	0.50951(8)	0.73726(9)	1.07(4)
Rb2	0.1417(1)	0.22750(9)	0.00657(9)	1.23(4)

[a] B values for anisotropically refined atoms are given in the form of the isotropic equivalent displacement parameter defined as $B_{eq} = (4/3)[a^2B(1, 1) + b^2B(2, 2) + c^2B(3, 3) + ab(\cos\gamma)B(1,2) + ac(\cos\beta)B(1,3) + bc(\cos\alpha)B(2, 3)$

Table 2-8.   Fractional Atomic Coordinates and B(eq) Values for Cs_2AgSbS_4 (III) with Estimated Standard Deviations in Parentheses.

atom	x	y	z	B_{eq}[a]$Å^2$
Ag1	0.7921(2)	0.0252(1)	0.4285(1)	3.09(5)
Sb1	0.3017(1)	0.21431(8)	0.43906(6)	1.27(4)
S1	0.1159(5)	0.0553(3)	0.3587(3)	1.8(1)
S2	0.6134(5)	0.2143(3)	0.3918(3)	1.9(1)
S3	0.3489(5)	0.1831(3)	0.6177(3)	1.8(1)
S4	0.1525(6)	0.3933(3)	0.3956(3)	2.6(1)
Cs1	0.3841(2)	0.00680(9)	0.16619(7)	2.52(4)
Cs2	-0.1306(1)	0.2431(1)	0.15744(8)	2.83(4)

[a] B values for anisotropically refined atoms are given in the form of the isotropic equivalent displacement parameter defined as $B_{eq} = (4/3)[a^2B(1, 1) + b^2B(2, 2) + c^2B(3, 3) + ab(\cos\gamma)B(1,2) + ac(\cos\beta)B(1,3) + bc(\cos\alpha)B(2, 3)$

Table 2-9.   Fractional Atomic Coordinates and B(eq) Values for $Cs_3Ag_2Sb_3Se_8$ (V) with Estimated Standard Deviations in Parentheses.

atom	x	y	z	$B_{eq}{}^a Å^2$
Ag1	0.8692(1)	-0.0359(2)	0.89192(8)	2.00(5)
Sb1	0.8658(1)	1/4	1.2073(1)	0.97(5)
Sb2	0.7659(1)	1/4	0.6241(1)	0.93(5)
Sb3	0.1806(1)	1/4	0.8882(1)	1.02(5)
Se1	0.6953(1)	-0.0028(2)	1.1902(1)	1.24(5)
Se2	0.7862(2)	1/4	0.4415(2)	2.00(9)
Se3	0.3172(2)	1/4	1.0688(1)	1.27(5)
Se4	0.5449(2)	1/4	0.6472(2)	1.66(8)
Se5	0.9136(2)	1/4	1.0205(1)	1.25(7)
Se6	0.8850(1)	-0.0184(2)	0.6984(1)	1.61(5)
Cs1	0.5841(1)	1/4	0.9316(1)	1.47(5)
Cs2	0.1393(1)	1/4	0.5599(1)	1.97(5)
Cs3	0.5554(1)	-1/4	0.6512(1)	1.96(5)

^{a} B values for anisotropically refined atoms are given in the form of the isotropic equivalent displacement parameter defined as $B_{eq} = (4/3)[a^2B(1, 1) + b^2B(2, 2) + c^2B(3, 3) + ab(\cos\gamma)B(1,2) + ac(\cos\beta)B(1,3) + bc(\cos\alpha)B(2, 3)$

3. Results and Discussion

3.1 Description of Structures.

Structure of K_2AgSbS_4 (I). The structure features tetrahedral Ag and Sb atoms linked by bent sulfur atoms forming the $[AgSbS_4]^{2n-}$ framework, see Figure 2-1. This framework is constructed from $[AgSb_2S_8]^{5-}$ units sharing corners to four Ag^+ sites forming channels filled by K^+ cations. The $[AgSb_2S_8]^{5-}$ unit is formed from two $[SbS_4]^{3-}$ units edge sharing to a central Ag^+ cation. A polyhedral representation of (I) down the c - axis is shown in Figure 2-2. The two crystallographic silver ions are both located on a 2-fold crystallographic sites. The two Ag sites have significantly elongated tetrahedral coordination, with a single Ag-S contact of 2.669(4)Å for Ag(1) while Ag(2) has distances in the range from 2.510(3)Å and 2.692(4)Å, average : 2.63(5)Å. The S–Ag(1)– S angles range from of 82.1(1)° to 115.6(2)°, average: 110(7)°. The S-Ag(2)-S angles range from 93.4(1) to 159.3(1), average: 110(11)°. Inspection of the S(2)–Ag(1)–S(3') angle of 128.1(1)° and the S(2)–Ag(1)–S(3) angle of 88.5(1)° reveal a significant deviation from an ideal tetrahedral geometry. These obtuse and acute angles are due to a strained four-membered (Sb(1)–S(3)–Ag(1)–S(2)) rings brought about by the neighboring edge sharing tetrahedrons. The second silver site is as distorted as the first with S(4)– Ag(2)–S(4') and S(1)–Ag(2)–S(1') angles of 159.3(2)° and 127.0(2)° respectively. The $[SbS_4]^{3-}$ ligand is a regular tetrahedron, with Sb–S distances in the range of 2.332(4) to 2.340(3)Å, av: 2.331(4)Å. The S–Sb–S angles range from 104.8(2)° to 112.2(2)°, average : 109(1)°. The three - dimensional $[AgSbS_4]_n^{2n-}$ framework is separated by K^+ ions that are located in three different sites. In K_2AuSbS_4, K(1) is coordinated by seven S atoms [range of K(1)-S distances, 3.311(7)-4.368(5)Å; av: 3.37(3)Å], K(2) is 8-

coordinate [3.187(4)-3.373(6)Å; av: 3.29(2)Å], and K(3) is 6 - coordinate [3.163(3) - 3.431(5)Å, av: 3.26(5)Å]. Selected bond distances and angles are given in Table 2-10.

Structure of Rb$_2$AgSbS$_4$ (II). The structure of Rb$_2$AgSbS$_4$ is a layered compound consisting of tetrahedral Ag$^+$ cations linked to [SbS$_4$]$^{4-}$ units. The layers propagate along the [b101] direction and are separated by two Rb$^+$ cations. A polyhedral representation of (II), viewed parallel to the layers, is shown in Figure 2-3. The layer can be thought of as a two-dimensional array of interconnected [Ag$_2$Sb$_2$S$_8$]$^{4-}$ building blocks. The [Ag$_2$Sb$_2$S$_8$]$^{4-}$ unit is isostructural to the [Ag$_2$Sb$_2$S$_8$]$^{4-}$ unit observed in α - Cs$_2$AgSbS$_4$[14a] and related to the [Cd$_4$S$_6$]$^{4-}$ cluster observed in K$_2$Cd$_2$S$_3$[22]. The [Ag$_2$Sb$_2$S$_8$]$^{4-}$ consist of two eclipsed AgSbS$_2$ rhombi connected by bridging sulfides, see Figure 2-4a. The final sulfide from the [SbS$_4$]$^{3-}$ unit then corner shares to the silver atom of an adjacent [Ag$_2$Sb$_2$S$_8$]$^{4-}$ unit coordinatively saturating the Ag$^+$ and forming the layer. The Ag – S distances range from 2.511(5)Å to 2.759(5)Å with an average Ag–S contact of 2.63(5)Å. The coordination environment for the Ag$^+$ site is a slightly distorted tetrahedron. The S-Ag-S angles range from 86.2(1)°, for the S–Ag–S angle associated with the AgSbS$_2$ rhombus, to 119.6(2)°, average: 109(5)°. The [SbS$_4$]$^{3-}$ is a regular tetrahedron, with Sb-S distances in the range from 2.319(5) Å to 2.340(5) Å, average : 2.331(4)Å. The S-Sb-S angles range from 104.8(2)° to 112.2(2)° , average: 109(1)°.

The structure of the [AgSbS$_4$]$^{2n-}$ anion is closely related to the Zintl phase CaAl$_2$Si$_2$[23]. The CaAl$_2$Si$_2$ compound is a layered compound constructed of [Al$_2$Si$_2$]$^{2-}$ rhombi linked in two dimensions with the gallery space filled by Ca^{2+} ions. The structure of CaAl$_2$Si$_2$ is unique in that the silicon atoms have an unusual "umbrella" coordination, with three Si–Al bonds in a pyramidal coordination and a fourth axial bond perpendicular to the plane of the base. A portion of the [Al$_2$Si$_2$]$^{2-}$ layer, highlighting the "umbrella" coordination of the silicon, is shown in Figure 2-4b. Although rare, chalcogenide examples of this coordination are known, and include Cu$_3$VS$_4$[24] and Na$_6$Cd$_7$S$_{10}$[22]. The

$[AgSbS_4]^{2n-}$ polyanion can be thought of as a defect of the $Al_2Si_2^{2-}$ framework. In the $[AgSbS_4]^{2-}$ anionic framework the two Al^{+3} sites are replaced by a monovalent and a pentavalent metal ion, (M^+) and a (M^{+5}) and the two Si^{4-} anions are replaced by four sulfides providing the necessary negative charge. With the removal of two aluminum atoms from the opposite corners of the Al_6Si_6 double six ring the $[Ag_2Sb_2S_8]^{4-}$ building block is formed, see Figure 2-4c. The strain of the "umbrella" coordination of the silicon atoms is removed by the low coordination preference of the sulfides.

The layer can alternatively be described as being composed of 15–membered rings of alternating metal and sulfur atoms. These rings are connected by bridging sulfides to form the layer. A single layer, containing the 15–membered ring, is shown in Figure 2-5. The layers stack with their 15–menbered rings in registry so that they form channels running down the c–axis. The dimensions of the ring are 13.63Å from S(2) to S(2') by 4.69Å from S(1) to S(3).

The $[AgSbS_4]_n^{2n-}$ layers are separated by Rb^+ ions that are located in two different sites. In Rb_2AgSbS_4, Rb(1) is coordinated by seven S atoms [range of Rb(1)-S distances, 3.270(5)-3.670(5)Å; av: 3.40(5)Å], and Rb(2) is 8-coordinate [3.346(5)-3.762(5)Å; av: 3.46(6)Å]. Selected bond distances and angles are given in Table 2-11.

Structure of Cs_2AgSbS_4 (III). The structure found for (III) is isostructural to α - Cs_2AgSbS_4 reported earlier.[14a] The $[AgSbS_4]_n^{2n-}$ macroanion is a chain running along the a-axis, see Figure 2-6. The chains are comprised of the same $[Ag_2Sb_2S_8]^{4-}$ building blocks observed in (II) connected through the formation of a Ag_2S_2 rhombi, see Figure 2-7. The Ag_2S_2 rhombus is characterized by a long Ag-S contact of 2.899(4)Å and a normal Ag-S bond of 2.610(4)Å. The AgS_4 tetrahedron is fairly distorted, with Ag-S bonds in the range from 2.483(4)Å to 2.899(4)Å and S-Ag-S angles in the range from 127.6(1)° to 85.8(1)°. The $[SbS_4]^{3-}$ unit has a fairly regular tetrahedral geometry with Sb-S bond distances in the range from 2.312(4)Å to 2.348(4)Å, average: 2.31(1)Å and an

average S-Sb-S bond angle of 109.5(9)$^\circ$. The $[AgSbS_4]_n^{2n-}$ chains are separated by Cs^+

cations that are located on two different sites. In Cs_2AgSbS_4, Cs(1) is coordinated by

seven S atoms [range Cs(1)-S distances, 3.497(4)Å - 3.872(4)Å; av: 3.65(5)Å], and Cs(2)

is coordinated by seven S atoms [range Cs(2)-S distances, 3.550(4)Å - 3.744(4)Å; av:

3.64(4)Å]. Selected bond distance and angles are given in Table 2-12.

Structure of $Cs_3Ag_2Sb_3Q_8$ (Q = S (IV), Se (V)). Since these two compounds

are isostructural the single-crystal structure determination was performed only on the

selenide compound (V), therefore the discussion will refer mainly to this compound. The

structure of the $[Ag_2Sb_3Se_8]_n^{3n-}$ macroanion is a complicated one - dimensional

corrugated ribbon running along the crystallographic b-axis, separated by Cs^+ cations

(Figure 2-8). The $[Ag_2Sb_3Se_8]_n^{3n-}$ anion is more accurately described as $[Ag_2$

$(SbSe_4)(Sb_2Se_4)]_n^{3n-}$, providing the first selenide example of the rare class of mixed

valent quaternary antimony chalcogenides. The $[Sb_2Se_4]^{2n-}$ unit is an infinite chain of

pyramidal Sb^{3+} units sharing opposite corners, leaving the third selenide terminal. This

is typical for Sb^{3+} species with the lone pair stereochemically expressed. The third

antimony is in a tetrahedral coordination environment common for Sb^{5+}. The $[SbSe_4]^{3-}$

unit is a regular tetrahedron with Sb–Se distances in the range from 2.460(2)Å to

2.491(2)Å, average: 2.476(8)Å. The Se-Sb-Se angles range from 104.22(6)$^\circ$ to 113.3(1)$^\circ$

: average 109(1)$^\circ$. The terminal selenium atoms display the shorter bond distances. The

$[Sb_2Se_4]^{2n-}$ infinite chain contains two crystallographic Sb sites with Sb-Se distances in

the range of 2.613(2)Å to 2.628(2)Å and 2.540(3)Å to 2.623(2)Å for Sb(1) and Sb(2),

respectively. Selected bond distances and angles for (V) are given in Table 2-13. The

two terminal selenides of the $[Sb_2Se_4]^{2n-}$ oligomer bind asymmetrically to silver ions in

an alternating bridging and four-coordinate binding modes. The two - coordinate

selenide (Se(3)) has one symmetry equivalent Sb-Se distance of 2.708(2)Å. The four-

coordinate selenide, Se(5), has two crystallographically distinct Ag-Se distances of

2.725(2)Å and 2.891(2)Å, respectively. Figure 2-9 shows a view perpendicular to a single chain, highlighting the different Ag-Se binding modes.

The structure of (V) can also be viewed as a Ag_2Se ribbon surrounded by $[Sb_xSe_y]^{n-}$ units. The ribbon is built from corner-sharing Ag_2Se_2 rhombi. The corrugated ribbon structure is a result of the alternating nature of the $[Sb_2Q_4]^{2n-}$ oligomer, binding to silver in an alternating four- and two-coordinate motif. The $[Ag_2Sb_3Se_8]_n^{3n-}$ chains are separated by Cs^+ cations that are located in three different sites. In $Cs_3Ag_2Sb_3Se_8$ Cs(1) is coordinated by eight sulfur atoms [range of Cs(1)-Se distances, 3.637(2) - 3.917(2)Å; av: 3.66(4)Å] , Cs(2) is 7 - coordinate [3.821(3) - 4.115(2)Å; av: 3.67(5)Å], and Cs(3) is 7 - coordinate [3.647(3) - 4.189(2); av: 3.74(3)Å].

Table 2-10.   Selected Distances (Å) and Angles (deg) for K$_2$AgSbS$_4$ (I) with Standard Deviations in Parentheses[a].

Sb(1)–S(1)	2.340(3)	S(1)-Sb(1)-S(2)	104.8(2)
Sb(1)–S(2)	2.355(4)	S(1)-Sb(1)-S(3)	111.1(2)
Sb(1)–S(3)	2.343(3)	S(1)-Sb(1)-S(4)	112.2(2)
Sb(1)–S(4)	2.332(4)	S(2)-Sb(1)-S(3)	111.1(2)
Sb–S(mean)	2.331(4)	S(2)-Sb(1)-S(4)	112.1(2)
		S(3)-Sb(1)-S(4)	105.6(2)
Ag(1)–S(2)	2.669(4) x 2		
Ag(1)–S(3)	2.669(4) x 2		
Ag(1)–S(mean)	2.669(4)	S(1)-Ag(1)-S(2)	104.2(2)
		S(1)-Ag(1)-S(3)	117.9(1)
Ag(2)–S(1)	2.692(4) x 2	S(1)-Ag(1)-S(4)	119.6(2)
Ag(1)–S(4)	2.510(3) x 2	S(2)-Ag(1)-S(3)	114.1(2)
Ag–S(mean)	2.63(5)	S(3)-Ag(1)-S(4)	86.2(1)
K(1)–S(1)	3.282(7)		
K(1)–S(2)	3.311(7)	Sb(1)-S(1)-Ag(1)	115.6(2)
K(1)–S(2')	3.432(5)	Sb(1)-S(2)-Ag(1)	114.0(2)
K(1)–S(3)	3.387(7)	Sb(1)-S(3)-Ag(1)	82.1(1)
K(1)–S(3')	3.351(5)	Sb(1)-S(4)-Ag(1)	84.5(1)
K(1)–S(4)	3.542(5)		
K(1)–S(4')	3.330(7)		
K(1)–S(mean)	3.37(3)		
K(2)–S(1)	3.187(4) x 2	K(3)–S(1)	3.431(5) x 2
K(2)–S(2)	3.331(6) x 2	K(2)–S(2)	3.163(3) x 2
K(2)–S(3)	3.373(6) x 2	K(2)–S(3)	3.199(4) x 2
K(2)–S(4)	3.271(4) x 2	K(3)–S(mean)	3.26(5)
K(2)–S(mean)	3.29(2)		

[a]The estimated standard deviations in the mean bond lengths and the mean bond angle are calculated by the equations $\sigma l = \{\Sigma_n(l_n - l)^2/n(n - 1)\}^{1/2}$, where l_n is the length (or angle) of the nth bond, l the mean length (or angle), and n the number of bonds (or angles).

Table 2-11. Selected Distances (Å) and Angles (deg) for Rb_2AgSbS_4 (II) with Standard Deviations in Parentheses[a].

Sb(1)-S(1)	2.334(4)	S(1)-Sb(1)-S(2)	104.8(2)
Sb(1)-S(2)	2.340(5)	S(1)-Sb(1)-S(3)	111.1(2)
Sb(1)-S(3)	2.331(5)	S(1)-Sb(1)-S(4)	112.2(2)
Sb(1)-S(4)	2.319(5)	S(2)-Sb(1)-S(3)	111.1(2)
Sb-S(mean)	2.331(4)	S(2)-Sb(1)-S(4)	112.1(2)
		S(3)-Sb(1)-S(4)	105.6(2)
Ag(1)-S(1)	2.511(5)	S-Sb-S(mean)	109(1)
Ag(1)-S(2)	2.567(5)		
Ag(1)-S(3)	2.759(5)	S(1)-Ag(1)-S(2)	104.2(2)
Ag(1)-S(4)	2.663(5)	S(1)-Ag(1)-S(3)	117.9(1)
Ag-S(mean)	2.63(5)	S(1)-Ag(1)-S(4)	119.6(2)
		S(2)-Ag(1)-S(3)	114.1(2)
Rb(1)-S(1)	3.270(5)	S(3)-Ag(1)-S(4)	86.2(1)
Rb(1)-S(2)	3.382(5)	S-Ag-S(mean)	109(5)
Rb(1)-S(2')	3.670(5)		
Rb(1)-S(3)	3.454(5)	Sb(1)-S(1)-Ag(1)	115.6(2)
Rb(1)-S(3')	3.367(5)	Sb(1)-S(2)-Ag(1)	114.0(2)
Rb(1)-S(4)	3.393(5)	Sb(1)-S(3)-Ag(1)	82.1(1)
Rb(1)-S(4')	3.308(5)	Sb(1)-S(4)-Ag(1)	84.5(1)
Rb-S(mean)	3.40(4)		
Rb(2)-S(1)	3.687(5)		
Rb(2)-S(1')	3.439(5)		
Rb(2)-S(2)	3.596(5)		
Rb(2)-S(2')	3.422(5)		
Rb(2)-S(3)	3.402(5)		
Rb(2)-S(3')	3.556(5)		
Rb(2)-S(4)	3.762(5)		
Rb(2)-S(4')	3.346(5)		
Rb-S(mean)	3.46(6)		

[a]The estimated standard deviations in the mean bond lengths and the mean bond angle are calculated by the equations $\sigma l = \{\Sigma_n(l_n - l)^2/n(n - 1)\}^{1/2}$, where l_n is the length (or angle) of the nth bond, l the mean length (or angle), and n the number of bonds (or angles).

Table 2-12.   Selected Distances (Å) and Angles (deg) for Cs_2AgSbS_4 (III) with Standard Deviations in Parentheses[a].

Sb(1)-S(1)	2.348(4)	S(1)-Sb(1)-S(2)	108.7(1)
Sb(1)-S(2)	2.345(4)	S(1)-Sb(1)-S(3)	106.2(1)
Sb(1)-S(3)	2.344(4)	S(1)-Sb(1)-S(4)	113.6(1)
Sb(1)-S(4)	2.312(4)	S(2)-Sb(1)-S(3)	109.8(1)
		S(2)-Sb(1)-S(4)	108.6(1)
Ag(1)-S(1)	2.610(4)	S(3)-Sb(1)-S(4)	109.9(1)
Ag(1)-S(2)	2.483(4)	S-Sb-S(mean)	109.5(9)
Ag(1)-S(3)	2.595(4)		
Ag(1)-S(3')	2.899(4)	S(1)-Ag(1)-S(2)	103.8(1)
		S(1)-Ag(1)-S(3)	110.0(1)
Ag(1)-Ag(1')	3.121(3)	S(2)-Ag(1)-S(3)	127.6(1)
Cs(1)-S(1)	3.497(4)	Sb(1)-S(1)-Ag(1)	111.7(1)
Cs(1)-S(2)	3.872(4)	Sb(1)-S(2)-Ag(1)	112.8(1)
Cs(1)-S(2')	3.435(4)	Sb(1)-S(3)-Ag(1)	86.6(1)
Cs(1)-S(3)	3.604(4)	Ag(1)-Ag(1')-S(1)	60.00(9)
Cs(1)-S(3')	3.741(4)	Ag(1)-Ag(1')-S(2)	128.9(1)
Cs(1)-S(4)	3.768(4)	Ag(1)-Ag(1')-S(3)	102.7(1)
Cs(1)-S(4')	3.691(4)		
Cs-S(mean)	3.65(5)		
Cs(2)-S(1)	3.581(4)		
Cs(2)-S(1')	3.554(4)		
Cs(2)-S(2)	3.607(4)		
Cs(2)-S(2')	3.896(4)		
Cs(2)-S(3)	3.550(4)		
Cs2-S(3')	3.550(4)		
Cs(2)-S(4)	3.744(4)		
Cs-S(mean)	3.64(4)		

[a]The estimated standard deviations in the mean bond lengths and the mean bond angle are calculated by the equations $\sigma l = \{\Sigma n (ln - l)^2/n(n - 1)\}^{1/2}$, where ln is the length (or angle) of the nth bond, l the mean length (or angle), and n the number of bonds (or angles).

Table 2-13.　Selected Distances (Å) and Angles (deg) for $Cs_3Ag_2Sb_3Se_8$ (V) with Standard Deviations in Parentheses[a].

Sb(1)–Se(1)	2.628(2) x 2	Se(1)–Sb(1)–Se(1')	92.98(9)
Sb(1)–Se(5)	2.613(2)	Se(1)–Sb(1)–Se(5)	100.62(6)
Sb(1)–Se(mean)	2.626(1)	Se(1')–Sb(1)–Se(5)	100.62(6)
Sb(3)–Se(1)	2.623(2) x 2	Se(1)–Sb(3)–Se(1')	90.55(8)
Sb(3)–Se(3)	2.540(3)	Se(1)–Sb(3)–Se(3)	96.99(6)
Sb(3)–Se(mean)	2.59(2)	Se(1')–Sb(3)–Se(3)	96.99(6)
Sb(2)–Se(2)	2.460(2)	Se(2)–Sb(2)–Se(4)	113.3(1)
Sb(2)–Se(4)	2.463(2)	Se(2)–Sb(2)–Se(6)	104.22(6)
Sb(2)–Se(6)	2.491(2) x 2	Se(2)–Sb(2)–Se(6')	104.22(6)
Sb(2)–Se(mean)	2.476(8)	Se(4)–Sb(2)–Se(6)	112.85(5)
		Se(4)-Sb(2)-Se(6')	112.85(5)
Ag(1)-Se(3)	2.708(2)	Se(6)–Sb(2)–Se(6')	108.6(1)
Ag(1)-Se(5)	2.725(2)		
Ag(1)-Se(5')	2.891(2)	Se(3)–Ag(1)–Se(5)	113.49(7)
Ag(1)-Se(6)	2.593(2)	Se(3)–Ag(1)–Se(5)	99.51(7)
Ag(1)-Se(mean)	2.72(6)	Se(3)–Ag(1)–Se(6)	114.45(7)
		Se(6)–Ag(1)–Se(6)	99.47(6)
Ag(1)–Ag(1')	3.228(3)	Se(5)–Ag(1)–Se(6)	122.26(7)
Ag(1)–Ag(1")	3.632(2)	Se(5)–Ag(1)–Se(6)	102.44(7)
Cs(1)–Se(1)	3.881(2) x 2	Sb(3)–Se(3)–Ag(1)	82.14(7)
Cs(1)–Se(1')	3.637(2) x 2	Sb(3)–Se(3)–Ag(1)	82.14(7)
Cs(1)–Se(3)	3.691(3)	Sb(3)–Se(3)–Ag(1)	73.18(8)
Cs(1)–Se(3')	3.917(2) x 2	Sb(1)–Se(6)–Ag(1)	126.3(2)
Cs(1)–Se(4)	3.688(3)	Sb(1)–Se(6)–Ag(1')	126.3(2)
Cs(1)–Se(mean)	3.78(4)	Sb(1)–Se(6)–Ag(1)	89.3(2)
		Sb(1)–Se(6)–Ag(1)	89.3(2)
Cs(2)–Se(1)	3.896(2) x 2	Sb(3)-Se(6)-Ag(1)	109.8(3)
Cs(1)–Se(2)	3.821(3)		
Cs(2)–Se(2')	3.855(2) x 2	Ag(1)–Se(3)–Ag(1)	75.2(2)
Cs(2)–Se(6)	4.115(2) x 2	Ag(1)–Se(6)–Ag(1)	99.0(3)

Cs(2)–Se(mean)	3.93(5)	Ag(1)–Se(6)–Ag(1)	135.95(7)
		Ag(1)–Se(6)–Ag(1)	77.6(1)
Cs(3)–Se(1)	4.189(2) x 2	Ag(1)–Se(6)–Ag(1)	67.88(8)
Cs(3)-Se(2)	3.647(3)	Ag(1)–Se(6)–Ag(1)	135.95(7)
Cs(3)-Se(3)	3.673(3)	Ag(1)–Se(6)–Ag(1)	80.53(6)
Cs(3)-Se(4)	3.771(3) x 2		
Cs(3)-Se(6)	3.900(2) x2	Sb(1)–Se(1)–Sb(3)	98.38(6)
Cs(3)–Se(mean)	3.88(5)		

[a]The estimated standard deviations in the mean bond lengths and the mean bond angle are calculated by the equations $\sigma l = \{\Sigma_n(l_n - l)^2/n(n - 1)\}^{1/2}$, where l_n is the length (or angle) of the nth bond, l the mean length (or angle), and n the number of bonds (or angles).
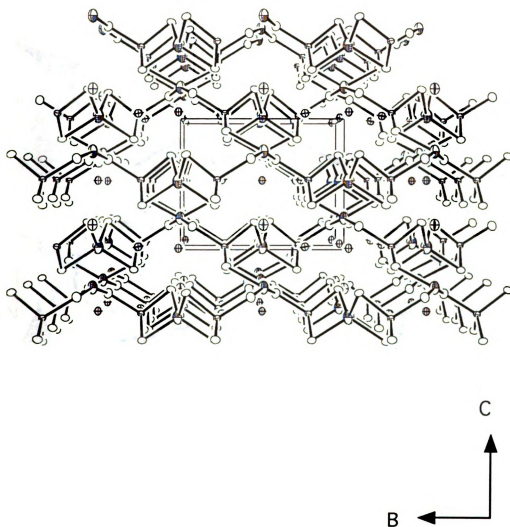
Figure 2-1:   ORTEP representation of K$_2$AgSbS$_4$ as viewed down the *a*- axis. Small
octant shaded ellipsoids; Ag, principal axis ellipsoids; Sb, boundary
ellipsoids; S, boundary and axis ellipsoids; K. (50% probability
ellipsoids).
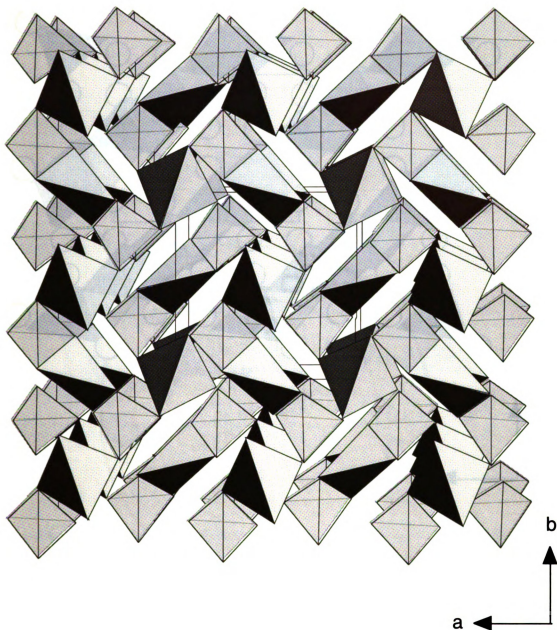
Figure 2-2:   Polyhedral representation of K_2AgSbS_4 (I) as viewed down the c - axis .
Filled polyhedra; SbS_4, pattern shaded polyhedra; AgS_4, alkali
catons are omitted for clarity.
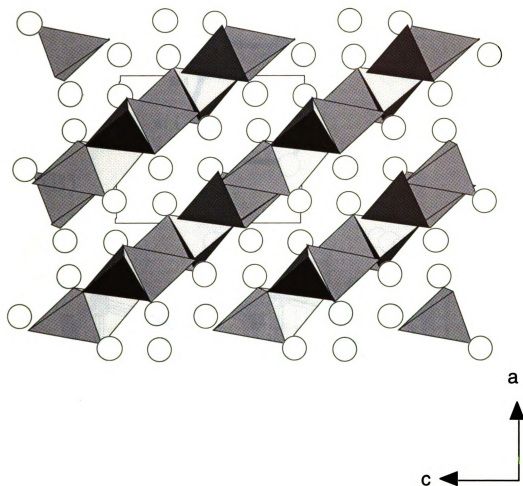
Figure 2-3:   Polyhedral representation of Rb$_2$AgSbS$_4$ (II), as viewed down the a - axis. Filled polyhedra; SbS$_4$, pattern shaded polyhedra; AgS$_4$, large open circles Rb$^+$ cations.

(A)
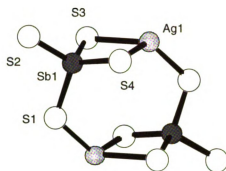
(B)
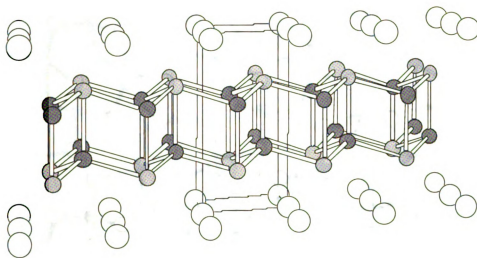
(C)
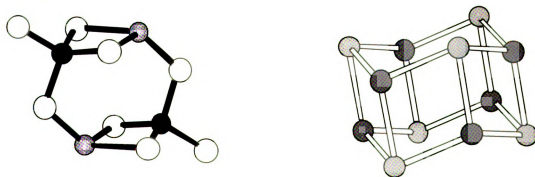
Figure 2-4: (A) The $[Ag_2Sb_2S_8]^{4-}$ building block with labeling. (B) A portion of the $[Al_2Si_2]^{2-}$ layer adapted from Reference #23. (C) Relationship between the $[Ag_2Sb_2S_8]^{4-}$ building block in (II) and the double six-rings in $CaAl_2Si_2$.
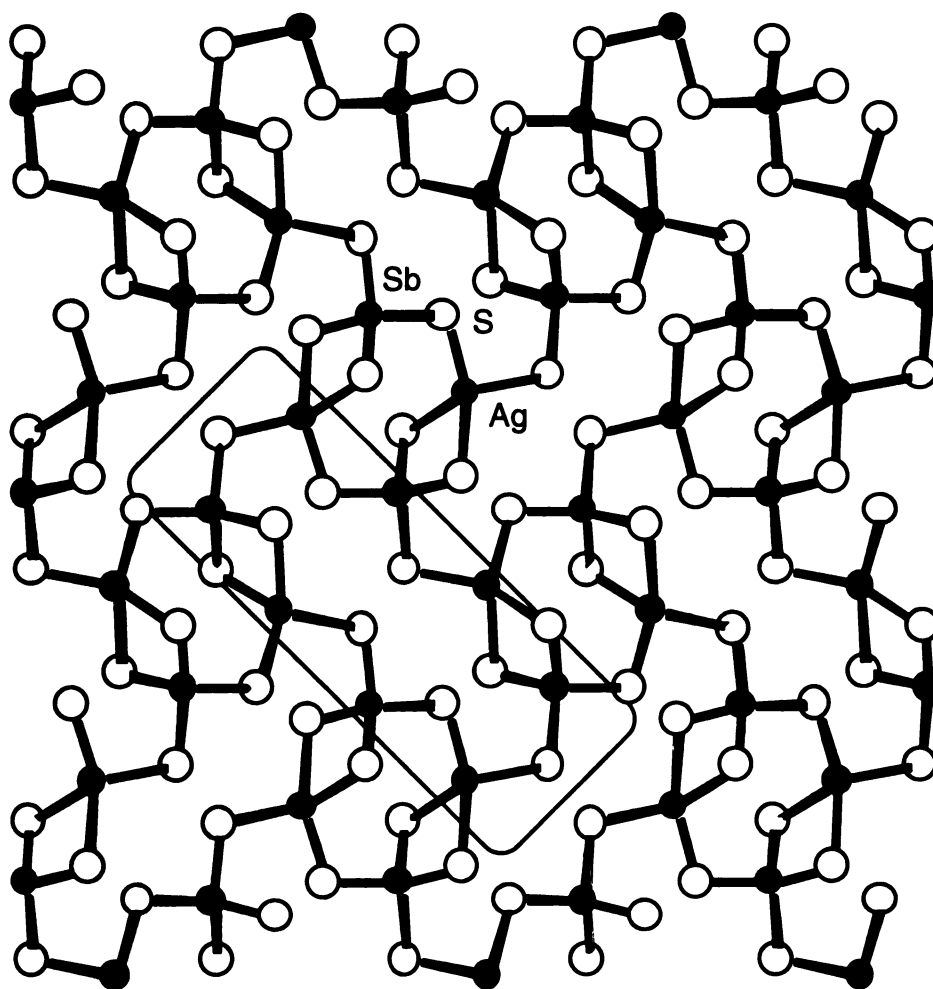
Figure 2-5: A single layer of Rb_2AgSbS_4 (II) with labeling, highlighting the 15–membered rings.
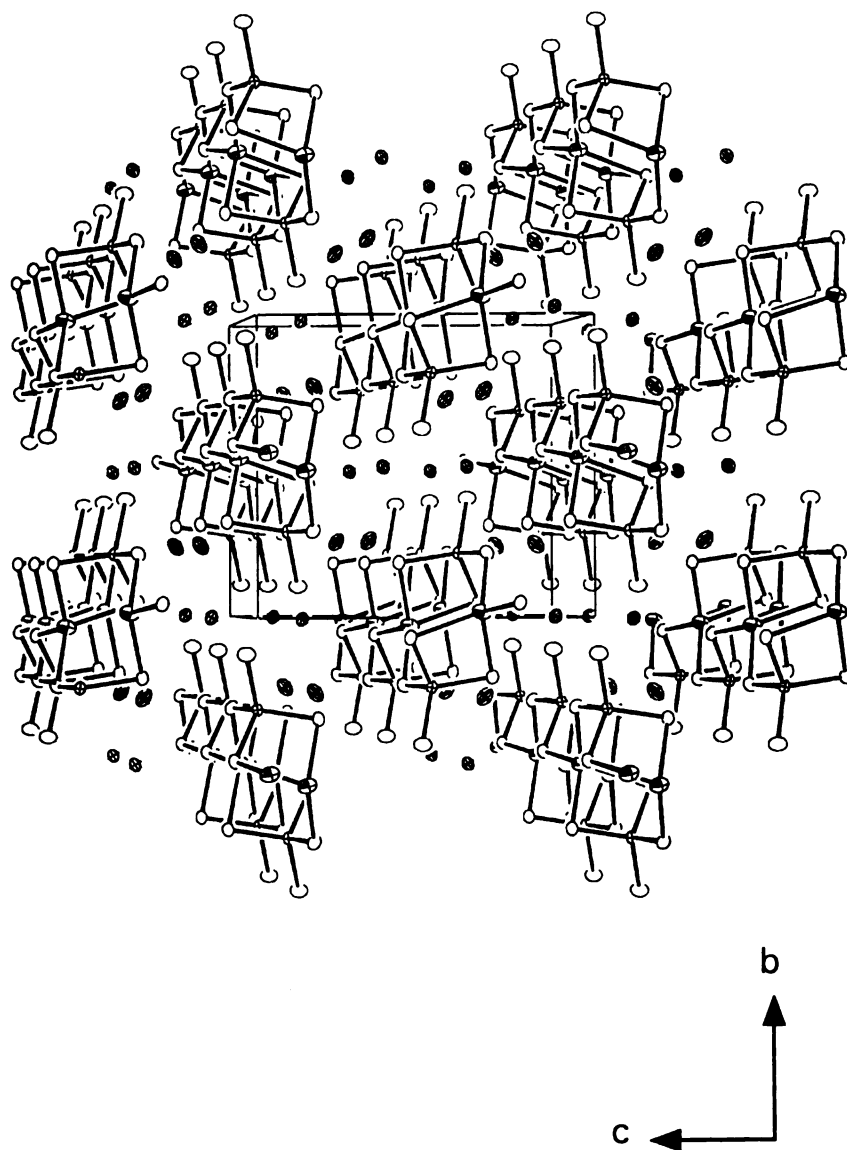
Figure 2-6: ORTEP representation of Cs_2AgSbS_4 (III) as viewed down the a- axis. Small octant shaded ellipsoids; Ag, principal axis ellipsoids; Sb, boundary ellipsoids; S, boundary and axis ellipsoids; Cs. (50% probability ellipsoids).
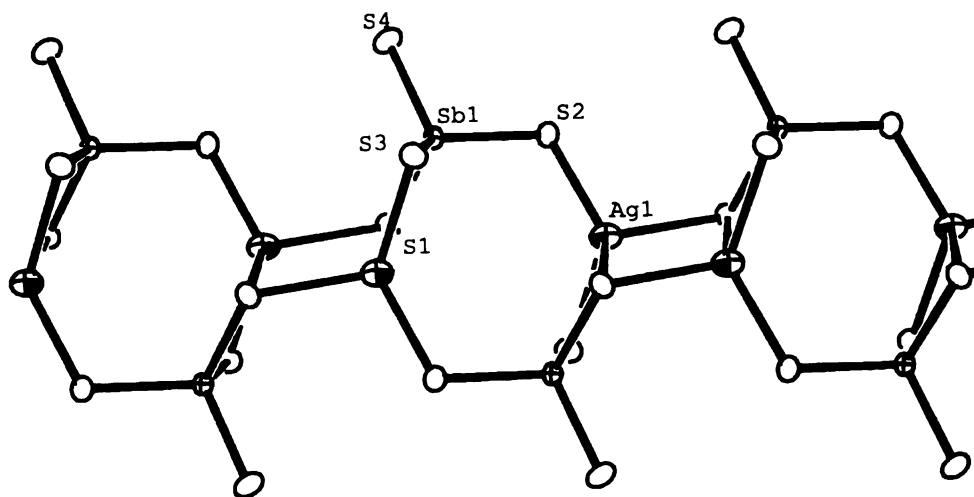
Figure 2-7:   ORTEP representation of a single chain of Cs_2AgSbS_4 (III), with labeling. (50% probability ellipsoids).
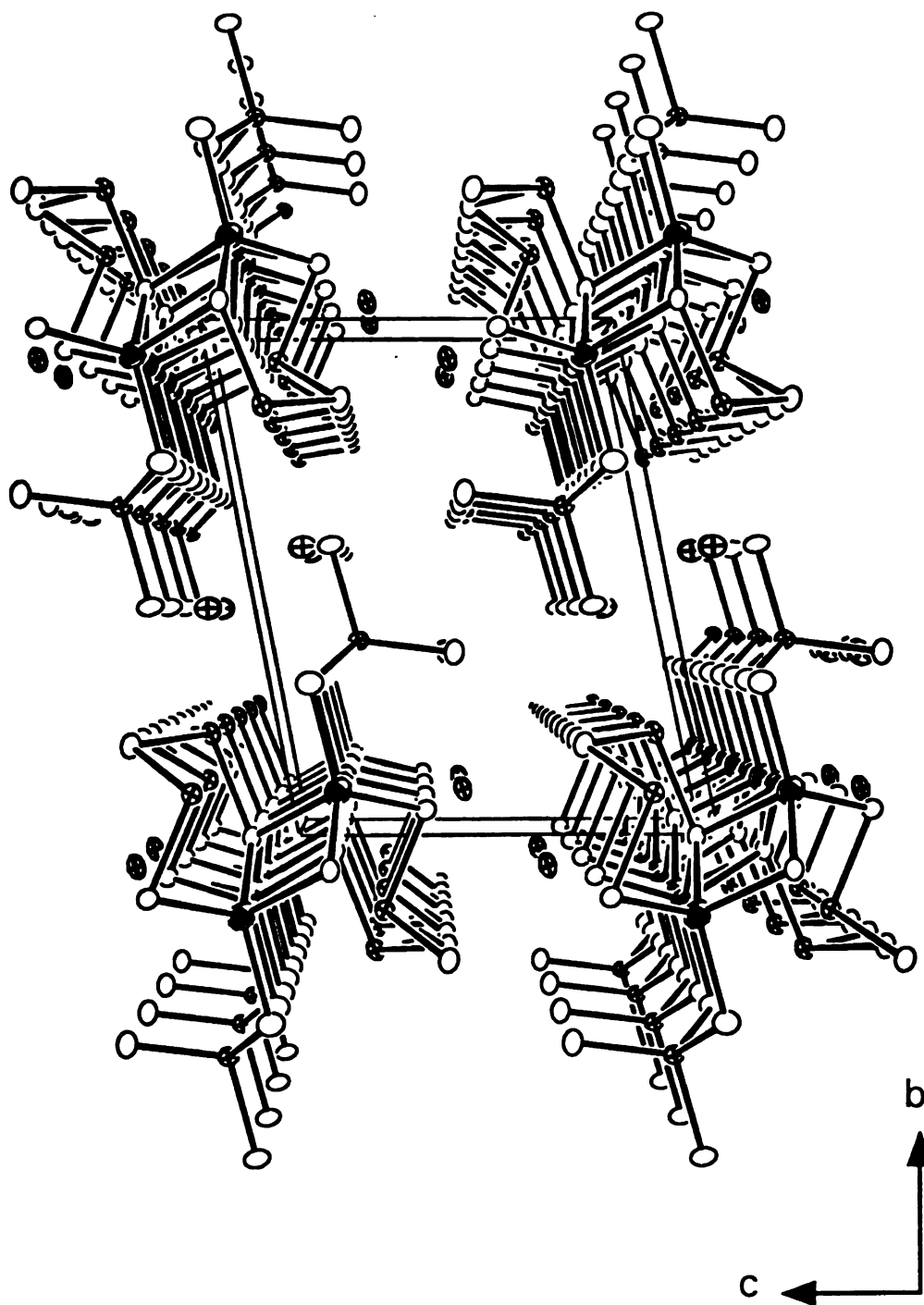
Figure 2-8: ORTEP representation of $Cs_3Ag_2Sb_3Se_8$ (V) as viewed down the b-axis. Small octant shaded ellipsoids; Ag, principal axis ellipsoids; Sb, boundary ellipsoids; S, boundary and axis ellipsoids; Cs (50% probability ellipsoids)
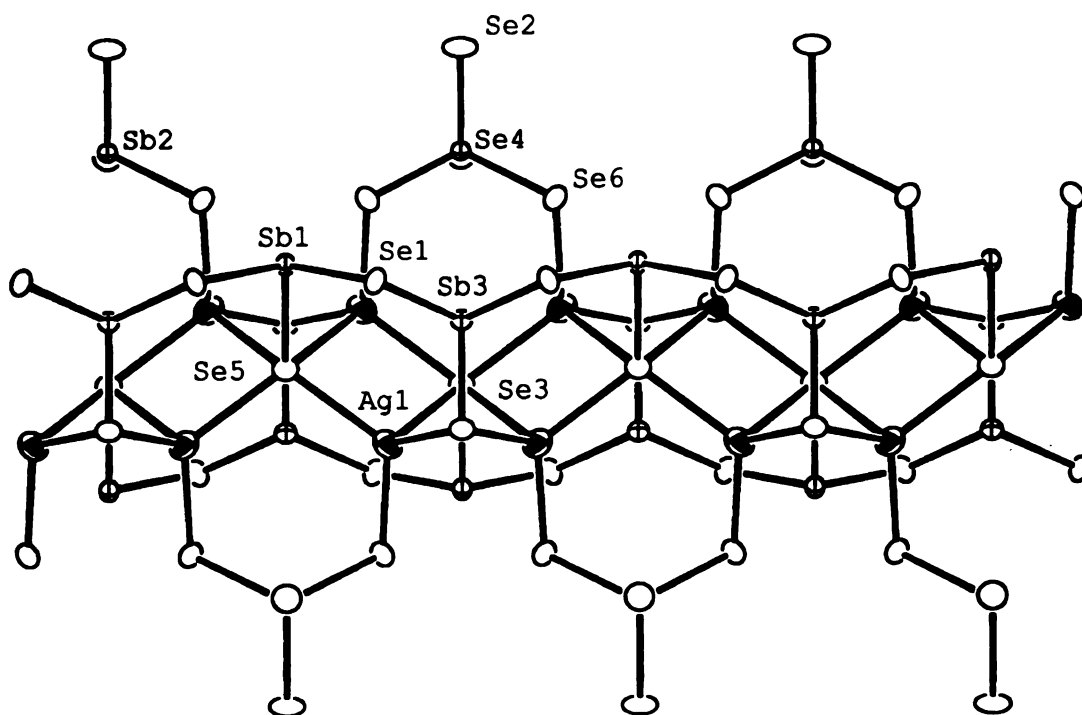
Figure 2-9:   ORTEP representation of a single chain of Cs₃Ag₂Sb₃Se₈ (V) with labeling, highlighting the different Ag-Se binding modes. (50% probability ellipsoids).

3.2. Synthesis, Spectroscopy and Thermal Analysis

This work dealt with the reactivity of group 11 metals with $A_x[Sb_yQ_z]$ fluxes (A = K, Rb, Cs; Q = S, Se). The syntheses were the result of a redox reaction in which the group 11 metal was oxidized by polychalcogenide ions in the $A_x[Sb_yQ_z]$ flux. The M^{n+} cations are then coordinated by the highly basic $[Sb_xQ_y]^{n-}$ units. The molten *polychalcoantimonate flux* is very effective for crystal growth in this system and is conducive to the isolation of pure materials because the residual $A_x[Sb_yQ_z]$ flux is soluble in aqueous and polar organic solvents.

In the $A_2S/Cu/Sb/S$ system (A = K, Rb, Cs) a large number of reactions, with a variety of conditions, resulted in the formation of black crystals. Microprobe analysis carried out on several randomly selected crystals gave an average composition of $Cu_{2.5}SbS_{3.6}$. The powder XRD experiments confirmed the black crystals were Cu_3SbS_4.[25] In sharp contrast, the reaction of silver metal with a $A_x[Sb_yQ_z]$ flux (A = K, Rb, Cs; Q = S, Se) produced a variety of quaternary alkali silver polychalcoantimonate compounds. For the sake of simplicity, each system will be discussed individually.

In the $K_2S/Ag/Sb/S$ system, yellow-orange polyhedral crystals of (I) form from a metal/antimony ratio of 1:1.5 in a basic $3K_2S_3$ flux at 400° C. Reactions varying either the Sb concentration or the basicity of the flux afforded severely twinned crystals of (I). Different compounds form with varying the metal/antimony compositions. A metal/antimony ratio of 1.5:1 gave a mixture of (I) and dark red crystals that had an average composition of $KAg_{2.2}Sb_{1.1}S_{4.6}$. The powder X-ray diffraction (XRD) experiment confirmed it was isostructural to $(NH_4)Ag_2AsS_4$.[26] The $[Ag_2AsS_4]^{n-}$ macroanion has a three - dimensional structure built from layers of corner sharing AgS_4 tetrahedrons, stitched together by edge sharing tetrahedral $[AsS_4]^{3-}$ units forming tunnels

filled by NH_4^+ cations. Reactions with a metal/antimony ratio above 2:1 resulted in phase separation.

In the $Rb_2S/Ag/Sb/S$ system, yellow crystals of (II) were synthesized from a metal/antimony ratio of 1:1 in a Lewis basic $2Rb_2S_5$ flux at 350_0 C. Varying the flux composition resulted in different compounds. Increasing the Ag/Sb ratio to 1.5:1 in a less basic Rb_2S_9 flux resulted in the formation of a new phase as evidenced by EDS and XRD. This product crystallizes as orange hexagonal plates that are air and water stable.[27] Lowering the reaction temperature also afforded a different compound. Decreasing the Ag/Sb ratio to 1:1.5 in a Rb_2S_9 flux at 300 °C resulted in red-brown crystals that had an average composition of $RbAg_5Sb_2S_7$. Attempts to grow single crystals suitable for single crystal diffraction studies are also underway.[28]

In the $Cs_2S/Ag/Sb/S$ system, yellow crystals of α-Cs_2AgSbS_4 were synthesized from a metal/antimony ration of 1:1 in a basic $2Cs_2S_5$ flux at 350° C. Rational attempts to synthesize β-Cs_2AgSbS_4[14a] from a molten alkali metal polysulfide flux were unsuccessful. Lower reaction temperatures also resulted in a different compound. Red crystals of (IV) were synthesized from an metal/antimony ratio of 1:1.5 in a less basic Cs_2S_9 flux at 280 °C. At this temperature a small amount (~ 5%) of Ag_3SbS_3[29] was observed as an impurity. Red crystals of (IV) were synthesized in a pure form by increasing the reaction temperature to 350°C.

In the $Cs_2S/Ag/Sb/Se$ system, black crystals of (V) were synthesized from a metal/antimony ratio of 1:1.5 in a $Cs_2Se_{6.33}$ flux at 280° C. The synthesis of (V) does not appear to be dependent on the Sb concentration in the flux. However, the formation of (V) appears to be very dependent on the flux composition. Changing the basicity, by changing either the Se (decreasing basicity) or the Cs_2Se (increasing basicity), resulted a mixture of orange water-soluble crystals and black powder. Semiquantiative microprobe analysis of the orange crystals indicate they are Cs_3SbSe_4.[30]

Investigations in the $K_2S/Au/Sb/Q$ (S = S, Se) system resulted in largely amorphous black glassy chunks for both systems. Microprobe analysis revealed that both systems were quaternary, however the largely amorphous nature of the materials made further characterization difficult. Attempts to grow crystals suitable for further characterization are in progress.[28]

A comparison of the polychalcoantimonate to the polychalcophosophate fluxes provides insight into the structural and chemical complexity of the two systems. The polychalcoantimonate system follows the experimentally observed trend of the polychalcophosphate system.[31] Basic conditions (increasing A_2Q) favor the tetrahedral $[EQ_4]^{3-}$ unit (E = P, Sb; Q = S, Se). Under these conditions, the $[SbQ_4]^{3-}$ unit is observed as a discrete tetrahedral species, while the $[PQ_4]^{3-}$ unit can participate in complex condensation equilibra, forming higher nuclearity chalcophosphate units such as $[P_2S_7]^{4-}$, $[P_2Se_8]^{4-}$,[31], and $[P_2Se_9]^{4-}$,[32]. Under acidic conditions (increasing Q or decreasing A_2Q) both P and Sb favor reduced species. In the polythiophosphate system the reduced P^{+4} species is readily observed in the ethane - like $[P_2Q_6]^{4-}$ unit (Q = S, Se). While the antimony analog of the $[P_2Q_6]^{4-}$ unit has yet to be reported, the pyramidal Sb^{3+} species is the only variable oxidation state species observed. The pyramidal $[SbQ_3]^{3-}$ unit (Q = S, Se) also participates in a separate yet complex condensation equilibria, forming higher nuclearity $[Sb_xQ_y]^{n-}$ units.

The far-IR and Raman data were in good agreement and the results are summarized in Table 2-14. The far-IR spectra of (I) - (III) display an ill resolved doublet at ~385 cm^{-1} which are tentatively assigned as Sb-S and Ag-S stretching. Since both metals have very similar coordination geometries, accurate assignment is very difficult. The far-IR spectra of (IV) - (V) are more complicated due to the complex binding modes of the $[Sb_2Q_4]^{2n-}$ (Q = S, Se) oligomer. The spectra shows an absorption assigned to the $[SbQ_4]^{3-}$ unit at 388 cm^{-1} and 269 cm^{-1} for (IV) - (V), respectively. The spectra also shows two absorptions assigned to the $[Sb_2Q_4]^{2n-}$ oligomer at 373 cm^{-1} and 357 cm^{-1} for

(IV) and 258 cm^{-1} and 250 cm^{-1} for (V), respectively. The Raman spectra of (I) - (IV) display absorptions in the 405 - 380 cm^{-1} region that are tentatively assigned to Sb - S vibrations and the absorptions below 380 cm^{-1} are assigned to Ag-S stretching vibrations. Similarly, the Raman spectrum of (V) displays absorptions in the 267 cm^{-1} - 256 cm^{-1} region that are tentatively assigned to Sb - Se vibrations and the absorptions below 220 cm^{-1} are assigned to Ag - Se stretching vibrations. The Raman spectra of (I) -(III) are shown in Figure 2-10 and the Raman spectra of (IV) and (V) are shown in Figure 2-11.

Differential thermal analysis (DTA) data, followed by careful XRD analysis of the residue was examined for all seven compounds. The DTA of (I) displayed a single endothermic peak at ~441°C, but two exothermic peaks at ~423°C and ~391°C appear upon cooling. The two exothermic peaks did not increase in intensity with a second cycle. Examination of the residue, after the second cycle, by powder XRD revealed that the sample melted congruently, suggesting a reversible phase change. The DTA of (II) indicates that it melts congruently at ~418°C. The DTA of (III) shows that it melts incongruently at ~407°C forming a mixture of (III) and decomposition products. Although the glassy nature of the resultant powder pattern made accurate indexing of the decomposition products difficult, β - Cs_2AgSbS_4[14a] was not observed.

The DTA of (IV) shows a single sharp endothermic peak at ~386°C but no exothermic peaks are observed upon cooling, see Figure 2-12a. Although no exothermic peaks were observed upon cooling, suggesting a glass transition[9], the powder XRD was crystalline and was indexed as a mixture of (IV) and $Cs_2Sb_4S_7$[33]. As shown in Figure 2-12b, upon subsequent heating of (IV), a broad exothermic peak at ~273 °C is observed, followed by a sharp endothermic peak at ~384 °C. Upon cooling, a broad exothermic peak is observed at ~285 °C. Examination of the residue by powder XRD indicated that it was weakly crystalline and all the peaks were indexed to (IV), suggesting the bulk of the material had had undergone a glass transition. The DTA of (V) also shows a single sharp endothermic peak at ~336°C with no peaks observed upon cooling, see Figure 2-

13a. Examination of the residue by powder XRD showed similar behavior to (IV) revealing a mixture of (V) and ternary decomposition products. As shown in Figure 2-13b, upon subsequent heating of (V), a two broad exothermic peaks were observed at ~247°C and ~282°C, followed by a sharp endothermic peak at ~323°C. Upon cooling, a broad exothermic peak is observed at ~368°C. Examination of the residue by powder XRD revealed a mixture of (V), $Cs_2Sb_2Se_4$[34a] and $AgSbSe_2$[34b]. Table 2-15 summarizes the melting point and optical data (see below) for all five compounds.

The optical absorption properties of (I) - (V) were evaluated by examining the solid - state UV/vis diffuse reflectance and/or single crystal optical transmission spectra of the materials. The spectra obtained from both methods are in good agreement and confirm the semiconducting nature of the materials by revealing the presence of sharp optical gaps (see Table 15). The transparent crystals of (I) - (IV) were suitable for single crystal optical transmission measurements. The A_2AgSbS_4 (A = K, Rb, Cs) compounds exhibit steep absorption edges from which the band-gap, E_g, can be estimated at 2.35 eV (I), 2.58 eV (II), and 2.61 eV (III), respectively. Representative spectra for (I) - (III) are given in Figure 2-14. This is in good agreement with that reported earlier for α-Cs_2AgSbS_4[14a]. The trend in widening band-gaps from (I) - (III) correlates nicely with the change in the dimensionality of the compounds. As the dimensionality of the $[AgSbS_4]^{2n-}$ framework decreases the extent of the Ag–S orbital overlap also decreases, causing a narrowing of the bands and increasing the energy gap. The band-gaps of $Cs_3Ag_2Sb_3Q_8$ (Q = S, Se) are 2.06 eV (IV) and 1.50 eV for (V), respectively (see Figure 2-15). The change in the band-gaps of (IV) - (V) can be attributed to the substitution of the smaller S^{2-} for the larger Se^{2-}. The larger more diffuse orbitals of the selenide ions broadenthe bands, increasing the extent of Ag - Se overlap, thus lowering the band-gap.

Table 2-14. Infrared and Raman Data (cm^{-1}) for (I) - (V).

K_2AgSbS_4 (I)		Rb_2AgSbS_4 (II)		Cs_2AgSbS_4 (III)		$Cs_3Ag_2Sb_3S_8$ (IV)		$Cs_3Ag_2Sb_3Se_8$ (V)	
IR	Raman	IR	Raman	IR	Raman	IR	Raman	IR	Raman
				619					
				519					
			405		408				
			395			397	395		
	392		392		392				
387			382	384		388			
		380					382		
		369	369	370		373	367		
366					362				
	361		361			357			
					332	321	323		
						309	316		
		288					283		
						263		269	267
							255	258	256
								250	
240	241	237	244	241					
						235	238	234	
								222	
									212
	206								
193			193					199	
								180	183
	173		176		175				
		164		161			160		
					153	158		154	
								143	

Table 2-15.   Optical Band Gaps from Powder and Single Crystal Measurements and Melting Point Data for (I) – (V).

Formula	E_g (eV) Powder	E_g (eV) Single Crystal	Melting Point (°C)
K_2AgSbS_4	2.38	2.35	441
Rb_2AgSbS_4	2.58	2.58	418
Cs_2AgSbS_4	2.66	2.61	407i
$Cs_3Ag_2Sb_3S_8$	2.03	2.06	386i
$Cs_3Ag_2Sb_3Se_8$	1.50	–NA–	336i

i = incongruent melting.

(A)
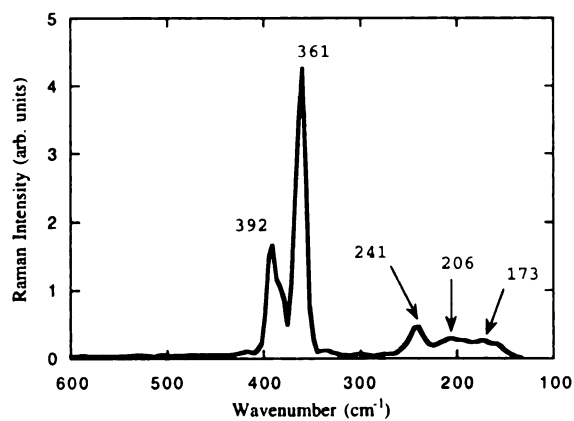
(B)
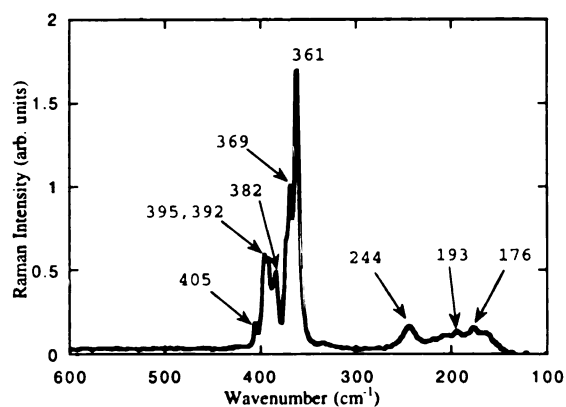
(C)
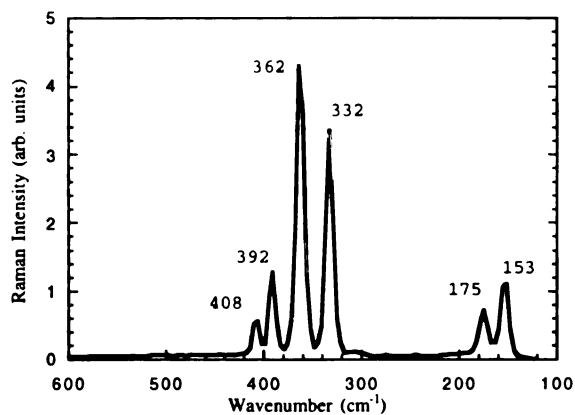
Figure 2-10:   Raman spectra of (A) K_2AgSbS_4 (I), (B) Rb_2AgSbS_4 (II) , and
              (C) Cs_2AgSbS_4 (III).

(A)
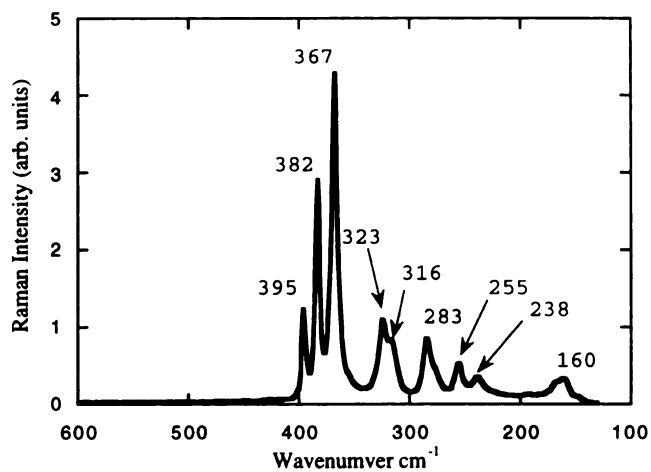
(B)
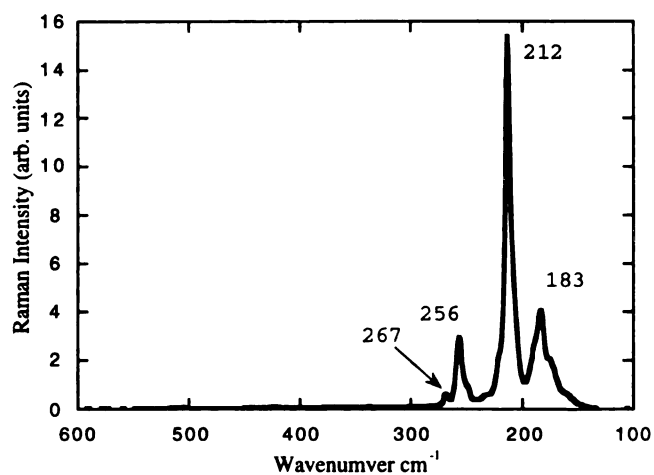
Figure 2-11: Raman spectra of (A) $Cs_3Ag_2Sb_3S_8$ (IV) and (B) $Cs_3Ag_2Sb_3Se_8$ (V).
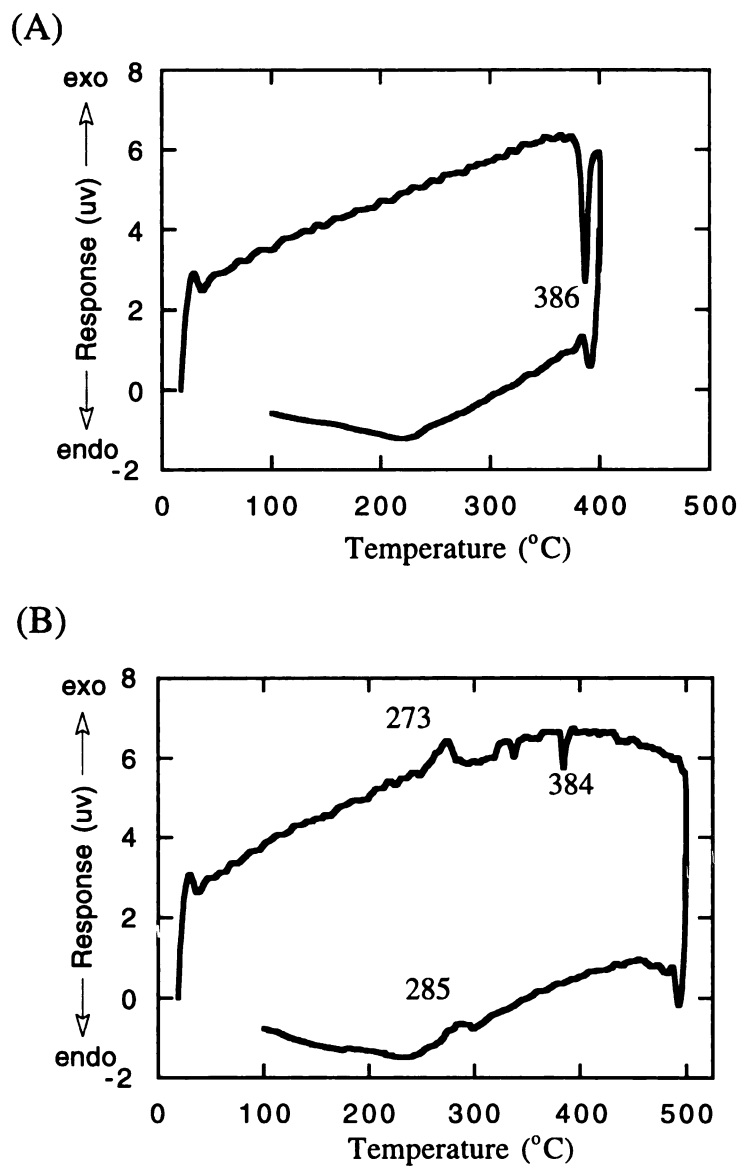
Figure 2-12:   (A) DTA diagram for $Cs_3Ag_2Sb_3S_8$ (first cycle). Heat is absorbed at
386 °C as the material melts but no corresponding exothermic peak is observed.
(B) Second DTA cycle showing the crystallization of $Cs_3Ag_2Sb_3S_8$ at 273 °C,
followed by its subsequent melting and recrystallization at 384 °C and 285 °C,
respectively.

Figure 2-13:   (A) DTA diagram for $Cs_3Ag_2Sb_3Se_8$ (first cycle). Heat is absorbed at
336 °C as the material melts but no corresponding exothermic peak is
observed. (B) Second DTA cycle showing the crystallization of
$Cs_3Ag_2Sb_3Se_8$ at 274 °C and 282 °C, followed by its subsequent melting
and thermal decomposition at 323 °C and 368 °C, respectively.

(A)
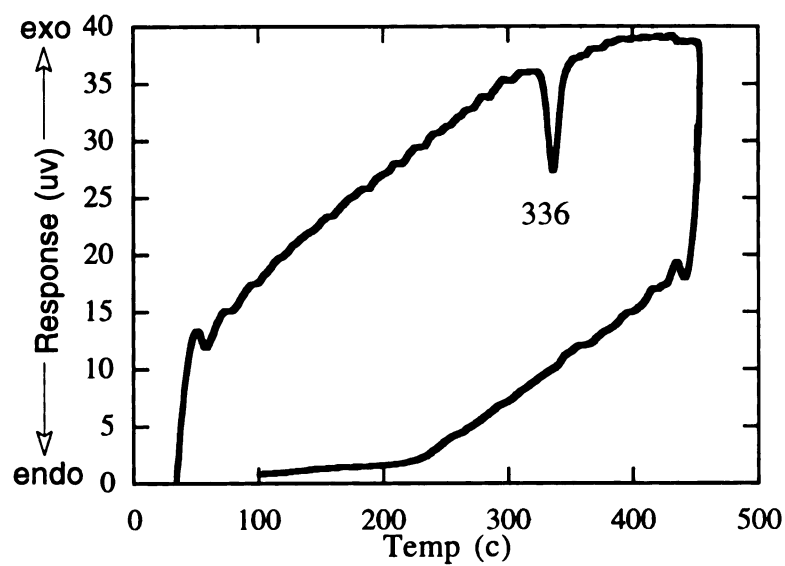
(B)
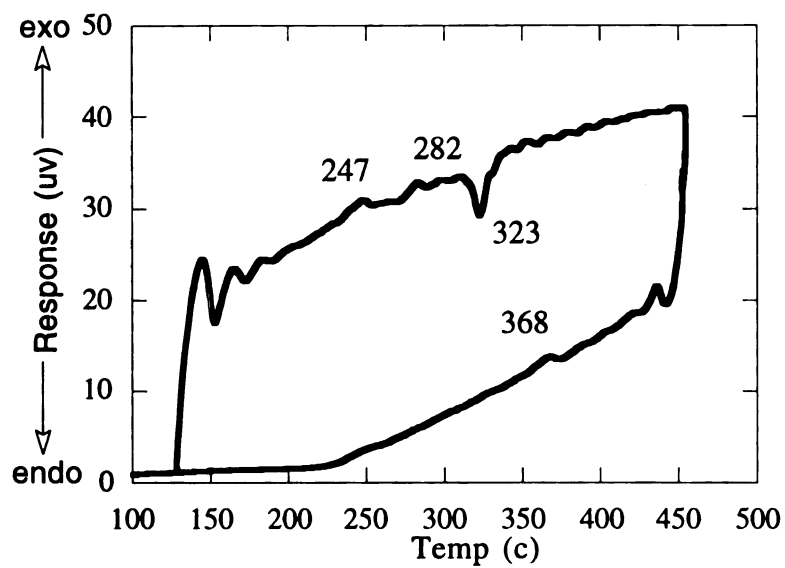
(A)
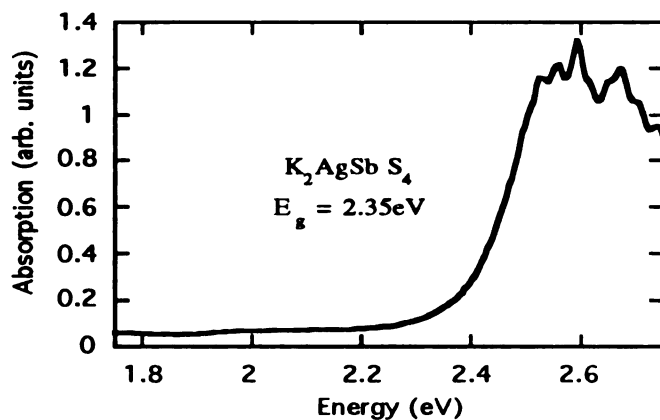
(B)
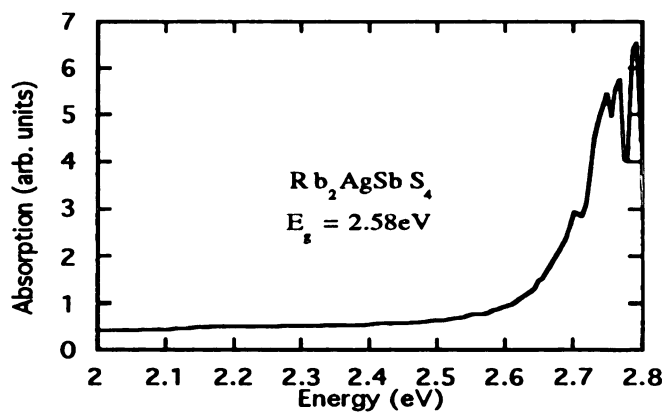
(C)
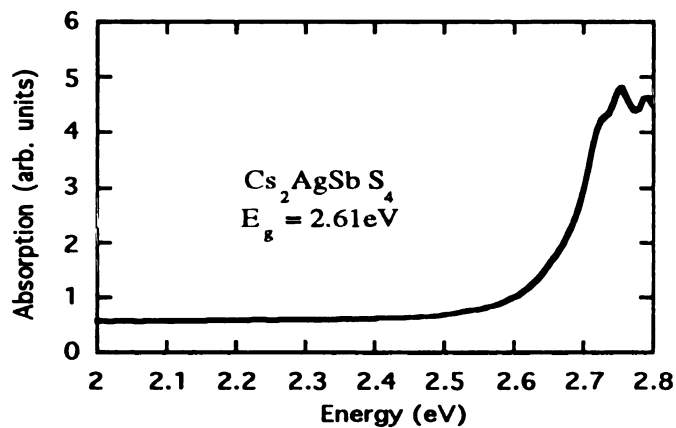
Figure 2-14: Single crystal optical absorption spectra of (A) K_2AgSbS_4 (I), (B) Rb_2AgSbS_4 (II), and (C) Cs_2AgSbS_4 (III). The sharp features at high absorbance are noise and due to the very low transmission of light.

(A)

$Cs_3Ag_2Sb_3S_8$
$E_g = 2.06eV$

(B)

$Cs_3Ag_2Sb_3Se_8$
$E_g = 1.50eV$
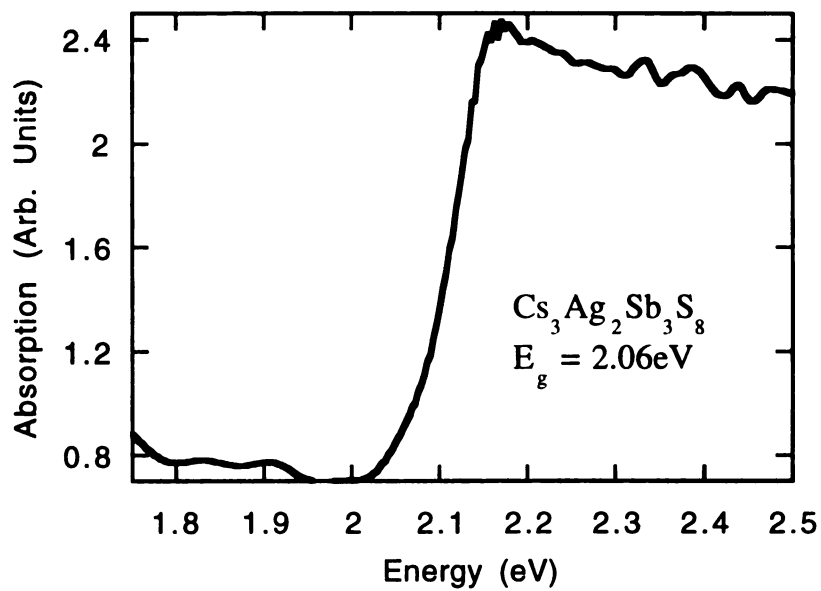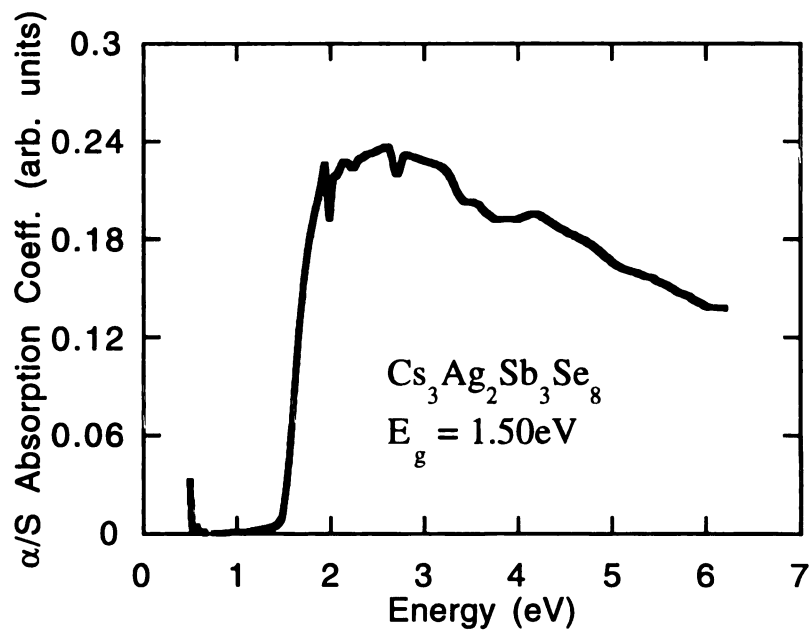
Figure 2-15:   (A) Single crystal optical absorption spectrum of $Cs_3Ag_2Sb_3S_8$ (IV).
(B) Solid-state optical absorption spectrum of $Cs_3Ag_2Sb_3Se_8$ (V).

3.3. Structural Relationships in A_2AgSbS_4 (A = K, Rb, Cs): The Counterion Effect.

The compounds (I) - (III) illustrate a beautiful example of the counterion effect. The counterion effect[35] is a qualitative observation that in some systems, a change in the counterion size will lead to a change in the dimensionality and/or the coordination number of a compound. The structural change is brought about to remove repulsions caused by ineffective screening of the anions. This example provides a unique illustration of this effect, for the anionic stoichiometry is invariant, consisting of varying arrangements of $[SbS_4]^{3-}$ units bonded to Ag^+ cations. Although no change in the coordination number of the Ag^+ cation is observed, the high mobility of the Ag^+ cations allows for the dramatic changes observed in the anionic structure upon variation of the cation volume. In K_2AgSbS_4 (I) the three - dimensional structure is favored with the small K^+ counterion. The larger Rb^+ counterion forces the $[AgSbS_4]^{4-}$ framework found in (I) to adopt a layered structure. The layers in (II) are built from $[Ag_2Sb_2S_8]^{4-}$ clusters linked together through bridging sulfides, increasing the anionic volume to sufficiently screen the larger Rb^+ cations. The larger Cs^+ cations slices the $[AgSbS_4]^{2-}$ layers found in (II) into $[AgSbS_4]_n^{2n-}$ chains separated by Cs^+ cations. The $[AgSbS_4]_n^{2n-}$ chains consist of the same $[Ag_2Sb_2S_8]^{4-}$ clusters observed in (II) but are now connected through the formation of a Ag_2S_2 rhombi. If a hypothetical compound $(Ph_4P)_2AgSbS_4$ were synthesized, its structure may result in a "zero - dimensional", molecular compound. The larger cation should cause the further rearrangement in the $[AgSbS_4]^{2-}$ framework to make it a discrete molecule, possibly some kind of $[Ag_2Sb_2S_8]^{4-}$ cluster.

4. Conclusions.

The synthesis of these new members of the A/Ag/Sb/Q family emphasizes the value of the polychalcoantimonate $A_x[Sb_yQ_z]$ (Q = S, Se) fluxes in the synthesis of new chalcoantimonate compounds. The complex structural diversity displayed is primarily due to the variety of binding modes of the $[Sb_yQ_z]^{n-}$ units, further expanding our concept of using molecular building blocks in the synthesis of extended structures. These fluxes provide a convenient entry into the unknown group 11 chemistry and preliminary results indicate that several more quaternary and possibly the unknown ternary Au/Sb/Q (Q = S, Se) compounds may also be synthesized and structurally characterized. The use of low temperatures (280 - 350°C) allows the synthesis of thermodynamically unstable compounds. Their metastable nature can be clearly seen in their thermal analysis. Although more experimental information is needed, it appears that control of flux composition-basicity results in compounds with different $[Sb_yQ_z]^{n-}$ units. This may enable us to achieve a level of synthetic control over the reaction outcome and ultimately allow us to construct structures with preselected ligands. The related selenoantimonate chemistry suggests that both the thio- and seleno-antimonates should be explored to fully understand the $[Sb_yQ_z]^{n-}$ anion chemistry.

List of References

1. Sutorik A. C.; Kanatzidis M. G. *Progr. Inorg. Chem.*, **1995**, *43*, 151-265.

2. (a) Liao, J.-H.; Varotis, C.; Kanatzidis M. G. *Inorg, Chem.*, **1993**, *32*, 2453. (b) Liao, J.-H.; Kanatzidis M. G. *Chem. Mater.*, **1993**, *5*, 1561.

3. (a) Zhang, X.; Kanatzidis M. G. *J. Am. Chem. Soc.*, **1994** *116*, 1890. (b) Zhang, X.; Kanatzidis M. G. *Inorg, Chem.*, **1994** *33*, 1238.

4. McCarthy, T. J.; Kanatzidis M. G. *Chem. Mater.*, **1993**, *5*, 1061.

5. (a) McCarthy, T. J.; Kanatzidis M. G. *J. Chem. Soc., Chem. Commun.*, **1994**, 1089. (b) McCarthy, T. J.; Kanatzidis M. G. *Inorg. Chem.*, **1995**, *34*, 1257.

6. (a) Marking, G. A.; Kanatzidis, M. G. Abstract from 210th Fall ACS Meeting, Chicago Il. (b) Marking, G. A.; Kanatzidis, M. G. *Submitted for publication.*

7. (a) Olivier-Fourcade, E.; Phillippot, J.; M. Maurin *Z. Anorg. Allg. Chem.*, **1978**, *446*, 159-168. (b) Graf, H. A.; Schafer, H. *Z. Anorg. Allg. Chem.*, **1975**, *414*, 211-219. (c) Kanishcheva, A. S.; Kuznetsov, V. G.; Lazasrev, V. B.; Tarasova, T. G.; *Zh. Strukt. Khim.*, **1977**, *18*, 1069. (d) Kanishcheva, A. S.; Mikhailov, Y. N.; Kuznetsov, V. G.; Batog, V. N. *Dolk. Adad. Nauk SSSR*, **1980**, *251*, 603-605. (e) Cordier, G.; Schafer, H. *Rev. Chem. Min.*, **1981**, *18*, 218-223. (f) Dorrscheidt, W.; Schafer, H. *Z. Naturforsch.*, **1981**, *36b*, 410-414. (g) Cordieer, G.; Schwidetzky, C.; Schafer, H. *Rev. Chem. Min.*, **1982**, *19*, 179-186.

8. (a) Ko Y. H.; Tan K. M.; Parise J. B.; Darovsky A. *Chem. Mater.*, **1996**, *8*, 493-496. (b) Parise J.B.; Ko Y.H. *Chem. Mater.*, **1992**, *4*, 1446-1450. (c) Parise J. B. *J. Chem. Soc., Chem. Commun.*, **1990**, 1553-1554. (d) Sheldrick, W. S.; Hausler, H.-J. *Z. Anorg. Allg. Chem.*, **1988**, *561*, 149-156. (e) Dittmar, V. G.; Schafer, H. *Z. Anorg. Allg. Chem.*, **1978**, *441*, 93-97. (f) Sheldrick, W. S.; Hausler, H.-J. *Z. Anorg. Allg. Chem.*, **1988**, *557*, 105-111. (g) Eisenmann, B.; Schafer, H. *Z. Narurforsch.* **1979**, *34b*, 383-385. (h) Graf, H. A.; Schafer, H. *Z. Narurforsch.* **1972**, *27b*, 735-739.

9.   McCarthy, T. J.; Kanatzidis M. G. *Inorg. Chem.*, **1994**, *33* , 1205.

10. Takeuchi, Y.; Sadanaga, R. *Z. Krstallogr.* ,**1969**, *130*, 346.

11. Dittmar, V. G.; Schafer, H. *Z. Anorg. Allg. Chem.,* **1977**, *437*, 183.

12. Dittmar, V G.; Schafer, H. Z. ; Schwidetzky, C. *Z. Anorg. Allg. Chem.*, **1978**, *441*, 93-97.

13. Imafuku, M.; Nakai, I.; Nagashima, K.; *Mat. Res. Bull.*, **1986**, *21*, 493-501.

14. (a) Schimek, G. L.; Pennigton, T. L.; Wood, P. T.; Kolis, J. W. *J. Solid State Chem.*, **1996**, *123*, 277-284. (b) Wood, P. T.; Schimek, G. L.; Kolis, J. W. *Chem. Mater.*, **1996**, *8*, 721-726.

15. (a) Wernic, J. H. *Am. Miner.*, **1960**,*45*, 591 . (b) Hoda, S. N.; Chang, L. L. Y. *Am. Miner.*, **1975**, *60*, 621. (c) Sawada, H.; Kswada, I.; Hellner, E.; Toknami, M. *Zeitschrift fuer Kristallographie*, **1987**, *180*, 141. (d) Megarskaya, L.; Rykl, D.; Taborsky Z. *Am. Miner.*, **1987**, *72*, 227. (e) Makovicky, E.; Munne, W.; Neuss, G.; *Jahrbuch fuer Mineralogie Abhandlungen.*, **1983**, *147*, 58.

16. (a) McCarthy, T. J.; Hogan, T.; Kannewurf, C. R.; Kanatzidis, M. G. *Chem. Mater.*, **1994**, *6*, 1072.   (b) Feher, F. In Handbuch der Praparativen Anorganischen Chemie; Brauer, G., Ed.; Ferdinand Enke: Stuttgart, Germany, **1954**; pp 280.

17. CERIUS[2], Version 1.6, Molecular Simulations Inc., Cambridge, England, **1994**.

18. McCarthy, T. J.; Ngeyi, S.-P.; Liao, J.-H.; DeGroot, D.; Hogan, T.; Kannewulf, C. R.; Kanatzidis, M. G. *Chem. Mater.*, **1993**, *5*, 331.

19. Sheldrick, G. M. In Crystallographic Computing 3; Sheldrick, G. M., Kruger, C., Doddard, R., Eds.; Oxford University Press: Oxford, England, **1985**; pp 175.

20. TEXSAN: Single Crystal Structure Analysis Software, Version 5.0; Molecular Structure Corp.: The Woodlands, TX 77381, **1981**.

21. Walker, N.; Stuart, D. *Acta Crystallogr.* **1983**, *A39*, 158.

22. Enos A. Axtell, Ph.D. Dissertation, Michigan State University, East Lansing, MI, **1995**.

23. Zheng, C.; Hoffmann, R.; Nesper, R.; von Schering, H.-G. *J. Am. Chem Soc.*, **1986**, *108*, 18767.

24. (a) Kanishcheva, A. S.; Mikhailov, Y. U.; Lazarev, V.; Moshchalkova N. A. *Doklady Akademii Nauk SSSR*, **1980**, *252*, 872. (b) Geller, S.; Wernick, J. H. *Acta. Cryst.*, **1959**, *12*, 46.

25. Troger, F. J. *Am. Mineralogist*, **1966**, *51*, 890.

26. Auernhammer, M.; Effenberger, H.; Irran, E,; Pertlik, F.; Rosenstingl, *J. Solid State Chem.* **1993**, *106*, 421.

27. Hanko, J. A.; Kanatzidis, M. G. *Manuscript in preparation.*

28. Hanko, J. A.; Kanatzidis, M. G. *Work in progress.*

29. Indexed Ag_3SbS_3 using "Powder Diffraction File-Inorganic Phases", vol. 21,. pp. 1173, and vol. 25, pp. 1187, **1993**.

30. Sugaki, A.; *Sci. Rep. Tohoku Univ.*, **1993**, *106*, 421.

31. Chondroudis, K.; Hanko, J. A.; Kanatzidis, M. G. *Inorg. Chem.* ,**1997**, *37* , 2323.

32. Chondroudis, K.; McCarthy, T. J.; Kanatzidis, M. G. *Inorg. Chem.*, **1995**, *34*, 1257.

33. Indexed $Cs_2Sb_4S_7$ using "Powder Diffraction File-Inorganic Phases", vol. 32,. pp. 214, **1987**.

34. (a) Drake, G. W.; Kolis, J. W. *Coord. Chem. Rev.*, **1994**, *137*, 131. (b) Sheldrick, W.; Wackhold, M. *Angew. Chem. Int. Ed. Engl.*, **1997**, *36*, 206.

35. Kanatzidis, M. G. *Phosphorous, Sulfur, and Silicon*, **1994**, *93-94*, 159.

CHAPTER 3

Thioantimonate Flux Synthesis of α,β - $RbAg_2SbS_4$: Two New Three-Dimensional Compounds With Acentric Structures.

1. Introduction

The alkali polychalcogenide fluxes are conducive to the intermediate temperature synthesis of new multinary chalcometalates.[1] Alkali polychalcogenide fluxes allow the easy incorporation of alkali metal cations into the compound. The incorporation of alkali metal can lower the dimensionality of a compound or cause a structural transformation to a previously unknown structure.

The motivation for the research reported here is to develop a methodology using molecular building blocks or recognizable structural fragments in the synthesis of new multinary compounds with potentially useful properties. To further develop this general methodology, we have explored the *polythioantimonate flux* method as a convenient way to synthesize new quaternary compounds with transition metals. Several unusual examples have been reported, these include: $Cs_2Sb_4S_8$, $CsSbS_6$,[2] A_2AgSbS_4 (A = K, Rb, Cs),[3,4] $Cs_3Ag_2Sb_3Q_8$ (Q = S,Se),[3,4] $KThSb_2Se_6$,[5] $A_2Ag_{20}Sb_4S_{19}$ (A = Rb, Cs),[6] A_2AuSbS_4 (A = Rb, Cs),[7] $Rb_2Au_6Sb_4S_{10}$[8] and $KHgSbS_3$[9].

These building blocks form by the *in situ* fusion of $A_2Q/Sb/Q$ (A = Alkali metal; Q = S, Se) to form various $A_x[Sb_yQ_z]$ species in a molten polychalcogenide solvent. The metal atoms are dissolved by reaction with the polychalcogenide ligands and, along with the various $[Sb_yQ_z]^{n-}$ units, act as mineralizers in the flux to promote single crystal growth. Although ligands such as $[SbS_4]^{3-}$ and $[SbS_3]^{3-}$ are interesting because of the many potentially different bonding modes they can exhibit, relatively little is known about their coordination chemistry in the solid state. Continuing our investigations with the group 11 transition metals, here we report the synthesis, structural characterization, optical, and thermal properties of α,β - $RbAg_2SbS_4$, two new quaternary thioantimonates with an acentric structure. While α - $RbAg_2SbS_4$ was under investigation in our laboratory, its synthesis and

structure, in supercritical ammonia, was reported[4b]. The highly unusual thermal properties exhibited by this compound, however, were not studied and merit further investigation.

2. Experimental Section

2.1. Reagents

The reagents mentioned in this study were used as obtained unless noted otherwise: (i) antimony powder 99.999% purity, -200 mesh, Cerac Inc., Milwaukee, WI; (ii) silver powder 99.95% purity, -325 mesh Alfa AESAR Group, Seabrook, NH; (iii) rubidium metal, analytical reagent, Johnson Matthey/AESAR Group, Seabrook, NH; (iv) sulfur powder, sublimed, J.T. Baker Chemical Co., Phillipsburg, NJ; (v) N,N-Dimethylformalide (DMF) reagent grade, EM Science, Inc., Gibbstown, NJ. (vi) diethyl ether, ACS anhydrous, EM Science, Inc., Gibbstown, NJ.

2.2. Syntheses.

Rb$_2$S was prepared by reacting stoichiometric amounts of the elements in liquid ammonia as described in Chapter 2 Section 2.2.

Preparation of α-RbAg$_2$SbS$_4$ (I). An amount of Rb$_2$S (0.51g, 0.50 mmole), Ag (0.041g, 0.375 mmole), Sb (0.015g, 0.125 mmole), and S (0.064g, 2 mmole) were thoroughly mixed and transferred to a 6-ml Pyrex tube which was subsequently flame-sealed *in vacuo* (~10^{-3} Torr). The reaction mixture was heated

to 350°C over 12 hours in a computer-controlled furnace. It was isothermed at 350°C for 4 days, cooled to 150°C at a rate of 4°C/hr, and then cooled to room temperature in 10 hours. The product, which is stable in water and air, was isolated by dissolving the Rb_2S_x and any $Rb_x[Sb_yS_z]$ flux with DMF under an inert atmosphere to give well-formed orange hexagonal and red-orange polyhedral crystals in 52% yield, based on Sb. Quantitative microprobe analysis from both crystals gave an average formula of $Rb_{1.9}Ag_{1.1}SbS_{4.7}$. Powder X-ray diffraction experiment confirmed that the orange and red crystals were identical, having only different morphologies.

Preparation of β-RbAg$_2$SbS$_4$ (II). An amount of Rb_2S (0.110g, 0.50 mmole), Ag (0.108g, 1 mmole), Sb (0.031g, 0.25 mmole), and S (0.128g, 4 mmole) were thoroughly mixed and transferred to a 6-ml Pyrex tube which was subsequently flame-sealed *in vacuo* ($\sim 10^{-3}$ Torr). The reaction mixture was heated to 500°C over 15 hours in a computer-controlled furnace. It was isothermed at 500°C for 4 days, cooled to 110°C at a rate of 4°C/hr, and then cooled to room temperature in 1 hour. The product, which is stable in water and air, was isolated by dissolving the Rb_2S_x and any $Rb_x[Sb_yS_z]$ flux with DMF under an inert atmosphere to give bright red crystals in 60% yield, based on Sb. Quantitative microprobe analysis of single crystals gave $RbAg_{2.1}Sb_{1.5}S_{6.6}$

2.3. Physical Measurements

Powder X-ray Diffraction The compounds were examined by Powder X-ray Diffraction for the purpose of phase purity. Analysis for (I) and (II) were performed using a calibrated Rigaku-Denki/RW400F2 (Rotaflex) rotating anode powder diffractometer controlled by an IBM computer, operating at 45 kV/ 100 mA

and with a 1º/min scan rate, employing Ni-filtered Cu radiation in a Bragg-Brentano geometry. Powder patterns were calculated with the CERIUS[2] software.[10] Tables of calculated and observed XRD patterns for α-RbAg$_2$SbS$_4$ and β- RbAg$_2$SbS$_4$ are given in Tables 3-1 and 3-2, respectively.

Infrared Spectroscopy Infrared spectra, in the far-IR region (600-50 cm^{-1}), were recorded on a computer controlled Nicolet 750 Magna-IR Series II spectrophotometer equipped with a TGS/PE detector and silicon beam splitter in 4 cm^{-1} resolution. The samples were ground with dry CsI into a fine powder and pressed into translucent pellets.

Raman Spectroscopy Raman spectra were recorded with a BIO-RAD FT Raman spectrometer with a Spectra-Physics Topaz T10-106c 1,064 nm YAG laser running at 11 to 11.5 amps equipped with a Ge detector. The samples were ground into a fine powder and loaded into melting point capillary tubes.

Single crystal optical transmission spectroscopy Room temperature single crystal optical transmission spectra were obtained on a Hitachi U-6000 Microscopic FT Spectrophotometer mounted on an Olympus BH2-UMA metallurgical microscope over a range of 380 to 900 nm. Crystals lying on a glass slide were positioned over the light source and the transmitted light was detected from above.

Differential Thermal Analysis (DTA) DTA experiments were performed on a computer-controlled Shimadzu DTA-50 thermal analyzer. Typically a sample ($\sim$ 25 mg) of ground crystalline material was sealed in quartz ampoules under vacuum. A quartz ampoule of equal mass filled with Al$_2$O$_3$ was sealed and placed on the reference side of the detector. The sample was heated to the desired temperature at 10 ºC/min, then isothermed for 10 minutes and finally cooled to 50 ºC at the same rate. The residues of the DTA experiments were examined by X-ray powder diffraction. To evaluate congruent melting we compared the X-ray powder diffraction patterns before and after the DTA experiments. The

stability/reproducibility of the samples were monitored by running at multiple cycles.

Differential Scanning Calorimetry (DSC)   DSC experiments were performed on a computer-controlled Shimadzu DSC-50 thermal analyzer under a nitrogen atmosphere at a flow rate of 35 ml/min. The samples (~ 5 mg) of the crystalline material were crimped in an aluminum pan. The pan was placed on the sample (right) side of the DSC-50 detector and a crimped empty aluminum pan of equal mass was placed on the reference (left) side of the detector. The samples were heated to the desired temperature at 5 °C/min, isothermed for 5 minutes, and finally cooled at the same rate to 50°C. The temperatures associated with each peak in the spectrum have a standard deviation of 0.2 degrees. The adopted convention in displaying the data is as follows: exothermic peaks are associated with a positive heat flow while endothermic peaks are associated with a negative heat flow.

Semiquantitative microprobe analyses   The analyses were performed using a JEOL JSM-6400V scanning electron microscope (SEM) equipped with a TN 5500 EDS detector. This technique was used to confirm the presence of all elements in the compounds. Data acquisition was performed with an accelerating voltage of 20kV and thirty seconds accumulation time.

Single crystal X-ray Crystallography. Intensity data for (I) was collected on a Siemens SMART-CCD diffractometer using graphite-monochromatized MoKα radiation. The data collection covered the full sphere of reciprocal space, out to 58° 2Θ. The individual frames were measures with a detector to crystal distance of 5 cm with an omega rotation of 0.3 deg. and an acquisition time of 30 seconds, leading to a total measurement time of about 18 hours. The SMART software[11] was used for the data acquisition and SAINT[11] for data reduction. The space group was determined from systematic absences and intensity statistics. No crystal decay was detected for (I). A correction for Lorentz polarization effects and an empirical

absorption correction (SADABS)[12] were applied to the data. The structure of (I) was solved using direct methods and refined with a full-matrix least squares techniques of the SHELXTL[13] package of crystallographic programs. With a full sphere of data, the correct enantiomorph could be refined to determine the correct structure. The structure as refined had a flack parameter of 0.02(2), confirming the structure as solved was the correct enantiomorph.

Intensity data for (II) were collected using a Rigaku AFC6S four-circle automated diffractometer equipped with a graphite crystal monochromator. Crystal stability was monitored with three standard reflections whose intensities were checked every 150 reflections, and unless noted, no crystal decay was detected in any of the compounds. The space groups were determined from systematic absences and intensity statistics. An empirical absorption correction based on ψ scans was applied to all data during initial stages of refinement. The structures were solved by direct methods using SHELXS-86 software[14a], and full matrix least squares refinement was performed using the TEXSAN software package[14b]. An empirical DIFABS correction[15] was applied as recommended after full isotropic refinement, after which full anisotropic refinement was performed. Since the structure of β - $RbAg_2SbS_4$ is non-centrosymmetric, a refinement on the other enantiomorph should be performed to determine the correct structure. Only unique data was collected for this data set, preventing the determination of the correct enantiomorph.

The complete data collection parameters and details of the structure solution and refinement for α-$RbAg_2SbS_4$ and β- $RbAg_2SbS_4$ are given in Table 3-3. The coordinates of all atoms, average temperature factors, and their estimated standard deviations are given in Tables 3-4 to 3-5.

Table 3-1.   Calculated and Observed X-ray Powder Patterns for
α-RbAg$_2$SbS$_4$ (I).

hkl	d_{calc}, Å	d obsd, Å	I/I_{max}(obsd)
003	5.55	5.51	100
101	5.42	5.38	12
103	3.99	3.97	25
104	3.37	3.35	100
110	3.31	3.29	60
111	3.24	3.23	24
112	3.07	3.06	9
105	2.88	2.87	31
113	2.84		
201	2.82	2.77	34
203	2.54	2.56	20
204	2.36	2.35	18
115	2.34	2.26	8
107	2.19	2.19	12
205	2.17	2.17	7
211	2.14	2.14	5
116	2.12	2.12	12
212	2.09	2.08	6
213	2.01	2.01	11
206	1.99	1.99	5
108	1.95	1.95	41
214 300	1.92	1.92	12
301	1.89	1.89	13
302	1.863	1.862	11
207	1.831	1.834	10
215	1.817	1.816	11
118 109	1.763	1.764	7

Table 3-2.   Calculated and Observed X-ray Powder Patterns for
               β-RbAg$_2$SbS$_4$ (II).

hkl	d_{calc}, Å	d_{obsd}, Å	I/I_{max}(obsd)
101	5.51	5.50	30
200	3.62	3.61	33
020	3.39	3.39	26
112	3.23	3.22	66
211	2.99	2.98	6
121	2.89	2.88	8
202	2.75	2.75	6
103	2.64	2.64	6
013	2.62	2.61	6
220	2.47	2.47	25
004 213	2.12	2.12	9
123	2.08	2.08	5
312	2.00	2.00	22
114	1.95	1.99	13
132	1.928	1.924	100
321	1.917	1.919	56
204	1.837	1.836	8
400	1.810	1.808	32
024	1.805	1.803	38
033	1.771	1.769	9
411	1.713	1.712	4
040	1.698	1.694	8
105	1.660	1.658	5
323 224	1.616	1.615	7
420	1.597	1.596	5

Table 3-3.　　Crystallographic Data for α-RbAg$_2$SbS$_4$ and β-RbAg$_2$SbS$_4$.

Formula	α-RbAg$_2$SbS$_4$	β-RbAg$_2$SbS$_4$
FW	551.19	551.19
a, Å	6.616(2)	7.240(3)
b, Å	6.616(2)	6.795(3)
c, Å	16.588(3)	8.528(3)
α (deg)	90.00	90.00
β (deg)	90.00	90.00
γ (deg)	120.00	90.00
Z, V(Å^3)	3; 628.8(5)	4, 419.5 (3)
λ (Mo Kα), Å	0.71069	0.71069
space group	P 3$_2$21 (#154)	I 222 (#23)
D$_{calc}$, g/cm^3	3.64	4.45
μ, cm^{-1}	14.99	251.93
2θmax, deg	57.6	49.8
Temp ($^\circ$C)	-73	23
Final R$_1$/wR$_2$[a] %	2.7/7.9	NA
Final R/R$_w$,[b] %	NA	3.0/4.8
Octants collected	$\pm$h, $\pm$k, $\pm$l	h, k, l
Total Data Measured	6604	233
Total Unique Data (ave)	1040	233
Data F$_o$^{2}>2σ(Fσ^{2})	1040	NA
Data F$_o$^{2}>3σ(Fσ^{2})	NA	219
No. of Variables	39	21
Crystal Dimen., mm	0.20x0.20x0.10	0.16x0.080.40

[a]$R = \Sigma(|F_o{}^2| - |F_c{}^2|)/\Sigma|F_o{}^2|$, $R_w = \{\Sigma_w(|F_o{}^2| - |F_c{}^2|)^2/\Sigma_w|F_o{}^2|^2\}^{1/2}$.

[b]$R = \Sigma(|F_o| - |F_c|)/\Sigma|F_o|$, $R_w = \{\Sigma_w(|F_o| - |F_c|)^2/\Sigma_w|F_o|^2\}^{1/2}$.

Table 3-4.   Atomic Coordinates (x 10^4) and Equivalent Isotropic Displacement Parameters (Å^2 x 10^3) for α-$RbAg_2SbS_4$ (I) with Estimate Standard Deviations in Parentheses.

Atom	X	Y	Z	U_{eq}[a]
Sb1	7200(1)	0	6667	5(1)
Rb1	4434(1)	4434(1)	5000	12(1)
Ag1	948(1)	-2874(1)	5954(1)	21(1)
S1	5053(2)	-191(2)	5529(1)	10(1)
S2	7587(3)	-3315(3)	6743(1)	9(1)

[a] U(eq) is defined as one third of the trace of the orthogonalized Uij tensor.

Table 3-5.   Fractional Atomic Coordinates and B(eq) Values for β-$RbAg_2SbS_4$ (II) with Estimated Standard Deviations in Parentheses.

Atom	X	Y	Z	B_{eq}[a]Å^2
Sb1	1/2	0	0	1.12(6)
Ag1	1/2	1/2	-0.2031	4.2(1)
Rb1	0	1/2	0	2.0(1)
S1	0.6884(5)	-0.1980(6)	0.1575(4)	1.6(1)

[a] B values for anisotropically refined atoms are given in the form of the isotropic equivalent displacement parameter defined as $B_{eq} = (4/3)[a^2B(1, 1) + b^2B(2, 2) + c^2B(3, 3) + ab(\cos\gamma)B(1,2) + ac(\cos\beta)B(1,3) + bc(\cos\alpha)B(2, 3)$

3. Results and Discussion

3.1. Description of Structures

Structure of α-RbAg₂SbS₄ (I). The three-dimensional structure of α-RbAg₂SbS₄ is isostructural to RbAg₂SbS₄[4b] reported by Kolis, et. al., and similar to the structure of SrCu₂SnS₄[16]. The acentric three-dimensional framework is formed by the complex condensation of corner-sharing AgS_4 tetrahedrons and $[SbS_4]^{3-}$ units, see Figure 3-1. This complex binding scheme produces Rb^+ filled channels that run in a non-interconnecting criss-cross fashion along the crystallographic a - and b - axes, and in the [110] direction, see Figure 3-2. A view down the c- axis, highlighting the hexagonal arrangement, is shown in Figure 3-3. This unusual arrangement for three channels is the result of the successive application of the 3_2 screw axis parallel to the c - axis. A polyhedral representation showing the helical nature of the $[SbS_4]^{3-}$ units is shown in Figure 3-4.

The $[SbS_4]^{3-}$ unit adopts a symmetric binding mode with all four sulfur atoms coordinating with two Ag^+ ions as shown in Scheme 1.

Scheme 1
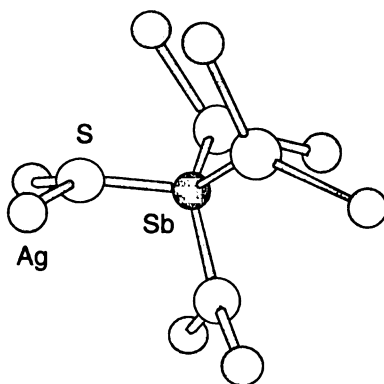
The $[SbS_4]^{3-}$ unit is a fairly regular tetrahedron with Sb-S distances in the range from 2.327(2)Å to 2.335(2)Å and an average S-Sb-S angle of 109.4(2)°. The Ag^+ ion has a distorted tetrahedral geometry with Ag-S bond distances in the range from 2.490(2)Å to 2.733(2)Å. The S-Ag-S bond angles range from 91.82(4)° to 146.19(3)°. The closest Ag-Ag contact is 4.065(3)Å which does not indicate any significant interactions.

Our refinement of the structure of α-RbAg$_2$SbS$_4$ compares well with the results reported by Kolis and coworkers.[4b] Although there are slight discrepancies in the final reported residuals (3.7/3.8 vs. 2.7/7.9) and the standard deviations, a direct comparison cannot be made because of the different temperature used to collect the data. The structure of α-RbAg$_2$SbS$_4$ was initially solved with the space group P3$_1$. After discovering the published refinement of α-RbAg$_2$SbS$_4$[4b] with the higher symmetry space group, a solution on our original data set was attempted with this new space group. Initial refinements in the higher symmetry space group (P3$_2$21) were unsuccessful and a related compound, SrCu$_2$SnS$_4$, was solved with the lower symmetry space group (P3$_1$), casting doubt as to the correct space group. This problem was already encountered by Kolis et. al.[4b] and upon careful consideration of the possible space groups the correct space group, P3$_2$21, was determined. The space group choice was confirmed, of the CCD data set, by utilizing the SHELXL[13] package of crystallographic programs to convert the lower symmetry solution to the higher symmetry space group.

The structure of α-RbAg$_2$SbS$_4$ is unique in that the binary "Ag$_2$S$_4$" portion of the structure forms a three-dimensional framework in which the Sb^{5+} species reside. Polyhedral and ball stick representations of the stable "Ag$_2$S$_4$" framework are shown in Figures 3-5 and 3-6, respectively. This represents a departure from other chalcoantimonate and chalcophosphate compounds, dominated by the various $[E_xQ_y]^{n-}$ (E = P, Sb; Q = S, Se, Te) units coordination to the metal ions, not the

metal ions framework coordinating to the various $[E_xQ_y]^{n-}$ units. The $[Ag_2SbS_4]^{n-}$ framework is stabilized by an eight-coordinate Rb^+ ion located in the channels [range of Rb-S distances, 3.352(2) - 3.483(2)Å; mean 3.42(1) Å] Tables of selected distances and angles for α-RbAb$_2$SbS$_4$ are given in Table 3-6.

Structure of β-RbAg$_2$SbS$_4$ (II). The three-dimensional structure of β-RbAg$_2$SbS$_4$ is similar, but not identical, to the structure of BaAg$_2$GeS$_4$[17] and KAg$_2$SbS$_4$[4b]. A view down the a - axis is given in Figure 3-7. The three-dimensional framework is best described as a series of tetrahedral AgS$_4$ units that form layers via corner-sharing in the fashion of HgI$_2$[18], see Figure 3-8. These layers are linked by $[SbS_4]^{3-}$ tetrahedral which edge-share to AgS$_4$ units in opposite layers, resulting in channels in which the Rb^+ cations reside. A polyhedral representation (Figure 3-9) clearly shows the acentric nature of the structure by highlighting the fact that all the tetrahedral $[SbS_4]^{3-}$ units all point along the crystallographic c - direction. This arrangement produces criss-cross channels along the a and b directions. The dimensions of the channels (5.059Å (Ag - Ag) by 7.240Å (Sb - Sb)) appear to be just large enough to stabilize the Rb^+ ions.

The small difference between the $[Ag_2SbS_4]^{n-}$ framework observed in β-RbAb$_2$SbS$_4$ and that of KAg$_2$SbS$_4$[4b] is not readily apparent, see Scheme 2. As shown in Scheme 2, the projections down the crystallographic c - axis appear to be identical. Although, when the structure is stabilized by the larger Rb^+ cation, the framework distorts, breaking the 4-fold rotation and lowering the symmetry. Since both compounds are acentric, it is the length of the cell edges that is important, not the choice of the unit cell. The tetrahedral AgS$_4$ units (Figure 3-9) are highly distorted, resulting in a compressed Ag-S contact of 2.495(4)Å and a severely elongated Ag-S contact of 2.883(4)Å. The bond angles of the tetrahedral AgS$_4$ unit are just as distorted, ranging from 91.17(2)° to 162.0(2)°, respectively. This

highly anisotropic nature of the tetrahedral AgS_4 units is a common feature of this structure type.[13] The $[SbS_4]^{3-}$ unit is a fairly regular tetrahedron, with a single Sb-S distance of 2.340(4)Å and S-Sb-S angles in the range from 108.7(2)° to 110.2(3)°.

Scheme 2
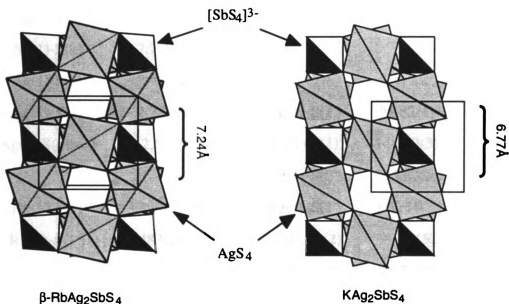
$[SbS_4]^{3-}$

7.24Å

6.77Å

AgS_4

β-RbAg$_2$SbS$_4$ KAg$_2$SbS$_4$

The $[Ag_2SbS_4]^{n-}$ framework is stabilized by an eight-coordinate Rb+ ion located in the channels [range of Rb-S distances, 3.332(4)-3.493(4)Å; mean 3.38(2) Å] Tables of selected distances and angles for β-RbAb$_2$SbS$_4$ are given in Table 3-7.

Table 3-6.   Selected Distances (Å) and Angles (deg) for α-RbAg$_2$SbS$_4$ (I) with Standard Deviations in Parentheses [a].

Sb(1)-S(1)	2.327(2) x2	S(1)-Sb(1)-S(1')	108.64(8)
Sb(1)-S(2)	2.335(2) x2	S(1)-Sb(1)-S(2)	109.40(5) x2
Sb(1)-S(mean)	2.33(1)	S(1)-Sb(1)-S(2')	110.10(5) x2
		S(2')-Sb(1)-S(2)	109.19(8)
Ag(1)-S(1)	2.490(2)	S-Sb-S (mean)	109.4(2)
Ag(1)-S(2)	2.720(2)		
Ag(1)-S(3)	2.469(2)		
Ag(1)-S(4)	2.733(2)	S(1)-Ag(1)-S(1')	91.82(4)
Ag(1)-S(mean)	2.60(7)	S(2)-Ag(1)-S(1)	146.19(3)
		S(1)-Ag(1)-S(2')	105.87(5)
Rb(1)-S(1)	3.399(2) x2	S(2)-Ag(1)-S(1')	114.34(2)
Rb(1)-S(1')	3.483(2) x2	S(1')-Ag(1)-S(2)	90.66(5)
Rb(1)-S(2)	3.352(2) x2	S(2)-Ag(1)-S(2')	95.33(4)
Rb(1)-S(2')	3.439(2) x2	S-Ag(1)-S (mean)	107(8)
Rb(1)-S (mean)	3.41(1)		

[a]The estimated standard deviations in the mean bond lengths and the mean bond angles are calculated by the equation $\sigma l = \{\Sigma_n(l_n - l)^2/n(n - 1)\}^{1/2}$, where l_n is the length (or angle) of the nth bond, l the mean length (or angle), and n the number of bonds.

Table 3-7. Selected Distances (Å) and Angles (deg) for β-RbAg$_2$SbS$_4$ (II) with Standard Deviations in Parentheses [a].

Sb(1)-S(1)	2.340(4)	S(1)-Sb(1)-S(2)	108.7(2)
Sb(1)-S(1')	2.340(4)	S(1)-Sb(1)-S(3)	110.2(3)
Sb(1)-S(1")	2.340(4)	S(1)-Sb(1)-S(4)	109.7(3)
Sb(1)-S(1''')	2.340(4)	S(2)-Sb(1)-S(3)	109.2(2)
		S(2)-Sb(1)-S(4)	109.8(3)
		S(3)-Sb(1)-S(4)	109.2(2)
Ag(1)-S(1)	2.495(4) x2	S-Sb-S (mean)	109(2)
Ag(1)-S(1')	2.883(4) x2		
Ag(1)-S(mean)	2.6(7)	S(1)-Ag(1)-S(1')	162.0(2)
		S(1)-Ag(1)-S(1")	96.22(7)
		S(1')-Ag(1)-S(1''')	91.17(7)
		S(1)-Ag(1)-S(1")	162.0(2)
Ag(1)-Ag(1')	3.464(5)	S(1')-Ag(1)-S(1")	96.22(7)
		S(3)-Ag(1)-S(4)	131.3(2)
Rb(1)-S(1)	3.493(4) x4	S-Ag(1)-S (mean)	123(13)
Rb(1)-S(1)	3.332(4) x4		
Rb(1)-S(mean)	3.38(2)	Ag(1)-S(1)-Ag(1')	138.4(1)

[a]The estimated standard deviations in the mean bond lengths and the mean bond angles are calculated by the equation $\sigma l = \{\Sigma_n (l_n - l)^2/n(n-1)\}^{1/2}$, where l_n is the length (or angle) of the nth bond, l the mean length (or angle), and n the number of bonds.
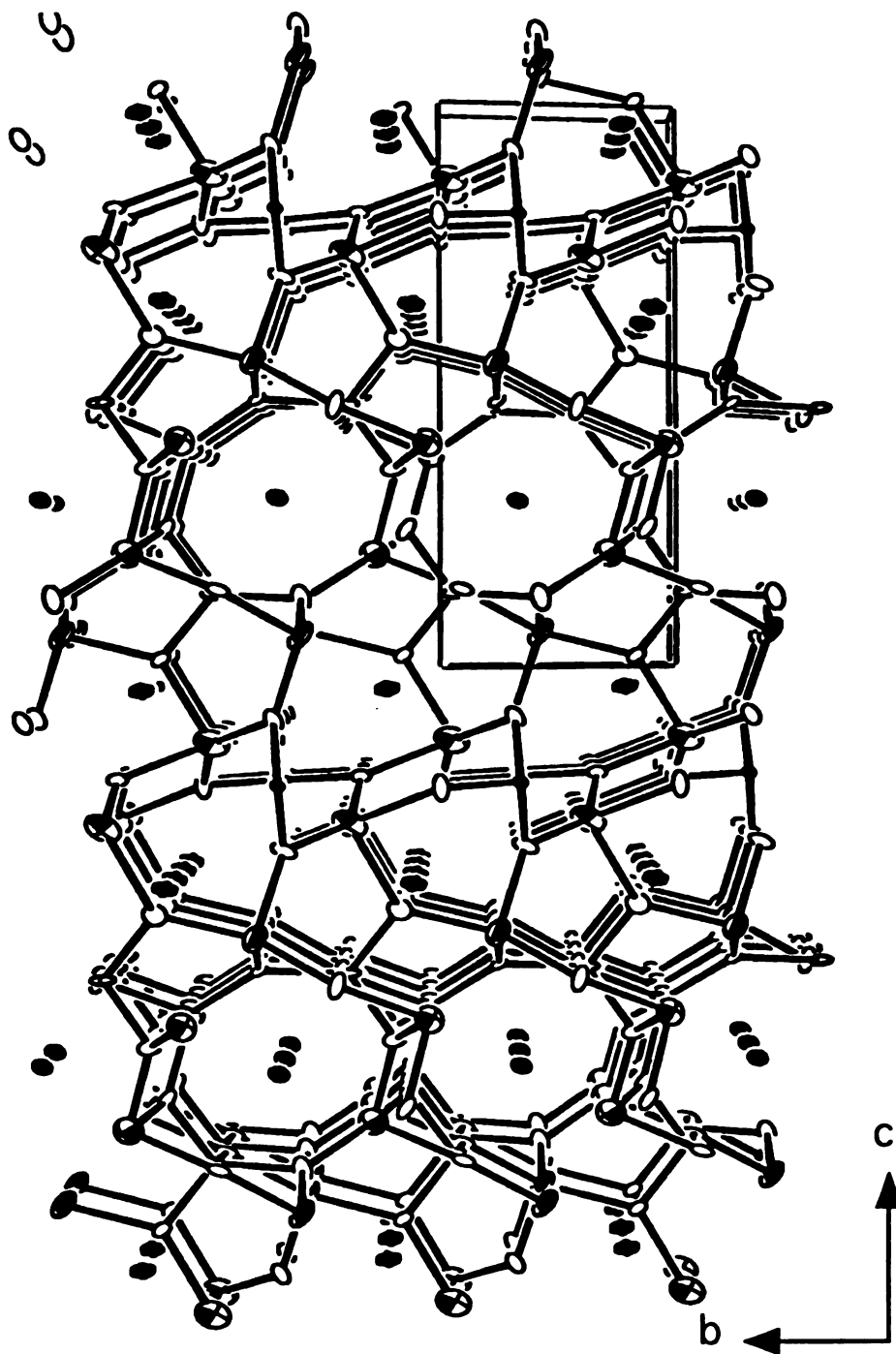
Figure 3-1:   ORTEP representation of α-RbAg$_2$SbS$_4$ as viewed down the *a*-axis. Small octant shaded ellipsoids; Ag, principal axis ellipsoids; Sb, boundary ellipsoids; S, boundary and axis ellipsoids; Rb. (50% probability ellipsoids).
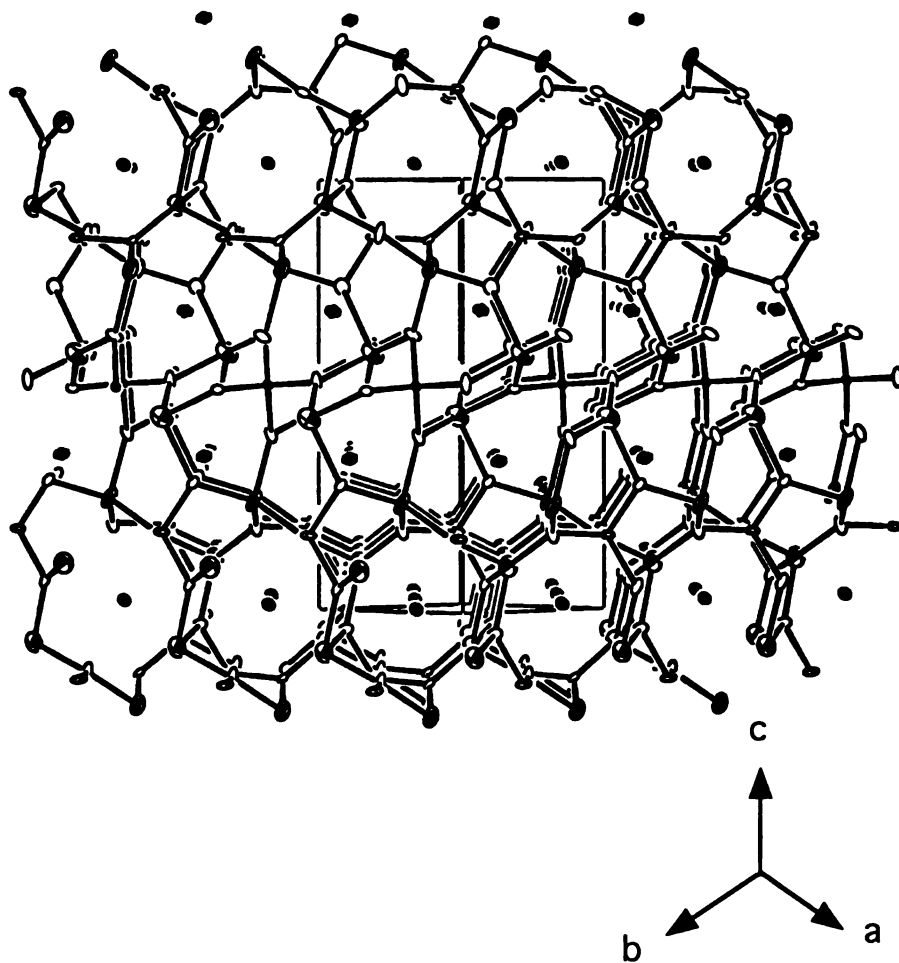
Figure 3-2:   ORTEP representation of α-RbAg₂SbS₄ as viewed down the [110]
               direction. Small octant shaded ellipsoids; Ag, principal axis
               ellipsoids; boundary ellipsoids; S, boundary and axis ellipsoids; Rb.
               (50% probability ellipsoids).
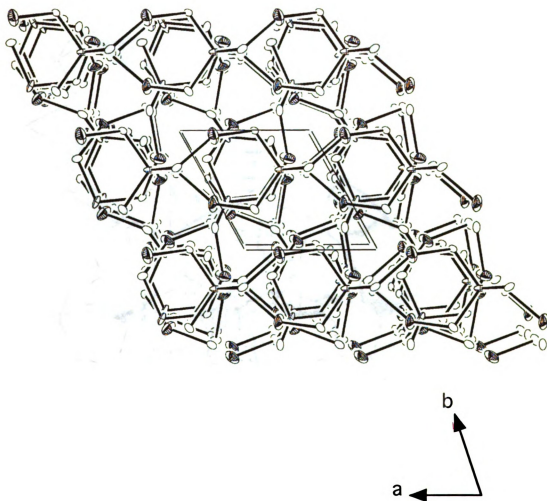
Figure 3-3:   ORTEP representation α-RbAg$_2$SbS$_4$ as viewed along the
                c - direction. Small octant shaded ellipsoids; Ag, principal axis
                ellipsoids; boundary ellipsoids; S. The cations are removed for
                clarity. (50% probability ellipsoids).
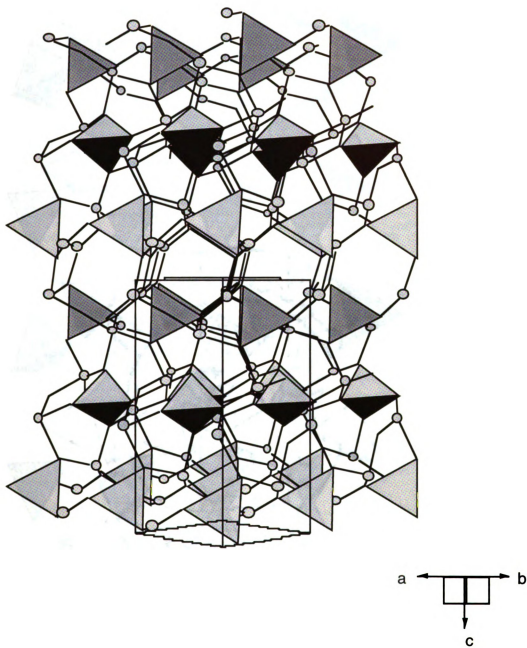
Figure 3-4:   Polyhedral representation of α-RbAg$_2$SbS$_4$ as viewed down the [110] direction, pattern shaded polyhedra; SbS$_4$, ball and stick polyhedra; AgS$_4$. The cations are omitted for clarity.

b ← → a

↓ c
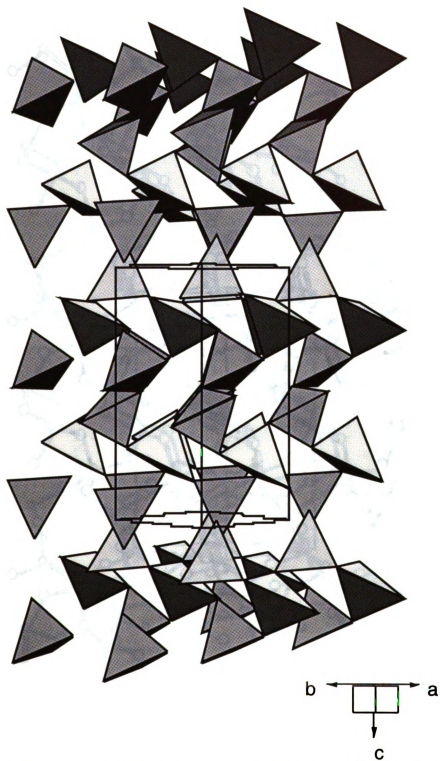
Figure 3-5:   Polyhedral representation of the "Ag$_2$S$_4$" framework in
α-RbAg$_2$SbS$_4$.
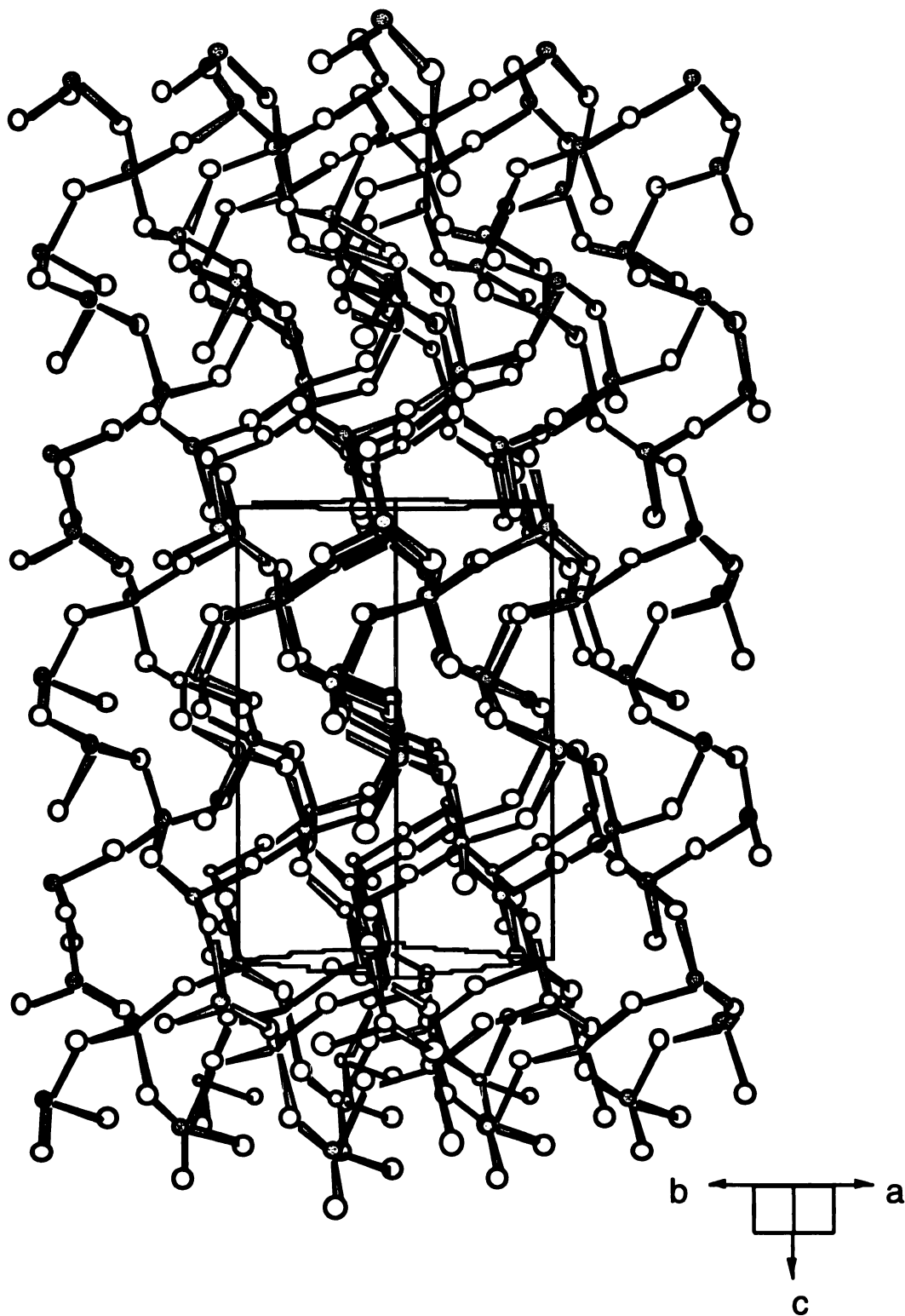
Figure 3-6:   Ball and Stick view of the "Ag$_2$S$_4$" framework α-RbAg$_2$SbS$_4$.
Open circles; S, and shaded circles; Ag
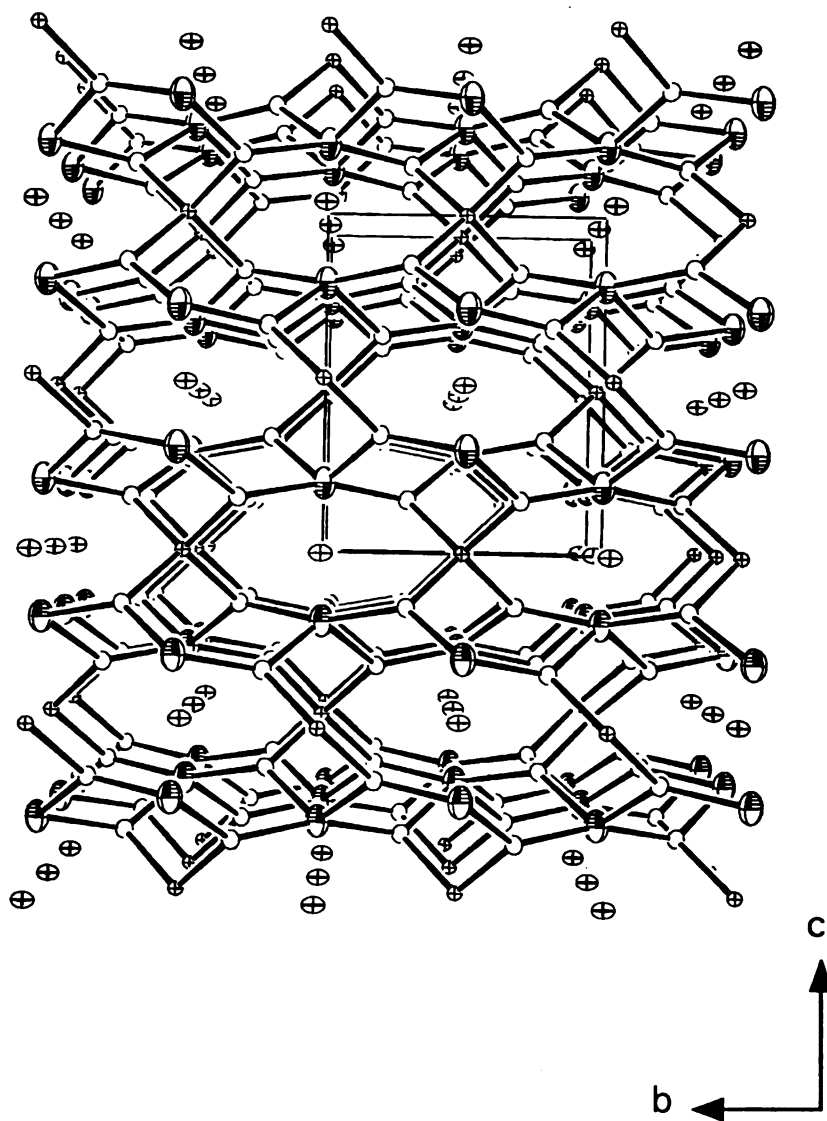
Figure 3-7:   ORTEP representation of β-RbAg$_2$SbS$_4$, as viewed down the a -
axis. Small octant shaded ellipsoids; Ag, principal axis ellipsoids;
boundary ellipsoids; S, boundary and axis ellipsoids; Rb. (50%
probability ellipsoids)

Figure 3-8: ORTEP representation of the "Ag$_2$S$_4$" layer in β-RbAg$_2$SbS$_4$ Small octant shaded ellipsoids; Ag, boundary ellipsoids; S. (50% probability ellipsoids)
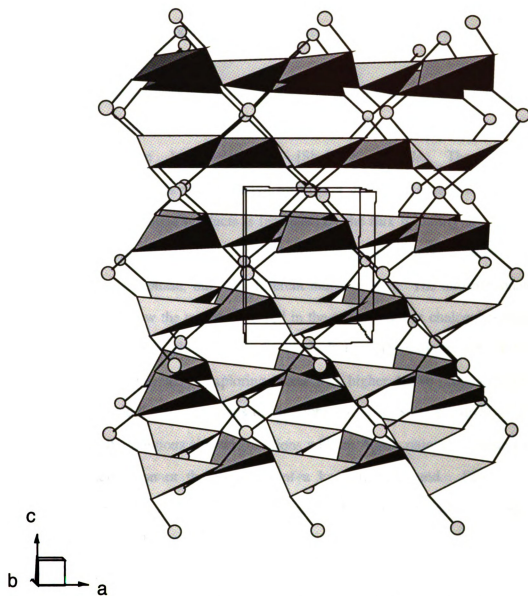
Figure 3-9:   Polyhedral representation of β-RbAg$_2$SbS$_4$ (II) as viewed down the
                   b - axis highlighting the highly distorted AgS$_4$ units. Pattern shaded
                   polyhedra; AgS$_4$, ball and stick polyhedra; SbS$_4$. The cations are
                   omitted for clarity.

3.2. Synthesis and Physicochemical Properties:

The syntheses were the result of redox reactions in which the silver is oxidized by polysulfide ions in the $A_x[Sb_yS_z]$ flux. The Ag^+ centers are then coordinated by the highly charged $[Sb_yS_z]^{n-}$ ligands. The molten polythioantimonate flux is very effective for crystal growth in this system. The isolation of pure crystalline products is facilitated by the flux solubility in aqueous and organic solvents. In α-$RbAg_2SbS_4$, the orange and red-orange crystals were found to be the same phase, but with different morphologies. The thioantimonate fluxes appear to follow the trends observed in the corresponding chalcophosphate fluxes, where Lewis basic fluxes favors the tetrahedral $[EQ_4]^{3-}$ units (E = P, Sb; Q = S, Se). We were interested in exploring fluxes with higher Ag/Sb ratios in hopes of incorporating additional equivalents of Ag^+ ions into the resulting $[Ag_xSb_yS_z]^{n-}$ framework. In the previous chapter, reactions with an Ag/Sb ratio = 2 resulted in either phase separation or the formation of a known compound. Silver rich frameworks were only stabilized when the Ag/Sb ratio $\geq$ 3. In addition, the Rb^+ cation may provide the best combination of size and basicity to stabilize novel $[Ag_xSb_yS_z]^{n-}$ frameworks.

The optical absorption properties of were evaluated by examining the single crystal optical transmission spectra of the materials. The spectra confirm the semiconducting nature of the materials by revealing the presence of sharp optical gaps. The spectrum of α-$RbAg_2SbS_4$ exhibits a steep absorption edge, from which the band-gap, E_g, can be assessed at 2.23 eV. The spectrum of β-$RbAg_2SbS_4$ also exhibits a steep absorption edge with a band-gap, E_g, of 1.96 eV. Representative spectra for (I) and (II) are given in Figure 3-10. Since the optical gap was determined by single crystal data, plots of $(abs)^2$ vs. hv and $\sqrt{abs}$ vs. hv,

shown in Figures 3-11 and 3-12, can be used to distinguish between a direct and an indirect band gap in semiconductors.[19] The spectra confirm the indirect nature of the band gap for both (I) and (II).

The infrared spectrum of α-RbAg$_2$SbS$_4$ and β-RbAg$_2$SbS$_4$ show a strong absorption at *ca.* 390 cm^{-1}, characteristic of the tetrahedral [SbS$_4$]$^{3-}$ unit[3,4]. The Raman spectrum of (I) and (II) show absorbencies at *ca.* 361 cm^{-1}, and 174 cm^{-1} are characteristic of the tetrahedral [SbS$_4$]$^{3-}$ unit by comparison with the Raman spectrum of Na$_3$SbS$_4$·9H$_2$O.[20] The absorptions at *ca.* 392 cm^{-1} and 380 cm^{-1} are assigned to Ag-S vibrations. The far-IR and Raman data are summarized in Table 3-8. The Raman spectra for (I) and (II) are shown in Figure 3-13.

3.3. Thermal Analysis

The thermal behavior of chalcogenide compounds is investigated to determine the stability of the materials. Materials which melt congruently can be mechanically processed, making large single crystals or thin films from a melt. This is property is essential for materials to be viable candidates for applications requiring well-formed single crystals. The acentric structures of (I)-(II) makes these materials candidates for several potential applications especially if they melt congruently.

Materials that melt incongruently highlight the metastable nature of the compounds synthesized by polychalcometalate fluxes. Careful examination of the residue by powder x-ray diffraction offers insight into the compounds stability. In materials that melt incongruently, identification of the decomposition products often allows for the determination of the kinetically and thermodynamically stable phases when multiple phases of the same formula exist or when proposing possible mechanisms for product decomposition[21]. Occasionally, some materials exhibit interesting thermal properties, such as reversible glass formation[22]. The thermal

behavior of α-RbAg$_2$SbS$_4$ was so completely unprecedented that we are struggling to understand the results.

The results that follow are extraordinary in the research of chalcogenide compounds. These results differ from batch to batch as well as from sample to sample from the *same* batch. The latter happens in seemingly pure single phase samples. The complex thermal behavior of α-RbAg$_2$SbS$_4$ is summarized in Table 3-8. The first sample from Batch I displayed reversible glass formation. Although rare, this behavior is observed in the (Ph$_4$P) [M(Se$_6$)$_2$] (M = Ga, In, Tl)[22a] and Cs$_2$Hg$_3$M$_2$S$_8$ (M = Sn, Ge).[22b] Reversible glass formation is characterized by an endothermic peak upon heating and the corresponding exothermic peak is observed upon subsequent heating. As shown in Figure 3-14A, upon heating the first sample of α-RbAg$_2$SbS$_4$, a single endothermic peak is observed at 396°C. Upon cooling, no corresponding exothermic peak is observed. Upon subsequent heating, a broad exothermic peak is observed at 306°C, followed by a sharp endothermic peak at 392°C. Upon cooling, again no corresponding exothermic peak is observed, see Figure 3-14B. The compounds sixth cycle is shown in Figure 3-14C. The powder X-ray diffraction pattern of the residue at room temperature was very weak, showing only a few peaks, indexed to Sb and Ag metal.

A second sample, from Batch I, showed a completely different series of thermal events. Upon heating, three endothermic peaks are observed at 326°C, 400°C, and 430°C, respectively. Upon cooling, two exothermic peaks are observed at 364°C and 267°C, respectively, see Figure 3-15A. Upon subsequent heating, the three exothermic peaks are again observed at 326°C, 400°C, and 430°C, respectively. Upon cooling, only a single endothermic peak at 364°C was observed, see Figure 3-15B. Upon heating for a third cycle two exothermic peaks were observed at 246°C and 306°C; followed by two endothermic peaks at 400°C and 430°C, respectively. A single sharp exothermic peak at 357°C was observed

upon cooling. A fourth cycle showed an exothermic peak, at 246°C, upon heating folloowed by the two endothermic peaks at 400°C, and 430°C, respectively. Upon cooling, only a single sharp exothermic peak at 357°C is observed. The third and fourth DTA cycle of sample 2 from Batch I are shown in Figure 3-16. Examination of the ingot by powder X-ray diffraction revealed that α-$RbAg_2SbS_4$ had undergone a structural transformation to a new material with a large unit cell, as determined by the low angle peaks observed in the powder X-ray diffraction of the residue. A new sample from a second batch (Sample 1 Batch II) was run to confirm the results from the second sample of the first batch, see Table 3-8. Examination of the ingot by powder X-ray diffraction revealed that the material had undergone a structural transformation, forming a mixture of α-$RbAg_2SbS_4$ and the phase observed in the x-ray powder pattern observed for Sample 2 Batch I.

The thermal analysis of α-$RbAg_2SbS_4$ was also investigated by Differential Scanning Calorimetry (DSC). Although the results obtained by the two methods are very similar, the sample containers are not. The sample container for the DSC is a crimped alumina pan while the sample container for the DTA is an evacuated quartz ampoule. The sample container for the DSC allows for oxygen contamination leading to the decomposition of the material, dramatically effecting the results. Upon heating a sample from a third batch of crystals (Sample 1 Batch III), two sharp endothermic peaks were observed at 330°C and 400°C, respectively. Upon cooling two groups of weak exothermic peaks were observed ca. 347°C and 306°C, see Figure 3-17. Subsequent heating showed a weak exothermic peak at 246°C followed by a single endothermic peak at 407°C. Upon cooling, the weak exothermic peaks had resolved into four peaks at 406 °C, 355°C, 305°C, and 279°C, respectively. A third cycle was attempted but oxygen contamination rendered the results unreliable. Due to oxidation of the sample, a powder pattern was not be run on the residue.

A second sample (Sample 2 Batch III) was examined by DTA in order to evaluate the results obtained by the DSC measurement. Surprisingly, the first three cycles were fairly consistent, showing a single endothermic peak at *ca.* 405°C upon heating. Upon cooling a single exothermic peak at 314°C for the first two cycles and at 307°C for the third cycle, see Figure 3-18. The fourth cycle showed two endothermic peaks at 390°C and 405°C, indicating the formation of a second phase. Upon cooling two exothermic peaks were observed at 333°C and 310°C, respectively. If a second phase formed, the endothermic peak at 390°C was strangely absent in the fifth cycle. A single endothermic peak was observed at 405°C upon heating and two exothermic peaks were observed at 350°C and 305°C, upon cooling.

Another sample from a fourth batch of crystals (Sample 1 Batch IV) was examined by DTA. This sample displayed two endothermic peaks at 332°C and 403°C upon heating and a single exothermic peak at 313°C upon cooling, see Figure 3-19. The next three cycles were fairly consistent, see Table 3-8. The spectra reported here consistently display an endothermic peak at *ca.* 400°C, suggesting a melting point. Variable temperature powder X-ray diffraction experiments confirm that the material was still weakly crystalline at $390°C$. Rational attempts to synthesize this unknown phase above 400°C resulted in the formation of a third phase $A_2Ag_{20}Sb_4S_{19}$ (A = Rb, and Cs). The unknown phase may be a polytype of $A_2Ag_{20}Sb_4S_{19}$ (A = Rb, and Cs) with a narrow window of thermal stability, see Chapter 4. This could explain the above thermal results where once in the molten state, the high mobility of the Ag^+ could cause areas of inhomogenity in the sample, resulting in the formation of an amorphous material from which the phase is produced. At this point, any attempts to propose a mechanism for the observed decomposition product are only speculation. What is

amazing is that we never observed the conversion of α–RbAg$_2$SbS$_4$ to β-RbAg$_2$SbS$_4$ in these experiments.

In stark contrast to the thermal behavior of α-RbAg$_2$SbS$_4$, the DTA data showed that β-RbAg$_2$SbS$_4$ melted with decomposition at 400°C, forming a mixture of (II) and Ag$_3$SbS$_3$. Attempts to index the powder pattern of the residue with α-RbAg$_2$SbS$_4$ were inconclusive, due to the overlap of α-RbAg$_2$SbS$_4$ with β-RbAg$_2$SbS$_4$, and Ag$_3$SbS$_3$.

Table 3-8.   Summary of the thermal behavior of α-RbAg$_2$SbS$_4$

Batch I

Sample	cycle	endothermic heating (^{o}C)	exothermic cooling (^{o}C)	Figure
1	1	396	-NA-	3-14A
	2	306[a],392	-NA-	3-14B
	3-6	306[a], 390	-NA-	3-14C
2	1	326, 400, 430	364, 267	3-15A
	2	326, 400, 430	364	3-15B
	3	246[a], 306[a] 400, 430		3-16A
			357	
	4	246[a]		3-16B
		400, 430	357	

Batch II

Sample	cycle	endothermic heating (^{o}C)	exothermic cooling (^{o}C)
1	1	326, 400 ,430	364, 267

[a] exothermic peak upon heating.

Batch III

Sample	cycle	endothermic heating (°C)	exothermic cooling (°C)	Figure
1[b]	1[b]	330 404	347 306	3-17A
	2[b]	246 [a]		
		407	406, 359, 305, 279	3-17B
2	1	405	314	3-18A
	2	405	314	
	3	403	307	
	4	390, 405	333, 310	
	5	405	307	
	6	405	350, 305	3-18B

Batch IV

Sample	cycle	endothermic heating (°C)	exothermic cooling (°C)	Figure
1	1	332, 403	313	3-19A
	2	405	334	3-19B
	3	403	306	3-19C
	4	405	302	

[a] exothermic peak upon heating.
[b] examined by DSC.

Table 3-9. Infrared and Raman Data for (I) and (II).

α-RbAg$_2$SbS$_4$		β-RbAg$_2$SbS$_4$	
IR	Raman	IR	Raman
		547(m)	
		509(m)	
		435(m)	
	392(w, sh)		396(w)
386(m)	384 (m)	385(s)	380 (w)
	361(s)		361(s)
	332(m)	327(m)	
304(w)		300(m)	
	260(b, sh)	279(m)	
253(m)		246(m)	250(b, sh)
	247(m)	227(m)	227(w)
		203(m)	
170(m)	174(w)	176(m)	174(b)
146(w)		150(m)	

(A)
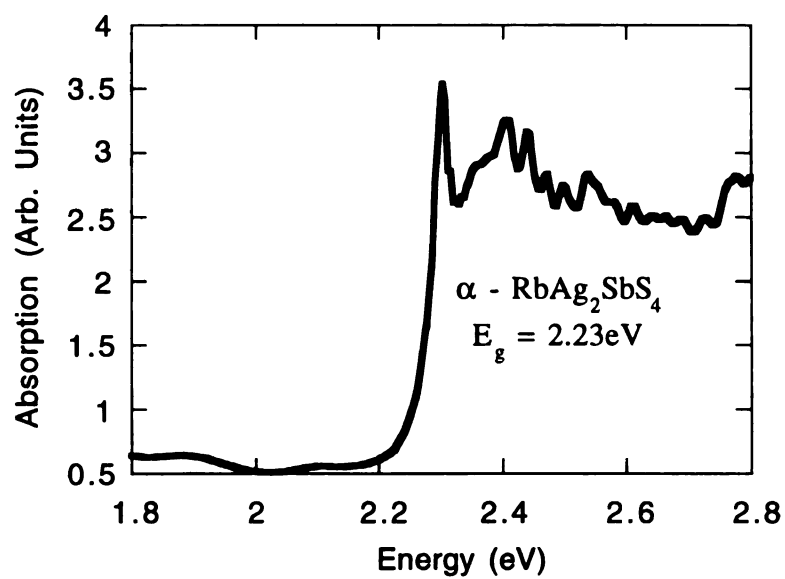
(B)
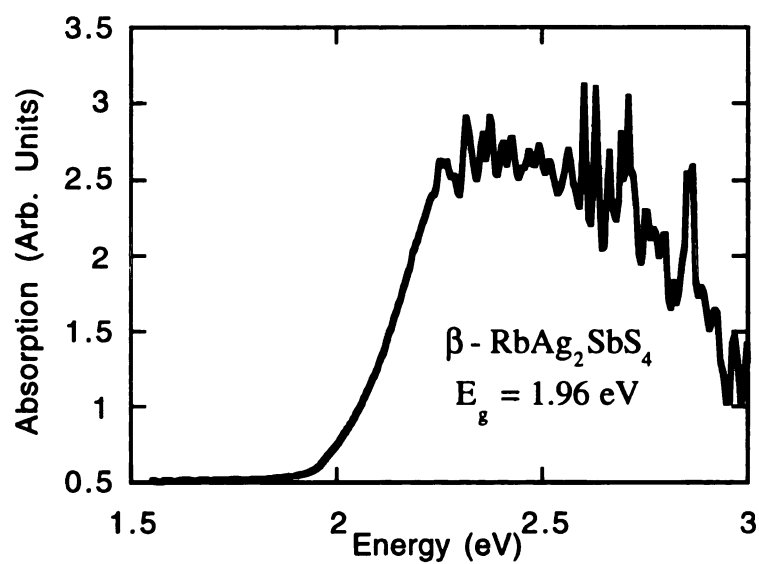
Figure 3-10:   Single-crystal optical transmission spectra of α-RbAg₂SbS₄ (I) and β-RbAg₂SbS₄ (II)

(A)

α - RbAg$_2$SbS$_4$

— — — y = -160.08 + 71.55x R= 0.90735

Y-axis: (Abs.)^2 arb. units

X-axis: Energy (eV)

(B)

α - RbAg$_2$SbS$_4$

— — — y = -24.703 + 11.401x R= 0.97968

Y-axis: (Abs.)$^{1/2}$ arb. units

X-axis: Energy (eV)
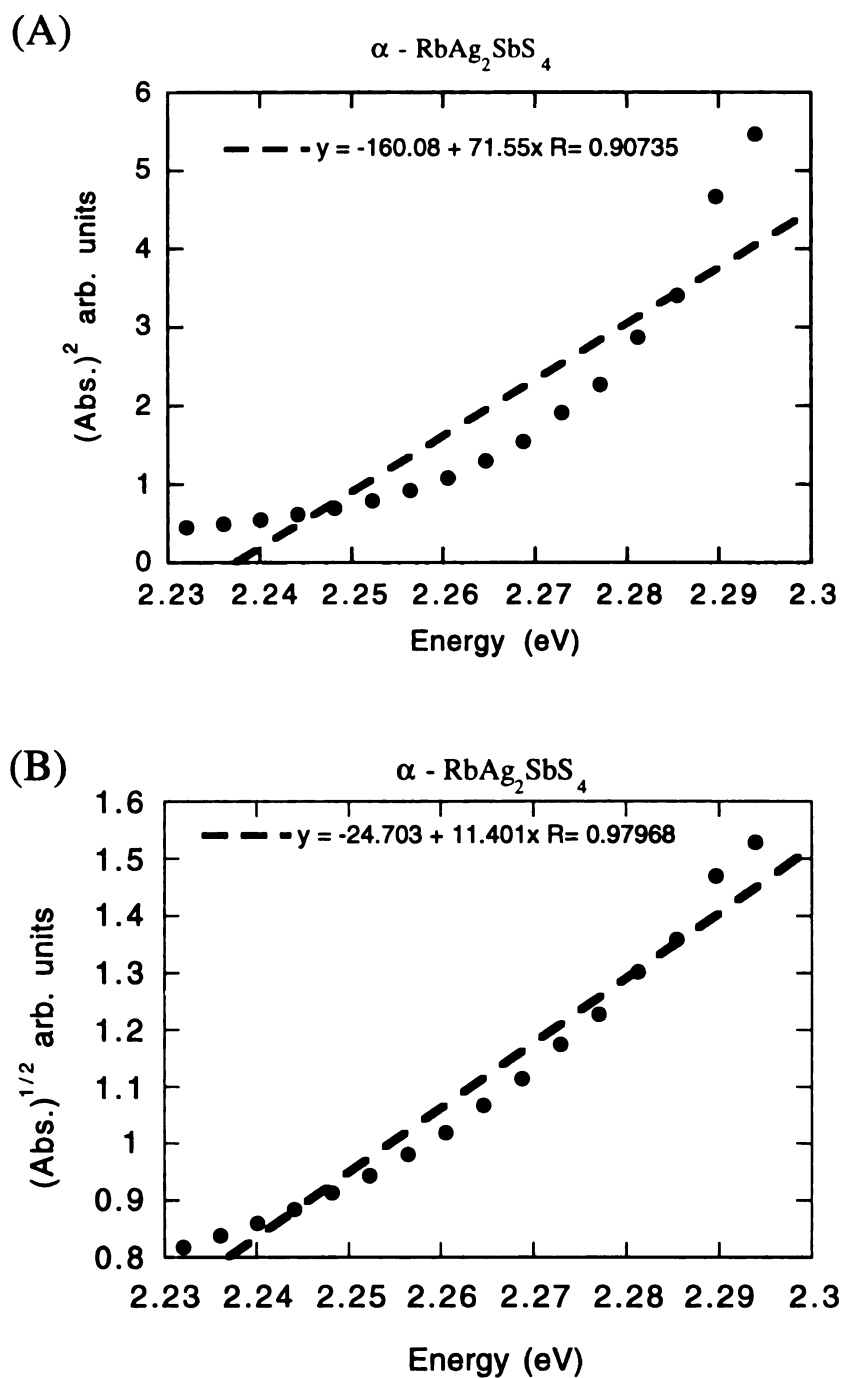
Figure 3-11: Absorption edge of α-RbAg$_2$SbS$_4$ (I) as a function of energy: (A) (abs) dependence (direct gap) and (B) $\sqrt{abs}$ dependence (indirect gap).

(A)

β - RbAg$_2$SbS$_4$

(B)
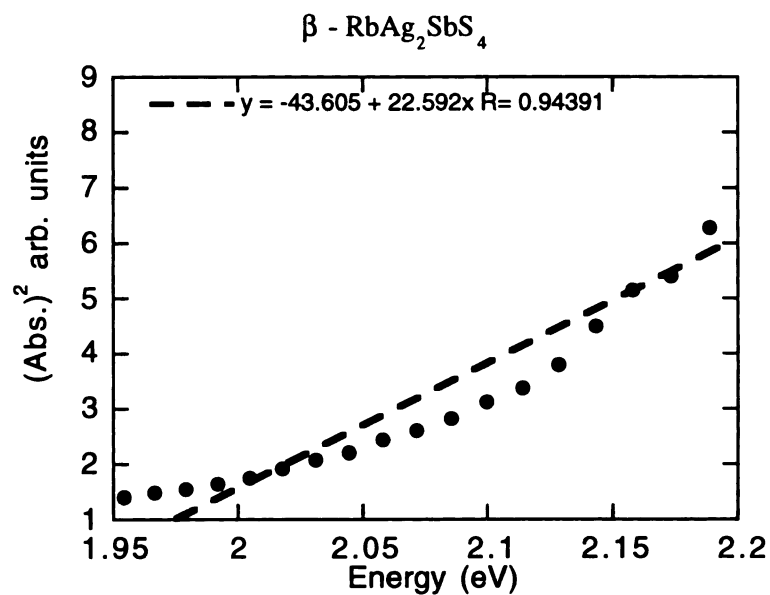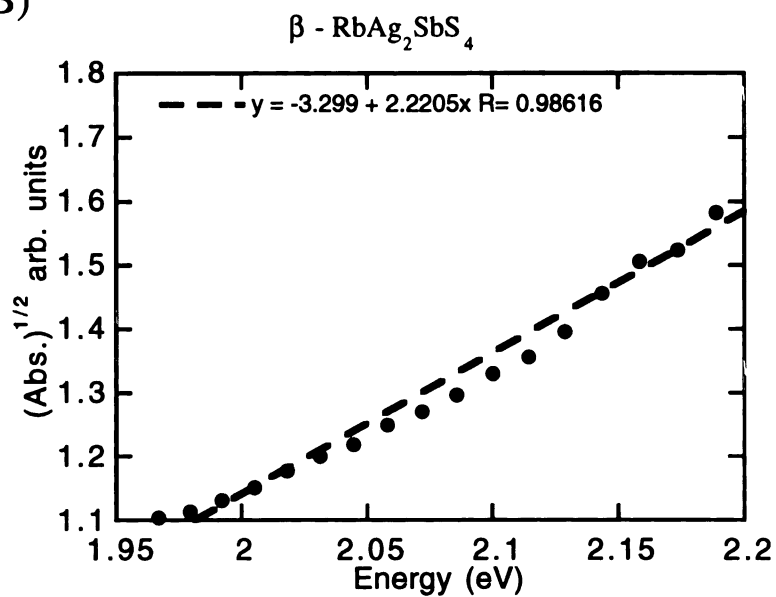
β - RbAg$_2$SbS$_4$

Figure 3-12:   Absorption edge of β-RbAg$_2$SbS$_4$ (I) as a function of energy: (A)
(abs) dependence (direct gap) and (B) $\sqrt{abs}$ dependence (indirect
gap).

(A)
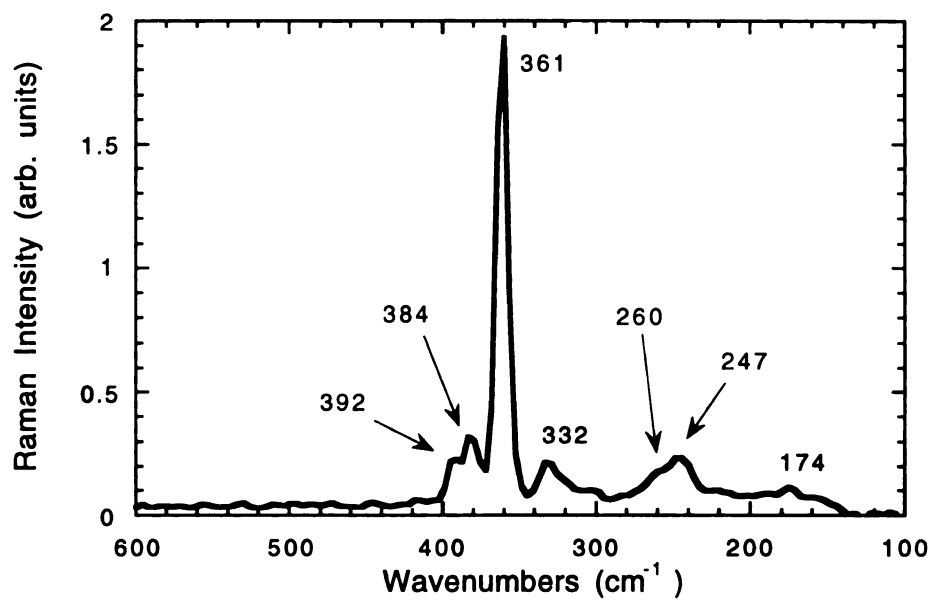
(B)
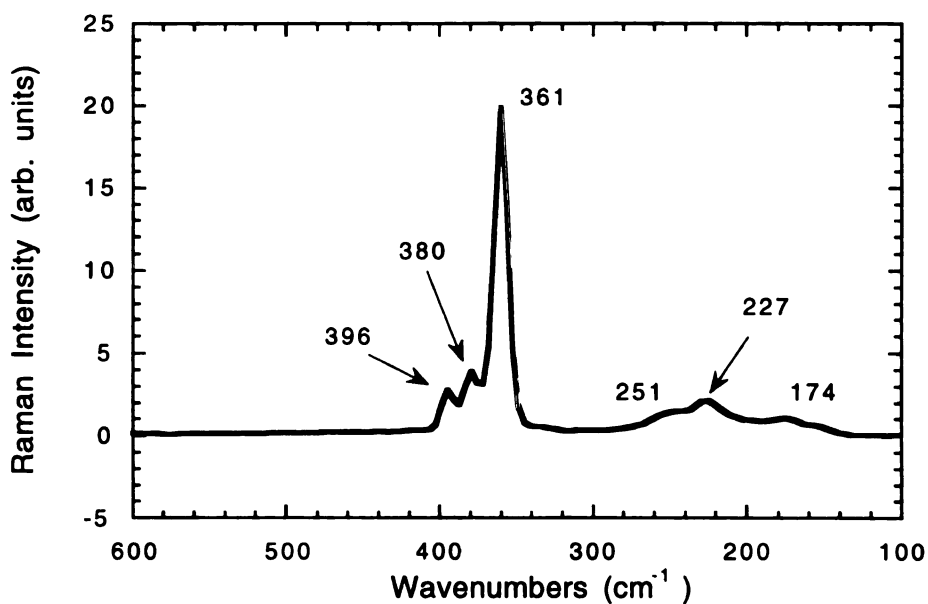
Figure 3-13: The Raman spectra of polycrystalline samples of (A) α-RbAg₂SbS₄ (I) and (B) β-RbAg₂SbS₄ (II)

(A)
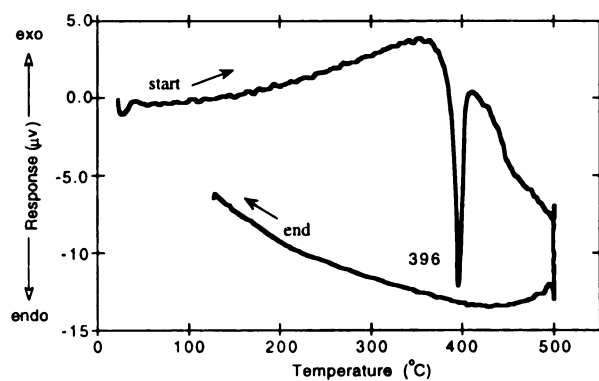
(B)
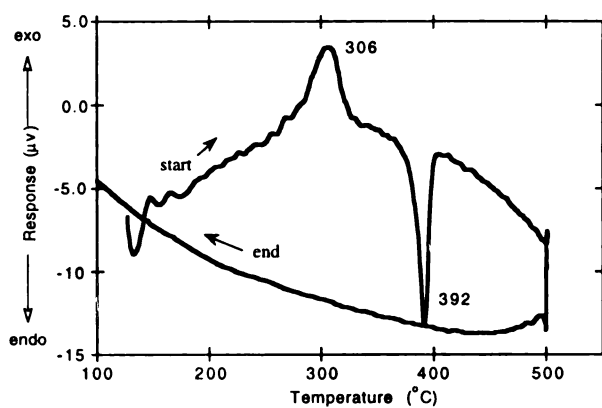
(C)
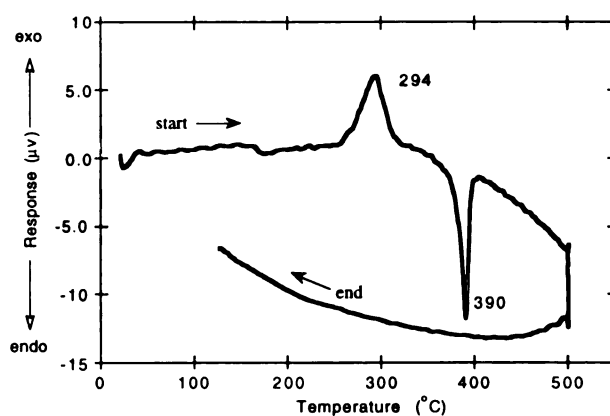
Figure 3-14: (A) DTA diagram for α-RbAg$_2$SbS$_4$ (first cycle) (B) Second DTA cycle of α-RbAg$_2$SbS$_4$, showing the exothermic peak upon heating. (C) Sixth DTA cycle of α-RbAg$_2$SbS$_4$.
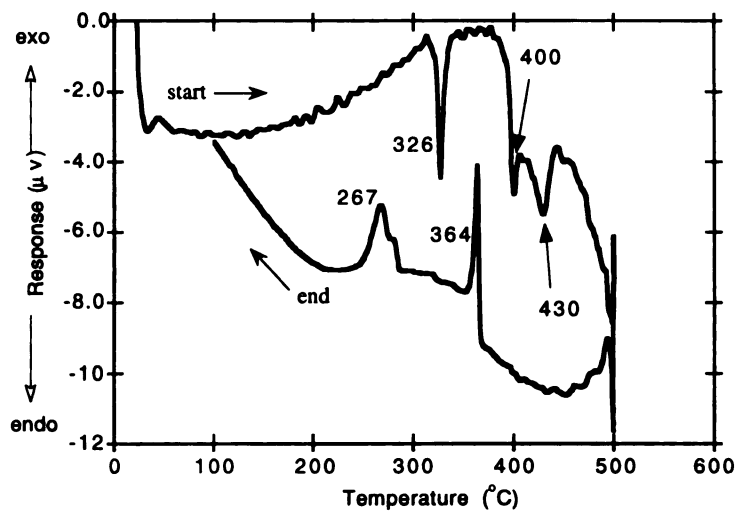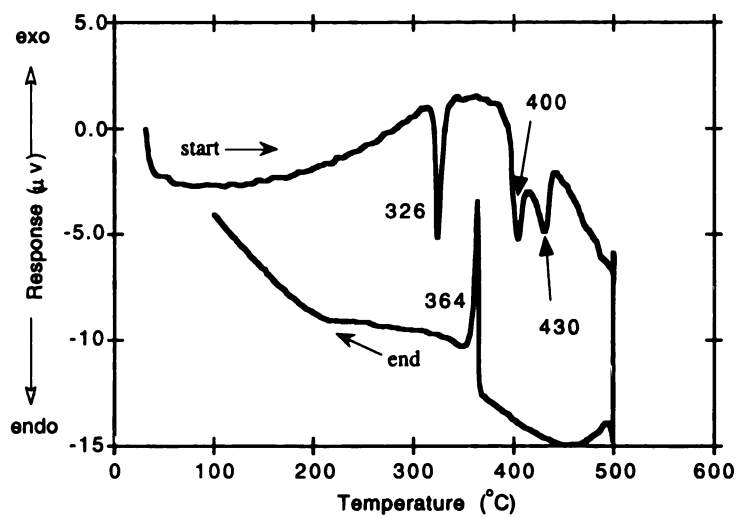
Figure 3-15:   (A) DTA diagram for α-RbAg₂SbS₄ (first cycle).

(B) Second DTA cycle of α-RbAg₂SbS₄, showing two phases.
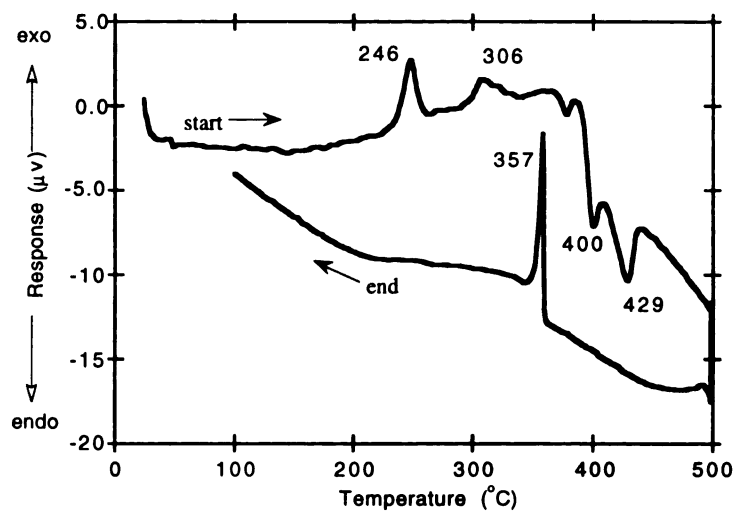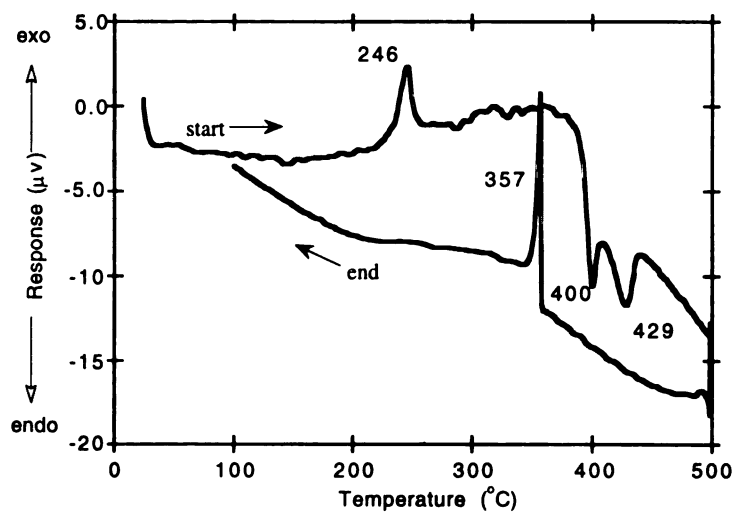
Figure 3-16:   (A) Third DTA cycle of α-RbAg₂SbS₄.
              (B) Fourth DTA cycle of α-RbAg₂SbS₄.
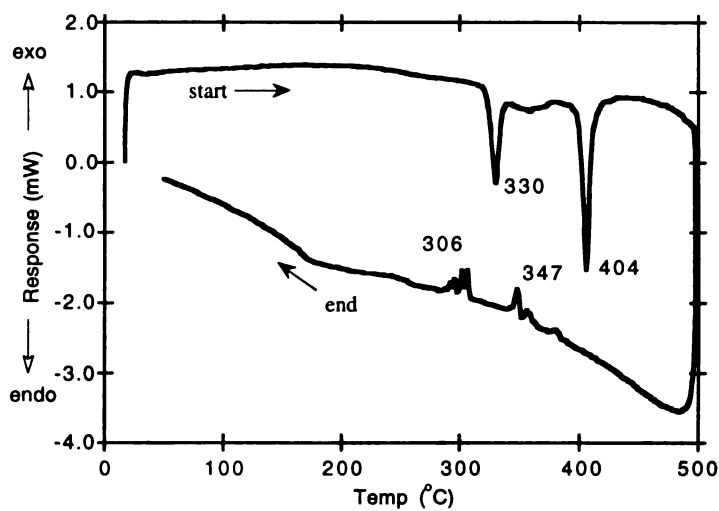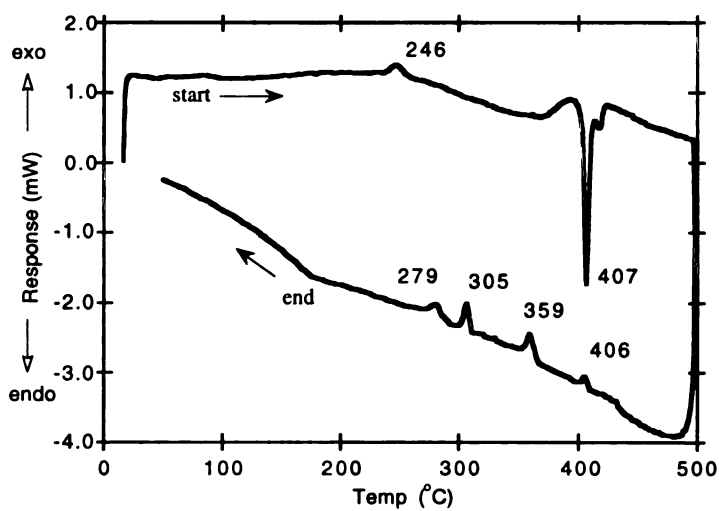
Figure 3-17: (A) DSC diagram for α-RbAg₂SbS₄ (first cycle). (B) Second DSC cycle of α-RbAg₂SbS₄.
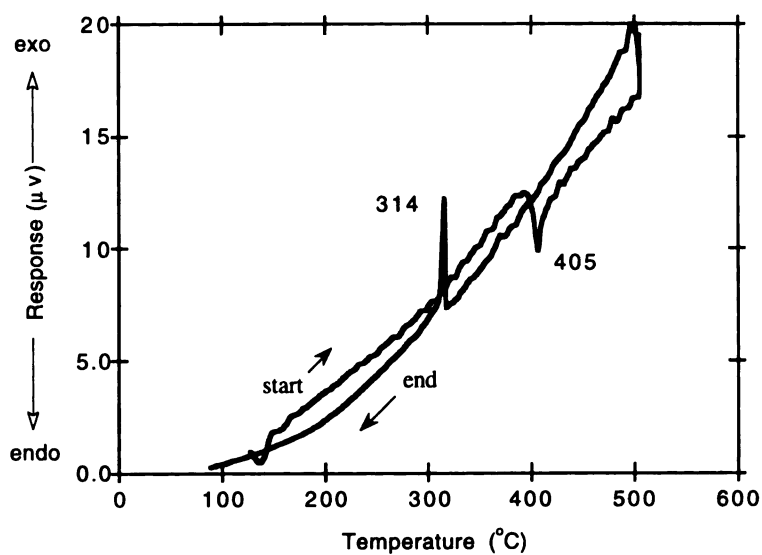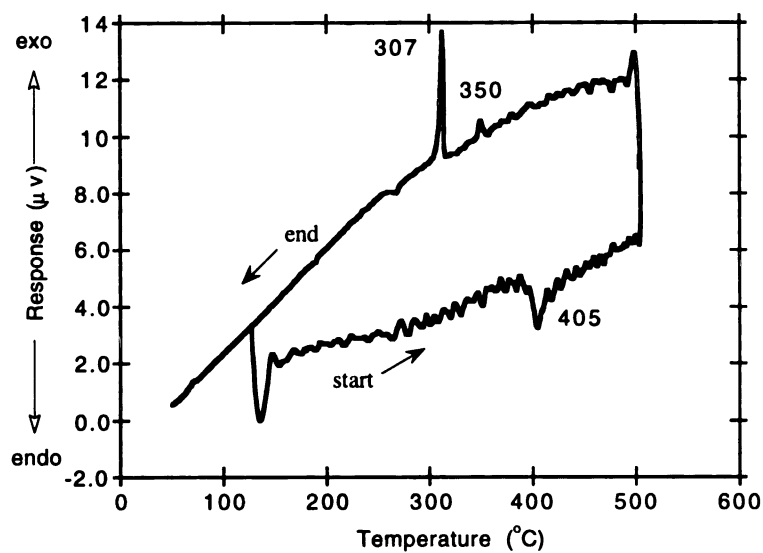
Figure 3-18: (A) DTA diagram for α-RbAg₂SbS₄ (first cycle) (B) Sixth DTA cycle of α-RbAg₂SbS₄.

(A)
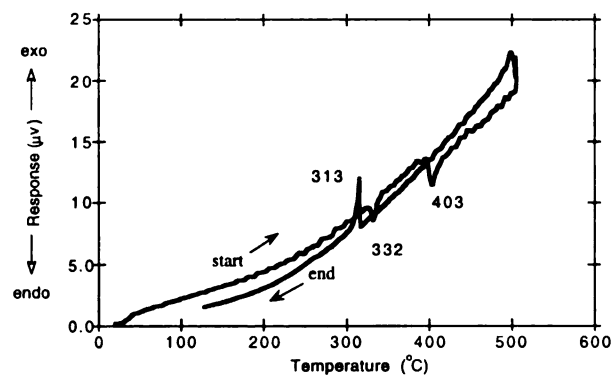
(B)
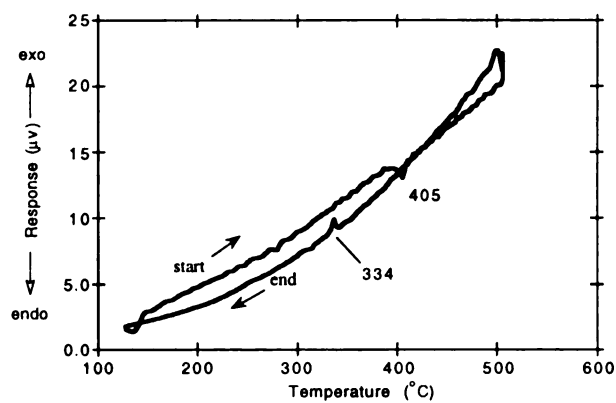
(C)
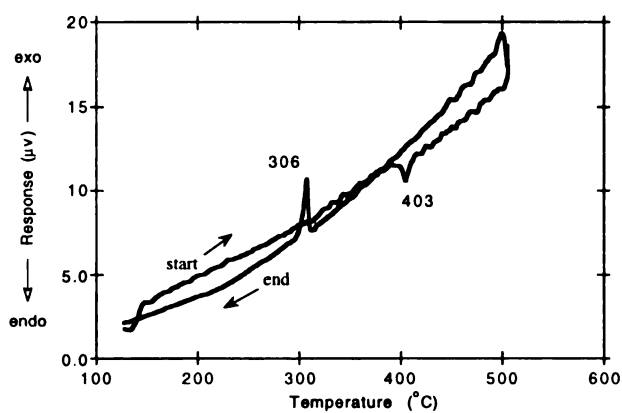
Figure 3-19: (A) DTA diagram for α-RbAg$_2$SbS$_4$ (first cycle). (B) Second DTA cycle of α-RbAg$_2$SbS$_4$. (C) Third DTA cycle of α-RbAg$_2$SbS$_4$.

4. Conclusions

The great structural diversity displayed in these $[Ag_xSb_4]^{(3-x)n-}$ frameworks is fascinating and is due to the large number of binding modes available to the $[SbS_4]^{3-}$ group and the tetrahedral AgS_4 units. The thermal behavior of α-$RbAg_2SbS_4$ was unanticipated, and calls for further exploration of this property. The isolation of α, β -$RbAg_2SbS_4$ and the decomposition product(s) of α-$RbAg_2SbS_4$ suggests that there may be several phases in the Rb/Ag/Sb/S system which may yet be discovered.

137

List of References

1. (a) Sutorik, A.; Kanatzidis, M. G. *Progr. Inorg. Chem.*, **1995**, *43*, 151. (b) Kanatzidis, M. G. *Curr. Opinion Solid State and Mater. Sci.*, **1997**, *2*, 139.

2. McCarthy, T. M.; Kanatzidis, M. G. *Inorg. Chem.*, **1994**, *33*, 1205.

3. Hanko, J. A.; Kanatzidis, M. G. Abstract #0413 from 210th Fall ACS Meeting, Chicago IL **1995**.

4. (a) Schimek, G. L.; Pennigton, T. L.; Wood, P. T.; Kolis, J. W. *J. Solid State Chem.*, **1996**, *123*, 277. (b) Wood, P. T.; Schimek, G. L.; Kolis, J. W. *Chem. Mater.*, **1996**, *8*, 721.

5. Choi, K.-S.; Iordanidis, L.; Chondroudis, K.; Kanatzidis, M. G. *Inorg. Chem.*, **1997**, *34*, 1234.

6. Hanko, J. A.; Kanatzidis, M. G. manuscript in preparation.

7. Hanko, J. A.; Kanatzidis, M. G. *J. Alloys Comp.*, Accepted for publication.

8. Hanko, J. A.; Kanatzidis, M. G. *J. Chem. Soc. Chem. Commun.*, **1998**, 724.

9. Imafuku, M.; Nakai, I.; Nagashima, K. *Mat. Res. Bull.*, **1986**, *21*, 493.

10. CERIUS^2, Version 1.6, Molecular Simulations Inc., Cambridge, England, 1994.

11. SMART and SAINT. Data collection and Processing Siftware for the Smart CCD system. Siemens Analutical X-ray Instruments Inc., 1995.

12. Blessing , R. H. *Acta Crystallogr.*, **1995**, *A51*, 33.

13. SHELXTL Version 5, Reference Manual. Siemens Industrial Automation Inc., **1994**.

14. (a) Sheldrick, G. M., in *Crystallographic Computing 3* ; Sheldrick, G. M., Kruger, C., Doddard, R., Eds.; Oxford University Press: Oxford, England, 1985, p. 175. (b) Gilmore G. J., *Appl. Cryst.* ; **1984**, *17*, 42.

15. Walker, N.; Stuart, D. *Acta Cryst.*, **1983**, *A39*, 158.

16. Hönle, W.; Wibbelmann C.; Brockner, W. *Z. Naturforsch.* **1984**, *39b*, 1088.

17. (a) Teske, C.L.; *Z. Naturforsch, B*, **1979**, *34*, 1979. (b) Auernhammer, M.; Effenberger, H.; Irran, E,; Pertlik, F.; Rosenstingl, *J. Solid State Chem.*, **1993**, *106*, 421.

18. Jeffery, G.A.; Vlasse, M. *Inogr. Chem.*, **1967**, *6*, 396.

19. Hanko, J. A.; Sayettat, J.; Jobic, S.; Brec, R.; Kanatzidis, M. G. Submitted for publication.

20. Siegert, H. *Z. Anorg. Allg. Chem*, **1954**, *275*, 225.

21. Chondroudis, K; Hanko, J. A.; Kanatzidis, M. G. *Inorg. Chem.*, **1997** *37*, 2323.

22. (a) Dhingra, S.-D.; Kanatzidis, M. G. *Science*, **1992**, *258*, 1769. (b) Marking, G. A.; Hanko, J. A.; Kanatzidis, M. G. *Chem. Mater.* **1998**, *10*, 1191.

CHAPTER 4

Synthesis and Characterization of the Novel Mixed Valent Quaternary Silver-Rich Thioantimonates $A_2Ag_{20}Sb_4S_{19}$ (A = Rb, Cs) and β-$Rb_2Ag_{20}Sb_4S_{19}$. A Thioantimonate with a Large Supercell.

1. Introduction

In previous chapters, we have demonstrated that the molten *polychalcoantimonate flux* method is conducive to the synthesis of new multinary chalcoantimonate compounds[1-9]. The polychalcoantimonate fluxes form by the *in situ* fusion of $A_2Q/Sb/Q$ (A = Na, K, Rb, Cs; Q = S, Se) and contain various $[Sb_xQ_y]^{n-}$ units in a molten polychalcogenide solvent. Solid state frameworks can be generated by the self-assembly of these various $[Sb_xQ_y]^{n-}$ units with dissolved metal ions, forming extended lattices stabilized by alkali cations. Examples include: $KThSb_2Se_6$,[2] A_2AgSbS_4 (A = K, Rb, Cs)[3,4], KAg_2SbS_4,[4] α-$RbAg_2SbS_4$,[4,3] $Cs_3Ag_2Sb_3Q_8$ (Q = S, Se)[3,4] $KHgSbS_3$,[5] $Rb_2Au_6Sb_4S_{10}$,[6] and A_2AuSbS_4 (A = Rb, Cs)[7]. More recently, the rare earth chalcoantimonates $K_2La_{2-x}Sb_{4+x}Se_{12}$ (Ln = La, Ce, Pr, and Gd)[8] and $K_2La_2Sb_2Q_9$ (Ln = La, Q = S; Ln = Gd, Q = Se)[9] have been reported. Although the various chalcoantimonate $[Sb_xQ_y]^{n-}$ units are interesting because of the many different binding modes they can exhibit, relatively little is known about their coordination chemistry in the solid state. In particular, it is necessary to elucidate the correlation between Lewis basicity and the $[Sb_xQ_y]^{n-}$ (Q = S, Se) units stabilized from the chalcoantimonate flux. As experimentally observed, in the chalcoantimonate system Lewis basic conditions favor the tetrahedral $[SbQ_4]^{3-}$ units (Q = S, Se), while Lewis acidic conditions produce an even more complicated systems by the greater stability of the Sb^{3+} species, forming higher nuclearity $[Sb_xQ_y]^{n-}$ units in the resulting frameworks.[3,6,9] While the chalcophosphate system the $[PQ_4]^{3-}$ units (Q = S, Se) units are stabilized under Lewis basic conditions, Lewis acidic fluxes produce chemically divergent results between the selenophosphate[10] and thiophosphate systems.[11] Continuing our investigations of the coordination chemistry of the $[Sb_xQ_y]^{n-}$ units with the coinage metals, we report the synthesis, structural characterization, and physical properties of two isostructural quaternary silver thioantimonate compounds, $A_2Ag_{20}Sb_4S_{19}$ (A = Rb, Cs) (I)–(II) and the related high-symmetry compound β-$Rb_2Ag_{20}Sb_4S_{19}$ (III). The

structures of (I)-(II), and the related compound (III), are layered, featuring discrete tetrahedral $[Sb^V S_4]^{3-}$ and pyramidal $[Sb^{III} S_3]^{3-}$ units aggregated to opposite sides of $[Ag_{10}Sb_2S_9]$ "sub-layers" for (I)-(III). In both cases, the different "sub-layers" are connected together in a centrosymmetric fashion with sulfur atoms forming a "sandwiched" double layer. Due to their high silver concentration, these compounds may display interesting Ag^+ ion mobility. As previously described for several silver systems such as Ag_2Se,[12] γ-Ag_8GeTe_6,[13] and $Ag_2Ti_2P_2S_{11}$,[14] Ag^+ ion mobility may be evaluated by examining the anharmonic thermal parameters of their sites.

2. Experimental Section

2.1. Reagents

Chemicals were used as obtained: (i) antimony powder 99.999% purity, -200 mesh, Cerac Inc., Milwaukee, WI; (ii) silver powder 99.95% purity, -325 mesh Alfa AESAR Group, Seabrook, NH; (iii) cesium metal, analytical reagent, Johnson Matthey/AESAR Group, Seabrook, NH; (iv) rubidium metal, analytical reagent, Johnson Matthey/AESAR Group, Seabrook, NH; (v) sulfur powder, sublimed, J.T. Baker Chemical Co., Phillipsburg, NJ; (vi) N,N-dimethylformamide (DMF) reagent grade, EM Science, Inc., Gibbstown, NJ. (vii) diethyl ether, ACS anhydrous, EM Science, Inc., Gibbstown, NJ.

2.2. Syntheses.

A_2S (A = Rb, Cs) were prepared by reacting stoichiometric amounts of the elements in liquid ammonia as described in Chapter 2 Section 2.2.

Preparation of $Rb_2Ag_{20}Sb_4S_{19}$ (I). An amount of Rb_2S (0.051g, 0.25 mmole), Ag (0.054g, 0.50 mmole), Sb (0.016g, 0.125 mmole), and S (0.080g, 2 mmole) were thoroughly mixed and transferred to a 6-ml Pyrex tube which was subsequently flame-sealed *in vacuo* ($\sim 10^{-3}$ Torr). The reaction mixture was heated to 500°C over 15 hrs in a computer-controlled furnace. It was isothermed at 500°C for 4 days, followed by cooling to 100°C at a rate of 4°C/hr and then to room temperature in 1 hour. The product, which is air and water stable, was isolated by dissolving the Rb_2S_x and any $Rb_x[Sb_yS_z]$ flux with DMF under inert atmosphere to give black crystals in 45% yield, based on Sb. Quantitative microprobe analysis of several single crystals gave $RbAg_6Sb_{1.2}S_6$.

Preparation of $Cs_2Ag_{20}Sb_4S_{19}$ (II). An amount of Cs_2S (0.079g, 0.25 mmole), Ag (0.054g, 0.50 mmole), Sb (0.016g, 0.125 mmole), and S (0.080g, 2 mmole) were thoroughly mixed and transferred to a 6-ml Pyrex tube as above and heated as in (I). The product, which is air and water stable, was isolated by removing the excess flux as in (I) to give black crystals in 58% yield, based on Sb. Quantitative microprobe analysis on single crystals gave $CsAg_6Sb_{1.3}S_{6.7}$.

Preparation of β-$Rb_2Ag_{20}Sb_4S_{19}$ (III). An amount of Rb_2S (0.051g, 0.25 mmole), Ag (0.054g, 0.50 mmole), Sb (0.016g, 0.125 mmole), and S (0.080g 2 mmole) were thoroughly mixed and transferred to a 6-ml Pyrex tube which was subsequently flame-sealed *in vacuo* ($\sim 10^{-3}$ Torr). The reaction mixture was ramped to 400°C over 15 hrs in a computer-controlled furnace. It was isothermed at 400°C for 4 days, followed by cooling to 100°C at a rate of 4°C/hr and then to room temperature in 1 hour. The product, which is air and water stable, was isolated by dissolving the Rb_2S_x and any $Rb_x[Sb_yS_z]$ flux with DMF under inert atmosphere to give black crystals in approximately 10% yield, based on Sb. Quantitative microprobe analysis of single crystals gave $RbAg_{9.7}Sb_{2.1}S_{9.6}$.

Crystals suitable for single crystal X-ray diffraction studies were produced from the following conditions: an amount of Rb_2S (0.102g, 0.50 mmole), Ag (0.108g, 1 mmole), Sb (0.032g, 0.25 mmole), and S (0.160g, 4 mmole) were thoroughly mixed and transferred to a 6-ml Pyrex tube which was subsequently flame-sealed *in vacuo* ($\sim 10^{-3}$ Torr). The reaction mixture was heated to 350°C over 15 hrs in a computer-controlled furnace. It was isothermed at 350°C for 4 days, followed by cooling to 100°C at a rate of 4°C/hr and then to room temperature in 1 hour. The product, which is air and water stable, was isolated by dissolving the Rb_2S_x and any $Rb_x[Sb_yS_z]$ flux with DMF under inert atmosphere to give a mixture of black, orange, and yellow crystals. The black crystals were the major phase, with an estimated yield of 60%, based on Sb. Quantitative microprobe analysis of single crystals gave $RbAg_8Sb_{2.4}S_{12.2}$. The yellow and orange crystals were determined by powder X-ray diffraction experiments to be Rb_2AgSbS_4 and α-$RbAg_2SbS_4$, respectively.

2.3. Physical Measurements

Powder X-ray Diffraction. Analyses were performed using a calibrated Rigaku-Denki/RW400F2 (Rotaflex) rotating anode powder diffractometer controlled by an IBM computer, operating at 45 kV/ 100 mA and with a 1°/min scan rate, employing Ni-filtered Cu radiation in a Bragg-Brentano geometry. The theoretical X-ray powder pattern was calculated using the CERIUS^2 software package.[15] Calculated and observed XRD patterns for (II) are given in Table 4-1.

Infrared Spectroscopy. Infrared spectra in the far-IR region (600-50 cm^{-1}) for (I) - (III) were recorded on by a DHK (pc) computer controlled Nicolet 750 Magna-IR Series II spectrometer equipped with a TGS/PE detector and a silicon beam splitter with 4 cm^{-1}

resolution. The samples were ground with dry CsI into a fine powder and pressed into translucent pellets.

Raman Spectroscopy. Raman spectra (1000-100 cm⁻¹) were recorded with a BIO-RAD FT Raman spectrometer with a Spectra-Physics Topaz T10-106c 1,064 nm YAG laser operating at 11 amps. Samples of (I) - (III) were ground with dry CsI into a fine powder and loaded into melting point capillary tubes.

Solid State UV/Vis/Near IR Spectroscopy. Optical diffuse reflectance measurements were performed at room temperature using a Shimadzu UV-3101PC double beam, double monochromator spectrophotometer. The instrument is equipped with integrating sphere and controlled by a AST Bravo 3/255 computer. $BaSO_4$ was used as a 100% reflectance standard for all materials, compacted into a sample holder. Samples were prepared by grinding them to the fine powder and spreading them on the compacted surface of the powdered standard material. The reflectance versus wavelength data generated can be used to estimate a material's band gap by converting reflectance to absorption data as described elsewhere.[16]

Differential Thermal Analysis (DTA). DTA experiments were performed by a AST Bravo/386SX computer-controlled Shimadzu DTA-50 thermal analyzer. Typically a sample (~ 20 mg) was ground into a microcrystalline powder and sealed in a quartz ampoule under vacuum. A quartz ampoule of equal mass filled with Al_2O_3 was sealed and placed on the reference side of the detector. The sample was heated to the desired temperature at 10 °C/min, then isothermed for 10 minutes and finally cooled to 50 °C at -10 °C/min. The residue of the DTA experiment was examined by X-ray powder diffraction. To evaluate congruent melting the X-ray powder diffraction patterns before and after the DTA experiments were compared. The stability of the sample and the reproducibility of the melting point was monitored by conducting multiple cycles with the same heating profile.

Differential Scanning Calorimetry (DSC). DSC experiments were performed on a computer-controlled Shimadzu DSC-50 thermal analyzer under a nitrogen atmosphere at a

flow rate of 20 ml/min. The samples (~ 5 mg) of the crystalline material were crimped in an aluminum pan. The pan was placed on the sample (right) side of the DSC-50 detector and a crimped empty aluminum pan of approximately equal mass was placed on the reference (left) side of the detector. A sample of (III) was heated to the desired temperature at 5 °C/min, isothermed for 5 minutes, and finally cooled at the same rate to 50°C. The temperatures associated with each peak in the spectrum have a standard deviation of 0.2 degrees. The adopted convention in displaying the data is as follows: exothermic peaks are associated with a positive heat flow while endothermic peaks are associated with a negative heat flow.

Semiquantitative microprobe analyses. The analyses were performed using a JEOL JSM-6400V scanning electron microscope (SEM) equipped with a TN 5500 EDS detector. Data acquisition was performed with an accelerating voltage of 20kV and a twenty-second accumulation time.

Single crystal X-ray Crystallography. Intensity data for $Cs_2Ag_{20}Sb_4S_{19}$ (II) were collected on a Rigaku AFC6 diffractometer, using $\omega/2\theta$ scans at 23°C with graphite-monochromatized radiation. The crystals showed no significant intensity decay, as determined by monitoring three standard reflections measured every 150 reflections throughout the data collection. The space group was determined from systematic absences and intensity statistics. An empirical absorption correction based on ψ scans was applied to the data set during the initial stages of refinement. An empirical DIFABS[17] correction was applied as recommended after full isotropic refinement, then full anisotropic refinement was performed. The structure was solved by direct methods using SHELXS-86[18] and refined by the full-matrix least-squares techniques of the TEXSAN package of crystallographic programs.[19]

With the room temperature data collection for (II) and the large number of Ag^+ sites in the structure increases the potential of thermal motion, as monitored by the size of the thermal ellipsoids. After full refinement of (II), three of the silver sites (Ag(10), Ag(13),

and Ag(20)) had large thermal ellipsoids suggesting silver disorder on the sites. The final refined occupancies for Ag(10), Ag(13), and Ag(20) were found to be 80/20%, 48/52%, and 50/50%, respectively. Further investigations into the anharmonic refinement of the Ag$^+$ sites are currently underway[20].

A starting unit cell for (III) was found using the Rigaku AFC6 diffractometer. A primitive hexagonal cell of 7.523(4)Å x 62.95(3)Å was determined. To confirm the cell edges, one hour axial photographs were taken along the *a* and *b* directions. The photographs revealed a 4a x 4b supercell. The resulting cell, 30.57(2)Å x 62.95(3)Å, was determined to be too large for data collection on the Rigaku AFC6 diffractometer. Subsequently, the crystals were sent to Dr. Victor Young at the University of Minnesota for data collection on a Siemens CCD diffractometer. The subcell (7.4902(1)Å x 62.663(1)Å) was confirmed but the correct supercell was found to be 4a x 4b x 2c, producing a rhombohedral cell with dimensions of 29.9673(2)Å x 125.6272(6)Å. Intensity data for the subcell and the supercell was collected.

Intensity data for (III) were collected on a Siemens SMART-CCD diffractometer using graphite-monochromatized MoKα radiation. The data collections for both the subcell and supercell covered more than a hemisphere of reciprocal space, up to 52° 2Θ. The individual frames were measured with a detector to crystal distance of 5 cm and an omega rotation of 0.3 deg with an acquisition time of 45 seconds per frame, leading to a total measurement time of approximately 24 hours. The SMART software[21] was used for the data acquisition, SAINT[21] for data extraction and reduction. The space group was determined from systematic absences and intensity statistics. No crystal decay was detected for (III). A correction for Lorentz polarization effects and an empirical absorption correction (SADABS)[22] were applied to the data. The structure of (III) was solved using direct methods and refined by full-matrix least squares techniques of the SHELXTL[23] package of crystallographic programs utilizing the subcell data.

The complete data collection parameters and details of the structure solution and refinement for $Cs_2Ag_{20}Sb_4S_{19}$ and $\beta\text{-}Rb_2Ag_{20}Sb_4S_{19}$ are given in Table 4-2. The cell parameters for the $\beta\text{-}Rb_2Ag_{20}Sb_4S_{19}$ supercell are also given in Table 4-2. The coordinates of all atoms, average temperature factors, and the estimated standard deviations for (II) and (III) are given in Tables 4-3 and 4-4, respectively.

Table 4-1.   Calculated and Observed X-ray Powder Patterns for $Cs_2Ag_{20}Sb_4S_{19}$ (II).

hkl	d_{calc}, Å	d obsd, Å	I/I_{max}(obsd)
2 0 0	21.283	21.267	100
1 1 0	14.142	14.025	23
4 0 0	10.640	10.532	36
6 0 0	7.093	7.084	21
2 0 $\bar{2}$	6.502	6.551	11
0 2 1	6.469	6.461	13
2 2 1	6.021	6.015	14
4 2 1	5.293	5.306	20
2 $\bar{1}$ 5	5.042	5.068	18
6 0 2 6 2 $\bar{2}$ 8 2 1 3 3 1	4.337	4.336	19
5 3 0	4.310	4.300	22
1 1 3	4.012	3.991	18
2 2 $\bar{3}$ 6 2 2	3.767		
0 4 0 8 0 2 10 2 $\bar{1}$ 4 2 $\bar{3}$	3.734	3.729	59
6 2 $\bar{3}$ 2 2 3 4 4 0	3.550	3.529	41
9 1 $\bar{3}$ 9 3 $\bar{1}$	3.446	3.449	27
2 0 $\bar{4}$ 10 0 2 12 2 $\bar{1}$ 2 4 $\bar{2}$	3.251	3.250	24
11 1 $\bar{3}$	3.134	3.147	25
11 3 $\bar{1}$ 1 1 4	3.077	3.073	23
14 0 0	3.040	3.033	68
8 0 $\bar{4}$ 4 4 2 2 2 $\bar{4}$	3.010	3.005	83
3 5 0	2.934		
5 3 3 11 3 1 10 0 $\bar{4}$ 2 2 4	2.845	2.840	24
10 4 $\bar{2}$ 4 2 4 5 3 $\bar{4}$	2.705	2.706	22
1 3 4 16 0 0 12 0 $\bar{4}$	2.657	2.650	40

16 0 $\bar{2}$ 14 2 1	2.649	2.644	61
11 3 2 12 4 $\bar{1}$	2.600	2.60	21
751	2.586	2.584	20
8 0 4 12 4 $\bar{2}$	2.521	2.518	33
13 1 $\bar{4}$			
42 $\bar{5}$ 22 $\bar{5}$ 10 4 2	2.460	2.459	30
18 0 $\bar{2}$ 2 4 4	2.376	2.375	29
16 2 1			
18 0 0	2.364	2.357	36
11 0 0 14 4 $\bar{2}$	2.337	2.332	24
20 $\bar{6}$ 4 6 $\bar{3}$	2.167	2.160	24
20 0 $\bar{2}$ 19 1 $\bar{3}$	2.149	2.150	18
15 1 3	2.147	2.146	28
8 2 5	2.061	2.063	18
2 5 2 14 4 $\bar{4}$	2.166	2.156	5
18 4 $\bar{2}$	2.008	2.008	19
22 0 0 12 6 $\bar{3}$	1.932	1.929	26
20 0 2	1.907	1.903	20
12 4 4	1.877	1.874	35
17 3 3	1.850	1.847	25

Table 4-2.   Crystallographic Data for $Cs_2Ag_{20}Sb_4S_{19}$ and β-$Rb_2Ag_{20}Sb_4S_{19}$.

Formula	$Cs_2Ag_{20}Sb_4S_{19}$	β-$Rb_2Ag_{20}Sb_4S_{19}$ subcell data	β-$Rb_2Ag_{20}Sb_4S_{19}$ supercell data
FW	3424.48	3424.48	300 447.63
a, Å	43.917(3)	7.4902 (1)	29.967(4)
b, Å	14.995(2)	7.4902 (1)	29.967(4)
c, Å	14.968(3)	62.663 (1)	125.62(2)
α (deg)	90.00	90.00	90.00
β (deg)	91.84 (9)	90.00	90.00
γ (deg)	90.00	120.00	120.00
Z; V(Å³)	24; 10952(8)	3; 3044.60(9)	60; 97 701(1)
λ (Mo Ka), Å	0.71069	0.71069	0.71069
Space group	C2/c (#15)	$R\bar{3}$ (#148)	$P\bar{3}$ (#147)
D_{calc}, g/cm³	5.168	5.603	5.106
μ, cm⁻¹	152.84	15.37	13.38
Temp (°C)	23	23	23
Final R/R_w,[a] %	6.8/8.6	NA	NA
$R1/wR2$[b] %	NA	13.3/25.8	NA
TotalData Measured	1722	5976	352 001
Total Unique Data	1545	1221	64 634
Data $F_o^2>3\sigma(F_o^2)$	927	NA	NA
Data $F_o^2>2\sigma(F_o^2)$	NA	1219	44 800
No. of Variables	126	73	
Crystal Dimen., mm	0.49 x 0.42 x 0.25	0.39 x 0.28 x 0.17	0.10 x 0.10 x 0.10

[a] $R = \Sigma(|F_o| - |F_c|)/\Sigma|F_o|$, $R_w = \{\Sigma_w(|F_o| - |F_c|)^2/\Sigma_w|F_o|^2\}^{1/2}$.

[b] $R1 = \Sigma(|F_o|^2 - |F_c|^2)/\Sigma|F_o|$, $wR2 = \{\Sigma_w(|F_o|^2 - |F_c|^2)^2/\Sigma_w|F_o|^2\}^{1/2}$.

Table 4-3.   Fractional Atomic Coordinates and B(eq) Values for $Cs_2Ag_{20}Sb_4S_{19}$ (II) with Estimated Standard Deviations in Parentheses.

Atom	x	y	z	B(eq) [a]
Cs(1)	0.4798(1)	0.6190(4)	0.0699(40)	2.9(3)
Cs(2)	0.5201(1)	0.8716(4)	-0.0722(0)	2.6(3)
Sb(1)	0.4343(1)	0.8755(4)	0.2045(30)	0.9(2)
Sb(2)	0.2749(1)	0.8730(4)	0.4279(40)	1.4(2)
Sb(3)	0.4323(1)	0.3737(4)	0.2024(30)	0.9(2)
Sb(4)	0.2270(1)	0.8629(4)	0.0637(40)	1.4(2)
Ag(1)	0.2150(2)	1.0092(5)	0.2910(50)	3.4(4)
Ag(2)	0.3609(2)	0.8827(6)	0.3442(50)	3.8(3)
Ag(3)	0.4038(2)	1.1263(5)	0.2130(50)	3.6(3)
Ag(4)	0.4082(2)	0.7298(5)	0.4169(50)	3.6(4)
Ag(5)	0.2806(2)	0.6220(5)	0.4038(40)	2.9(3)
Ag(6)	0.4149(2)	0.7618(5)	-0.0619(0))	3.7(4)
Ag(7)	0.4116(2)	0.6296(5)	0.2154(50)	3.5(3)
Ag(8)	0.3087(2)	1.1276(5)	0.3951(40)	3.5(3)
Ag(9)	0.3608(2)	0.9927(5)	0.0240(70)	4.8(4)
Ag(10)	0.3513(3)	0.5366(7)	0.163(10)	4.0(4)
Ag(10')	0.361(1)	0.537(2)	0.124(30)	1(1)
Ag(11)	0.3603(2)	0.7674(5)	0.5439(60)	4.0(4)
Ag(12)	0.3356(2)	0.0832(6)	0.1836(50)	4.4(4)
Ag(13)	0.3615(4)	0.648(1)	-0.154(1)	4.2(4)
Ag(13')	0.3570(4)	0.700(1)	-0.179(1)	4.5(4)
Ag(14)	0.2750(2)	1.0155(5)	0.2017(50)	3.0(3)
Ag(15)	0.2823(2)	0.2285(5)	0.1872(50)	3.1(3)
Ag(16)	0.4095(2)	0.4768(5)	-0.0801(6)	3.9(4)
Ag(17)	0.1898(2)	1.2110(5)	0.2664(50)	4.0(4)
Ag(18)	0.3580(2)	0.7224(5)	0.0575(60)	3.7(4)
Ag(19)	0.4129(2)	0.9759(5)	-0.0819(6)	3.4(4)
Ag(20)	0.3409(6)	0.461(1)	-0.068(2)	6.6(5)
Ag(20')	0.3458(6)	0.508(2)	-0.082(2)	7.0(5)
S(1)	0.3035(5)	0.876(2)	0.288(10)	2(1)
S(2)	0.3020(6)	0.994(1)	0.536(10)	2(1)

S(3)	0.4505(5)	0.499(1)	0.301(20)	1(1)
S(4)	0.4511(4)	0.372(1)	0.048(10)	1.1(8)
S(5)	0.3761(5)	0.373(1)	0.162(10)	1.3(9)
S(6)	0.4495(6)	0.245(1)	0.294(10)	2(1)
S(7)	0.4002(5)	1.122(1)	0.012(10)	2(1)
S(8)	0.1999(5)	0.992(1)	-0.028(1)	0.9(9)
S(9)	0.4517(5)	1.007(1)	0.294(20)	2(1)
S(10)	0.4526(6)	0.751(1)	0.303(20)	2(1)
S(11)	0.4540(5)	0.874(1)	0.052(10)	1.6(9)
S(12)	0.3793(5)	0.871(2)	0.168(10)	2(1)
S(13)	0.3624(4)	0.367(1)	-0.181(1)	1.3(8)
S(14)	0.3028(5)	0.368(1)	0.297(10)	2(1)0
S(15)	0.3633(5)	0.131(2)	0.348(10)	2.2(9)
S(16)	0.2499(5)	1.139(1)	0.283(10)	3(1)
S(17)	0.3984(5)	0.381(1)	0.517(10)	2.0(9)
S(18)	0.3025(6)	0.750(1)	0.524(20)	2(1)
S(19)	0.1980(7)	0.745(1)	-0.037(2)	3(1)

[a] B values for anisotropically refined atoms are given in the form of the isotropic equivalent

displacement parameter defined as $B_{eq} = (4/3)[a^2B(1, 1) + b^2B(2, 2) + c^2B(3, 3) +$

$ab(\cos\gamma)B(1,2) + ac(\cos\beta)B(1,3) + bc(\cos\alpha)B(2, 3)]$

Table 4-4.   Atomic coordinates (x 10^4) and equivalent isotropic displacement parameters (Å^2 x 10^3) for β-$Rb_2Ag_{20}Sb_4S_{19}$ (III) with Estimated Standard Deviations in Parentheses.

	x	y	z	U(eq)	Occ.
Sb(1)	3333	6667	1244(1)	25(1)	1
Sb(2)	6667	3333	162(1)	36(2)	1
Ag(1)	5263(19)	4705(19)	748(1)	49(4)	0.47(3)
Ag(1')	6160(42)	5818(47)	739(3)	70(9)	0.24(2)
Ag(2)	1430(11)	2864(11)	206(1)	62(3)	0.64(2)
Ag(2')	-282(35)	5930(46)	738(3)	72(9)	0.23(2)
Ag(3)	8648(12)	7296(15)	1062(3)	55(3)	0.64(6)
Ag(3')	-1456(21)	7092(24)	1132(5)	42(6)	0.32(6)
Ag(4)	11094(18)	2187(19)	401(2)	51(5)	0.32(2)
Rb(1)	6667	3333	1535(2)	63(3)	1
S(1)	3333	6667	864(2)	33(4)	1
S(2)	1642(16)	3282(15)	1365(2)	34(2)	1
S(3)	5040(15)	4945(15)	356(2)	36(2)	1
S(4)	6667	3333	1014(3)	35(4)	1
S(5)	0	0	753(3)	62(6)	1
S(6)	0	0	0	109(16)	1

U(eq) is defined as one third of the trace of the orthogonalized Uij tensor.

3. Results and Discussion

3.1 Description of Structures

Structure of $A_2Ag_{20}Sb_4S_{19}$ (A = Rb, Cs) (I) - (II): Since $A_2Ag_{20}Sb_4S_{19}$ (A = Rb, Cs) are isostructural, the single-crystal structure determination was only conducted on $Cs_2Ag_{20}Sb_4S_{19}$; therefore, this discussion will refer primarily to this compound. The structure of $Cs_2Ag_{20}Sb_4S_{19}$ is strikingly complex, with $[Ag_{20}Sb_4S_{19}]^{2n-}$ layers separated by Cs^+ cations, see Figure 4-1. The $[Ag_{20}Sb_4S_{19}]^{2n-}$ layers are actually composed of two $[Ag_{10}Sb_2S_9]$ "sub-layers" connected by sulfur atoms. The $[Ag_{10}Sb_2S_9]$ "sub-layers" are in turn composed of three different interconnecting sheets: two ternary Ag_3SbS_3 and Ag_3SbS_4 layers segregated to opposite sides of the binary Ag_2S sheet. As a result $(Cs_2S)(Ag_2S)_4(Ag_3SbS_3)_2(Ag_3SbS_4)_2$ is a more descriptive formula. A unique feature of this compound is the presence of both Sb^{+5} and Sb^{+3} species segregated to opposite sides of the $[Ag_{10}Sb_2S_9]$ "sub-layers". Although $Cs_3Ag_2Sb_3Q_8$ (Q = S^4, Se^3) was the first reported alkali chalcoantimonate compound to contain both Sb^{+5} and Sb^{+3} species, the Sb^{+3} species was observed as an oligomeric $[Sb_2Q_4]_n^{2n-}$ (Q = S, Se) chain, not as discrete pyramidal $[SbS_3]^{3-}$ units.

The Ag_3SbS_4 sheet is comprised of two tetrahedral $[SbS_4]^{3-}$ units exhibiting a complex bonding motif with Ag^+ ions, see Figure 4-2A. The three basal sulfides are doubly bridging to Ag^+ ions while the fourth apical sulfide binds to three Ag^+ ions. The Ag^+ ions are bridged by the basal sulfides of neighboring $[SbS_4]^{3-}$ units, forming two different Ag_3S_3 rings linking the Sb^{+5} species together. The two different Ag_3S_3 rings resemble a cyclohexane ring in a chair configuration. Figure 4-3A shows a view parallel to the $[Ag_{10}Sb_2S_8]$ "sub-layer" and a perpendicular view of the Ag_3SbS_4 sheet, highlighting the extended connectivity shown in Figure 4-3B. A third view (Figure 4-3C) shows the

connectivity of the Ag^+ atoms bonded to the apical sulfide, connecting the Ag_3SbS_4 to the Ag_2S sheet. The two tetrahedral $[SbS_4]^{3-}$ units are regular tetrahedrons with Sb-S bond distances in the range from 2.30(2) to 2.33(2) and 2.32(2) Å to 2.38(3) Å for Sb(1) and Sb(3), respectively. The S-Sb-S angles range from 107.0(9)° to 111.5(8)°. and 109.2(8) to 110.2(8) for Sb(1) and Sb(3), respectively.

The sheet containing the two pyramidal $[SbS_3]^{3-}$ units displays an even more complex bonding mode with Ag^+ ions, see Figure 4-2B. Two sulfides from the $[SbS_3]^{3-}$ units bond to three Ag^+ ions while the third sulfide bonds to four Ag^+ ions in a rare distorted square pyramidal coordination. Although rare, this coordination is observed in the structure of $Cs_3Ag_2Sb_3S_8$.[3] Figure 4-4A shows a view parallel to the Ag_3SbS_3 sheet in the $[Ag_{10}Sb_2S_8]$ "sub-layer" and a perpendicular view (Figure 4-4B), highlighting the extended connectivity. The complex Ag-S bonding arrangement forms highly distorted Ag_3S_3 rings, connecting the Sb^{+3} species together by bridging neighboring pyramidal $[SbS_3]^{3-}$ units. As shown in Figure 4-4C, the darker shaded Ag^+ ions bridge the ternary Ag_3SbS_3 layer to the binary Ag_2S sheet. The pyramidal $[SbS_3]^{3-}$ units are highly distorted, with Sb-S bond distances in the range from 2.41(2)Å to 2.45(2)Å and 2.37(2)Å to 2.45(2) for Sb(2) and Sb(4), respectively. The S-Sb-S angles range from 97.7(7)° to 99.4(7)°. and 93.3(7) to 99.8(8) for Sb(2) and Sb(4), respectively.

The union of the three sheets into the $[Ag_{10}Sb_2S_9]$ "sub-layer" involves a very complicated bonding scheme that is best described graphically. As shown in Figure 4-5, the two ternary Ag_3SbS_3 and Ag_3SbS_4 and the binary Ag_2S "belt" combine together to assemble the $[Ag_{10}Sb_2S_9]$ "sub-layer" which are in turn connected by bridging monosulfide ions, forming $[Ag_{20}Sb_4S_{19}]^{2-}$ double layers. The parallel views of the ternary Ag_3SbS_4 and Ag_3SbS_3 sheets (Figures 4-3C, and Figure 4-4C) highlight the Ag^+ ions used to assemble the "sub-layer". As the ternary Ag_3SbS_4 sheet is brought next to the binary Ag_2S "belt" the apical sulfide (S(5) and S(12)) of the tetrahedral $[SbS_4]^{3-}$ unit binds to three Ag^+ ions from the Ag_2S "belt", connecting the layers together. The connection of

the ternary Ag_3SbS_3 sheet to the binary Ag_2S "belt" is slightly more complicated due to the participation of all three sulfides of the pyramidal $[SbS_3]^{3-}$ unit in bonding to the Ag_2S "belt". As shown in the fragment of the Ag_3SbS_3 sheet (Figure 4-5), two of the three sulfides (S(1) and S(18) for Sb(2) and S(14) and S(19) for Sb(6)) from the pyramidal $[SbS_3]^{3-}$ unit binds to one Ag^+ while the third sulfide (S(2) and S(8)) binds to two Ag^+ ions, and these four Ag^+ ions connect the sheets together. The resulting $[Ag_{10}Sb_2S_9]$ "sub-layers" are further connected together by bridging sulfides in a centrosymmetric fashion, forming the $[Ag_{20}Sb_4S_{19}]^{2-}$ double layers.

The coordination environments around the Ag^+ ions can be assembled into three groups; trigonal planar, tetrahedral, and linear. The geometries around Ag(1), Ag(2), Ag(5), Ag(9), Ag(10), Ag(11), Ag(13), Ag(14), Ag(15), and Ag(18) are distorted trigonal planar with Ag-S bond distances in the range from 2.45(3)Å to 2.80(3)Å. The geometries around Ag(3), Ag(4), Ag(6), Ag(7), Ag(8), Ag(16), Ag(17) , and Ag(19) are tetrahedral. The geometries around six of these tetrahedral Ag^+ ions are highly distorted with two normal Ag-S distances[3,4] at 2.62(3)Å and 2.58(3)Å, and two Ag-S bond distances that range from 2.77(2)Å to 2.75(3)Å. The S-Ag-S angles for these six Ag^+ ions range from 91.0(8)° to 120.7(8)°. The environment about the remaining two tetrahedral Ag^+ ions is even more highly distorted with very long Ag-S contacts at 2.82(3)Å and three normal Ag-S distances[3,4] that range from 2.71(3)Å to 2.54(2)Å. The S-Ag-S angles reflect this highly distorted nature in the range from 91.5(8)° to 139.5(8)°. The geometry around Ag(12) and Ag(20) are best described as "linear" with slightly compressed Ag-S distances that range from 2.38(2)Å to 2.54(2)Å, and S-Ag-S angles that range from 139(1)° to 165.6(8)°. Selected bond distances and angles are given in Tables 4-5 and 4-6, respectively.

Structure of β-$Rb_2Ag_{20}Sb_4S_{19}$ (III): The structure of β-$Rb_2Ag_{20}Sb_4S_{19}$ is related to (I) and (II), with $[Ag_{20}Sb_4S_{19}]^{2n-}$ layers separated by Rb^+ cations, see Figure 4-6. The $[Ag_{20}Sb_4S_{19}]^{2n-}$ layers are similar to the layers observed in the structure of (I)-(II).

The difference between the structures is that the layers in (I)-(II) stack in registry, while in (III) they are shifted with respect to one another, giving rise to the hexagonal packing arrangement. A more descriptive formula for β-$Rb_2Ag_{20}Sb_4S_{19}$ is the same that can be written for (I)-(II), $(Rb_2S)(Ag_2S)_4(Ag_3SbS_3)_2(Ag_3SbS_4)_2$, it represents a new member of a class of compounds with the general formula $(A_2S)_w(Ag_2S)_x(Ag_3SbS_3)_y(Ag_3SbS_4)_z$. The $[SbS_4]^{3-}$ unit is regular tetrahedron with Sb-S bond distances in the range from 2.321(9) Å to 2.39(2) Å and S-Sb-S angles in the range from 109.0(3)° to 110.0(2)°.

The sheet containing the two pyramidal $[SbS_3]^{3-}$ unit is fairly regular, with a single Sb-S bond distance of 2.42(1)Å, and a single S-Sb-S angle of 92.2(3)°.

Although the structure of (III) can also be assembled as the combination of two ternary Ag_3SbS_3 (Figure 4-7) and Ag_3SbS_4 (Figure 4-8) and a binary Ag_2S sheet, it is difficult to accurately describe the connections due to the highly disordered nature of the Ag^+ sites.

Although the refinement is still in progress, the basic $[Ag_xSb_yS_z]^{n-}$ layer found in (III) is similar to (I) - (II) but with partial occupancy observed in all Ag^+ sites. This partial occupancy is attributed to the folding of the 4a x 4b x 2c supercell in to the subcell. The occupancies of each Ag^+ site were refined independently and are given in Table 4-4. Attempts to achieve charge neutrality for the model resulted in silver deficient layers; assuming the empirical formula for (III) is $Rb_{0.33}Ag_{3.33}Sb_{0.67}S_{3.167}$. Attempts to establish charge neutrality by decreasing the sulfur concentration or locating the missing Ag^+ density were unsuccessful.

Although none of the sulfur sites appeared to be disordered, there was one problematic position at the origin. Extensive attempts to model the site with disorder or substitution of the site with Ag^+ gave significantly higher residuals. The site is octahedrally coordinated an unusual environment for sulfur. The origin of the supercell may be attributed to slight movement of this sulfur atom from cell to cell. During the course of refinement, the Sb and

Rb sites do not appear to be disordered. The final R1 for the isotropically refined structure at this stage is 13.26%.

The Ag^+ ions adopt two different coordination environments, trigonal planar and tetrahedral. The geometry around Ag(1), Ag(1'), Ag(2), and Ag(3') is distorted trigonal planar with Ag-S bond distances in the range from 2.45(2)Å to 2.70(3)Å and S-Ag-S angles from 98.2(8)° to 139.8(5)°. The geometry around Ag(2'), Ag(3), and Ag(4) is best described as tetrahedral with Ag-S bond distances that range from 2.53(2)Å to 2.88(3)Å. The S-Ag-S angles for these 3 Ag^+ ions range from 84.9(6)° to 125.3(9)°. Selected bond distances and angles are given in Tables 4-7 and 4-8, respectively.

An attempt was made to solve the supercell (see Table 4-2) with little success. The immense size of the supercell makes its solution a very interesting challenge. As shown in Table 4-2 over 350,000 reflections were collected, resulting in a useable data set of well over 40,000 reflections. The current subcell refinement was sent to Dr. Michel Evain, at the Institut des Matériaux de Nantes in France, for further examination. Preliminary examination of the subcell refinement suggests that (III) may be an ion conductor and that a possible diffusion path has been observed.[20]

Table 4-5. Selected Distances (Å) for $Cs_2Ag_{20}Sb_4S_{19}$ (II) with standard deviations in parentheses.[a]

Sb(1)-S(9)	2.32(3)	Ag(10)-S(5)	2.65(3)
Sb(1)-S(10)	2.30(2)	Ag(10)-S(8)	2.58(3)
Sb(1)-S(11)	2.32(2)	Ag(10)-S(13)	2.49(3)
Sb(1)-S(12)	2.33(2)		
Sb(1)-S(mean)	2.31(5)	Ag(10')-Ag(18)	2.91(4)
		Ag(10')-Ag(20)	2.67(4)
Sb(2)-S(1)	2.41(2)	Ag(10')-Ag(20')	2.67(5)
Sb(2)-S(2)	2.45(2)		
Sb(2)-S(18)	2.41(2)	Ag(10')-S(5)	2.53(4)
Sb(2)-S(mean)	2.42(3)		
		Ag(10')-S(8)	2.73(5)
Sb(3)-S(3)	2.33(2)	Ag(10')-S(17)	2.60(5)
Sb(3)-S(4)	2.33(2)		
Sb(3)-S(5)	2.38(2)	Ag(11)-Ag(12)	3.20(1)
Sb(3)-S(6)	2.31(2)		
Sb(3)-S(mean)	2.33(4)	Ag(11)-S(5)	2.65(2)
		Ag(11)-S(7)	2.48(2)
Sb(4)-S(8)	2.45(2)	Ag(11)-S(18)	2.49(3)
Sb(4)-S (14)	2.44(2)		
Sb(4)-S(19)	2.37(3)	Ag(12)-Ag(14)	2.87(1)
Sb(4)-S(mean)	2.42(4)	Ag(12)-Ag(15)	3.19(1)
Ag(1)-Ag(5)	3.09(1)	Ag(12)-S(2)	2.47(2)
Ag(1)-Ag(10)	3.09(2)	Ag(12)-S(15)	2.35(2)
Ag(1)-Ag(14)	3.07(1)		

Ag(1)-Ag(17)	3.21(1)	Ag(13)-Ag(13')	0.84(2)
		Ag(13)-Ag(18)	3.01(2)
Ag(1)-S(8)	2.58(2)	Ag(13)-Ag(20')	2.49(3)
Ag(1)-S(14)	2.44(2)		
Ag(1)-S(16)	2.47(3)	Ag(13)-S(5)	2.61(2)
		Ag(13)-S(14)	2.53(3)
Ag(2)-Ag(11)	3.13(1)	Ag(13)-S(17)	2.51(3)
Ag(2)-Ag(19)	3.11(1)		
Ag(2)-Ag(4)	3.09(1)	Ag(13')-Ag(18)	3.10(2)
Ag(2)-Ag(9)	2.99(1)	Ag(13')-S(5)	2.65(3)
		Ag(13')-S(14)	2.52(3)
Ag(2)-S(1)	2.45(2)	Ag(13')-S(15)	2.55(3)
Ag(2)-S(7)	2.49(2)		
Ag(2)-S(12)	2.62(2)	Ag(14)-S(1)	2.58(2)
		Ag(14)-S(2)	2.66(2)
Ag(3)-Ag(11)	3.05(1)	Ag(14)-S(16)	2.51(2)
Ag(3)-Ag(12)	2.98(1)		
Ag(3)-Ag(19)	3.05(1)	Ag(15)-S(14)	2.60(2)
		Ag(15)-S(16)	2.48(2)
Ag(3)-S(6)	2.72(2)	Ag(15)-S(18)	2.47(2)
Ag(3)-S(7)	2.61(2)		
Ag(3)-S(9)	2.78(3)	Ag(16)-Ag(20)	2.99(3)
Ag(3)-S(15)	2.72(2)	Ag(16)-Ag(20')	2.83(3)
Ag(4)-Ag(7)	3.05(1)	Ag(16)-S(3)	2.65(2)
Ag(4)-Ag(11)	2.97(1)	Ag(16)-S(4)	2.71(2)
Ag(4)-Ag(16)	3.09(1)	Ag(16)-S(13)	2.72(3)

		Ag(16)-S(17)	2.57(2)
Ag(4)-S(4)	2.74(2)		
Ag(4)-S(7)	2.60(2)	Ag(17)-S(1)	2.59(2)
Ag(4)-S(10)	2.66(2)	Ag(17)-S(13)	2.62(3)
Ag(4)-S(13)	2.54(3)	Ag(17)-S(16)	2.78(3)
		Ag(17)-S(19)	2.61(2)
Ag(5)-Ag(14)	2.99(1)		
Ag(5)-Ag(15)	3.19(1)	Ag(18)-S(12)	2.68(2)
Ag(5)-Ag(17)	3.08(1)	Ag(18)-S(17)	2.47(2)
Ag(5)-Ag(20)	2.88(3)	Ag(18)-S(19)	2.48(3)
Ag(5)-S(8)	2.56(2)	Ag(19)-S(7)	2.63(2)
Ag(5)-S(16)	2.56(2)	Ag(19)-S(9)	2.58(2)
Ag(5)-S(18)	2.55(2)	Ag(19)-S(11)	2.68(2)
		Ag(19)-S(15)	2.70(3)
Ag(6)-Ag(13)	2.92(2)		
Ag(6)-Ag(13')	2.85(2)	Ag(20)-Ag(20')	0.75(3)
Ag(6)-S(6)	2.64(2)	Ag(20)-S(8)	2.47(3)
Ag(6)-S(11)	2.62(3)	Ag(20)-S(13)	2.37(3)
Ag(6)-S(15)	2.83(3)		
Ag(6)-S(17)	2.55(2)	Ag(20')-S(8)	2.65(3)
		Ag(20')-S(13)	2.66(4)
Ag(7)-Ag(10)	2.93(2)	Ag(20')-S(14)	2.81(4)
Ag(7)-Ag(10')	2.68(4)		
Ag(7)-Ag(16)	3.12(1)	Cs(1)-S(3)	3.93(2)
Ag(7)-Ag(18)	3.11(1)	Cs(1)-S(3)	3.91(2)

		Cs(1)-S(3)	3.62(3)
Ag(7)-S(3)	2.68(3)	Cs(1)-S(4)	3.91(2)
Ag(7)-S(10)	2.63(3)	Cs(1)-S(4)	3.65(2)
Ag(7)-S(13)	2.75(2)	Cs(1)-S(10)	4.02(2)
Ag(7)-S(17)	2.56(2)	Cs(1)-S(10)	3.68(3)
		Cs(1)-S(11)	3.98(2)
Ag(8)-Ag(9)	3.11(1)	Cs(1)-S(17)	3.46(3)
Ag(8)-Ag(14)	3.15(1)	Cs(1)-S (mean)	3.79(6)
Ag(8)-Ag(15)	3.12(1)		
		Cs(2)-S(10)	3.92(2)
Ag(8)-S(2)	2.78(2)	Cs(2)-S(11)	3.57(2)
Ag(8)-S(15)	2.58(2)	Cs(2)-S(11)	3.96(3)
Ag(8)-S(16)	2.67(3)	Cs(2)-S(4)	3.85(2)
Ag(8)-S(19)	2.63(2)	Cs(2)-S(6)	3.65(2)
		Cs(2)-S(6)	3.84(2)
Ag(9)-Ag(12)	2.90(1)	Cs(2)-S(7)	3.39(2)
Ag(9)-Ag(19)	2.88(1)	Cs(2)-S(9)	3.64(3)
		Cs(2)-S(9)	3.83(2)
Ag(9)-S(2)	2.60(3)	Cs(2)-S (mean)	3.73(6)
Ag(9)-S(7)	2.62(3)		
Ag(9)-S(12)	2.64(2)		
Ag(10)-Ag(10')	0.79(4)		
Ag(10)-Ag(18)	3.15(1)		
Ag(10)-Ag(20)	3.16(3)		

[a]The estimated standard deviations in the mean bond lengths and the mean bond angles are calculated by the equation $\sigma l = \{\Sigma_n(l_n - l)^2/n(n-1)\}^{1/2}$, where l_n is the length (or angle) of the nth bond, l the mean length (or angle), and n the number of bonds.

Table 4-6.   Selected Bond Angles (°) for $Cs_2Ag_{20}Sb_4S_{19}$ (II) with standard deviations in parentheses.[a]

S(9)-Sb(1)-S(10)	111.5(8)	S(15)-Ag(8)-S(16)	134.1(7)
S(9)-Sb(1)-S(11)	107.6(8)	S(15)-Ag(8)-S(19)	113.7(8)
S(9)-Sb(1)-S(12)	110.2(9)	S(16)-Ag(8)-S(19)	95.9(8)
S(10)-Sb(1)-S(11)	109.8(8)		
S(10)-Sb(1)-S(12)	107.0(9)	S(2)-Ag(9)-S(7)	127.0(8)
S(11)-Sb(1)-S(12)	110.7(8)	S(2)-Ag(9)-S(12)	100.2(7)
		S(7)-Ag(9)-S(12)	116.9(8)
S(1)-Sb(2)-S(2)	99.4(7)		
S(1)-Sb(2)-S(18)	97.7(8)	S(5)-Ag(10)-S(8)	98.5(8)
S(2)-Sb(2)-S(18)	97.5(7)	S(5)-Ag(10)-S(13)	121.4(9)
		S(8)-Ag(10)-S(13)	131.6(9)
S(3)-Sb(3)-S(4)	110.2(8)		
S(3)-Sb(3)-S(5)	110.1(9)	S(5)-Ag(10')-S(8)	98(1)
S(3)-Sb(3)-S(6)	110.2(8)	S(5)-Ag(10')-S(17)	115(2)
S(4)-Sb(3)-S(5)	109.7(8)	S(8)-Ag(10')-S17	119(2)
S(4)-Sb(3)-S(6)	107.4(8)		
S(5)-Sb(3)-S(6)	109.2(8)	S(5)-Ag(11)-S(7)	121.5(8)
		S(5)-Ag(11)-S(18)	96.7(8)
S(8)-Sb(4)-S(14)	93.3(7)	S(7)-Ag(11)-S(18)	140.9(9)
S(8)-Sb(4)-S(19)	99.8(8)		
S(14)-Sb(4)-S(19)	98.4(8)	S(2)-Ag(12)-S(15)	166.7(8)
S(8)-Ag(1)-S(14)	108.0(7)	S(5)-Ag(13)-S(14)	100.1(9)
S(8)-Ag(1)-S(16)	108.3(7)	S(5)-Ag(13)-S(17)	124(1)
S(14)-Ag(1)-S(16)	142.6(7)	S(14)-Ag(13)-S(17)	128.6(9)
S(1)-Ag(2)-S(7)	137.6(7)	S(1)-Ag(14)-S(2)	93.8(7)
S(1)-Ag(2)-S(12)	101.9(7)	S(1)-Ag(14)-S(16)	128.5(7)
S(7)-Ag(2)-S(12)	119.8(8)	S(2)-Ag(14)-S(16)	133.7(7)
S(6)-Ag(3)-S(7)	107.0(7)	S(14)-Ag(15)-S(16)	109.2(7)
S(6)-Ag(3)-S(9)	81.4(7)	S(14)-Ag(15)-S(18)	103.3(8)
S(6)-Ag(3)-S(15)	104.6(7)	S(16)-Ag(15)-S(18)	147.4(8)
S(7)-Ag(3)-S(9)	104.9(7)		
S(7)-Ag(3)-S(15)	137.3(8)	S(3)-Ag(16)-S(4)	89.3(7)
S(9)-Ag(3)-S(15)	107.5(7)	S(3)-Ag(16)-S(13)	109.7(7)
		S(3)-Ag(16)-S(17)	112.8(8)
S(4)-Ag(4)-S(7)	107.9(7)	S(4)-Ag(16)-S(13)	106.5(7)
S(4)-Ag(4)-S(10)	86.7(7)	S(4)-Ag(16)-S(17)	110.1(7)
S(4)-Ag(4)-S(13)	110.9(8)	S(13)-Ag(16)-S(17)	123.1(8)
S(7)-Ag(4)-S(10)	110.0(7)		
S(7)-Ag(4)-S(13)	123.6(8)	S(1)-Ag(17)-S(13)	115.6(8)
S(10)-Ag(4)-S(13)	111.5(7)	S(1)-Ag(17)-S(16)	104.2(8)
		S(1)-Ag(17)-S(19)	92.0(7)
S(8)-Ag(5)-S(16)	136.2(8)	S(13)-Ag(17)-S(16)	125.8(8)
S(8)-Ag(5)-S(18)	98.4(7)	S(13)-Ag(17)-S(19)	118.4(8)
S(16)-Ag(5)-S(18)	125.3(8)	S(16)-Ag(17)-S(19)	94.1(8)
S(6)-Ag(6)-S(11)	92.2(7)	S(12)-Ag(18)-S(17)	116.8(8)
S(6)-Ag(6)-S(15)	103.9(7)	S(12)-Ag(18)-S(19)	97.6(8)

S(6)-Ag(6)-S(17)	120.4(7)	S(17)-Ag(18)-S(19)	145.6(9)
S(11)-Ag(6)-S(15)	103.5(7)		
S(11)-Ag(6)-S(17)	121.6(7)	S(7)-Ag(19)-S(9)	115.8(8)
S(15)-Ag(6)-S(17)	112.1(8)	S(7)-Ag(19)-S(11)	110.8(7)
		S(7)-Ag(19)-S(15)	115.3(8)
S(3)-Ag(7)-S(10)	91.2(7)	S(9)-Ag(19)-S(11)	92.4(8)
S(3)-Ag(7)-S(13)	107.6(7)	S(9)-Ag(19)-S(15)	114.3(8)
S(3)-Ag(7)-S(17)	111.8(7)	S(11)-Ag(19)-S(15)	105.1(7)
S(10)-Ag(7)-S(13)	106.3(7)		
S(10)-Ag(7)-S(17)	118.7(8)	S(8)-Ag(20)-S(13)	153(1)
S(13)-Ag(7)-S(17)	117.8(8)		
		S(8)-Ag(20')-S(13)	125(1)
S(2)-Ag(8)-S(15)	113.4(8)	S(8)-Ag(20')-S(14)	81(1)
S(2)-Ag(8)-S(16)	100.8(7)	S(13)-Ag(20')-S(14)	119(1)
S(2)-Ag(8)-S(19)	88.9(6)		

[a]The estimated standard deviations in the mean bond lengths and the mean bond angles are calculated by the equation $\sigma l = \{\Sigma_n(l_n - l)^2/n(n-1)\}^{1/2}$, where l_n is the length (or angle) of the nth bond, l the mean length (or angle), and n the number of bonds.

Table 4-7.   Selected Distances (Å) for β-Rb$_2$Ag$_{20}$Sb$_4$S$_{19}$ (III) with standard deviations in parentheses.[a]

Sb(1)-S(2)	2.321(9) x3	Ag(2')-S(3)	2.53(2)
		Ag(2')-S(1)	2.60(2)
Sb(1)-S(1)	2.39(2)	Ag(2')-S(4)	2.75(3)
Sb(2)-S(3)	2.426(11) x3	Ag(2')-S(5)	2.95(3)
Ag(1)-Ag(1')	2.95(2)	Ag(3)-Ag(3')	3.18(2)
Ag(1)-Ag(2')	2.99(2)	Ag(3)-Ag(3)	3.04(2)
Ag(1)-Ag(3)	3.01(2)	Ag(3)-Ag(3)	3.04(2)
Ag(1)-Ag(3)	3.03(2)	Ag(3)-Ag(1)	3.01(2)
Ag(1)-Ag(1)	3.12(2)	Ag(3)-Ag(2')	2.58(3)
Ag(1)-Ag(1)	3.12(2)		
Ag(1)-Ag(3')	3.25(3)	Ag(3)-S(4)	2.589(9)
Ag(1')-Ag(3')	2.91(4)	Ag(3)-S(5)	2.62(3)
		Ag(3)-S(2)	2.73(2)
Ag(1)-S(4)	2.45(2)	Ag(3)-S(2)	2.73(2)
Ag(1)-S(3)	2.473(13)		
Ag(1)-S(1)	2.627(9)	Ag(3')-Ag(3')	3.27(3) x2
		Ag(3')-Ag(1')	2.91(4)
Ag(1')-Ag(2')	1.54(4)	Ag(3')-Ag(1)	3.26(2)
Ag(1')-Ag(3)	2.60(3)	Ag(3')-Ag(1)	3.25(3)
Ag(1')-Ag(2')	2.62(3)	Ag(3')-Ag(3)	3.18(2) x2
Ag(1')-Ag(1)	2.95(2)		
Ag(1')-Ag(2')	3.32(3)	Ag(3')-S(2)	2.49(2) x2
Ag(1')-Ag(4)	2.92(3)	Ag(3')-S(4)	2.549(13)
Ag(1')-S(3)	2.52(2)	Ag(4)-Ag(2)	3.098(14)
Ag(1')-S(1)	2.62(2)	Ag(4)-Ag(2)	3.096(14)
Ag(1')-S(4)	2.70(3)	Ag(4)-Ag(1')	2.92(3)
		Ag(4)-Ag(2')	2.86(3)
Ag(2)-Ag(2)	3.217(13) x2	Ag(4)-Ag(4)	2.46(2) x2
Ag(2)-Ag(2)	3.179(12) x2		
Ag(2)-Ag(4)	3.098(14)	Ag(4)-S(5)	2.62(2)

Ag(2)-Ag(4)	3.096(14)	Ag(4)-S(6)	2.88(1)
		Ag(4)-S(3)	2.65(2)
Ag(2)-S(3)	2.53(1) x2	Ag(4)-S(3')	2.64(2)
Ag(2)-S(6)	2.262(7)		
Ag(2')-Ag(1')	3.32(3)	Rb(1)-S(4)	3.27(2)
Ag(2')-Ag(1)	2.99(2)	Rb(1)-S(2)	3.895(11) x2
Ag(2')-Ag(3')	2.90(4)	Rb(1)-S(2)	3.893(11) x2
Ag(2')-Ag(4)	2.86(3)	Rb(1)-S(2)	3.452(12) x3
Ag(2')-Ag(3)	2.58(3)		
Ag(2')-Ag(1')	2.62(3)		

[a]The estimated standard deviations in the mean bond lengths and the mean bond angles are calculated by the equation $\sigma l = \{\Sigma_n (l_n - l)^2/n(n-1)\}^{1/2}$, where l_n is the length (or angle) of the nth bond, l the mean length (or angle), and n the number of bonds.

Table 4-8.   Selected Bond Angles (°) for β-Rb$_2$Ag$_{20}$Sb$_4$S$_{19}$ (III) with standard

deviations in parentheses.

S(2)-Sb(1)-S(2)	110.0(2) x3	S(4)-Ag(3)-S(5)	125.3(9)
S(2)-Sb(1)-S(1)	109.0(3) x3	S(5)-Ag(3)-S(2)	110.2(4) x2
		S(4)-Ag(3)-S(2)	109.4(6) x2
S(3)-Sb(2)-S(3)	97.2(3) x3	S(2)-Ag(3)-S(2)	84.9(6)
S(4)-Ag(1)-S(3)	139.8(5)	S(2)-Ag(3')-S(2)	95.6(10)
S(4)-Ag(1)-S(1)	121.1(5)	S(2)-Ag(3')-S(4)	119.1(8)
S(3)-Ag(1)-S(1)	99.1(5)	S(2)-Ag(3')-S(4)	119.0(8)
S(3)-Ag(1')-S(1)	98.2(8)	S(5)-Ag(4)-S(3)	117.2(5) x2
S(3)-Ag(1')-S(4)	124.9(1)	S(3)-Ag(4)-S(3)	93.3(6)
S(1)-Ag(1')-S(4)	112.7(9)	S(5)-Ag(4)-S(6)	117.8(5)
		S(3)-Ag(4)-S(6)	103.9(4) x2
S(6)-Ag(2)-S(3)	130.5(4)		
S(6)-Ag(2)-S(3)	130.7(4)		
S(3)-Ag(2)-S(3)	98.8(5)	S(4)-Rb(1)-S(2)	141.9(2) x3
		S(2)-Rb(1)-S(2)	64.6(3) x3
S(3) -Ag(2')-S(1)	98.4(9)		
S(3)-Ag(2')-S(4)	122.6(9)		
S(1)-Ag(2')-S(4)	111.6(9)		
S(3)-Ag(2')-S(5)	110.0(9)		
S(1)-Ag(2')-S(5)	104.0(9)		
S(4)-Ag(2')-S(5)	108.4(8)		

[a]The estimated standard deviations in the mean bond lengths and the mean bond angles are calculated by the equation $\sigma l = \{\Sigma_n(l_n - l)^2/n(n-1)\}^{1/2}$, where l_n is the length (or angle) of the nth bond, l the mean length (or angle), and n the number of bonds.
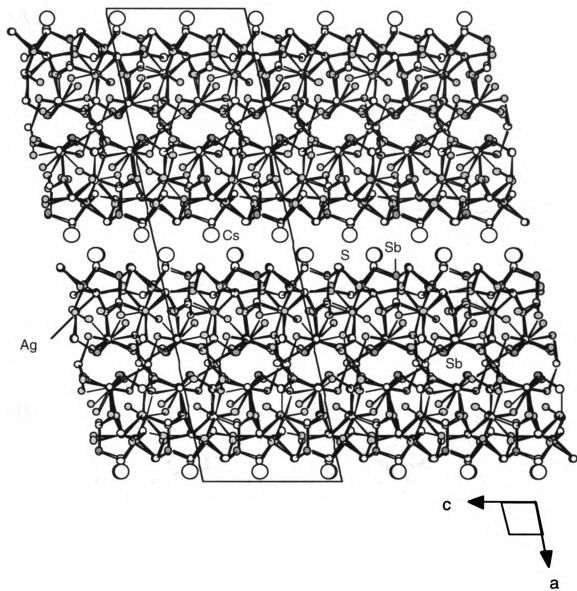
Figure 4-1: Packing diagram for $Cs_2Ag_{20}Sb_4S_{19}$ as viewed down the *b*-axis.

(A)
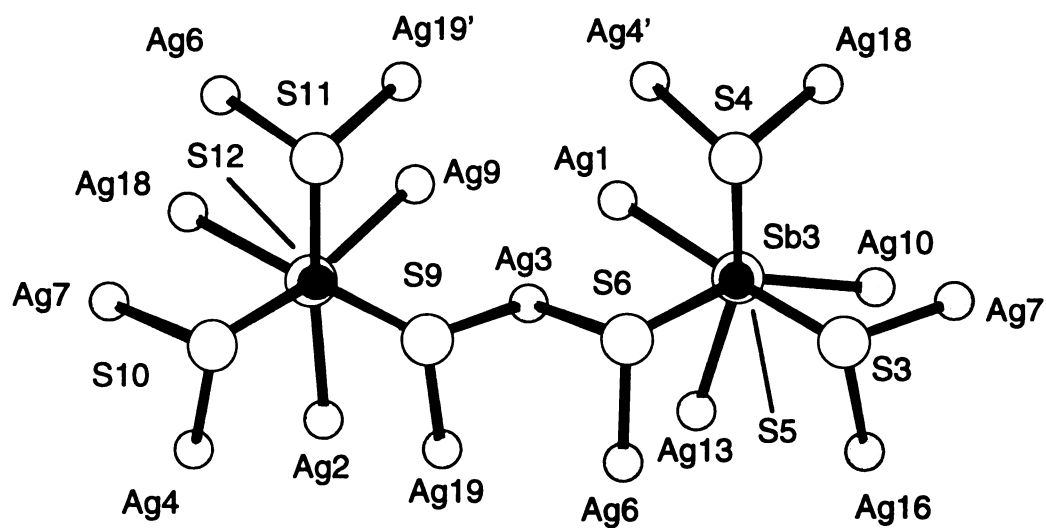
(B)
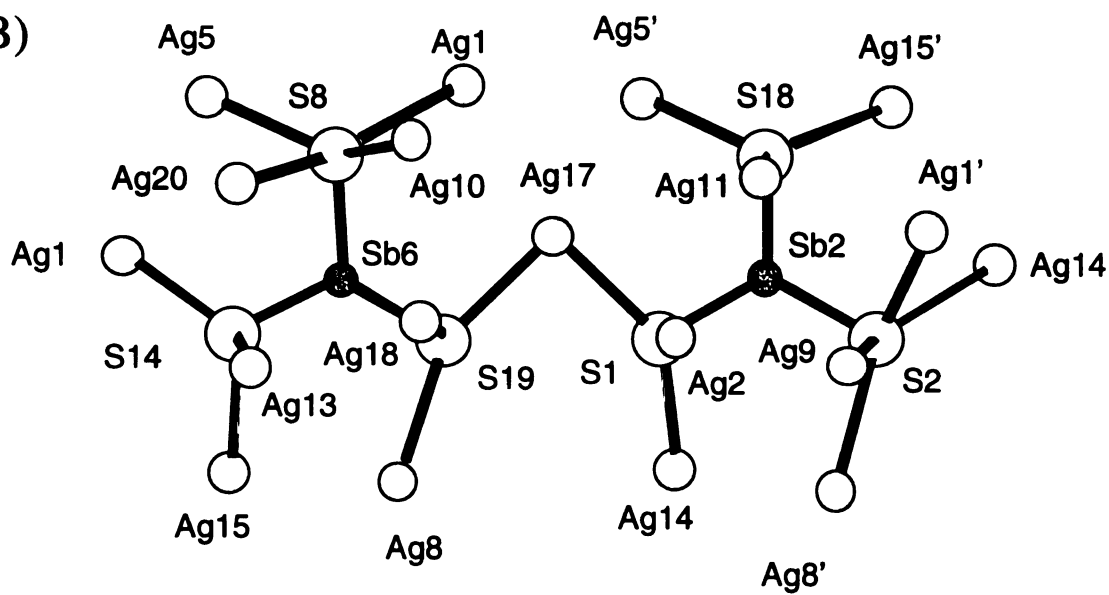
Figure 4-2:   (A) The coordination of the tetrahedral $[SbS_4]^{3-}$ units to Ag^+ ions, with labeling. (B) The coordination of the pryamidal $[SbS_3]^{3-}$ units to Ag^+ ions, with labeling.

Figure 4-3:   (A) A parallel view of the (Ag$_3$SbS$_4$) sheet in (II). (B) A perpendicular view of the (Ag$_3$SbS$_4$) sheet, highlighting the Ag$_3$S$_3$ rings connecting the neighboring tetrahedral [SbS$_4$]$^{3-}$ units. (C) A parallel view of the (Ag$_3$SbS$_4$) sheet highlighting the Ag$^+$ ions used in connecting the ternary (Ag$_3$SbS$_4$) sheet to the binary Ag$_2$S "belt", black circles; Sb, gray circles; Ag, open circles; S.

(A)
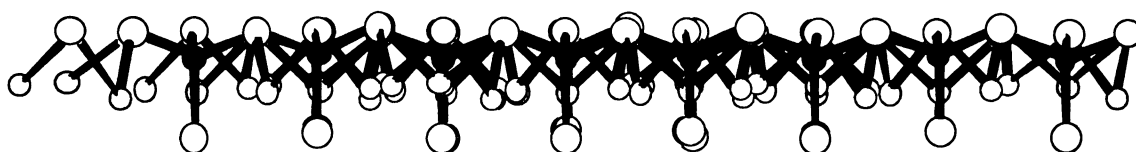
(B)
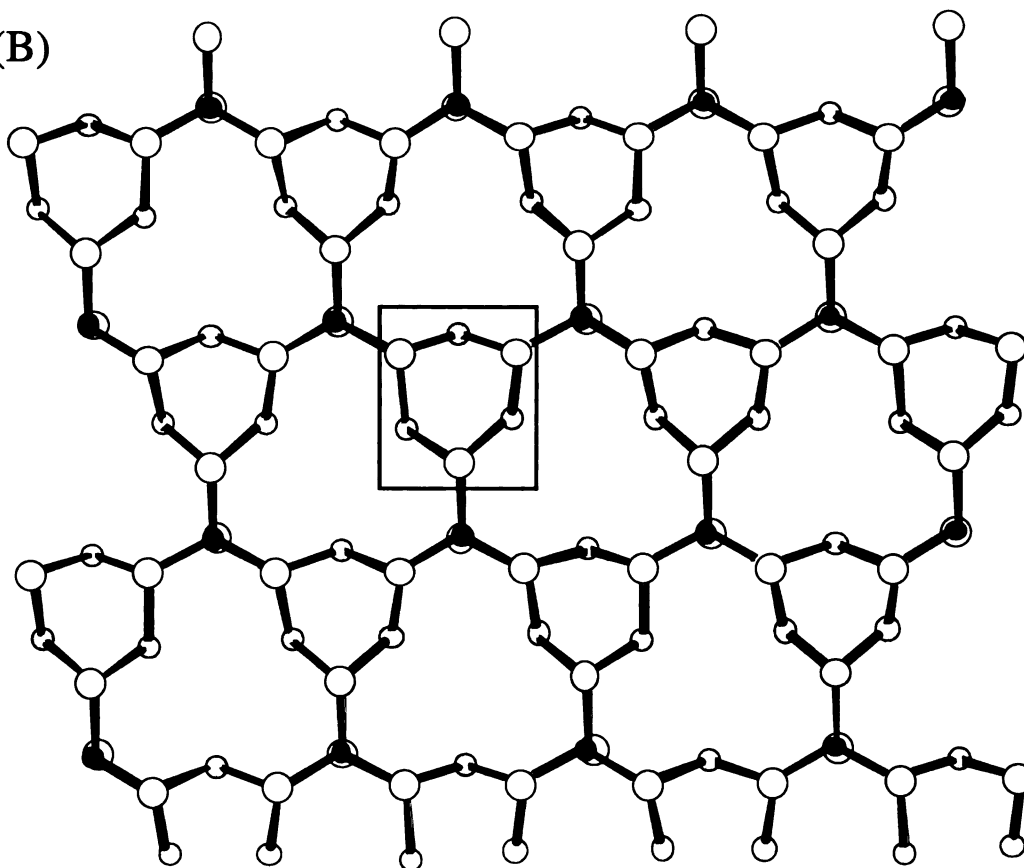
(C)
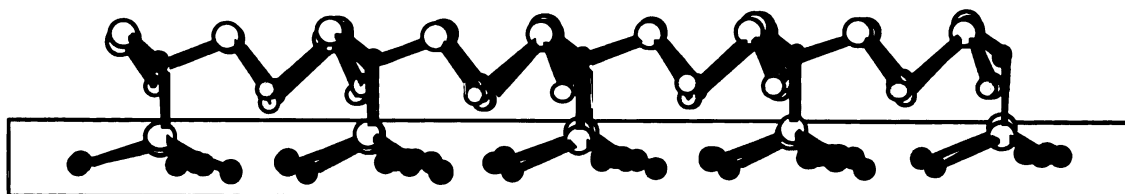
Figure 4-4:   (A) A parallel view of the (Ag$_3$SbS$_3$) sheet. (B) A perpendicular view of the (Ag$_3$SbS$_3$) sheet, highlighting the Ag$_3$S$_3$ rings connecting the neighboring pryamidal [SbS$_3$]$^{3-}$ units. (C) A parallel view of the (Ag$_3$SbS$_3$) sheet highlighting the Ag$^+$ ions used in connecting the ternary (Ag$_3$SbS$_3$) sheet to the binary Ag$_2$S "belt", black circles; Sb, gray circles; Ag, open circles; S.

(A)

(B)
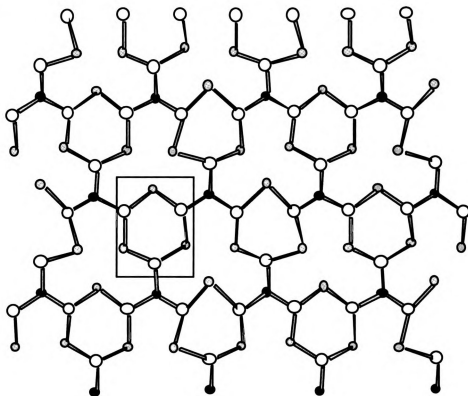
(C)
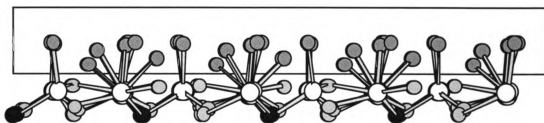
Figure 4-5:   A sequential decomposition of the $[Ag_{20}Sb_4S_{19}]^{2n-}$ layers to $[Ag_{10}Sb_2S_8]$
"sub-layers", and the further separation into the two ternary (Ag_3SbS_4) and
(Ag_3SbS_3) sheets and the binary Ag_2S "belt".

$[Ag_{20}Sb_4S_{19}]^{2n-}$ double layer

$[Ag_{10}Sb_2S_8]$ "sub-layer"

$[Ag_3SbS_3]$ sheet

$[Ag_2S]$ sheet
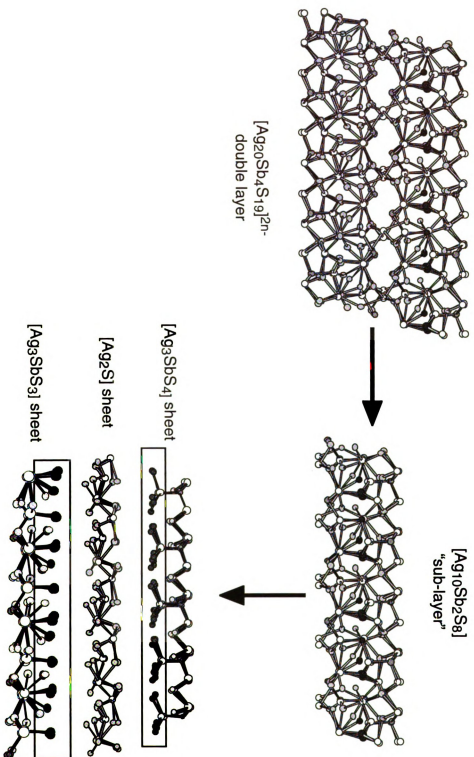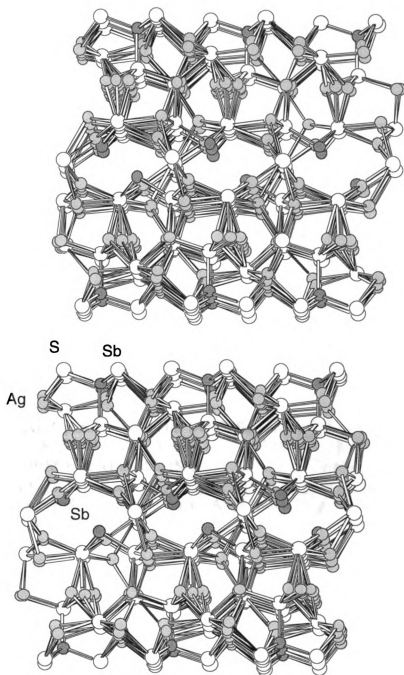
$[Ag_3SbS_4]$ sheet

Figure 4-6:   A view of a portion of the layers in β-Rb$_2$Ag$_{20}$Sb$_4$S$_{19}$ (III), with labeling.

Figure 4-7:   (A) A parallel view of the (Ag₃SbS₄) sheet in (III). (B) A perpendicular view of the (Ag₃SbS₄) sheet, highlighting the Ag₃S₃ rings connecting the neighboring tetrahedral [SbS₄]³⁻ units. (C) A parallel view of the (Ag₃SbS₄) sheet highlighting the Ag⁺ ions used in connecting the ternary (Ag₃SbS₄) sheet to the binary Ag₂S "belt", Sb, gray circles; Ag, light gray circles; S, open circles.

(A)

(B)
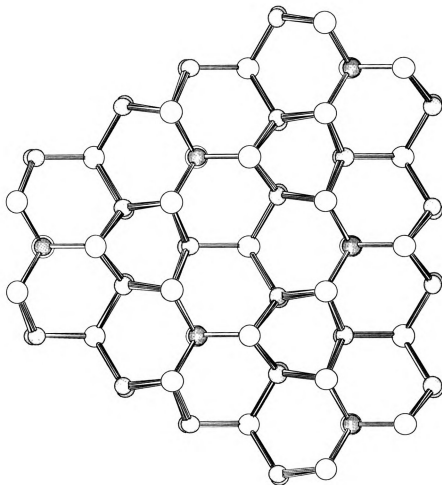
(C)
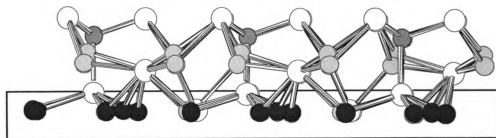
Figure 4-8:   (A) A parallel view of the (Ag$_3$SbS$_3$) sheet in (III) (B) A perpendicular
view of the (Ag$_3$SbS$_3$) sheet, highlighting the Ag$_3$S$_3$ rings connecting the
neighboring pyramidal [SbS$_3$]$^{3-}$ units. (C) A parallel view of the
(Ag$_3$SbS$_3$) sheet highlighting the Ag$^+$ ions used in connecting the ternary
(Ag$_3$SbS$_3$) sheet to the binary Ag$_2$S "belt", gray circles; Sb, light gray
circles; Ag, open circles; S.

3.2. Synthesis, Spectroscopy and Thermal Analysis.

The syntheses of these compounds was the result of a redox reaction in which the silver is oxidized by the polysulfide ions in the $A_x[Sb_yS_z]$ flux. The Ag^+ centers are then coordinated by the highly charged $[Sb_xQ_y]^{n-}$ units. Although a number of different $[Sb_xQ_y]^{n-}$ units have been isolated from the flux, the ability to predict which $[Sb_xQ_y]^{n-}$ units will be formed is not completely understood. In the present conditions the flux was silver rich and antimony poor. Similar conditions[3] favored the formation of oliogmeric $[Sb_xQ_y]^{n-}$ units containing the Sb^{+3} species. Instead, the compounds contain both discrete tetrahedral $[SbS_4]^{3-}$ and pyramidal $[SbS_3]^{3-}$ units containing Sb^{+3} and Sb^{+5} species, respectively. Although the stability of the lower oxidation sates, Sb^{+3} species, increases as one goes down the row, this unprecedented result suggests the presence of a complicated Lewis acid-base equilibrium. Continuing our exploration of thioantimonate fluxes with higher Ag/Sb rations we have been able to incorporate additional equivalents of Ag^+ ions forming silver-rich materials. The compounds described here represent a departure from other chalcometalate compounds, whose structural descriptions are dominated by the various $[E_xQ_y]^{n-}$ (E = P, Sb; Q = S, Se, Te) units coordinating to the metal ions, not the resulting framework coordinating to the various $[E_xQ_y]^{n-}$ units. The structures of (I)-(III) are almost completely dominated by the "Ag_2S" portion of the $[Ag_xSb_yQ_z]^{2n-}$ framework, to which the various $[Sb_xQ_y]^{n-}$ units coordinate. The structure of (III) represents a new member of a class of compounds with the general formula $(A_2S)_w(Ag_2S)_x(Ag_3SbS_3)_y(Ag_3SbS_4)_z$, further validating the use of the polychalcoantimonate fluxes for synthesis of new materials.

The optical absorption properties of (I) – (III) were obtained in the diffuse reflectance mode using polycrystalline samples of the compound. The spectra show that these materials are wide band-gap semiconductors. The $A_2Ag_{20}Sb_4S_{19}$ (A = Rb, Cs)

compounds exhibit steep absorption edges from which the band-gap, E_g, can be assessed at 1.21eV (I), and 1.37eV (II), respectively, see Figure 4-9. The band-gap of β-$Rb_2Ag_{20}Sb_4S_{19}$ is 1.63eV, see Figure 4-10.

The far-IR spectra of (I)-(II) display only a few absorptions in the 400 – 100 cm^{-1} range. The sharp absorption at $ca.$ 378 cm^{-1} is in between the values expected for the Sb-S vibrations of the $[SbS_4]^{3-}$ ($ca.$ 385 cm^{-1}) and the oligomeric $[Sb_2S_4]^{2-}$ units ($ca.$ 373, and 357 cm^{-1}) found in the far-IR spectrum of $Cs_3Ag_2Sb_3S_8$, making an assignment difficult. Absorptions observed below 350 cm^{-1} are probably due to Ag-S vibrations. Attempts to obtain a far-IR spectrum of (III) were unsuccessful. The Raman spectra of (I)-(II) display absorptions in the 400–350 cm^{-1} range that are assigned to Sb-S vibrations and the absorptions below 350 cm^{-1} are tentatively assigned to Ag-S vibrations. The sharp absorption at $ca.$ 360 cm^{-1} is characteristic of the $[SbS_4]^{4-}$ unit by analogy to A_2AuSbS_4.[24] The Raman spectrum for (III) was extremely weak, showing only a single peak at 358 cm^{-1}, confirming the presence of the $[SbS_4]^{3-}$ unit. The Raman spectra of (I) and (III) are shown in Figure 4-11.

Unlike the thermal analysis described in the previous chapter, increasing the Ag^+ ion concentration appears to have a stabilizing effect on the thermal properties of (I)-(II). Differential thermal analysis (DTA) data, followed by careful XRD analysis of the residues, show that α-$Rb_2Ag_{20}Sb_4S_{19}$ melts incongruently at 436°C, producing a mixture of α-$Rb_2Ag_{20}Sb_4S_{19}$ and Ag_3SbS_3, see Figure 4-12A. The DTA data for $Cs_2Ag_{20}Sb_4S_{19}$ reveals that the compound melts congruently at 416 °C, see Figure 4-12B. The DTA data, followed by careful XRD analysis of the residue revealed that β- $Rb_2Ag_{20}Sb_4S_{19}$ melts incongruently at 450 °C, forming a mixture of α-$Rb_2Ag_{20}Sb_4S_{19}$ and β- $Rb_2Ag_{20}Sb_4S_{19}$, see Figure 4-13A. The DSC data revealed that the there were two endothermic transitions at 179 °C and 210 °C, respectively. Upon cooling two exothermic peaks are observed at 206 °C and 167°C, suggesting a Ag^+ ion transition.

(A)
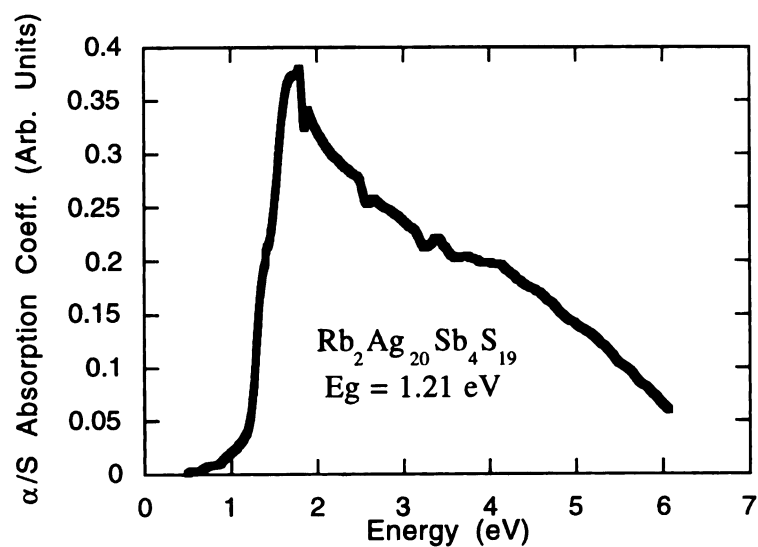
(B)
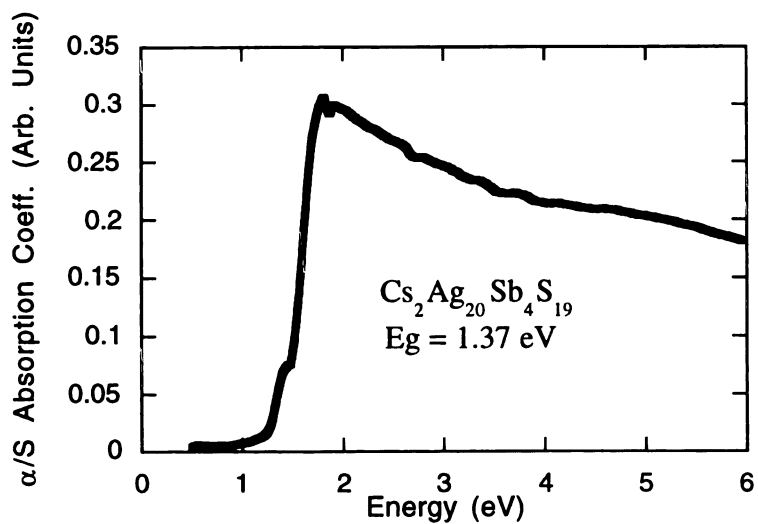
Figure 4-9:   (A) Solid-state optical absorption spectrum for $Cs_2Ag_{20}Sb_4S_{19}$.
              (B) Solid-state optical absorption spectrum for $Rb_2Ag_{20}Sb_4S_{19}$.
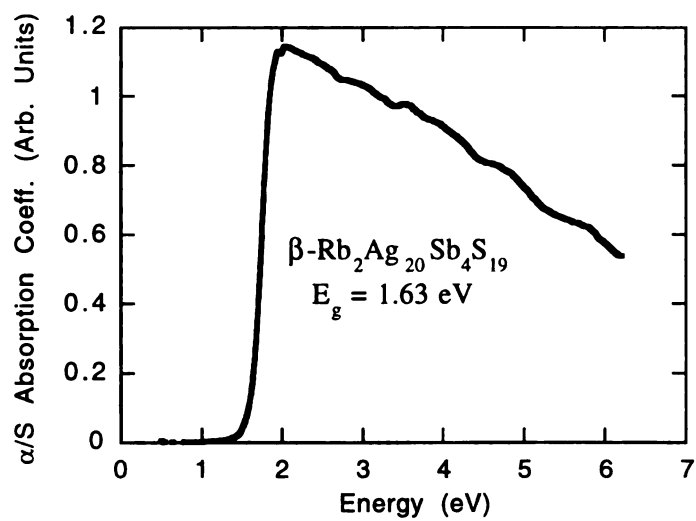
Figure 4-10:   Solid-state optical absorption spectrum for β-Rb₂Ag₂₀Sb₄S₁₉.
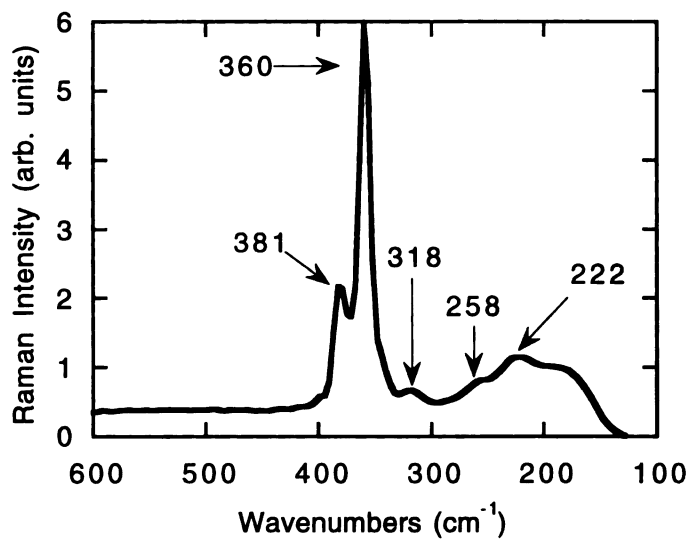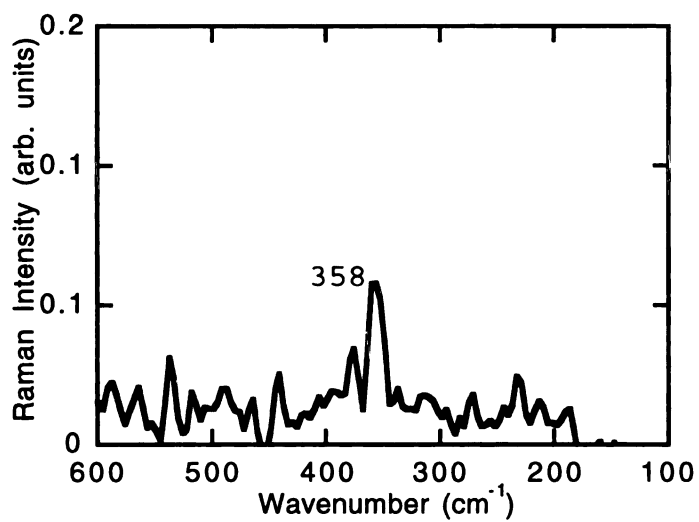
Figure 4-11: (A) Raman spectrum for $Rb_2Ag_{20}Sb_4S_{19}$ (I).
(B) Raman spectrum for $b-Rb_2Ag_{20}Sb_4S_{19}$ (III).
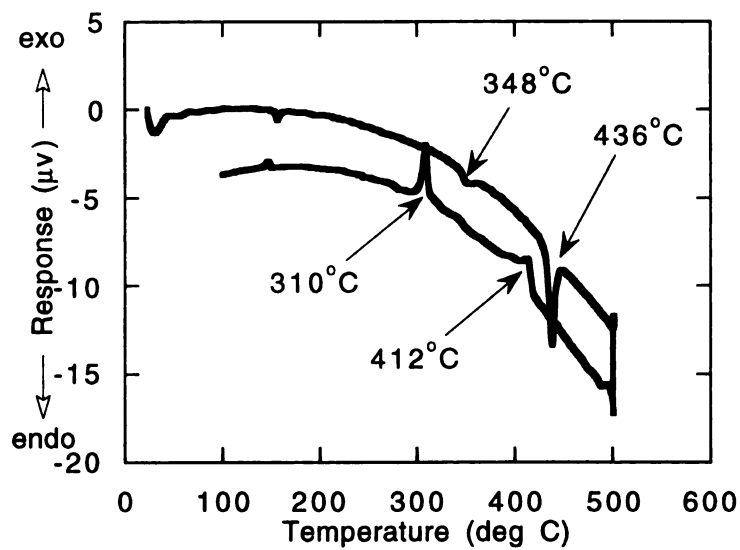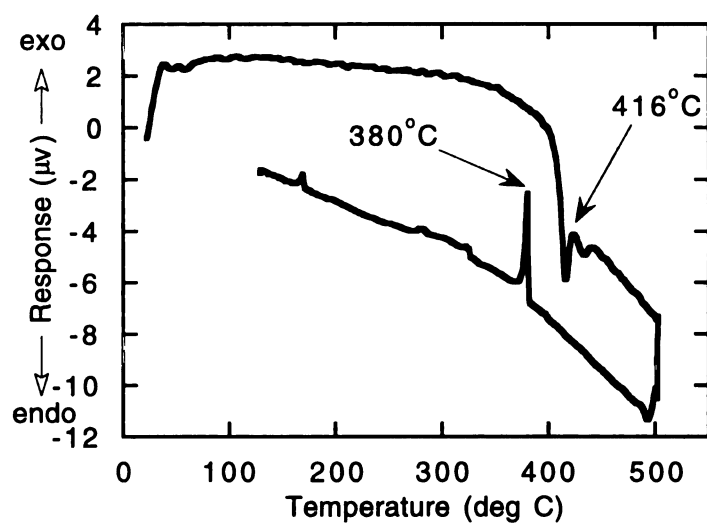
Figure 4-12: (A) DTA diagram for $Rb_2Ag_{20}Sb_4S_{19}$ (I).
              (B) DTA diagram for $Cs_2Ag_{20}Sb_4S_{19}$ (II).
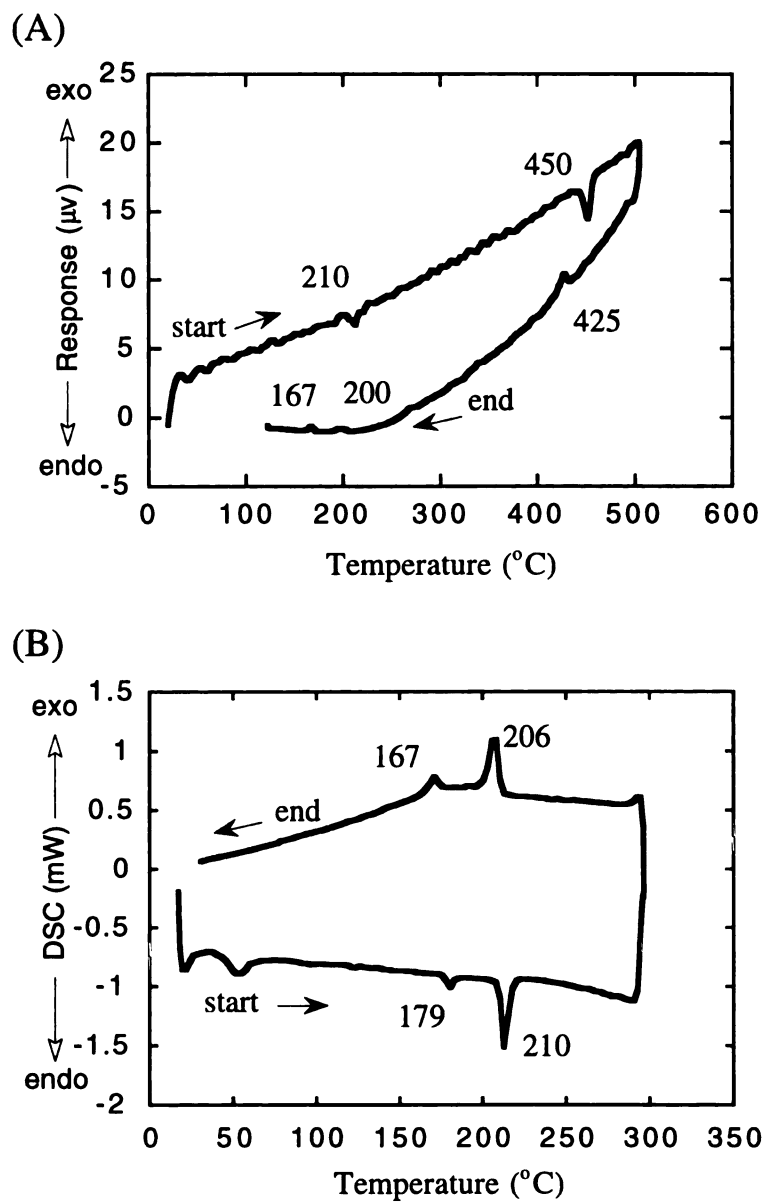
Figure 4-13: (A) DTA diagram for β-$Rb_2Ag_{20}Sb_4S_{19}$ (III). (B) DSC diagram for β-$Rb_2Ag_{20}Sb_4S_{19}$ (III).

4. Conclusions.

The exploration of the silver-rich fluxes produced three new thioantimonate compounds with a complicated layered structure. These compounds represent the first members of a new class of compounds with the general formula $(A_2S)_w(Ag_2S)_x(Ag_3SbS_3)_y(Ag_3SbS_4)_z$. The structure of (I)-(III) represent a new direction in the chalcometalate chemistry in which the structural description is dominated by the Ag_2S framework coordination to the various $[Sb_xS_y]^{n-}$ units. While the complicated layers observed in (I)-(III) are very intriguing from a structural standpoint, these materials sill require extensive characterization to determine if they exhibit properties which make them potenital candidated for ion conductors or other applications. The large supercell observed in (III) is unusual and further work to is needed to completely determine the structure.

List of References

1. McCarthy, T. J.; Kanatzidis, M. G. *Inorg. Chem.,* **1994**, *33*, 1205.

2. Choi, K.-S.; Iordanidis, L.; Chondroudis, K.; Kanatzidis, M. G. *Inorg. Chem.,* **1997**, *36*, 3804. (b) Chen, J. H.; Dorhout, P. K. *J. Alloys and Comp.,* **1997**, *249*, 199.

3. Hanko, J. A.; Kanatzidis, M. G. Abstract #0413 from 210th Fall ACS Meeting, Chicago Il 1995.

4. (a) Wood, P. T.; Schimek, G. L.; Kolis, J. W. *Chem. Mater.,* **1996**, *8*, 721. (b) Schimek, G. L.; Pennigton, T. L.; Wood, P. T.; Kolis, J. W. *J. Solid State Chem..,* **1996**, *123*, 272.

5. Imafuku, M.; Nakai, I.; Nagashima, K. *Mat. Res. Bull.,* **1986**, *21*, 493.

6. Hanko, J. A.; Kanatzidis M. G. *J. Chem. Soc: Chem. Comm.,* **1998**, 726.

7. Hanko J. A.; Kanatzidis,M. G. *J. Alloys and Comp.,* In press.

8. Chen, J. H.; Dorhout, P. K. *J. Alloys and Comp.,* 1997, **249**, 199.

9. Choi, K.-S.; Hanko, J. A; Kanatzidis, M. G. Inorg. Chem. Submitted

10. (a) Kanatzidis, M. G. *Curr. Opinion Solid State and Mater. Sci.,* **1997**, 2, 139. (b) Sutorik, A. C.; Kanatzidis, M. G. *Prog. Inorg Chem.,* **1995**, *43*, 151 and references therein.

11. Chondroudis, K.; Hanko, J. A.; Kanatzidis, M. G. *Inorg. Chem.,* **1997**, *36*, 2623.

12. Rom, I; Sitte, W. *Solid State Ionics ,* **1997**, *101,*: 381.

13. Boucher, F.; Evain, M.; Brec, R. *J Solid State Chem.,* **1993**, *107*, 332.

14. Gaudin, E.; Fischer, L.; Boucher, F.; Evain, M.; Petricek, V. *Acta. Crystallogr.,* **1997**, *B53*, 6775.

15. CERIUS2, Version 1.6, Molecular Simulations Inc., Cambridge, England, 1994.

16. McCarthy, T. J.; Ngeyi, S.-P.; Liao, J.-H.; DeGroot, D.; Hogan, T.; Kannewulf, C. R.; Kanatzidis, M. G. *Chem. Mater.,* **1993**, *5*, 331.

17. Walker, N.; Stuart, D. *Acta Crystallogr.,* **1983**, *A39*, 158.

18. Sheldrick, G. M., "Crystallographic Computing 3"; Sheldrick, G. M., Kruger, C., Doddard, R., Eds.; Oxford University Press: Oxford, England, 1985; pp 175.

19. TEXSAN: Single Crystal Structure Analysis Software, Version 5.0; Molecular Structure Corp.: The Woodlands, TX 77381, 1981.

20. Hanko, J. A.; Brec, R. Evain, M. Kanatzidis, M. G. Work in progress.

21. SMART and SAINT. Data collection and Processing Software for the Smart system. Siemens Analytical X-ray Instruments Inc.,**1995**.

22. Blessing , R. H. *Acta Crystallogr.,* **1995,** *A51,* 33-38.

23. SHELXTL Version 5, Reference Manual. Siemens Industrial Automation Inc., **1994**.

24. Hanko, J. A.; Kanatzidis, M. G. *J Alloys Comp.,* accepted for publication.

CHAPTER 5.

The Chemistry of Au in Molten Polythioantimonate Fluxes. Synthesis and Characterization of the New Multinary Gold Thioantimonates A_2AuSbS_4 (A = Rb, Cs) and $Rb_2Au_6Sb_4S_{10}$. A Novel Compound with a Binary and Ternary Interconnected Framework.

1. Introduction

As shown in previous chapters, the polychalcoantimonate fluxes can be used for the synthesis of new multinary thioantimonate and selenoantimonate compounds[1-6]. This method is complementary to conventional direct combination of the binary sulfides[7] or hydro(solvento)thermal synthesis.[8] The polychalcoantimonate fluxes are formed by the *in situ* fusion of $A_2Q/Sb/Q$ and contain $[Sb_xQ_y]^{n-}$ ligands (A = Na, K, Rb, Cs ; Q = S, Se) as well as polychalcogenide ligands. The key feature of this method is that the polychalcoantimonate units preferentially coordinate to coinage metal ions, building extended lattices. Examples include $KThSb_2Se_6$,[2] A_2AgSbS_4 (A = K, Rb, Cs)[3,4], $Cs_3Ag_2Sb_3Q_8$ (Q = S,Se)[3,4], $AAg_2 SbS_4$ (A = K, Rb)[3,4], $A_2Ag_{20}Sb_4S_{19}$ (A = Rb, Cs)[5] and $KHgSbS_3$[6]. The binding modes displayed by the $[Sb_yQ_z]^{n-}$ anions in the above materials are different from the binding modes observed in the coinage metal sulfosalt minerals, i.e. Cu_3SbS_4,[9] $CuPbSbS_3$,[10] $AgPbSbS_3$,[11] and $Cu_{12}Sb_4S_{13}$.[12] While a variety of ternary alkali gold chalcogenide compounds[13-14] are known, no well characterized ternary Au/Sb/S phase has been reported. Attempts to prepare a ternary Au/Sb/S phase via direct combination reactions were fruitless, leading us to address the question of whether a quaternary A/Au/Sb/S compound could be stabilized. Continuing our investigations of the coinage metals, particularly Au, we report here the synthesis, structural characterization, and physical properties of the new quaternary gold thioantimonate compounds, A_2AuSbS_4 (A = Rb, Cs) (I)-(II), and $Rb_2Au_6Sb_4S_{10}$ (III) . The novelty of $Rb_2Au_6Sb_4S_{10}$ is that its layers are comprised of two different, independent interwoven frameworks. The only other structurally characterized example of two interpenetrating frameworks is K_2PdSe_{10}[15]

2. Experimental Section

2.1 Reagents

The reagents used in ths study were used as obtained unless noted otherwide: (i) gold metal (99.99%) was acquired from Liberty Coins, Lansing MI; (ii) antimony powder 99.999% purity, -200 mesh, Cerac Inc., Milwaukee, WI; (iii) cesium metal, analytical reagent, Johnson Matthey/AESAR Group, Seabrook, NH; (iv) rubidium metal, analytical reagent, Johnson Matthey/AESAR Group, Seabrook, NH; (v) sulfur powder, sublimed, J.T. Baker Chemical Co., Phillipsburg, NJ; (vi) N,N-Dimethylformamide (DMF) reagent grade, EM Science, Inc., Gibbstown, NJ; (vii) diethyl ether, ACS anhydrous, EM Science, Inc., Gibbstown, NJ.

Finely divided Au metal. A Canadian Maple Leaf gold coin, (99.99%, 31.1g) was dissolved in 400 ml of aqua regia (300 ml concentrated HCl and 100 ml of concentrated HNO_3). The solution was boiled in an acid resistant fume hood to a volume of ~100 ml. The concentrate was neutralized with ammonium hydroxide and the gold was reduced with excess hydrazine hydrochloride, dissolved in 100 ml of distilled water. The resulting black suspension was heated gently, with stirring, for one hour to allow particle aggregation. The gold powder was filtered and washed with copious amounts of distilled water and acetone, and then heated in air at 130°C for 4 hours to drive off any remaining volative impurities, yielding 30.9 g of Au powder. Note: heating too long or at too high a temperature results in large intractable grain sizes.

2.2 Syntheses.

A_2S (A = Rb and Cs) were prepared by reacting stoichiometric amounts of the elements in liquid ammonia[16] as described in Chapter 2, Section 2.2.

Rb_2AuSbS_4 (I). A mixture of 0.102g (0.50 mmole) Rb_2S, 0.098g (0.50 mmole) Au, 0.031g (0.25 mmole) Sb, and 0.080g (2.5 mmole) S were thoroughly mixed and transferred into a 6-ml Pyrex tube which was subsequently flame-sealed *in vacuo* ($\sim10^{-3}$ Torr). The reaction mixture was ramped to 350°C over a 12 hour period in a computer-controlled furnace. The reaction was heated at 350°C for 3 days, followed by cooling to 150°C at a rate of 4°C/hr and then to room temperature in 10 hours. The product, which is slightly unstable in water and air, was isolated by dissolving the Rb_2S_x and any residual $Rb_x[Sb_yS_z]$ flux with DMF under inert atmosphere to give pale yellow crystals and a small amount of unreacted gold metal (1-5%). A yield of 75%, based on Sb was estimated. Quantitative microprobe analysis of single crystals gave $Rb_{2.3}Au_{1.4}SbS_6$.

Cs_2AuSbS_4 (II). A mixture of 0.149g (0.50 mmole) Cs_2S, 0.098g (0.50 mmole) Ag, 0.031g (0.25 mmole) Sb, and 0.080g (2.5 mmole) S was sealed under vacuum in a Pyrex tube and heated as in (I). The product, which is stable in air and water, was isolated as in (I) to give yellow crystals in 77% yield, based on Sb. Quantitative microprobe analysis on single crystals gave $Cs_{1.4}AgSbS_{4.3}$.

$Rb_2Au_6Sb_4S_{10}$ (III) was synthesized from a mixture of Rb_2S (0.102g ; 0.5 mmol) Au (0.098g ; 0.5 mmol) Sb (0.031g ; 0.25 mmol) and S (0.064g ; 2 mmol) was sealed under vacuum in a Pyrex tube and ramped to 350°C for 4d followed by cooling to 150°C at 4°C h^{-1}. The product, which is stable in water and air, was isolated by

dissolving the Rb_2S_x and any residual $Rb_x[Sb_yS_z]$ flux with DMF under inert atmosphere to give black needles in low yield (20% yield based on Sb). Microprobe analysis carried out on several randomly selected crystals gave an average composition of $RbAu_{4.6}Sb_{2.7}S_9$.

2.3. Physical Measurements.

Powder X-ray Diffraction. The compounds were examined by powder X-ray diffraction for the purpose of phase purity. Accurate d spacings obtained from the powder pattern for the three compounds were performed using a calibrated Rigaku-Denki/RW400F2 (Rotaflex) rotating anode powder diffractometer controlled by an IBM computer, operating at 45 kV/ 100 mA and with a 1o/min scan rate, employing graphite crystal filtered Cu radiation in a Bragg-Brentano geometry. The calculated powder patterns for (I) and (III) were prepared with the $CERIUS^2$ software.[17] Listings of calculated and observed powder patterns for (I) and (III) are given in Tables 5-1 and 5-2, respectively.

Infrared Spectroscopy. Infrared spectra, in the far-IR region ($600-50$ cm^{-1}), were recorded on a computer controlled Nicolet 750 Magna-IR Series II spectrophotometer equipped with a TGS/PE detector and silicon beam splitter with a resolution of 4 cm^{-1}. The samples were ground with dry CsI into a fine powder and pressed into translucent pellets.

Raman Spectroscopy. Raman spectra ($600-100$ cm^{-1}) were recorded on a BIO-RAD FT Raman spectrometer equipped with a Spectra-Physics Topaz T10-106c 1.064 nm YAG laser and a Ge detector. The samples for (I) and (II) were ground to a fine powder and loaded without modification into glass capillary tubes. The crystals for (III) were ground with CsI into a fine powder and loaded into a glass capillary tube.

Solid State UV/Vis/Near IR Spectroscopy. Optical diffuse reflectance measurements were performed at room temperature using a Shimadzu UV-3101PC double beam, double monochromator spectrophotometer. The instrument is equipped with integrating sphere and controlled by a personal computer. $BaSO_4$ was used as a 100%

reflectance standard for all materials. Samples are prepared by grinding them to a fine powder and spreading them on a compacted surface of the powdered standard material, preloaded into a sample holder. The reflectance versus wavelength data generated can be used to estimate a material's band gap by converting reflectance to absorption data as described elsewhere.[18]

Differential Thermal Analysis (DTA). DTA experiments were performed on a computer-controlled Shimadzu DTA-50 thermal analyzer. Typically a sample (~25 mg) of ground crystalline material was sealed in quartz ampoules under vacuum. A quartz ampoule of equal mass filled with Al_2O_3 was sealed and placed on the reference side of the detector. The sample was heated to the desired temperature at 10°C/min, then isothermed for 10 minutes and finally cooled to 50°C at the same rate. The stability of the sample and the reproducibility of the melting point for each sample was monitored by running multiple cycles. The residues of the DTA experiment were examined by X-ray powder diffraction. To evaluate congruent melting the X-ray powder diffraction patterns before and after the DTA experiments were compared.

Semiquantitative Microprobe Analyses. The analyses were performed using a JEOL JSM-6400V scanning electron microscope (SEM) equipped with a TN 5500 EDS detector. This technique was used to confirm the presence of all elements in the compounds. Data acquisition was performed with an accelerating voltage of 20kV and twenty second accumulation time.

Single Crystal X-Ray Crystallography . Intensity data for (I) was collected using a Rigaku AFC6S four-circle automated diffractometer equipped with a graphite crystal monochromator. Crystal stability was monitored with three standard reflections whose intensities were checked every 150 reflections. No crystal decay was detected for (I). The space group was determined from systematic absences and intensity statistics. An empirical absorption correction, based on ψ scans, was applied to the data set of (I) during initial stages of refinement. The structure of (I) was solved by direct methods using

SHELXS-86 software[19a], and full matrix least squares refinement was performed using the TEXSAN software package[19b]. An empirical DIFABS correction[20] was applied as recommended, after full isotropic refinement, after which full anisotropic refinement was performed.

Intensity data for (III) was collected on a Siemens SMART-CCD diffractometer using graphite-monochromatized MoKα radiation. The data collection covered over a hemisphere of reciprocal space, up to 52° 2Θ. The individual frames were measured with a detector to crystal distance of 5 cm and an omega rotation of 0.3 deg with an acquisition time of 45 seconds, leading to a total measurement time of about 24 hours. The SMART software[21] was used for the data acquisition, SAINT[21] for data extraction and reduction. The space group was determined from systematic absences and intensity statistics. A correction for Lorentz polarization effects and an empirical absorption correction (SADABS)[22] were applied to the data. The structure of (III) was solvend using direct methods and refined by full-matrix least squares techniques of the SHELXTL[23] package of crystallographic programs.

The complete set of data collection parameters and details of the structure solution and refinement for (I) and (III) are given in Table 5-3. The coordinates of all atoms, average temperature factors, anisopropic displacement parameters and their estimated standard deviations are given in Tables 5-4 to 5-5.

Table 5-1.   Calculated and Observed X-ray Powder Patterns for Rb_2AuSbS_4 (I).

hkl	d_{calc}, Å	d obsd, Å	I/I_{max}(obsd)
020	10.34	10.20	19
100	7.33	7.00	14
110	6.62	6.91	57
120	5.98	5.93	3
021	5.83	5.78	6
040	5.17	5.13	6
111	4.93	4.90	2
121	4.56	4.53	2
140	4.22	4.19	8
041	4.17	4.14	20
131	4.09	4.07	17
200	3.66	3.67	4
141	3.62	3.64	4
210 150	3.13	3.64	4
002	3.53	3.51	17
220	3.45	3.46	100
022	3.34	3.32	30
230	3.23	3.27	8
211	3.21	3.23	12
151	3.20	3.19	11
102	3.18		
112	3.14	3.12	29
221	3.10	3.08	20
122	3.04	3.02	5
042	2.91	2.92	5
132	2.88		
170	2.74	2.71	20
080	2.58	2.57	20
212	2.52	2.50	9
222 062	2.46	2.45	3
180	2.43	2.41	7
330	2.30	2.27	2
242	2.28	2.26	2

240	2.20	2.21	8
271	2.187	2.181	4
252	2.166	2.156	5
133	2.131	2.134	6
280	2.112	2.112	3
350	2.104		
324	2.068	2.077	2
321	2.000	2.039	7
241	1.984	1.984	4
322	1.972	1.975	4
153	1.970	1.966	10
223	1.945	1.939	3

Table 5-2. Calculated and Observed X - Ray Powder Patterns for $Rb_2Au_6Sb_4S_{10}$ (III).

h k l	$d_{calc.}$, Å	$d_{obs.}$, Å	I/I_{max}, (obs)
0 2 0	13.03	13.01	100
0 4 0	6.51	6.51	4
2 1 0	6.05	6.03	7
2 3 0	5.05	5.05	9
0 6 0	4.34	4.34	7
0 5 1	4.17	4.16	6
1 5 1	3.95	3.95	6
1 7 0 2 6 0 3 0 1	3.562	3.563	30
0 7 1	3.284	3.283	7
1 2 2 3 5 0	3.245	3.244	15
2 7 0	3.196	3.193	13
4 1 0	3.088	3.089	16
4 2 0	3.025	3.025	12
1 4 2	2.980	2.980	6
2 8 0	2.887	2.886	23
1 9 0	2.822	2.820	9
4 2 1	2.774	2.770	8
1 6 2 3 1 2	2.652	2.649	6
0 10 0 4 4 1	2.607	2.607	13
3 3 2	2.548	2.551	7
2 10 0 3 8 1	2.405	2.404	12
3 5 2	2.373	2.376	7
2 7 2	2.354	2.354	8
5 4 0	2.324	2.325	5
3 10 0	2.207	2.207	5
3 7 2	2.168	2.170	6
4 8 1 1 12 0	2.140	2.141	5
4 5 2	2.119	2.119	4
1 10 2	2.058	2.059	4
2 12 0 6 2 0	2.047	2.042	5
1 13 0 2 10 2	1.978	1.974	4
4 7 2 2 12 1	1.967	1.968	4

1 11 2	1.935	1.931	4
1 13 1	1.904	1.904	4
6 5 1	1.856	1.859	4
3 12 1	1.855	1.850	3
4 2 3	1.841	1.842	4
6 7 0	1.811	1.813	4
6 6 1	1.807	1.807	3
6 2 2	1.764	1.762	4
5 10 1	1.742	1.742	4
4 12 1	1.725	1.721	7
6 9 0 3 12 2	1.686	1.686	5
2 1 4	1.672	1.672	3
1 14 2	1.628	1.629	2
1 16 1 1 12 3	1.573	1.574	3
5 13 0	1.561	1.561	4

Table 5-3. Crystallographic Data for Rb_2AuSbS_4 and $Rb_2Au_6Sb_4S_{10}$.

	I	III
Formula	Rb_2AuSbS_4	$Rb_2Au_6Sb_4S_{10}$
fw	308.95	2160.33
a,Å	6.804(3)	12.4402(2)
b,Å	20.127(4)	26.0790(4)
c,Å	7.195(4)	6.9614(1)
α, deg	90.000	90.000
β, deg	90.000	90.000
γ, deg	90.000	90.000
Z; V, Å^3	8; 985(1)	4; 2258.3(7)
λ, Å	0.71069	0.71069
space group	P bcm (#57)	P nnm (#63)
d_{calc}, g/cm^3	4.165	4.043
μ(Mo Kα), cm^{-1}	278.81	48.83
Crystal dim (mm)	0.04 x 0.04 x 0.12	0.400 x 0.010 x ~0.005
secondary extension	3.3234x10^{-5}	NA
T, ^oC	23	-120
2θ max, deg	50.0	45
no. data collected	1016	15609
no. unique data	955	2340
no. data observed, $I > 3\sigma(I)$	548	1014
no. of variables	46	159
final R/R$_w$,^{a}%	4.5/6.6	8.0/9.6
GOF	3.06	1.56

a $R = \Sigma(|F_o|-|F_c|)/\Sigma|F_o|$; $R_w = [\Sigma w(|F_o| - |F_c|)^2/\Sigma w|F_o|^2]^{1/2}$

Table 5-4.   Fractional Atomic Coordinates and B(eq) Values for Rb_2AuSbS_4 with Estimated Standard Deviations in Parentheses.

atom	x	y	z	B_{eq}[a]$Å^2$
Au1	0.3929(2)	3/4	0	2.34(7)
Sb1	0.2086(3)	0.8896(1)	1/4	1.9(1)
S1	0.200(1)	1.0045(4)	1/4	2.4(4)
S2	0.393(1)	0.8638(3)	-0.014(1)	3.3(3)
S3	-0.092(1)	0.8377(5)	1/4	3.9(5)
Rb1	0.2981(5)	1.0118(2)	-1/4	2.7(2)
Rb2	-0.1064(7)	0.8297(2)	-1/4	3.8(2)

[a] B values for anisotropically refined atoms are given in the form of the isotropic equivalent displacement parameter defined as $B_{eq} = (4/3)[a^2B(1, 1) + b^2B(2, 2) + c^2B(3, 3) + ab(\cos g)B(1,2) + ac(\cos b)B(1,3) + bc(\cos a)B(2, 3)$

Table 5-5.   Fractional Atomic Coordinates and B(eq) Values for $Rb_2Au_6Sb_4S_{10}$ with Estimated Standard Deviations in Parentheses.

atom	x	y	z	B(eq)
Au(1)	0.6904(2)	0.19466(9)	-0.2422(3)	1.87(5)
Au(2)	0.6925(3)	0.3201(1)	0.5000	2.09(8)
Au(3)	0.4852(2)	0.26812(9)	-0.2514(3)	2.06(5)
Au(4)	0.7297(2)	0.2907(1)	0.0000	1.90(7)
Sb(1)	0.3175(4)	0.3976(2)	0.0000	1.6(1)
Sb(2)	0.9352(4)	0.3454(2)	0.5000	1.8(1)
Sb(3)	1.0332(4)	0.3762(2)	0.0000	1.6(1)
Sb(4)	0.4516(4)	0.3842(2)	0.5000	1.7(1)
Rb(1)	0.6643(6)	0.4329(3)	0.0000	2.7(2)
Rb(2)	0.1742(7)	0.4851(3)	0.5000	2.9(2)
S(1)	0.911(1)	0.4104(6)	0.251(2)	2.2(3)
S(2)	0.763(2)	0.2393(8)	-0.5000	2.2(5)
S(3)	0.913(2)	0.2803(8)	0.0000	2.3(5)
S(4)	0.640(2)	0.4046(8)	0.5000	2.0(5)
S(5)	0.637(2)	0.1405(8)	0.0000	1.8(5)
S(6)	0.161(2)	0.4538(9)	0.0000	2.7(5)
S(7)	0.553(2)	0.3163(9)	0.0000	2.5(5)
S(8)	0.408(1)	0.4486(5)	-0.251(2)	2.3(4)

3. Results and Discussion

3.1 Description of Structures

Structure of A_2AuSbS_4 (A = Rb, Cs) (I) - (II): Since A_2AuSbS_4 (A = Rb, Cs) are isostructural, the single-crystal structure determination was only done on Rb_2AuSbS_4, therefore this discussion will refer mainly to this compound. The structure of **(I)** and **(II)** belong to the same family as Cs_2AuPS_4.[16] This is the first example that we are aware of where a thioantimonate and a thiophosphate compound are isostructural. The infinite $[AuSbS_4]_n^{2n-}$ chains are comprised of alternating tetrahedral $[SbS_4]^{3-}$ units, linked together by sharing adjacent corners with monovalent gold cations, see Figure 5-1. The chains run parallel to the crystallographic c-axis and are separated by alkali cations, see Figure 5-2. The $[AuSbS_4]_n^{2n-}$ chains propagate by a glide plane forming a sinusoidal wave that runs along the crystallographic c direction, see Figure 5-3. The chains form a projection, down the chain axis, resembling the letter "C". The Au^+ ion resides on a 2-fold crystallographic axis, with a Au-S distance of 2.293(7) Å. The S-Au-S angle is essentially linear at $179.6(5)°$. The $[SbS_4]^{3-}$ unit is a regular tetrahedron with Sb-S bond distances in the range of 2.30(1)Å to 2.334(7)Å (mean 2.32(2)Å) and S-Sb-S angles in the range of $103.6(2)°$ to $115.6(4)°$. The Au-Au' distance is 3.598(2)Å, too long to represent any significant bonding interaction. The $[AuSbS_4]_n^{2n-}$ chains are separated by Rb^+ ions which are located in two different sites. In Rb_2AuSbS_4, Rb(1) is coordinated by nine S atoms [range of Rb(1)-S distances, 3.51(1)-3.94(1)Å; Ave 3.67(6)Å], and Rb(2) is coordinated by eight S atoms [3.58(1)-4.01(1)Å; Ave 3.80(6)Å]. Selected bond distances and angles are given in Table 5-6.

The structure of the $[AuSbS_4]_n^{2n-}$ anion is not subject to a cation effect[24] as one moves from the larger Cs^+ to the smaller Rb^+ cation. Presumably, the difference in cation volume between Rb^+ and Cs^+ is not large enough to overcome the strong preference of the Au^+ cations for linear coordination. As observed prevoiusly in this dissertation, and in other systems[25], structural changes may yet occur in the case of $[AuSbS_4]_n^{2n-}$ anion as one moves to the smaller K^+, Na^+ or Li^+ cations.

Structure of $Rb_2Au_6Sb_4S_{10}$. The strikingly complex structure of $Rb_2Au_6Sb_4S_{10}$ is composed of two different interpenetrating layered frameworks, $[Au_3Sb_4S_8]^-$ and $[Au_3S_2]^-$, see Figure 5-4. As a result, $Rb_2[Au_3Sb_4S_8][Au_3S_2]$ is a more descriptive formula, and to the best of our knowledge, represents the first reported example of a compound in which a binary framework is interpenetrating with a ternary one. As shown in Figure 5-5, the $[Au_3Sb_4S_8]^-$ layer is strongly undulating and consists of alternating $[Sb_4S_7]_n^{2n-}$ one-dimensional chains bound to $[Au_3S]^+$ units. The chains alternate above and below the layer in a staggered fashion. The $[Sb_4S_7]_n^{2n-}$ chain is comprised of four condensed SbS_3 pyramids forming a 12 membered Sb - S ring, see Figure 5-6. Two of the SbS_3 units share two corners leaving one sulfide terminal, while the other two SbS_3 units share all three corners. The dimensions of the ring are $6.49(3)Å$ $(Sb(4) - Sb(2))$ by $7.83(3)Å$ $(Sb(1) - Sb(3))$. The Sb atoms are in pyramidal coordination with Sb-S distances in the range from $2.21(6)Å$ to $2.65(6)Å$; (mean $2.46(3)Å$) and compare well with those reported for $Cs_2Sb_4S_8$[1] and $Cs_3Ag_2Sb_3S_8$[3,4]. The discrete $[Au_3S]^+$ unit has a pyramidal sulfide linked to three linear Au^+ cations. The Au - S distances range from $2.28(4)Å$ to $2.46(5)Å$ and compare well with those found in $KAuS_5$[13], $CsAu_3S_2$[14a], and $AAuS$[14b] (A = Na, K, Rb). The S - Au - S angles range from $170°$ to $174°$.

The second framework, which is interwoven with the one described above is a $[Au_3S_2]^-$ layer. The $[Au_3S_2]^-$ layer is puckered with 12 membered Au-S rings in an anti-

B_2O_3 motif: (ring dimensions: 6.91(2)Å Au(4) to Au(4) by 7.19(3)Å Au(3) to Au(3)). Figure 5-7 highlights the pyramidal sulfide and the puckered nature of the layer and Figure 5-8 shows a perpendicular view. The Au-S distances are in the range from 2.25(4)Å to 2.46(5)Å and the S - Au - S angles are in the range from 165° to 178°. The $[Au_3S_2]^-$ layered structure is similar but not identical to that observed in $CsAu_3S_2$[14a].

Upon further inspection, it was observed that the Au^+ centers in $Rb_2Au_6Sb_4S_{10}$ aggregate to form a column that runs along the c - axis. There are two types of Au···Au interactions: those at 3.25Å and below and those between 3.25 and 3.6Å. Figure 5-9 shows a view perpendicular to these Au-based columns. In Figure 5-8 the interactions below 3.25Å are represented as solid lines where the Au···Au interactions between and 3.25 and 3.60Å are represented as dashed lines. The layers are separated by ten - coordinate $Rb(1)^+$ [Rb(1) - S mean = 3.59(3)Å] and eight - coordinate Rb(2) $[Rb(2)^+$ [Rb(2) - S mean = 3.50(3)Å]. Selected bond distances and angles are given in Table 5-7.
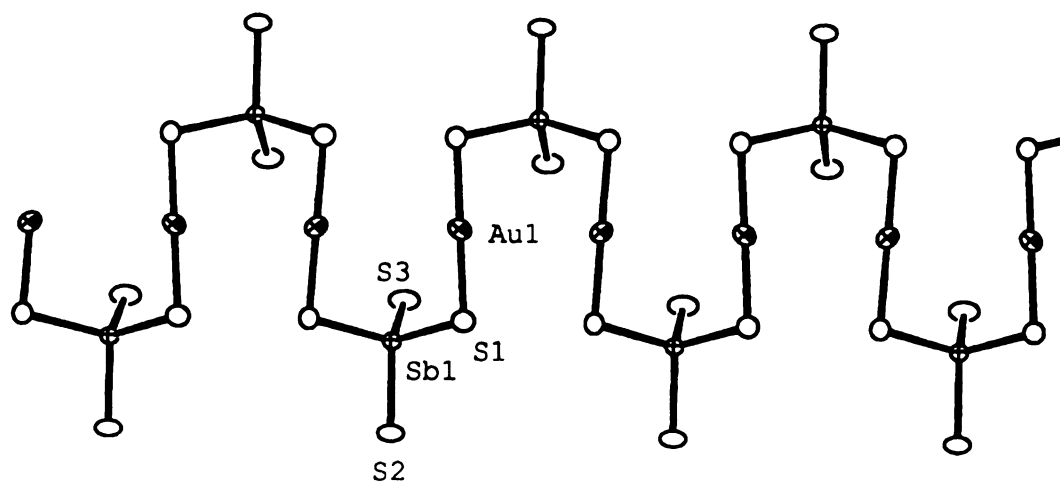
Figure 5-1: View of a single $[AuSbS_4]_n^{2n-}$ chain in Rb_2AuSbS_4 (I), with labeling.
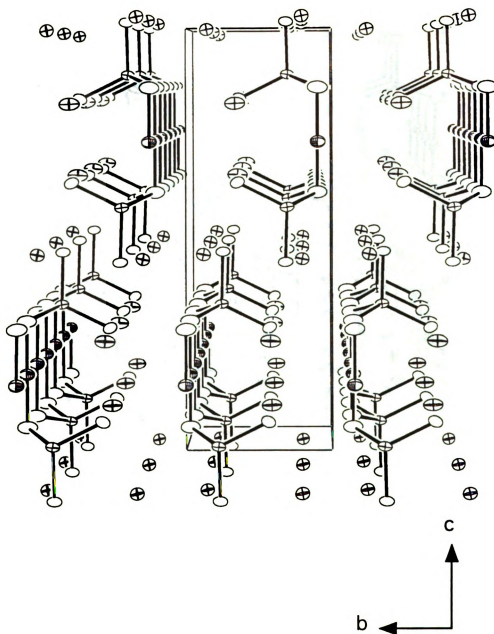
Figure 5-2: ORTEP representation of Rb_2AuSbS_4 (I) as viewed down the c-axis (50% probability ellipsoids).
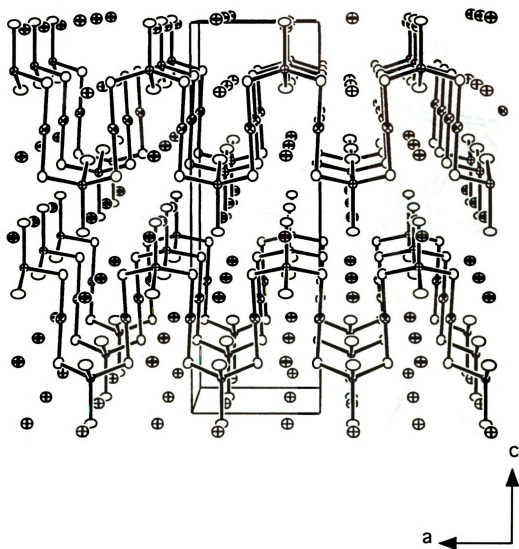
Figure 5-3: ORTEP representation of Rb_2AuSbS_4 (I) as viewed down the *b*-axis (50% probability ellipsoids).
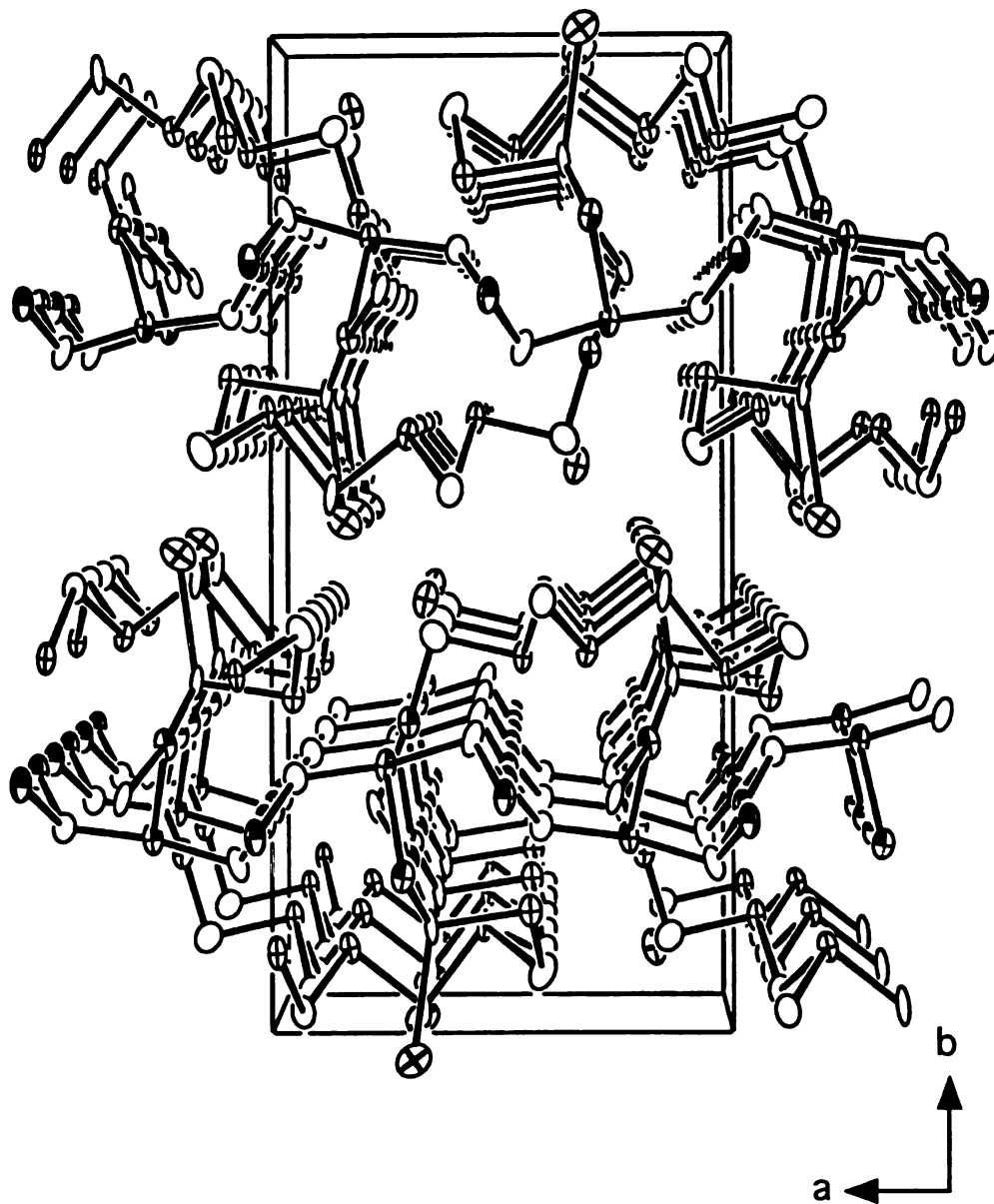
Figure 5-4:   ORTEP representation of $Rb_2Au_6Sb_4S_{10}$ (III) as viewed down the c-axis (50% probability elliposids).small octant shaded ellipsoids: Ag, principal axis ellipsoids: Sb, boundary ellipsoids: S, boundary and axis ellipsoids: Rb.
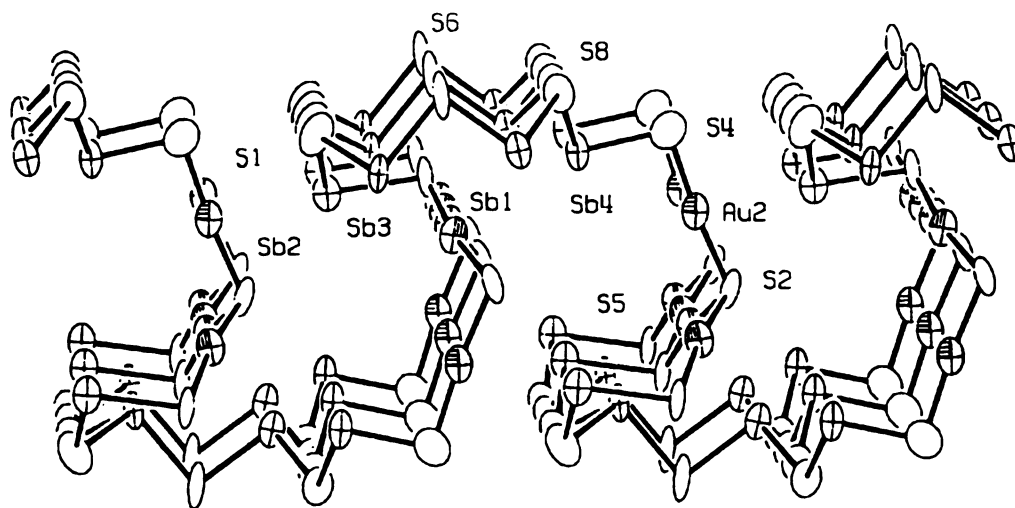
Figure 5-5: ORTEP representation of the [Au₃Sb₄S₈]⁻ undulating layer with labeling (50% probability elliposids).
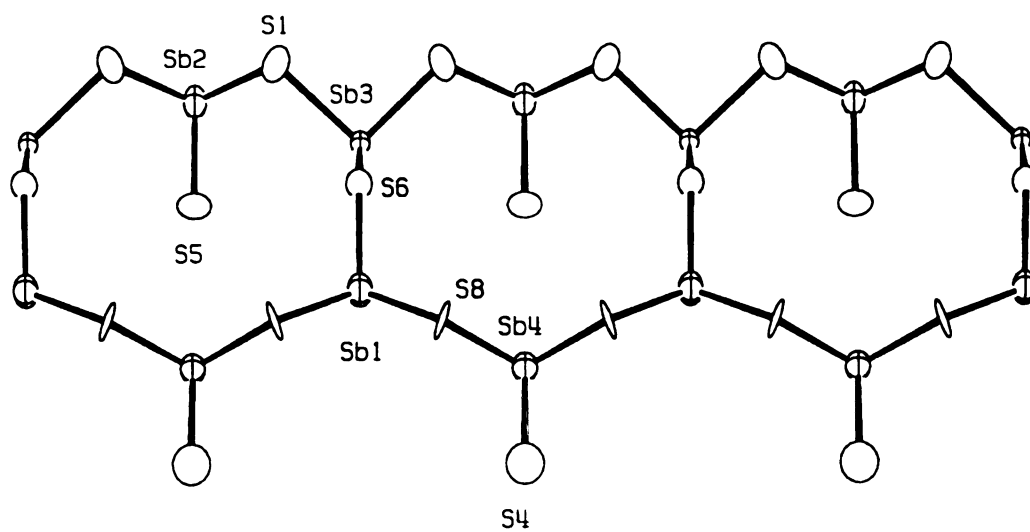
Figure 5-6: ORTEP representation of the [Sb$_4$S$_7$]$^{2-}$ chain with labeling (50% probability ellipsoids).
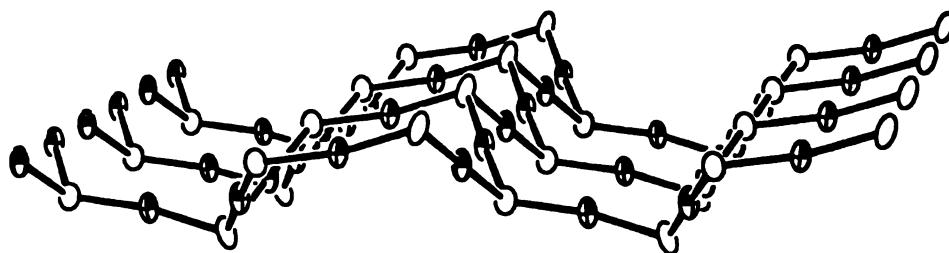
Figure 5-7:   ORTEP representation of the [Au₃S₂]⁻ layer highlighting the pyramidal sulfides in the undulating layer (50% probability elliposids).
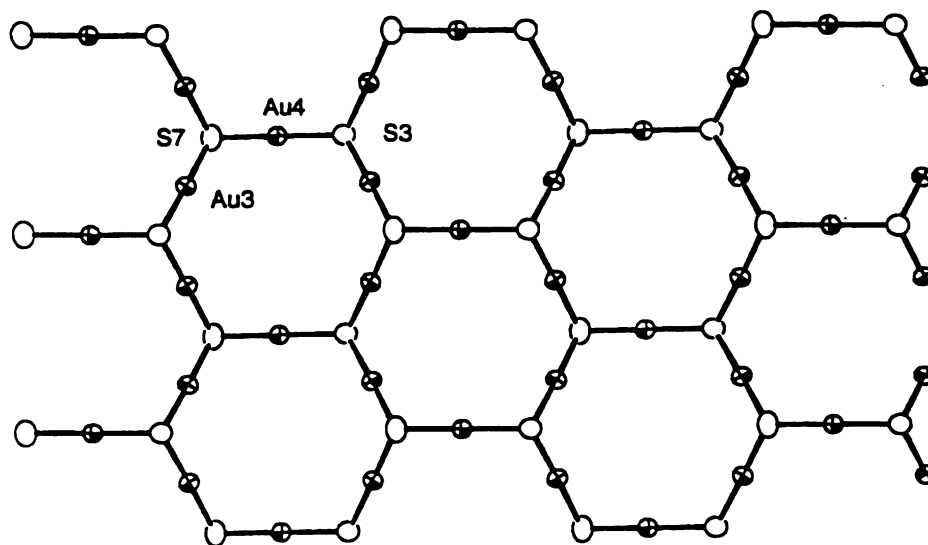
Figure 5-8:   ORTEP representation of a perpendicular view of the [Au$_3$S$_2$]$^-$ layer with labeling (50% probability elliposids).
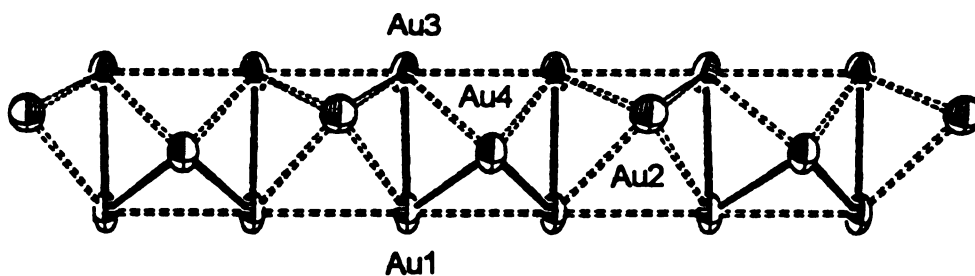
Figure 5-9:   ORTEP representation of the Au···Au interactions of the Au column. The solid lines represent Au···Au interactions under 3.25Å and the dotted lines represent Au···Au interactions between 3.25 and 3.60Å.

3.2. Synthesis, Spectroscopy and Thermal Analysis

The syntheses were the result of redox reactions in which the gold is oxidized by polychalcogenide ions in the $A_x[Sb_yS_z]$ flux. The Au^+ centers are then coordinated by the highly charged $[Sb_yS_z]^{n-}$ ligands. The molten polythioantimonate flux method is very effective for crystal growth in this system. The isolation of pure crystalline products is facilitated by the residual fluxes solubility in aqueous and organic solvents. Unlike other systems of this type, the thioantimnate system lacks the same control of the Lewis basicity as in the chalcophosphate systems. A reduced Sb^{3+} species can be stabilized under Lewis acidic conditions, but the difficulity arises from the ability to predict the exact nature of the Sb^{n+} species in that the Sb^{3+} species are typically observed in compounds containing ologomeric $[Sb_yS_z]^{n-}$ units.

Investigations in the $K_2S/Au/Sb/Q$ (S = S, Se) system resulted in largely amorphous black glassy chunks for both systems. Microprobe analysis gave an average composition of $K_2Au_{1.7}SbS_6$ for the thioantimonate system and $K_{1.5}AuSb_{2.1}Se_{2.2}$ for the selenoantimonate system. Attempts to grow crystals suitable for further characterization are in progress.[26]

In the $A_2S/Au/Sb/S$ system (A = Rb, Cs), (I) - (II) were synthesized from a metal/antimony ratio of 2:1 in a $2A_2S_6$ flux at 350° C. Although an excess of gold is required for the synthesis of (I) - (II), only a small amount of unincorporated Au metal is observed as an impunity in (I), while (II) is obtained in pure form. Unlike the silver system, increasing the metal concentration did not increase the incorporation of the coinage metal into the resulting compound. The systhesis of (III) was synthesized from a metal/antimony ratio of 2:1 in a $2A_2S_6$ flux at 350° C. Suggesting that the thioantimonate method is sensitive to even slight changes in the flux composition resulting is the stabilization of a totally different $[Sb_xS_y]^{n-}$ units.

The optical absorption properties of the compounds were evaluated by examining the solid-state UV/vis diffuse reflectance spectra these materials. The spectra confirm the semiconducting nature of the materials by revealing the presence of sharp optical gaps. The A_2AuSbS_4 (A= Rb, Cs) compounds exhibit steep absorption edges from which the band gaps (Eg) can be assessed at 2.43 eV (I) and 2.61 eV (II), respectively. The optical spectrum of $Rb_2Au_6Sb_4S_{10}$ reveals the presence of a sharp optical gap of 1.37eV, suggesting the material is a semiconductor. Representative spectra for (I) and (II) are given in Figure 5-10 and the spectrum for (III) is given in Figure 5-11.

The infrared spectrum of Rb_2AuSbS_4 displayed absorptions at 610(m), 410(s), 401(m), 390(m) 360(s) 345(w), 266(w, broad), 173(w), and 153(w) cm^{-1}. The absorption at ca. 390 cm^{-1}, is characteristic of the tetrahedral $[SbS_4]^{3-}$ unit[3,4]. The weak absorptions below 345 cm^{-1} are assigned to Au-S vibrations. The far-IR spectrum of $Rb_2Au_6Sb_4S_{10}$ displays absorptions at ca. 377 and 350 cm^{-1} which can be tentatively assigned to Sb - S stretching modes in the "Sb_2S_4" - like backbone of the $[Au_3Sb_4S_8]^-$ framework[1,3]. Absorptions in the 381-347 cm^{-1} range are tentatively assigned to the Sb-S vibrational stretching modes by analogy with the $Cs_2Sb_4S_8$[1] and $Cs_3Ag_2Sb_3S_8$[3]. Absorptions below 347 cm^{-1} are assigned to Au-S vibrations. By comparison with $KAuS_5$ the absorption at ~323 cm^{-1} is assigned as an Au-S stretching vibration.[13]

The Raman spectrum of Rb_2AuSbS_4 (ground crystals) showed absorbencies at 453(w) 407 (w), 391(m), 362(s), 332(s), 234(w), 175(w), and 153(w) cm^{-1}. The vibrations at ca. 362 cm^{-1}, 175 cm^{-1}, and 153 cm^{-1} are characteristic of the tetrahedral $[SbS_4]^{3-}$ unit by comparison with the Raman spectrum of $Na_3SbS_4 \cdot 9H_2O$.[27] By comparison with $KAuS_5$ the absorption at ca. 330 cm^{-1} can be assigned to a Au-S stretching vibration[12]. This stretching vibration is not observed in the infrared spectrum because the S-Au-S linkage resides on a center of symmetry. The Raman spectrum of $Rb_2Au_6Sb_4S_{10}$ displays absorptions in the range 377-350 cm^{-1} which are assigned to Sb-S

modes and the absorptions below 350 cm^{-1} are assigned to Au-S stretching vibrations. The Raman spectra for (I) and (III) are shown in Figure 5-12.

The DTA of (I) shows that it melts incongruently at *ca.* 400°C, converting partially to Au metal and residual amorphous $A_x[Sb_yS_z]$ flux. Compound (II) melts congruently at *ca.* 400°C, suggesting that large crystals may be grown from a melt. Representative spectrum for Cs2AuSbS$_4$ is shown in Figure 5-13. Differential thermal analysis (DTA) data, followed by careful XRD analysis of the residues, shows that Rb$_2$Au$_6$Sb$_4$S$_{10}$ melts incongruently at *ca.* 442°C. Examination of the residue by powder XRD revealed that the compound decomposes to an amorphous material and Au metal respectively. The DTA spectra for two cycles for (III) is shown in Figure 5-14.

Table 5-6.   Selected Distances (Å) and Angles (deg) for Rb_2AuSbS_4 with (I) Estimated Standard Deviations in Parentheses [a].

Sb(1)-S(1)	2.314(9)	S(2)-Au(1)-S(2')	179.9(4)
Sb(1)-S(2)	2.334(7) x2		
Sb(1)-S(3)	2.30(1)	Au(1)-S(3)-Sb(1)	100.7(3)
Sb(1)-S(mean)	2.32(1)		
		S(1)-Sb(1)-S(2)	103.6(2)
Au(1)-S(2)	2.293(7)	S(1)-Sb(1)-S(2')	103.6(2)
Au(1)-S(2')	2.293(7)	S(1)-Sb(1)-S(3)	115.6(4)
		S(2)-Sb(1)-S(2')	109.0(4)
Au(1)-Au(1')	3.598(2)	S(2)-Sb(1)-S(3)	112.1(2)
		S(2)-Sb(1)-S(3')	112.1(2)
		S-Sb-S (mean)	109(2)
Rb(1)-S(1)	3.662(3) x2	Rb(2)-S(1)	3.40(1)
Rb(1)-S(1')	3.43(1)	Rb(2)-S(2)	3.869(8) x2
Rb(1)-S(1")	3.40(1)	Rb(2)-S(2')	3.858(8) x2
Rb(1)-S(2)	3.488(7) x2	Rb(2)-S(3)	3.602(2) x2
Rb(1)-S(2')	3.782(8) x2	Rb(2)-S(3')	3.37(1)
Rb(1)-S(3)	3.34(1)	Rb(2)-S (mean)	3.67(7)
Rb(1)-S (mean)	3.55(5)		

[a]The estimated standard deviations in the mean bond lengths and the mean bond angles are calculated by the equation $\sigma l = \{\Sigma_n(l_n - l)^2/n(n-1)\}^{1/2}$, where l_n is the length (or angle) of the nth bond, l the mean mength (or angle), and n the number of bonds.

Table 5-7. Selected Distances (Å) and Angles (deg) for $Rb_2Au_6Sb_4S_{10}$ (III) with Standard Deviations in Parentheses.

Au(1) - S(3)	2.32(1)	Sb(1) - S(6)	2.43(2)
Au(1) - S(5)	2.30(1)	Sb(1) - S(8)	2.47(1) x2
Au(2) - S(2)	2.28(2)	Sb(2) - S(5)	2.54(2)
Au(2) - S(4)	2.30(2)	Sb(2) - S(1)	2.48(1) x2
Au(3) - S(3)	2.32(1)	Sb(3) - S(6)	2.58(2)
Au(3) - S(7)	2.31(1)	Sb(3) - S(1)	2.48(1) x2
Au(4) - S(3)	2.29(2)	Sb(4) - S(4)	2.40(2)
Au(4) - S(7)	2.30(2)	Sb(4) - S(8)	2.47(1) x2

Au(1) - Au(3)	3.192(3)	Au(1) - Sb(1)	3.393(5)
Au(1) - Au(4)	3.060(4)	Au(1) - Sb(3)	3.233(5)
Au(2) - Au(4)	3.09(1)	Au(2) - Sb(2)	3.090(6)
Au(1)-Au(1')	3.589(4)		
Au(1')-Au(3')	3.461(5)		
Au(3)-Au(3')	3.461(5)		

S(2)-Au(1)-S(5)	170.9(7)	S(1)-Sb(3)-S(1')	89.4(7)
S(2)-Au(2)-S(4)	173.9(8)	S(1)-Sb(3)-S(6)	95.6(5)
S(3)-Au(3)-S(7)	178.4(7)	S(1')-Sb(3)-S(6)	95.6(5)
S(3)-Au(4)-S(7)	170.0(8)		

(A)
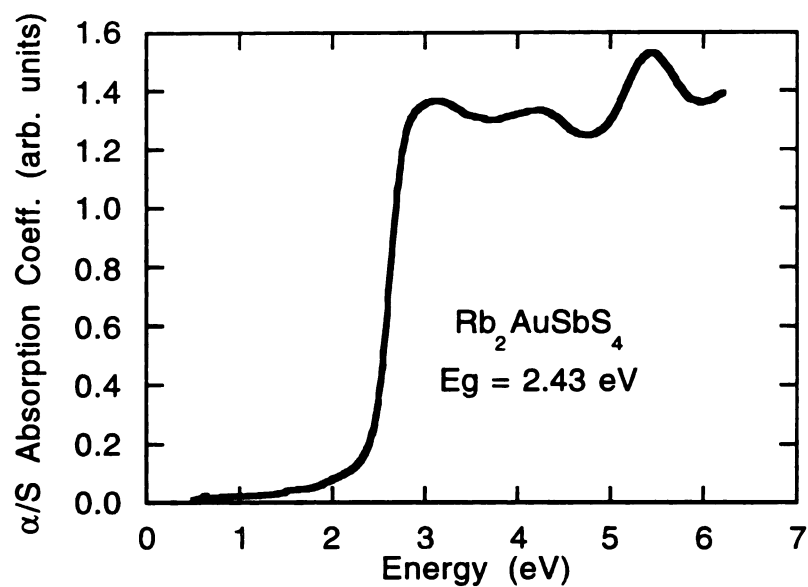
(B)
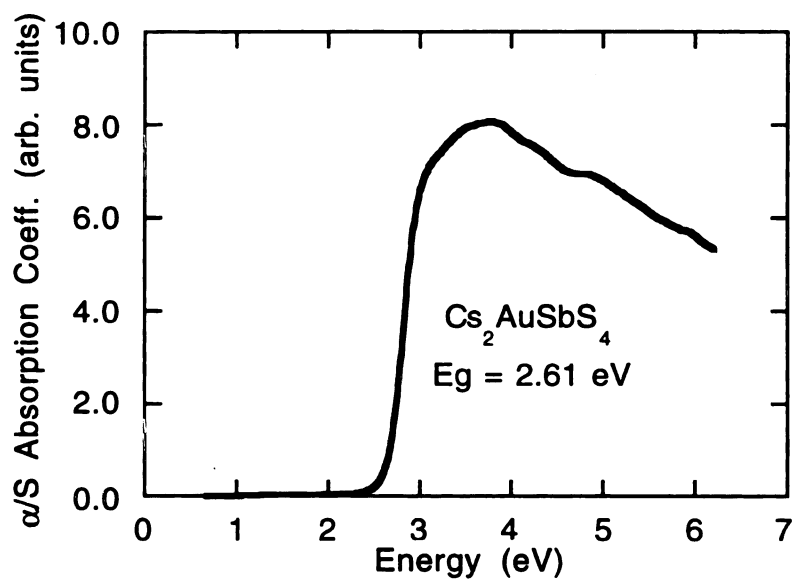
Figure 5-10:   Solid-state optical absorption spectra for Rb_2AuSbS_4 (I) and Cs_2AuSbS_4 (II).
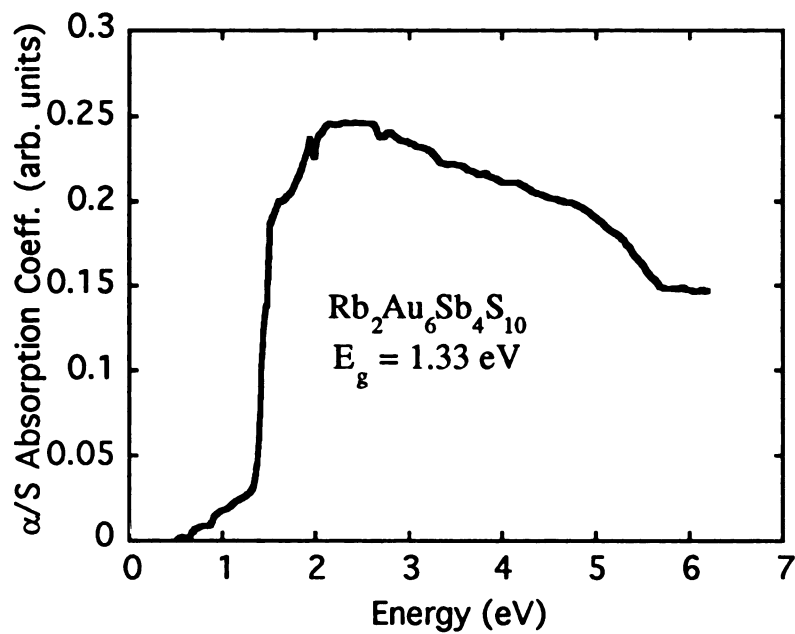
Figure 5-11:　Solid-state optical absorption spectrum for $Rb_2Au_6Sb_4S_{10}$ (III).

(A)
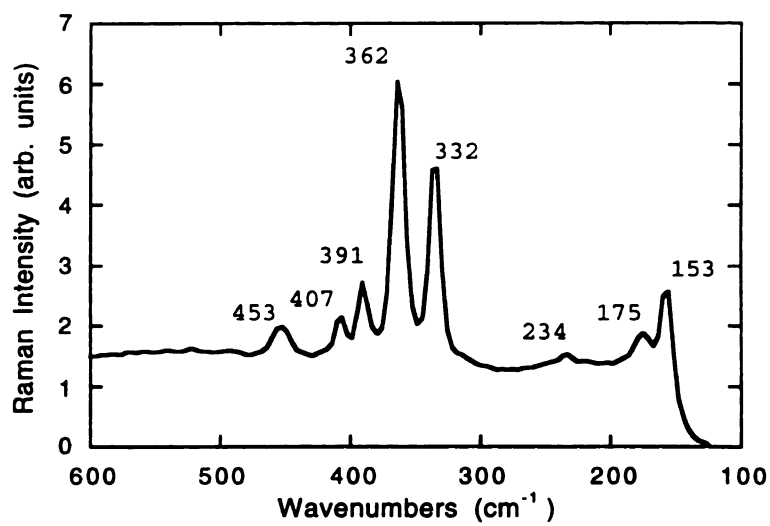
(B)
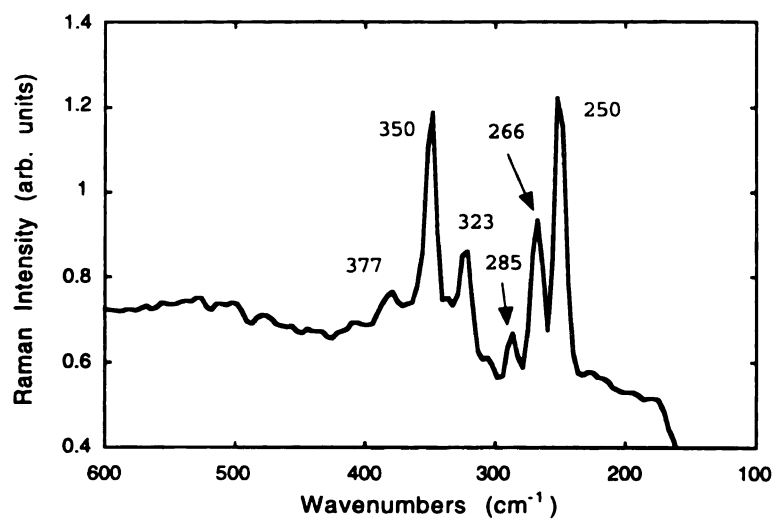
Figure 5-12: Raman spectra of Rb_2AuSbS_4 (I) and $Rb_2Au_6Sb_4S_{10}$ (III).
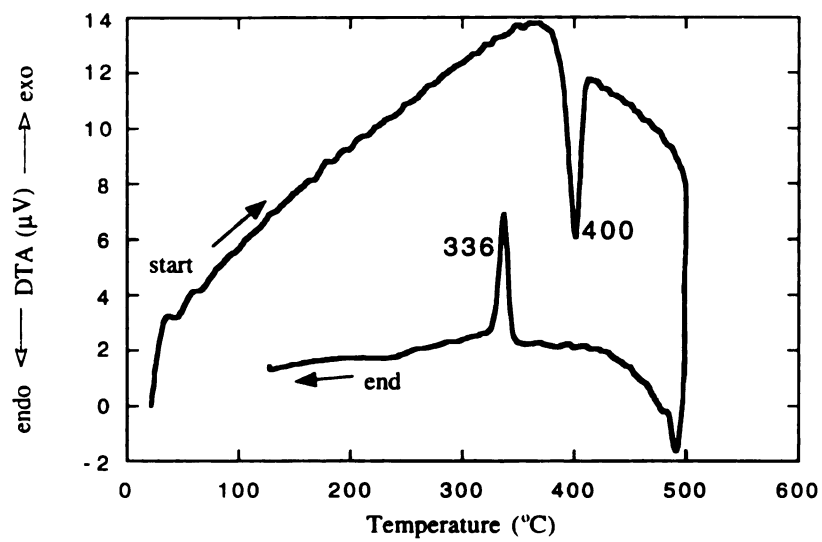
Figure 5-13:   DTA diagram for Cs_2AuSbS_4 (II).
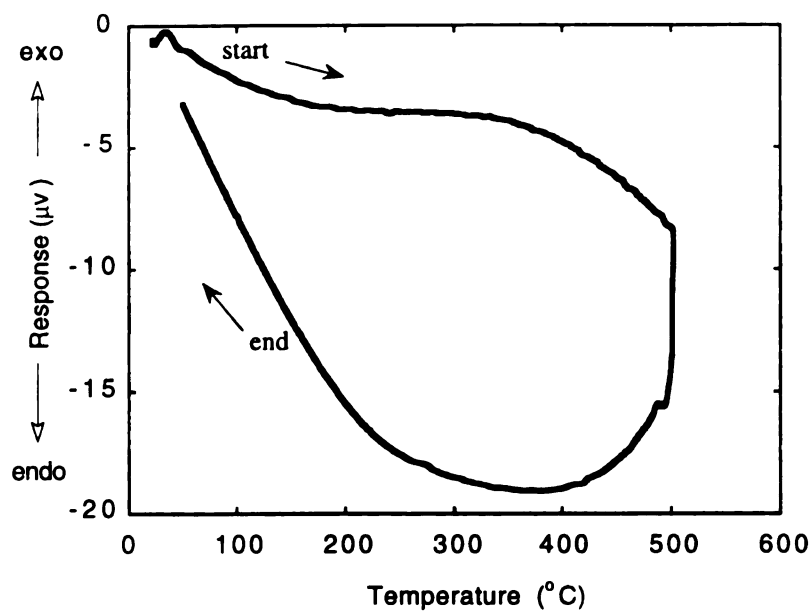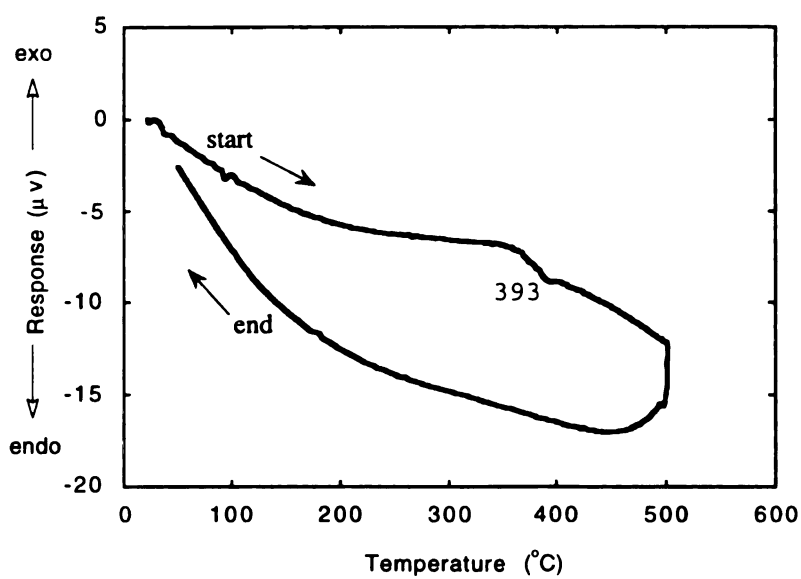
Figure 5-14: Two cycles for DTA diagrams for $Rb_2Au_6Sb_4S_{10}$ (III).

4. Conclusions

In summary, these new members of the A/Au/Sb/S family emphasize the value of the thioantimonate variation in the flux method. These fluxes provided a convenient entry into the previously unknown gold chemistry, and the potential exists that more quaternary and possibly the unknown ternary Au/Sb/Q (Q = S, Se) compounds[26] may yet be discovered. $Rb_2Au_6Sb_4S_{10}$ represents the first example of a sulfosalt with two different interpenetrating anionic frameworks.

228

List of References

1) McCarthy, T. J.; Kanatzidis, M. G. *Inorg. Chem.* **1994**, *33*, 1205.

2) Choi, K.-S.; Iordanidis, L.; Chondroudis, K.; Kanatzidis, M. G. *Inorg. Chem.*, **1997**, *34*, 1234.

3. (a) Hanko, J. A.; Kanatzidis, M. G. Abstract #0413 from 210th Fall ACS Meeting, Chicago IL **1995**.

4. (a) Schimek, G. L.; Pennigton, T. L.; Wood, P. T.; Kolis, J. W. J. Solid State Chem. **1996**, *123*, 272. (b) Wood, P. T.; Schimek, G. L.; Kolis, J. W. *Chem. Mater.*, **1996**, *8*, 721.

5. Hanko, J. A.; Kanatzidis, M.G. *in preparation*.

6. Imafuku, M.; Nakai, I.; Nagashima, K. *Mat. Res. Bull.* **1986**, *21*, 493.

7. For example see: (a) Cordier, G.; Schäfer, H. *Rev. Chem. Min.*, **1981**, *18*, 218. (b) Dorrscheidt, W.; Schäfer, H. *Z. Naturforsch.*, **1981**, *36b*, 410. (c) Cordier, G.; Schwidetzky, C.; Schäfer, H. *Rev. Chem. Min.*, **1982**, *19*, 179.

8. (a) Sheldrick, W.; Wachhold, M. Submitted for publication. (b) Drake, G. W.; Kolis, J. W. *Coord. Chem. Rev.*, **1994**, *137*, 131.

9. Garin, J.; Parthe, E.; Oswald, H.R.; *Acta Crystallogr.*, **1972**, *B28*, 3672.

10. Edenharter, A.; Nowacki, W.; Takeuchi, Y.; Z. *Kristallogr.*, **1970**, *131*, 397.

11. Ito, T.; Nowacki, W.; Z. *Kristallogr.*, **1974**, *139*, 85.

12. Wuensch, B. J. Z. *Kristallogr.*, **1964**, *119*, 437.

13. Park, Y.; Kanatzidis, M. G. *J. Alloys Compd.*, **1997**, *257*, 137.

14. (a) Klepp, K. O.; Weithhaler, C. *J. Alloys Comp.*, **1996**, *243*, 1. (b) Klepp, K. O.; Weithhaler, C. *J. Alloys Comp.*, **1996**, *243*, 12. (c) Bronger, W.; Kathage, H. U. *J. Alloys Comp.*, **1992**, *184*, 87. (d) K. O. Klepp, W. Bronger, *J. Less-Common Met.*, **1987**, *127*, 65. (e) Klepp, K. O.; Bronger, W. *J. Less-Common Met.*, **1987**, *132*, 173. (f) Klepp, K. O.; Bronger, W. *J. Less-Common Met.*, **1988**, *137*, 13. (g) Klepp, K. O.; Brunnbauer, G. *J. Alloys Comp.*, **1992**, *183*, 252.

15. Kim, K.- W.; Kanatzidis, M. G. *J. Am. Chem. Soc.*, **1992**, *114*, 4878.

16. Chondroudis, K.; Hanko, J.A.; Kanatzidis, M.G. *Inorg. Chem.*, **1997**, *36*, 2623.

17. CERIUS^2, Version 1.6, Molecular Simulations Inc., Cambridge, England, **1994**.

18. McCarthy, T. J.; Ngeyi, S.-P.; Liao J.-H.; DeGroot, D.; Hogan, T.; Kannewurf, C. R.; Kanatzidis, M. G. *Chem. Mater.*, **1993**, *5*, 331.

19. (a) Sheldrick, G. M. In *Crystallographic Computing* 3; Sheldrick, G.M., Kruger, C., Doddard, R., Eds.; Ocxford University Press: Oxford. England, 1985; pp 175-

189. (b) *TEXSAN: Single Crystal Structure Analysis Software*, Version 5.0; Molecular Structure Copr.; The Woodlands, TX 77381, **1981**.

20. Walker, N., Stuart, D. *Acta Crystallogr.* **1983**, *A39*, 158.

21 SMART and SAINT. Data collection and Processing Software for the Smart system. Siemens Analytical X-ray Instruments Inc.,**1995**.

22. Blessing , R. H. *Acta Crystallogr.* **1995**, *A51*, 33.

23. SHELXTL Version 5, Reference Manual. Siemens Industrial Automation Inc., **1994**.

24. Kanatzidis, M. G. *Phosphorous, Sulfur, and Silicon*, **1994**, *93-94*, 159.

25. McCarthy, T. J.; Kanatzidis M.G. *Inorg. Chem.*, **1995**, *34*, 1257.

26. Hanko, J. A.; Kanatzidis, M.G. *Work in Progress*.

27. Siebert, H. Z *Anorg. Allg. Chem.*, **1954**, *275*, 225.

CHAPTER 6

$A_2CuP_3S_9$ (A = K, Rb), $Cs_2Cu_2P_2S_6$, and $K_3CuP_2S_7$: New Phases from the Dissolution of Copper in Molten Polythiophosphate Fluxes.

1. Introduction

The recent activity in the application of chalcophosphate fluxes has uncovered a multitude of new materials with elaborate structure types arising from a variety new binding modes displayed by the $[P_xQ_y]_n^{n-}$ (Q = S, Se) units. An interesting trend, which has become evident from this work, is that the $[P_xSe_y]_n^{n-}$ species behave very differently than the corresponding $[P_xS_y]_n^{n-}$ species. This trend is manifested in not only in how the $[P_xQ_y]_n^{n-}$ (Q = S, Se) species bind to metal ions but also with respect to their relative stability. For example the tetrahedral $[PQ_4]^{3-}$ (Q = S, Se) unit, typically does not lead to the same structure types when they form compounds with the same formula. In fact, they do not give compounds with the same formula. This phenomenon is reminiscent of the similar differences previously observed between the polychalcogenide S_n^{2-} and Se_n^{2-} species.[2] Furthermore, the analogous synthetic conditions which may give rise to a certain $[P_xSe_y]_n^{2-}$ unit tend to give rise to a different $[P_xS_y]_n^{2-}$ unit, often the anions differing in the oxidation state of the phosphorous atom.[3] The latter is the consequence of the difference in the electronegativity between the S and Se atoms. These facts underscore the need for the simultaneous exploration of both the thiophosphate and selenophosphate fluxes for the same metal system, and the continued search for fundamental differences in the chemistry and reactivity.

The polychalcophosphate fluxes form by the *in situ* fusion of $A_2Q/P_2Q_5/Q$ (A = K, Rb, Cs; Q = S, Se) and contain various $[P_xQ_y]^{n-}$ units available for reaction with metal ions. Typically, this type of coordination chemistry leads anionic frameworks stabilized by alkali metal cations. The generality of this method has been demonstrated by the ability to incorporate main group[4], transition[5], lanthanide, and actinide[5e,6] metals into solid state chalcophosptate compounds. The highly basic nature of the fluxes permits the suppression of the highly stable $M_2P_2Q_6$ (Q = S, Se) phases. The $M_2P_2Q_6$ (Q = S, Se) structure type is related to that of CdI_2,[7,8] and it projects alternating, octahedrally coordinated, metal ions

and the ethane-like $[P_2Q_6]^{4-}$ (Q = S, Se) units. Some compounds possess interesting magnetic[9] and intercalation chemistry,[10] while others have been studied intensively as potential candidates for cathode materials in secondary lithium batteries.[11] Substitution on the divalent metal cations by monovalent coinage metal cations results in $M'_4P_2Q_6$ (e.g. M' = Ag, Q = S; M' = Cu, Q = Se),[12] whose structure retains the same $M_2P_2Q_6$ structural motif, but now each octahedral metal site is replaced by two M'^+ ions with trigonal planar coordination. The two divalent metal ions can also be replaced by a monovalent coinage and a trivalent main group metal ion to give $M'M''P_2Q_6$, again retaining the overall $M_2P_2Q_6$ structure type[13].

Based on the limited body of work in the multinary copper chalcophosphate systems, a rare example is the ternary Cu_3PQ_4 (Q = S^{14a}, Se^{14b}), we became interested in applying the alkali thiophosphate flux approach to these systems. The reaction of the coinage metals with polychalcophosphate fluxes has already resulted in a number of unusual compounds; examples include $Cs_2M_2P_2Se_6$ (M = Cu, Ag)[5a], $A_3AuP_2Se_8$ (A = K, Rb, Cs),[3] $A_2Au_2P_2Se_6$ (M = Rb, Cs),[3] $K_3Ag_3P_3Se_9$,[5a] $K_3Cu_3P_3Se_9$,[5e] $K_2Cu_2P_4Se_{10}$,[5f] A_2AuPS_4 (A = K, Rb, Cs),[3] $AAuP_2S_7$ (A = K, Rb)[3] and reciently $KAu_5P_2S_8$.[15] An interesting counterion effect exists in the $A_3Ag_3P_3Se_9$ system. The large Cs^+ counterion, gives $[M_2P_2Se_6]_n^{2n-}$ (M = Cu, Ag) consisting of infinite chains of alternating $[P_2Se_6]^{4-}$ units and M_2^{2+} dimers. Upon moving to the smaller K^+ cation, the $K_3Ag_3P_3Se_9$ (M = Cu^{5e}, Ag^{5a}) adopts a three-dimensional structure comprised of ethane-like $[P_2Se_6]^{4-}$ units and tetrahedral Cu^+ or Ag^+ ions in a complex but elegant bonding scheme. Although one might think that the thiophosphate and selenophosphate systems would produce isostructural compounds, the gold chalcophosphates[3] provide an excellent example of how chemically divergent the chemistry of two systems can be. The chemistry of copper presents similar differences between the sulfur and selenium systems. Here, we report the synthesis, structure spectroscopic and thermal properties of the quaternary copper thiophosphate compounds, $A_2CuP_3S_9$ (A = K, Rb), $Cu_2Cu_2P_2S_6$ and $K_3CuP_2S_7$. While

the selenide analog of $Cu_2Cu_2P_2S_6$ has already been reported, the selenide analogs for $A_2CuP_3S_9$ (A = K, Rb) and $K_3CuP_2S_7$ are still unknown and it seems unlikely that they would be stable. The $K_2CuP_3S_9$ features the unprecedented cyclic $[P_3S_9]^{3-}$ anion. The results of the band structure calculation for this compound will also be discussed.

2. Experimental Section

2.1. Reagents

The reagents mentioned in this study were used as obtained unless noted otherwise: (i) Cu metal powder electrochemical dust, Fisher Chemical Co., Pittsburgh, PA; (ii) phosphorous pentasulfide (P_2S_5) 99.999% purity, Aldrich Chemical Co., Milwaukee, WI.; (iii) Cesium metal, analytical reagent, Johnson Matthey/AESAR Group, Seabrook, NH; (iv) Rubidium metal, analytical reagent, Johnson Matthey/AESAR Group, Seabrook, NH; (v) Potassium metal, analytical reagent, Aldrich Chemical Co., Milwaukee, WI.; (vi) Sulfur powder, sublimed, J.T. Baker Chemical Co., Phillipsburg, NJ; (vii) Methanol (MeOH) ACS anhydrous, EM Science, Inc., Gibbstown, NJ. (viii) Diethyl ether, ACS anhydrous, EM Science, Inc., Gibbstown, NJ.

2.2. Syntheses.

A_2S (A = K, Rb, Cs) were prepared by reacting stoichiometric amounts of the elements in liquid ammonia as described in Chapter 2, Section 2.2.

Preparation of $K_2CuP_3S_9$ (I). An amount of 0.032g (0.50 mmole) Cu, 0.333g (1.50 mmole) P_2S_5 and 0.110g (1 mmole) K_2S was thoroughly mixed and sealed

under vacuum a Pyrex tube. The reaction was heated to 550°C in 15 hours in a computer controlled furnace. It was isothermed at 550°C for 4 days, cooled to 150°C at a rate of 4°C/hr, and then cooled to room temperature in 10 hours. The excess $K_x[P_yS_z]$ flux was removed by washing with degassed methanol under inert atmosphere revealing yellow crystals (75% yield based on Cu). The yellow crystals are stable in air for several months but decompose in the presence of water. The product is occasionally contaminated with brown-orange crystals of Cu_3PS_4 and/or an intractable black powder.

Preparation of $Rb_2CuP_3S_9$ (II): An amount of 0.032g (0.50 mmole) Cu, 0.220g (1 mmole) P_2S_5 and 0.203g (1 mmole) Rb_2S was sealed under vacuum in a Pyrex tube and heated as in (I). The product, which is stable in air but decompose in the presence of water, was isolated as in (I) to give yellow crystals (52% yield based on Cu).

Preparation of $Cs_2Cu_2P_2S_6$ (III): An amount of 0.032g Cu (0.50 mmole), 0.330g P_2S_5 (1.50 mmole) and 0.298g Cs_2S (1 mmole) was sealed under vacuum in a Pyrex tube and heated as in (I). The product was isolated as in (I) to give a mixture of dark violet and yellow crystals. The mixture was quickly washed with degassed water to give dark violet crystals in approximately 50% yield based on Cu. The resulting dark violet crystals are stable in air and water.

Preparation of $K_3CuP_2S_7$ (IV): An amount of 0.016g Cu (0.25 mmole), 0.110g P_2S_5 (0.50 mmole) , 0.550g K_2S (0.50 mmole), and 0.048g (1.5 mmole) S that was sealed under vacuum in a Pyrex tube. The reaction was heated to 500°C in 15 hours in a computer controlled furnace. It was isothermed at 500°C for 4 days, cooled to 110°C at a rate of 4°C/hr, and then cooled to room temperature in 10 hours. The product, is stable in air but decompose in water. The compound was isolated as in (I) to give transparent colorless crystals (40% yield based on Cu).

2.3. Physical Measurements.

Powder X-ray Diffraction. The compounds were examined by Powder X-ray diffraction to check for phase purity. Accurate d spacings obtained from the powder pattern for (I) were recorded on a CPS 120 INEL X-ray powder diffractometer using monochromatized radiation Cu K-L$_{III}$ (λ=1.540598Å). Accurate d spacings obtained from the powder patterns for (III) - (IV) were recorded on a Phillips XRG-3000 computer-controlled powder diffractometer with Ni filtered CuK$_\alpha$ radiation. Both diffractometers are equipped with a curved position-sensitive detector calibrated with Na$_2$Ca$_3$Al$_{12}$F$_{14}$. The calculated powder pattern for (I) was prepared with the Lazy Pulverix Program[16a]. While the calculated powder patterns for (III) - (IV) were prepared with the CERIUS^2 software.[16b] Tables of calculated and observed XRD patterns for (I), (III) and (IV) are given in Tables 6-1, 6-2, and 6-3, respectively. After crystal collection and structure refinement (*vide infra*) for (I), the final cell parameters were determined by least squares refinements made on the powder X-ray data and are given in Table 6-4.

Infrared Spectroscopy. Infrared spectra, in the far-IR region (600-50 cm^{-1}), were recorded on a computer controlled Nicolet 750 Magna-IR Series II spectrophotometer equipped with a TGS/PE detector and silicon beam splitter in 4 cm^{-1} resolution. The samples were ground with dry CsI into a fine powder and pressed into translucent pellets.

Raman Spectroscopy. Raman spectra (600-100 cm^{-1}) were recorded on a BIO-RAD FT Raman spectrometer equipped with a Spectra-Physics Topaz T10-106c 1.064 nm YAG laser and a Ge detector. Crystals of (I), - (III) were loaded without modification into glass capillary tubes. Crystals of (IV) were ground with CsI into a fine powder and loaded into a glass capillary tube.

Single Crystal Optical Transmission. Room temperature single crystal optical transmission spectra were obtained on a Hitachi U-6000 Microscopic FT Spectrophotometer mounted on an Olympus BH2-UMA metallurgical microscope over a range of 380 to 900 nm. Crystals lying on a glass slide were positioned over the light source and the transmitted light was detected from above.

Solid State UV/Vis/Near IR Spectroscopy. Optical diffuse reflectance measurements were performed at room temperature using a Shimadzu UV-3101PC double beam, double monochromator spectrophotometer. The instrument is equipped with integrating sphere and controlled by a personal computer. $BaSO_4$ was used as a 100% reflectance standard for all materials. Samples are prepared by grinding them to a fine powder and spreading them on a compacted surface of the powdered standard material, preloaded into a sample holder. The reflectance versus wavelength data generated can be used to estimate a material's band gap by converting reflectance to absorption data as described earlier.[17]

Differential Thermal Analysis (DTA). DTA experiments were performed on a computer-controlled Shimadzu DTA-50 thermal analyzer. Typically a sample (~25 mg) of ground crystalline material was sealed in quartz ampoules under vacuum. A quartz ampoule of equal mass, filled with Al_2O_3, was sealed and placed on the reference side of the detector. The sample was heated to the desired temperature at 10°C/min., then held there for 10 min. and finally cooled to 50°C at the same rate. The stability/ reproducibility of the samples were monitored by running multiple cycles. Residues of the DTA experiment were examined by X-ray powder diffraction. To evaluate congruent melting the X-ray powder diffraction patterns before and after the DTA experiments were compared.

Semiquantitative Microprobe Analyses. The analyses were performed using a JEOL JSM-6400V scanning electron microscope (SEM) equipped with a TN 5500 EDS detector. This technique was used to confirm the presence of all elements in the

compounds. Data acquisition was performed with an accelerating voltage of 20kV and twenty second accumulation time.

Electronic structure calculations. The band structure was calculated using density functional theory with the local density approximation. The one-electron Shrödinger equation was solved self consistently using the tight-binding (TB) linear muffin-tin orbital (LMTO) method in the atomic spheres approximation (ASA), including the combined correction.[18] This method splits the crystal space into overlapping atomic spheres (Wigner-Seitz spheres), whose radii are chosen to completely fill the crystal volume. In the present calculation, 29 additional empty spheres (E) had to be included to model the interstitial space. We allowed an overlap of 15% for the atoms centered spheres, 20% for the interstitial spheres with atomic ones, and 25% between empty spheres. A summary of the sphere radii used in our calculation is in reference (19). All reciprocal space integrations were performed with the tetrahedron method[20] using 128 k-points within the irreducible Brillouin zone. The basis sets consisted of 4s, 4p and 3d orbitals for Cu, 3s and 3p orbitals for P and S, and 4s orbitals for K. The 3d orbitals for P and S, the 4p and 3d orbitals for K and E (empty spheres) p-d states were downfolded using the Lowdin's technique.[20]

Single crystal X-Ray Crystallography. Intensity data for (I) were collected using a STOE Image Plate X-Ray diffractometer for room temperature data collection. The data was collected as a series of diffraction patterns recorded by rotating a randomly oriented crystal in the X-ray beam. Images were recorded over the range $\phi = 0.0°$ to $200.2°$ with a $0.7°$ increment angle and a 4 minute irradiation per image. Cell parameters were determined from a least square analysis of the setting angles of 5000 reflections in the $3.8° = 2\theta = 56.3°$ domain and led to the parameters $a = 6.8307(3)$Å, $b = 23.565(1)$Å, $c = 9.5398(5)$Å, $\beta = 100.213(5)°$. The reflection intensities were recorded in the $-18 \leq h \leq 18$, $-8 \leq k \leq 8$, and $-11 \leq l \leq 11$ space. After the Lorentz polarization correction of the 10692 raw data, a set of 4032 reflections with $I \leq 3\sigma(I)$ was used. A data analysis indicated a 2/m Laue

symmetry with limiting conditions consistent with the P2$_1$/n space group. The structure was then solved from direct methods using the SHELXTL program[21a] and refined using the JANA'96[21b] software package. Conventional atomic and anomalous scattering factors were taken from the usual sources. The atomic parameters and the scale factor were refined in a full matrix mode minimizing the function $wR=[\Sigma w(|F_o|-|F_c|)^2/\Sigma wF_o^2]^{1/2}$. A weighting scheme based on $\sigma(F_o)$ corrected with an instability coefficient was used. No anharmonic refinement was needed to account for the behavior of the Cu atom[22].

Intensity data for (III), and (IV) were collected using a Rigaku AFC6S four-circle automated diffractometer equipped with a graphite crystal monochromator. Unique data for (III) - (IV) were collected out to 50° in 2θ. Crystal stability was monitored with three standard reflections whose intensities were checked every 150 reflections. No crystal decay was detected for either (III) - (IV). The space groups were determined from systematic absences and intensity statistics. An empirical absorption correction based on ψ scans was applied to both data sets. An empirical DIFABS correction[23] was applied after full isotropic refinement, following which full anisotropic refinement was performed. The structures of (III) - (IV) were solved by direct methods using SHELXS-86 software[24a], and refined with full matrix least squares techniques using the TEXSAN software package[24b].

The complete data collection parameters and details of the structure solution and refinement for (I), (III), and (IV) are given in Table 6-4. The coordinates of all atoms, average temperature factors, and their estimated standard deviations are given in Tables 6-5 to 6-7.

Table 6-1. Calculated and Observed X-ray Powder Patterns for $K_2CuP_3S_9$ (I).

h	k	l	d_{calc}	d_{obs}	I_{obs} (%)
0	2	1	7.344	7.335	99
1	0	-1	5.995	6.000	17
0	4	0	5.891	5.887	19
1	2	0	5.840	5.837	65
1	0	1	5.058	5.054	3
1	1	1	4.945	4.944	8
0	0	2	4.695	4.693	14
1	4	0	4.431	4.432	7
0	2	2	4.361	4.363	9
1	3	1	4.252	4.254	9
0	5	1	4.212	4.207	6
1	4	-1	4.202	4.207	6
0	3	2	4.030	4.029	27
-1	2	2	3.971	3.971	11
0	6	0	3.927	3.929	50
1	4	1	3.837	3.840	7
0	4	2	3.671	3.675	4
0	6	1	3.623	3.624	4
1	5	1	3.445	3.445	2
1	2	2	3.411	3.411	2
2	1	-1	3.327	3.325	16
1	3	2	3.245	3.246	5
2	2	-1	3.232	3.232	25
-1	5	2	3.143	3.146	9
0	1	3	3.103	3.101	11
0	2	3	3.025	3.024	15
2	0	-2	2.997	2.996	11
2	1	1	2.976	2.978	9
0	8	0	2.945	2.946	50
0	3	3	2.907	2.906	10
1	5	2	2.842	2.843	3
2	3	1	2.803	2.802	72

0	4	3	2.764	2.764	37
0	7	2	2.736	2.735	7
1	8	0	2.698	2.698	11
2	4	1	2.674	2.674	20
1	0	3	2.662	2.664	9
0	5	3	2.607	2.609	4
2	5	-2	2.529	2.529	3
2	1	2	2.514	2.515	4
-2	2	3	2.470	2.470	9
0	6	3	2.448	2.449	4
2	7	0	2.379	2.380	12
0	10	0	2.357	2.356	16
0	1	4	2.336	2.337	6
-2	4	3	2.321	2.321	6
3	0	-1	2.273	2.275	2
0	3	4	2.249	2.249	4
2	5	2	2.228	2.228	5
1	6	3	2.204	2.204	3
-1	4	4	2.183	2.182	2
3	4	-1	2.121	2.121	2
-2	1	4	2.100	2.101	12
1	2	4	2.070	2.072	8
3	3	1	2.027	2.026	2
0	9	3	2.008	2.008	6
2	9	1	1.9727	1.9727	7
1	10	2	1.9654	1.9655	3
-1	7	4	1.9269	1.9265	7
2	5	3	1.9267	1.9265	7
0	10	3	1.8824	1.8825	7
2	10	-2	1.8524	1.8525	16
1	12	1	1.8304	1.8298	3
0	12	2	1.8115	1.8112	2
3	4	2	1.8047	1.8043	2
2	0	4	1.7817	1.7819	12
-2	1	5	1.7747	1.7742	12
0	11	3	1.7677	1.7682	10

2	11	1	1.7434	1.7437	4
3	9	0	1.7027	1.7029	6
2	12	-1	1.6954	1.6947	2
4	1	0	1.6768	1.6763	12
1	11	3	1.6689	1.6687	2
0	12	3	1.6633	1.6633	6
2	12	-2	1.6425	1.6427	3
2	11	2	1.6345	1.6347	4
3	10	0	1.6240	1.6235	2
1	13	2	1.6155	1.6152	1
3	1	-5	1.5813	1.5816	10
0	13	3	1.5685	1.5689	10
2	13	1	1.5514	1.5513	10
0	3	6	1.5348	1.5349	1
4	7	-1	1.5233	1.5234	9
2	2	5	1.5152	1.5148	5
2	4	-6	1.4776	1.4774	1
0	16	0	1.4727	1.4728	5
-2	14	-1	1.4679	1.4681	3
1	9	5	1.4438	1.4434	1
0	13	4	1.4346	1.4344	1
1	14	3	1.4226	1.4226	3
4	9	-2	1.4141	1.4144	4
-2	13	4	1.3745	1.3745	1
4	7	2	1.3703	1.3703	4
0	14	4	1.3678	1.3677	2
3	9	-5	1.3558	1.3556	4

Table 6-2. Calculated and Observed X-ray Powder Patterns for $Cs_2Cu_2P_2S_6$ (III).

hkl	d_{calc}, Å	d_{obsd}, Å	I/I_{max}(obsd)
100	6.67	6.62	17
020	6.39	5.80	11
111	5.54	5.65	5
012	4.70	4.76	13
$11\bar{2}$	4.62		
121	4.43	4.45	7
210	4.35	4.35	8
031 $12\bar{2}$ $20\bar{2}$	3.92	3.90	18
$13\bar{1}$ $21\bar{2}$	3.74	3.73	30
131	3.50	3.50	29
$22\bar{2}$ $11\bar{3}$	3.33	3.36	10
221	3.31	3.31	17
$13\bar{2}$ 040	3.23	3.23	100
040	3.19	3.18	20
202	3.07	3.07	12
$12\bar{3}$ 140 $21\bar{3}$	3.02	3.01	13
023	2.98	2.97	1
132	2.93		
$32\bar{1}$ 141	2.83	2.84	22
222	2.77	2.77	4
311	2.71	2.74	4
123 $1\bar{3}\bar{3}$	2.68	2.67	3
$24\bar{1}$ 240	2.63	2.62	3
$31\bar{3}$ 004	2.53	2.53	3
$24\bar{2}$	2.47	2.45	3
$15\bar{1}$ 133 213	2.42	2.41	14
024	2.35	2.35	10
104 223 $41\bar{2}$ 052	2.28	2.27	5
$34\bar{1}$	2.25	2.22	21
420	2.17	2.16	4
061	2.08	2.07	11
053	2.039	2.046	5
$40\bar{4}$ $22\bar{5}$	1.95	1.94	2
$26\bar{2}$	1.872	1.863	4
126	1.830	1.826	14

Table 6-3. Calculated and Observed X-ray Powder Patterns for $K_3CuP_2S_7$ (IV).

hkl	d_{calc}, Å	d_{obsd}, Å	I/I_{max}(obsd)
002	7.48	7.65	90
$20\bar{1}$	6.48	6.40	5
011	6.11	6.23	2
110	5.95	5.82	8
201	5.64	5.70	11
111	5.40	5.44	2
$20\bar{2}$	5.31	5.32	11
012 003	4.99	5.01	100
$21\bar{1}$	4.59	4.60	10
112	4.50	4.52	10
$20\bar{3}$	4.27	4.28	11
$21\bar{2}$	4.1636	4.06	6
013	4.00	4.00	9
212	3.77	3.86	46
004	3.741	3.744	24
$31\bar{2}$ 311	3.44	3.45	23
020	3.35	3.34	8
$11\bar{4}$ 021	3.271	3.270	11
120 400	3.240	3.224	29
$12\bar{1}$ $40\bar{2}$ 121	3.146	3.162	24
312	3.115	3.112	15
401	3.073	3.062	41
022 204	3.058	3.060	41
005	2.993	2.993	28
220 $22\bar{1}$	2.595	2.960	13
$20\bar{5}$	2.889	2.888	56
$41\bar{2}$	2.852	2.850	7
411	2.792	2.786	6
015	2.733	2.734	3
222	2.702	2.702	2
$41\bar{3}$	2.682	2.689	2
320 $22\bar{3}$	2.638	2.632	51
115 412	2.600	2.598	6
$12\bar{4}$ 006	2.498	2.493	39
$32\bar{3}$	2.434	2.425	7
$40\bar{5}$ 413	2.380	2.374	12
$42\bar{1}$	2.340	2.358	2
$51\bar{3}$ $42\bar{2}$	2.296	2.289	4
116 025	2.232	2.246	2
206 031	2.209	2.215	27
$51\bar{4}$	2.175	2.172	1

422 032	2.140	2.140	6
230 216 60$\overline{3}$	2.112	2.112	6
42$\overline{4}$	2.081	2.083	2
11$\overline{7}$	2.08	2.057	5
133	1.995	1.994	2
22$\overline{6}$ 117	1.969	1.964	2
514 233 32$\overline{6}$	1.911	1.906	6
51$\overline{6}$ 008	1.873	1.874	6

Table 6-4. Crystallographic data for $K_3CuP_3S_9$, $Cs_2Cu_2P_2S_6$, and $K_3CuP_2S_7$.

	I	III	IV
Formula	$K_3CuP_3S_9$	$Cs_2Cu_2P_2S_6$	$K_3CuP_2S_7$
FW	523.20	647.21	467.21
a, Å	6.8331 (6)	9.538 (3)	13.113 (6)
b, Å	23.562 (2)	12.793 (4) Å	6.702 (9)
c, Å	9.5415 (7)	10.429 (2) Å	15.141 (8)
α (deg)	90.00	90.00	90.00
β (deg)	100.242 (7)	103.76 (2)°	98.71 (4)
γ (deg)	90.00	90.00	90.00
Z, V(Å^3)	4; 1151.8(7)	4; 1236.1 (7)	4; 1315 (2)
(λ), Å	0.71069	0.71069	0.71069
space group	$P2_1/n$ (No.14)	$P2_1/c$ (No.14)	$P2_1/a$ (No.14)
D_{calc}, g/cm^3	2.298	3.478	2.359
μ, cm^{-1}	35.2	10.46	39.16
2θ max, deg	56.3	40	50
Temp, °C	23	23	23
Final R/R_w,[a] %	3.4/3.6	2.3/2.8	4.1/3.7

[a]$R = \Sigma(|F_o| - |F_c|)/\Sigma|F_o|$, $R_w = \{\Sigma w(|F_o| - |F_c|)^2/\Sigma w|F_o|^2\}^{1/2}$.

Table 6-5.   Fractional coordinates and equivalent isotropic atomic displacement parameters of $K_2CuP_3S_9$.

Atom	x	y	z	U_{eq} (Å^2)
Cu	0.5680(2)	0.10816(4)	0.3090(1)	2.82(3)
P(1)	0.0638(3)	0.09784(8)	0.3424(2)	1.95(6)
P(2)	0.8170(3)	0.22278(8)	0.2188(2)	2.22(6)
P(3)	0.7605(3)	0.10134(9)	0.0083(2)	2.21(6)
S(1)	0.5812(3)	0.20591(8)	0.3076(2)	2.96(7)
S(2)	0.3344(3)	0.07180(9)	0.4305(2)	2.56(6)
S(3)	0.8552(3)	0.07125(8)	0.4477(2)	2.44(6)
S(4)	0.5203(3)	0.07496(9)	0.0784(2)	3.04(7)
S(5)	0.2202(4)	0.92047(9)	0.1886(2)	3.30(7)
S(6)	0.0275(3)	0.06800(8)	0.1301(2)	2.49(6)
S(7)	0.0840(3)	0.18772(8)	0.3359(2)	2.43(6)
S(8)	0.7991(3)	0.19013(8)	0.0110(2)	2.83(7)
S(9)	0.8756(3)	0.30300(8)	0.1970(2)	3.28(7)
K(1)	0.1718(4)	0.80449(9)	0.3710(2)	4.59(8)
K(2)	0.2324(4)	0.54614(9)	0.7398(2)	4.86(8)

$U(_{eq})$ is defined as one third pf the trace of the orthogonalized U_{ij} tensor.

Table 6-6. Atomic coordinates (x 10^4) and equivalent isotropic displacement parameters ($\mathring{A}^2$ x 10^3) for $Cs_2Cu_2P_2S_6$.

atom	x	y	z	U(eq)
Cu(1)	5170(2)	8992(1)	5418(2)	29(1)
Cu(2)	10514(2)	9532(1)	9032(2)	27(1)
P(1)	7820(4)	10377(2)	6670(3)	16(1)
P(2)	12858(4)	1.0412(2)	1.1653(3)	15(1)
S(2)	9921(4)	10755(2)	7360(3)	21(1)
S(3)	12797(4)	9310(3)	10226(3)	21(1)
S(4)	8608(4)	8424(3)	0.8917(3)	2.1(1)
S(5)	7466(4)	9300(3)	5200(3)	25(1)
S(6)	5112(4)	9048(3)	7616(3)	22(1)
S(7)	6604(4)	11692(2)	6203(3)	22(1)
Cs(1)	1118(1)	6828(1)	1190(1)	28(1)
Cs(2)	6380(1)	6518(1)	6720(1)	29(1)

U(eq) is defined as one third pf the trace of the orthogonalized U_{ij} tensor.

Table 6-7.   Atomic coordinates (x 10⁴) and equivalent isotropic displacement parameters

(Å² x 10³) for K₃CuP₂S₇

atom	x	y	z	U$_{(eq)}$
Cu(1)	674(1)	223(3)	8046(1)	31(1)
P(1)	1134(2)	5007(5)	8380(2)	20(1)
P(2)	1676(2)	-2404(5)	6459(2)	21(1)
S(1)	17(2)	3024(5)	8600(2)	25(1)
S(2)	838(2)	5184(5)	6938(2)	22(1)
S(3)	921(3)	0.0196(5)	0.6625(2)	28(1)
S(4)	861(3)	-2377(5)	8974(2)	29(1)
S(5)	3138(2)	-0.2368(5)	7070(2)	28(1)
S(6)	2534(2)	3927(6)	8812(2)	32(1)
S(7)	1480(3)	-3104(6)	5144(2)	29(1)
K(1)	3187(2)	2611(5)	6961(2)	36(1)
K(2)	3437(3)	8518(6)	9289(2)	45(1)
K(3)	963(2)	2214(5)	4726(2)	35(1)

U$_{(eq)}$ is defined as one third pf the trace of the orthogonalized U$_{ij}$ tensor.

3. Results and Discussion

3.1 Description of Structures

Structure of $A_2CuP_3S_9$ (A = K, Rb). Because compounds I - II are isostructural and the discussion here will refer mainly to the K$^+$ salt. The structure of $K_2CuP_3S_9$ consists of $[CuP_3S_9]_n^{2n-}$ macroanions running along the [100] direction, see Figure 6-1. The shortest calculated interchain S-S distance is 3.516(3) Å, suggesting that the two potassium cations insure adequate screening of the anions.

The chains are built up from [CuS$_4$] tetrahedra bonded to the newly observed cyclic $[P_3S_9]^{3-}$ units. The only other remotely related species we could find is the binary thiosulfide P_4S_9 which has an adamantine structure where one of the phosphorous vertices has been reduced to a P^{3+} species. The cyclic $[P_3S_9]^{3-}$ unit is the result of three corner-sharing $[PS_4]^{3-}$ tetrahedra. As shown in Figure 6-2, the basal plane of a [CuS$_4$] tetrahedron defined by S(1), S(3), S(4) is common to one $[P_3S_9]^{3-}$ unit while the fourth apical sulfide (S(2)) of the copper tetrahedron is shared with a second neighboring $[P_3S_9]^{3-}$ unit. The structure can also be described in terms of a basic building block, the adamantane - like $[CuP_3S_9]^{2-}$ cluster. These clusters link to form a one-dimensional structure via the coordinative interaction of a terminal sulfide from one $[CuP_3S_9]^{2-}$ cluster to a copper atom of a neighboring $[CuP_3S_9]^{2-}$ cluster, filling the apical position of the [CuS$_4$] tetrahedron. The $[CuP_3S_9]_n^{2n-}$ chains are highly acentric in nature, see Figure 6-2, but pack in a centrosymetric fashion, preventing any dipole moment ti develope in the material. The Cu-S distances range from 2.299(2)Å to 2.332(2)Å. The average Cu-S distance of 2.310(3) Å in (I) compares well with previously studied compounds with tetrahedral [CuS$_4$] groups.[25] The S-Cu-S angles range from 99.49(8)° to 114.00(9)°. A perspective view of the $[P_3S_3]$ ring which highlights the chair configuration of the six-membered ring of the

trimetathiophoshate is shown in Figure 6-3. The $[P_3S_9]^{3-}$ unit represents a new member of the $[P_nS_{3n}]^{n-}$ anionic series of ring structures encompassing the $[P_2S_6]^{2-}$[26] and $[P_4S_{12}]^{4-}$[27] anions encountered in the 2D and 3D forms of NbP_2S_8, see Figures 6-3b and 6-3c.

In the $[P_3S_9]^{3-}$ unit, the P-S distances range from 1.951(3)Å to 2.131(3)Å with an average P-S distances of 2.054(3)Å, 2.045(3)Å and 2.049(3) for P(1), P(2) and P(3), respectively. The distances compare well with the sum of the ionic radii (rS^{2-}=1.84Å, rP^{5+}=0.17Å) and those previously reported.[3] The S-P-S angles reveal only a slight deviation from tetrahedral coordination and range from 103.4(1)° to 116.1(1)°. Selected bond distances and angles for $K_2CuP_3S_9$ are given in Table 6-8. The phosphorus atoms of the $[P_3S_3]$ chair-shaped ring define a almost-equilateral triangle with a mean P-P-P angle of 60.00(5)° and a mean P-P distance of 3.483(3)Å.

It is worth noting that there are two types of P-S distances in the $[P_3S_9]^{3-}$ unit. The average P-S distances in the $[P_3S_3]$ ring are slightly longer than the average terminal P-S distances, (2.121(1)Å versus 1.978(4)Å) for the bridging and terminal distances, respectively, see Figure 6-3. A similar trend is observed in the bi-tetrahedral $[P_2S_6]^{2-}$[26] (2.111(1)Å versus 1.993(1)), and quadri-tetrahedral $[P_4S_{12}]^{4-}$[27-28] units (2.113(3)Å versus 1.989(2)), respectively. In oxides, this segregation is more pronounced. Hence, from the structures of anhydrous sodium trimetalphosphate $Na_3P_3O_9$ and the monohydrate $Na_3P_3O_9,H_2O$[29], the average P-O $[P_3O_3]$ ring distance is 1.615Å and the average terminal P-O distance is 1.484Å.

The $[CuP_3S_9]_n^{2n-}$ chains are separated by A^+ ions that are located in two different sites. In $K_2CuP_3S_9$ K(1) is in eightfold coordination to sulfur atoms [range of K(1)-S distances, 3.200(3)Å to 3.688(3)Å; average 4.418(3)Å] and K(2) is nine-coordinate [range of K(2)-S distances, 3.286(3)Å to 3.767(3)Å; average 3.515(3)Å].

Structure of $Cs_2Cu_2P_2S_6$ (III). $Cs_2Cu_2P_2S_6$ is isostructural to the previously reported selenide analog.[5a] In this compound, alternating ethane-like $[P_2S_6]^{4-}$

units linked to Cu_2^{2+} dimers form infinite chains which run along the [101] direction, see

Figure 6-4. These chains pack side by side in a pseudo-hexagonal motif, see Figure 6-5.

This one-dimensional structure is closely realted to that of $KMnP_2S_6$.[30a] The average Cu-

Cu distance in $Cs_2Cu_2P_2S_6$ (2.720(5)Å) is slightly shorter than that reported for

$Cs_2Cu_2P_2Se_6$ (2.746(5)Å), and as in the latter it most likely reflects the presence of d^{10}-

d^{10} interactions. The P-P distance, of 2.242(7)Å, in (III) is slightly longer than the

average P-P distance, of 2.21(1)Å, reported for $KMnP_2S_6$,[30a] $KFeP_2S_6$,[30b] and

$Na_{0.16}Bi_{1.28}P_2S_6$.[31] The P-P distance of 2.242(7)Å observed for (III), is shorter than the

P-P distance of 2.260(6)Å observed for $Cs_2Cu_2P_2Se_6$. Selected bond distances and angles

for $Cs_2Cu_2P_2S_6$ are given in Table 6-9.

Structure of $K_3CuP_2S_7$ (IV). This compound contains infinite $[CuP_2S_7]_n^{3n-}$

which are parallel to the crystallographic a-axis (Figure 6-6) and are well separated by K^+

cations (Figure 6-7). The overall $[CuP_2S_7]_n^{3n-}$ chain structure is related to $A_2CuP_3S_9$

where the novel $[P_3S_9]^{3-}$ unit is replaced by the $[P_2S_7]^{4-}$ (pyrothiophosphate) unit. The

pyrothiophosphate $[P_2S_7]^{4-}$ unit consists of two corner-sharing $[PS_4]^{3-}$ tetrahedra and has

been previously observed in $ABiP_2S_7$ (A = K, Rb),[32] $RbVP_2S_7$,[33] and $AAuP_2S_7$ (A = K,

Rb).[3] The Cu^+ cation is in a trigonal planar coordination with Cu-S bond distances

ranging from 2.226(4)Å to 2.278(4)Å and S-Cu-S angles in the range from 115.3(1)° to

125.7(2)°. The coordination environment of the coinage metal site on (III) and $AAuP_2S_7$

(A = K, Rb) is worth discussing here. The square planar coordination of the Au^{3+} ions is

formed by bonding to two of the three terminal sulfides from each PS_4 tetrahedron. The

binding scheme for the coordination of the of Cu^+ ions in (IV) is completely different. One

$[P_2S_7]^{4-}$ unit chelates in a bidendtate fashion to the Cu^+ ion and the third coordination site

is filled by a sulfide from a neighboring $[P_2S_7]^{4-}$ unit.

The structure of (IV) is related to (I) where the chains are constructed by two of the

terminal sulfides of the polythiophosphate units binding to one Cu^+ ion and then bridging

the neighboring Cu^+ ion. In (I) the $[P_3S_9]^{3-}$ unit chelates in a tridentate fashion forming the basal plane of the coordination sphere. The removal of a second $[PS_2]$ vertex results in the $[P_2S_7]^{4-}$ unit that chelates in bidentate fashion to the Cu^+ ion forming six membered rings. This coordination twists the $[P_2S_7]^{4-}$ unit preventing the Cu^+ ion from adopting a tetrahedral coordination environment. Each PS_4 tetrahedron is slightly distorted with P-S distances ranging from 1.987(4)Å to 2.167(4)Å. and S-P-S angles ranging from $99.2(2)^o$ to $115.5(2)^o$, respectively. Selected bond distances and angles are given in Table 6-10.

The potassium cations located in three different sites. In $K_3CuP_2S_7$ K(1) is coordinated by seven sulfur atoms [range of K(1)-S distances, 3.178(5)Å-3.527(5)Å; average 3.32(4)Å]. K(2) is also seven-coordinate [3.325(5)Å-3.531(5)Å. average 3.38(1)Å], and K(3) is seven-coordinate [3.137(4)Å-3.642(5)Å, average 3.31(4)Å].

Table 6-8.   Selected band distances (Å) and angles (°) for $K_2CuP_3S_9$ (I) with Standard Deviations in Parentheses[a].

Cu-S(1)	2.305(2)	S(1)-Cu-S(2)	114.00(9)
Cu-S(2)	2.299(2)	S(1)-Cu-S(3)	110.25(8)
Cu-S(3)	2.332(2)	S(1)-Cu-S(4)	109.43(8)
Cu-S(4)	2.303(2)	S(2)-Cu-S(3)	99.49(8)
		S(2)-Cu-S(4)	111.23(8)
Cu-S(mean)	2.310(2)	S(3)-Cu-S(4)	112.18(8)
P(1)-S(2)	1.987(3)	S(2)-P(1)-S(3)	112.7(1)
P(1)-S(3)	1.986(3)	S(2)-P(1)-S(6)	104.1(1)
P(1)-S(6)	2.117(3)	S(2)-P(1)-S(7)	105.0(1)
P(1)-S(7)	2.124(3)	S(3)-P(1)-S(6)	114.0(1)
		S(3)-P(1)-S(7)	112.7(1)
P(1)-S(mean)	2.054(3)	S(6)-P(1)-S(7)	107.5(1)
P(2)-S(1)	1.989(3)	S(1)-P(2)-S(7)	112.5(1)
P(2)-S(7)	2.129(3)	S(1)-P(2)-S(8)	114.3(1)
P(2)-S(8)	2.109(3)	S(1)-P(2)-S(9)	115.8(1)
P(2)-S(9)	1.951(3)	S(7)-P(2)-S(8)	104.7(1)
		S(7)-P(2)-S(9)	105.0(1)
P(2)-S(mean)	2.045(3)	S(8)-P(2)-S(9)	103.4(1)
P(3)-S(4)	1.980(3)	S(4)-P(3)-S(5)	116.1(1)
P(3)-S(5)	1.975(3)	S(4)-P(3)-S(6)	112.4(1)
P(3)-S(6)	2.131(3)	S(4)-P(3)-S(8)	114.6(1)
P(3)-S(8)	2.108(3)	S(5)-P(3)-S(6)	103.1(1)
		S(5)-P(3)-S(8)	103.9(1)
P(3)-S(mean)	2.049(3)	S(6)-P(3)-S(8)	105.4(1)

Table 6-9.   Selected Distances (Å) and Angles (deg) for $Cs_2Cu_2P_2S_6$ (III) with Standard Deviations in Parentheses[a].

P(1)-S(1)	2.025(8)	S(1)-P(1)-S(2)	1113.8(2)
P(1)-S(2)	2.020(7)	S(1)-P(1)-S(3)	110.0(2)
P(1)-S(3)	2.032(7)	S(2)-P(1)-S(3)	113.5(2)
		S(1)-P(1)-P(2)	106.0(2)
P(2)-S(4)	2.032(7)	S(2)-P(1)-P(2)	105.0(2)
P(2)-S(5)	2.023(7)	S(4)-P(1)-P(2)	108.0(2)
P(2)-S(6)	2.014(8)		
P(1)-P(2)	2.245(5)	S(4)-P(2)-S(5)	113.3(2)
		S(4)-P(2)-S(6)	111.5(2)
Cu(1)-S(1)	2.293(4)	S(5)-P(2)-S(6)	112.9(2)
Cu(1)-S(2)	2.307(4)	S(4)-P(2)-P(1)	107.8(2)
Cu(1)-S(3)	2.264(4)	S(5)-P(2)-P(1)	104.7(2)
		S(6)-P(2)-P(1)	106.6(2)
Cu(2)-S(4)	2.314(4)		
Cu(2)-S(5)	2.262(4)		
Cu(2)-S(6)	2.293(4)	Cu(1)-Cu(1')-S(2)	81.1(1)
		Cu(1)-Cu(1')-S(6)	105.1(1)
Cu(1)-Cu(1')	2.716(3)	Cu(1)-Cu(1')-S(3)	96.8(1)
Cu(2)-Cu(2')	2.724(3)		
		S(2)-Cu(1)-S(6)	109.6(1)
		S(2)-Cu(1)-S(3)	124.0(1)
		S(6)-Cu(1)-S(3)	124.4(1)
		Cu(2)-Cu(2')-S(1)	101.4(1)
		Cu(2)-Cu(2')-S(4)	96.6(1)
		Cu(2)-Cu(2')-S(6)	83.4(1)
		S(1)-Cu(2)-S(4)	109.2(1)
		S(1)-Cu(2)-S(5)	122.2(1)
		S(4)-Cu(2)-S(5)	127.2(1)

[a]The estimated standard deviations in the mean bond lengths and the mean bond angles are calculated by the equation $\sigma l = \{\Sigma_n(l_n - l)^2/n(n-1)\}^{1/2}$, where l_n is the length (or angle) of the nth bond, l the mean mength (or angle), and n the number of bonds.

Table 6-10. Selected Distances (Å) and Angles (deg) for $K_3CuP_2S_7$ (IV) with Standard Deviations in Parentheses[a].

P(1)-S(1)	2.039(5)	S(1)-P(1)-S(2)	100.2(2)
P(1)-S(2)	2.167(4)	S(1)-P(1)-S(4)	108.2(2)
P(1)-S(4)	2.025(5)	S(1)-P(1)-S(7)	111.0(2)
P(1)-S(7)	1.987(5)	S(2)-P(1)-S(4)	112.3(2)
		S(2)-P(1)-S(7)	111.6(1)
P(2)-S(3)	2.043(5)	S(4)-P(1)-S(7)	112.7(2)
P(2)-S(2)	2.138(5)	S-P(1)-S (mean)	109(1)
P(2)-S(8)	2.017(5)		
P(2)-S(5)	1.994(5)	S(2)-P(2)-S(3)	108.5(2)
		S(2)-P(2)-S(5)	111.1(2)
Cu(1)-S(1)	2.278(4)	S(2)-P(2)-S(8)	99.2(2)
Cu(1)-S(3)	2.226(4)	S(3)-P(2)-S(5)	112.5(2)
Cu(1)-S(4)	2.226(4)	S(3)-P(2)-S(8)	109.0(2)
		S(5)-P(2)-S(8)	115.5(2)
		S-P(2)-S (mean)	109(1)
		P(1)-S(2)-P(2)	111.1(2)
		S(1)-Cu-S(3)	118.7(2)
		S(1)-Cu-S(4)	115.3(1)
		S(3)-Cu-(4)	125.7(2)

[a]The estimated standard deviations in the mean bond lengths and the mean bond angles are calculated by the equation $\sigma l = \{\Sigma_n (l_n - l)^2/n(n-1)\}^{1/2}$, where l_n is the length (or angle) of the nth bond, l the mean mength (or angle), and n the number of bonds.
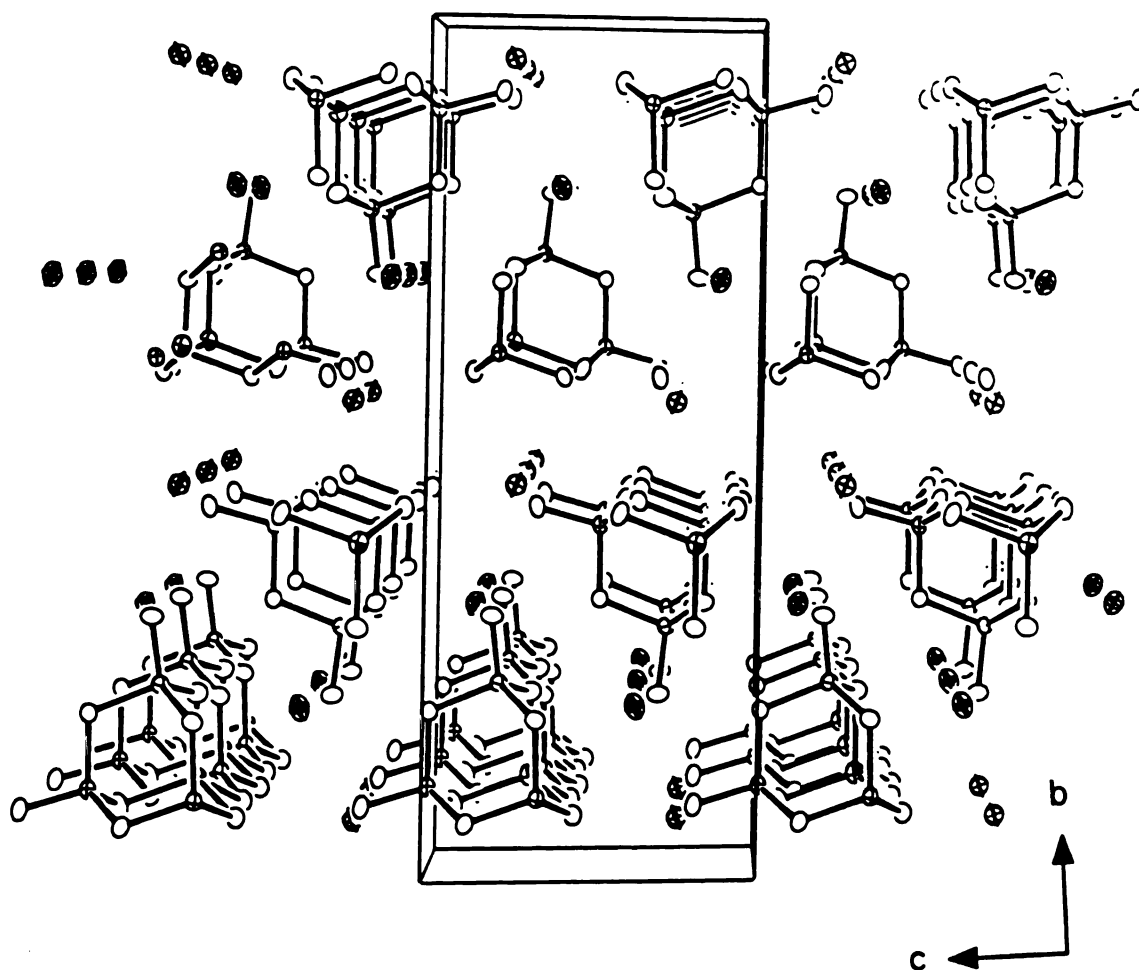
Figure 6-1:   ORTEP representaion of K$_2$CuP$_3$S$_9$ down the a-axis (50% probability ellipsoids). Small open cycles; Cu, small solid circles; P atoms, stripped cycles; S, and large cycles; K.
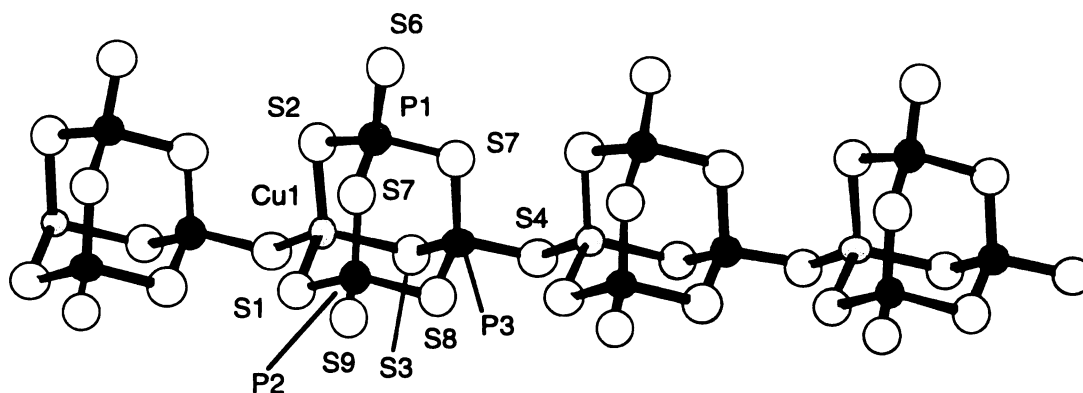
Figure 6-2: Perspective view of a [CuP$_3$S$_9$]$^{2-}$ chain with the labeling scheme.
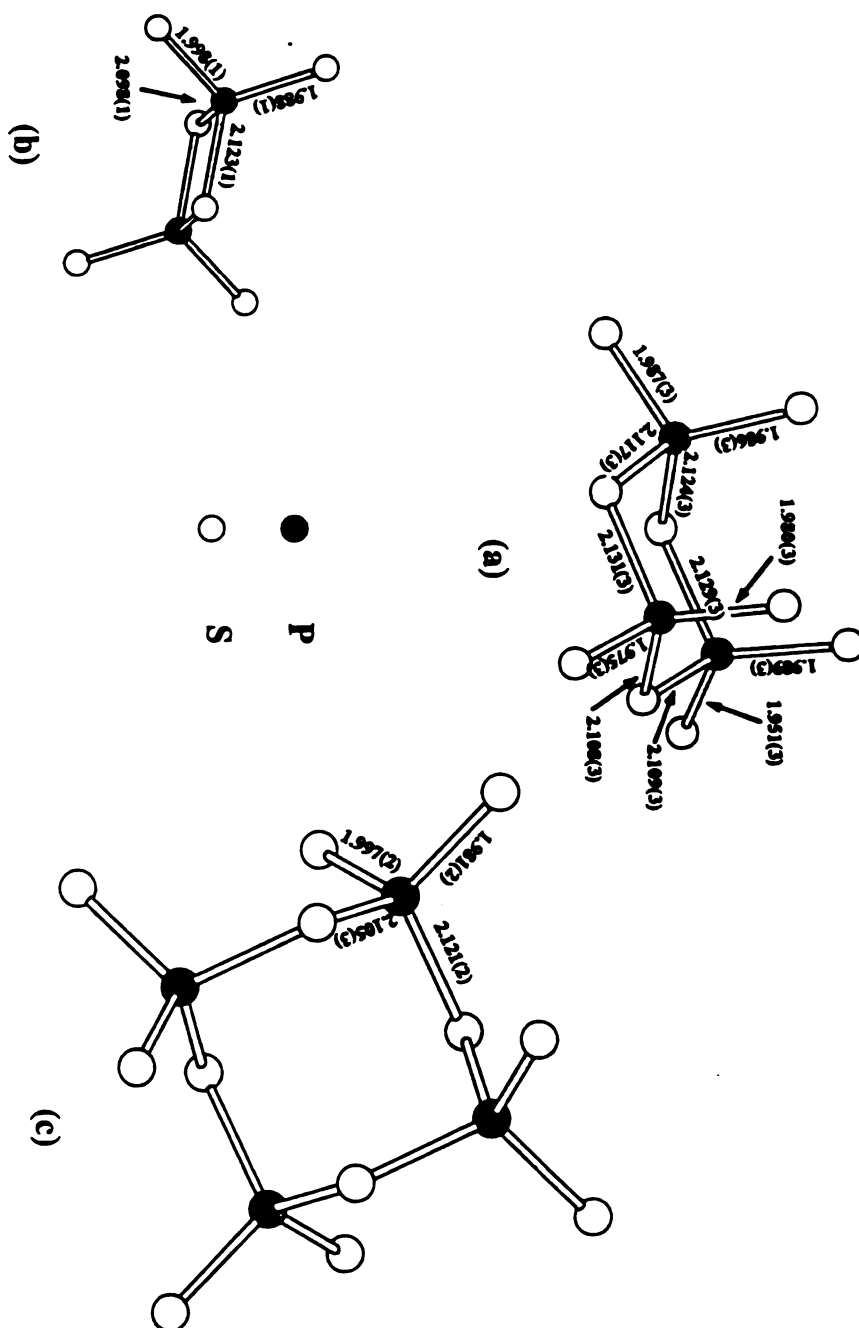
Figure 6-3:   Perspective views of the tri-tetrahedral $[P_3S_9]^{3-}$ ring observed in $K_2CuP_3S_9$ (a), the di-tetrahedral $[P_2S_6]^{2-}$ ring (b) and quadri-tetrahedral $[P_4S_{12}]^{4-}$ (c) observed respectively in 2D- and 3D-NbP_2S_8.
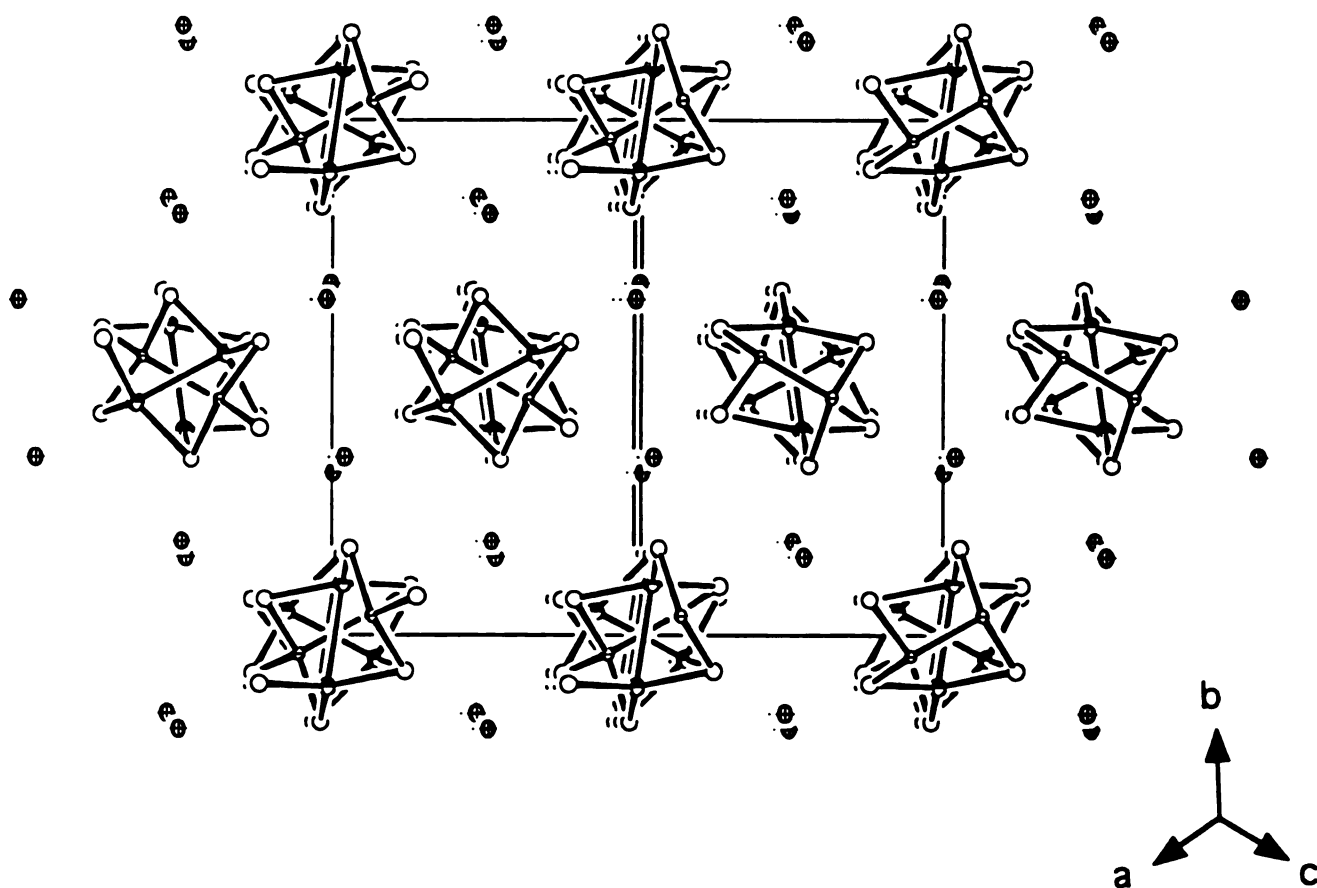
Figure 6-4:   ORTEP representation of the packing diagram of $Cs_2Cu_2P_2S_6$ as viewed along the [101] direction.
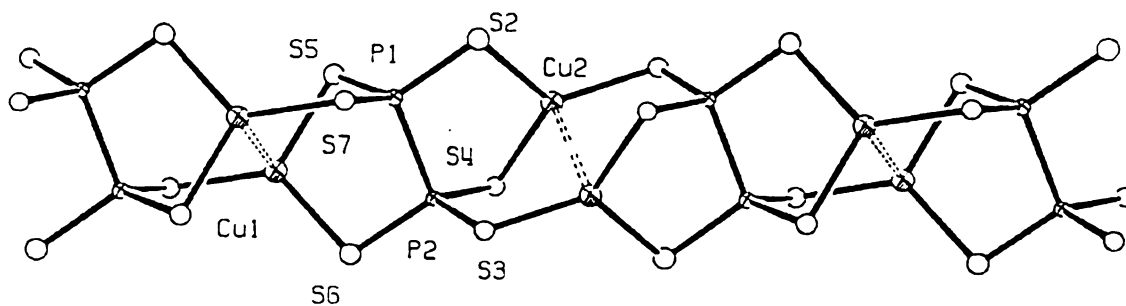
Figure 6-5:   View of a single $[Cu_2P_2S_6]^{2n-}$ chain, with labeling.
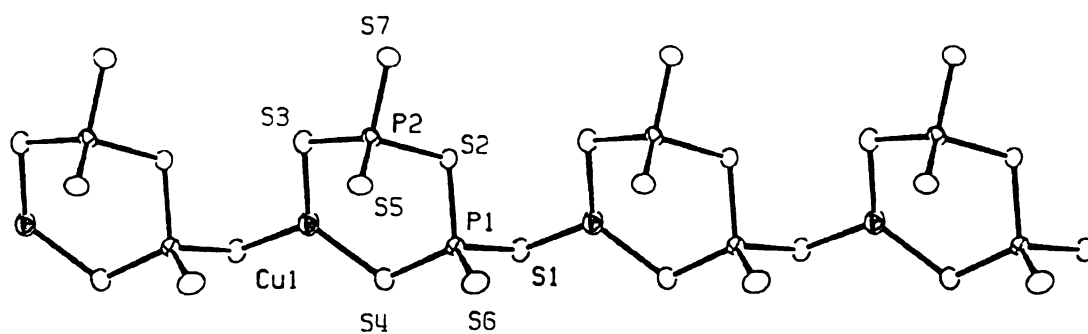
Figure 6-6:   View of a single $[CuP_2S_7]^{2n-}$ chain with labeling.
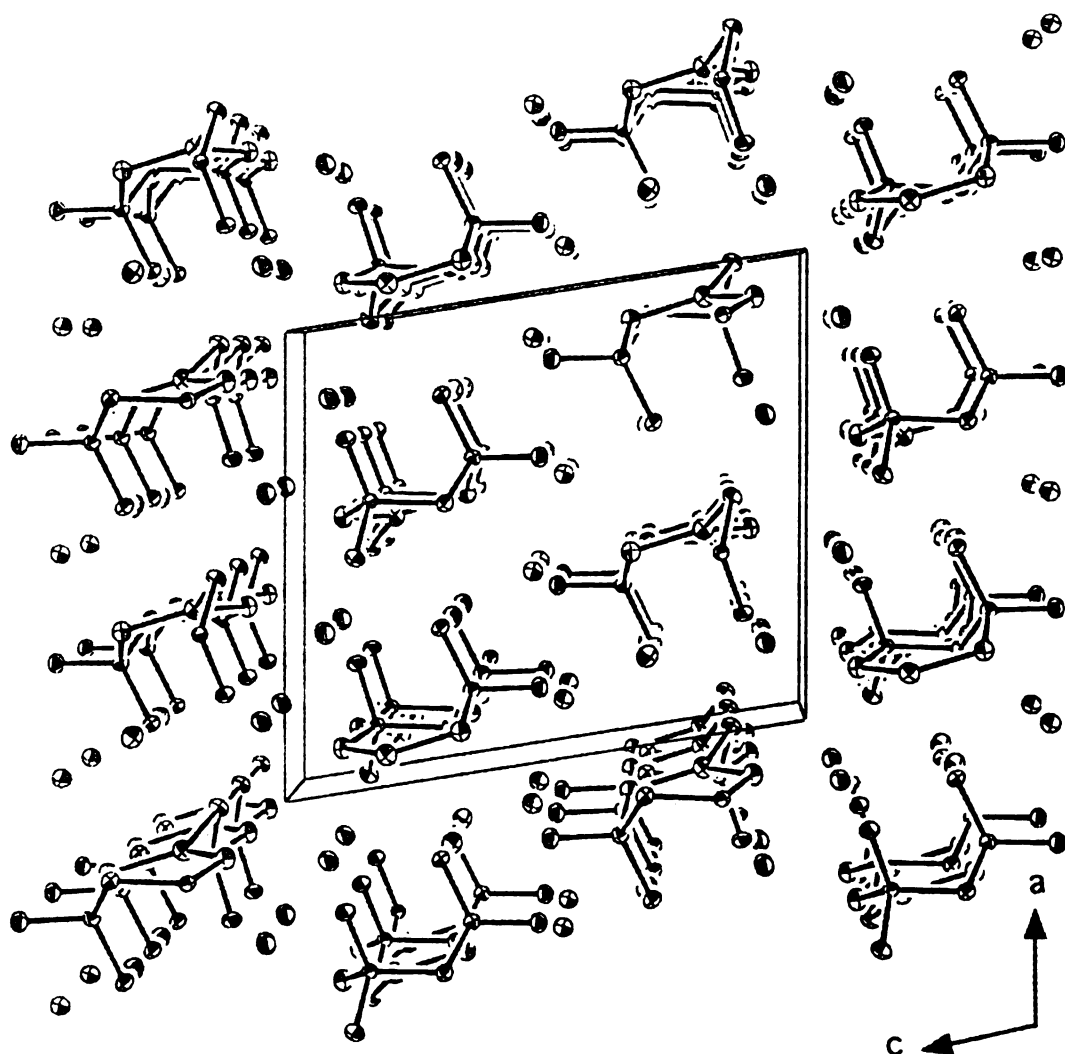
Figure 6-7: ORTEP representaion of K3CuP2S7 as viewed down the b-axis. Small open cycles; Cu, small solid circles; P atoms, stripped cycles; S, and large cycles; K.

3.2. Synthesis and Comparison between the Thiophosphate and Selenophosphate Fluxes:

Throughout our exploration of the chalcophosphate fluxes, we have observed a significant difference between the thiophosphate and selenophosphate systems. While the thiophosphate flux appears to favor the P^{5+} species, the selenophosphate flux displays a tendency to favor the reduced P^{+4} species. The stability of the reduced P^{+4} species is consistent with the lower oxidizing power of the Se_x^{2-} ligands compared to S_x^{2-} ligands.

The Lewis basicity of chalcophosphate flux controls the nature of the $[P_xQ_y]^{n-}$ units observed. In the selenophosphate system, the basicity is controlled by changing the A_2Se concentration, and in the thiophosphate system varying the P_2S_5 concentration changes the Lewis basicity. The tetrahedral $[PQ_4]^{3-}$ (Q = S, Se) unit is observed in both systems under highly basic conditions (high A_2Q or low P_2S_5). While the $[P_2Se_6]^{4-}$ unit is a repeatedly observed under Lewis acidic conditions (low A_2Q), other reduced phosphorous species have been reported.[5d] Further increasing the Lewis acidity, as observed in the synthesis of $K_2Cu_2P_4Se_{10}$,[5f] condenses two $[P_2Se_6]^{4-}$ units together via bridging selenides forming a $[P_4Se_{10}]^{4-}$ unit, containing a cyclohexane-like ring.

In contrast, in the thiophosphate system, decreasing the Lewis basicity of the flux (i.e. higher P_2S_5 concentration), favors the formation of higher nuclearity $[P_xS_y]^{n-}$ units with phosphorous centers mainly in the +5 oxidation state. To further explore these phosphorous-rich conditions the elemental sulfur was removed from the reaction conditions. A molten thiophosphate flux is still formed by the combination of A_2S and P_2S_5, but the oxidative properties would be different because of the absence of S-S bonds. Here a portion of the thiophosphate flu becomes sacrificial, oxidizing the coinage metal. The formation of the P^{+4} centers in $Cs_2Cu_2P_2S_6$ is rationalized this way. The exact influence of these phosphorous-rich conditions on product outcome is not well understood.

3.3. Physicochemical Properties

The optical properties of (I), (II) and (IV) were evaluated by examining their single crystal optical transmission spectra. The optical absorption properties of (III) was examined by UV/vis diffuse reflectance spectroscopy. The spectra show that these materials are wide band-gap semiconductors. The $A_2CuP_3S_9$ (A = K, Rb,) compounds exhibit steep absorption edges and band-gaps, E_g, of 2.57 eV (I), and 2.60 eV (II), respectively, see Figure 6-8. The band-gap of $K_3CuP_2S_7$ is 2.95 eV. The compound $Cs_2Cu_2P_2S_6$ exhibits a steep absorption edge and a band-gap, E_g, of 2.43 eV, see Figure 6-9.

The far-IR and Raman data of (I), (III) – (IV) are summarized in Table 6-11. The far-IR spectra of I, II and IV display several absorptions in the 600-400 cm^{-1} range. The sharp absorption at 400 cm^{-1} and 463 cm^{-1} represents the characteristic P-S-P stretching vibrations for I and IV, respectively. The doubly bridging bonding motif lowers the energy of the S-P-S vibration for I and II. The remaining absorptions are tentatively assigned to the $-PS_2$ stretching vibrations by analogy to $AAuP_2S_7$ (A = K, Rb)[5]. Absorptions below 400 cm^{-1} are assigned to Cu-S stretching vibrations. The far-IR spectrum of $Cs_2Cu_2P_2S_6$ displays an absorption at 441 cm^{-1}, which may be assigned to the P-P stretching vibration by analogy to $Na_4P_2S_6\cdot6H_2O$,[34] at 440 cm^{-1}.

The Raman spectra of I-II display absorptions in the 250-600 cm^{-1} range that are tentatively assigned to P-S and absorptions below 250 cm^{-1} are assigned to Cu-S stretching vibrations. The sharp absorption at ca. 391 cm^{-1} is assigned to the $-PS_3$ stretching vibration by analogy to $AAuPS_4$ and $AAuP_2S_7$ (A = K, Rb)[5]. The spectrum of III displays several absorptions below 200cm^{-1} are assigned to Cu-S stretching vibrations. The absorptions above 300 cm^{-1} are tentatively assigned to P-S or P-P vibrations. The spectrum of IV exhibited a high background problem and the spectrum was only obtained in a CsI matrix, therefore not all the absorptions may not be present. The absorption at ca.

217 cm^{-1} tentatively assigned to a Cs-S stretching vibration. The Raman spectra of I, III and IV is shown in Figure 6-10.

Differential thermal analysis (DTA) data followed by careful XRD analysis of the residues, show that I and II melt congruently, at 472°C, and 470°C, respectively. Crystals of III melt congruently at 716°C. The DTA of IV shows that it melts incongruently at ~500 ^{o}C to form a mixture of K$_3$CuP$_2$S$_7$ and an as of yet unknown phase. A typical thermogram for I and III are shown in Figure 6-11.
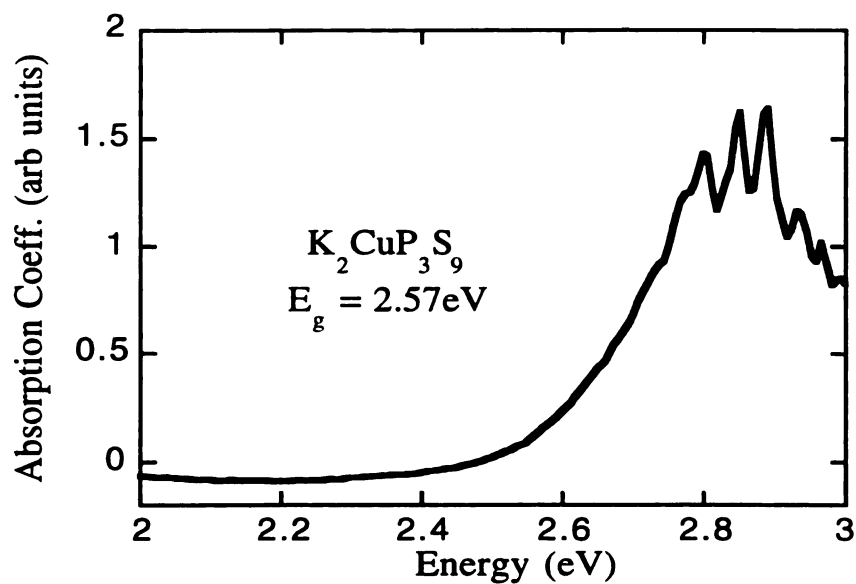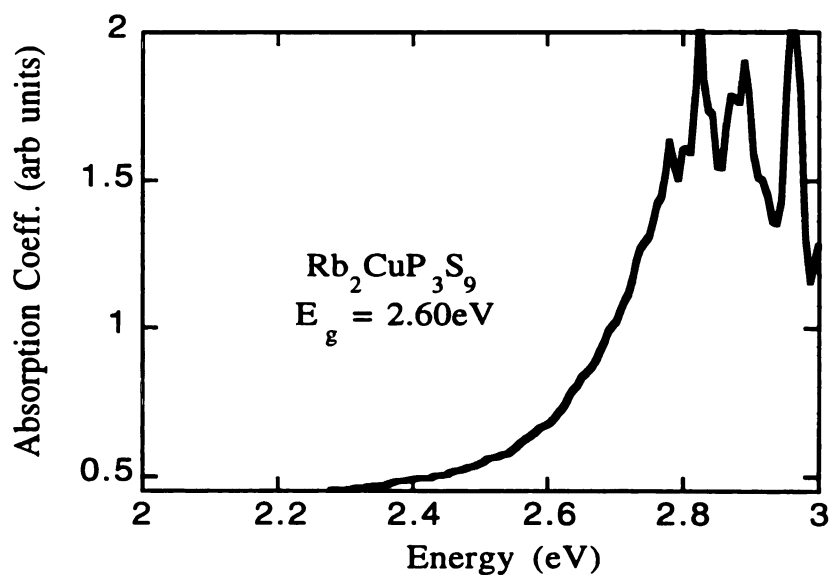
Figure 6-8: Single crystal optical absorption spectra of (A) $K_2CuP_3S_9$ (I) and (B) $Rb_2CuP_3S_9$ (II). The sharp features at high absorbance are noise and due to the very low transmission of light.
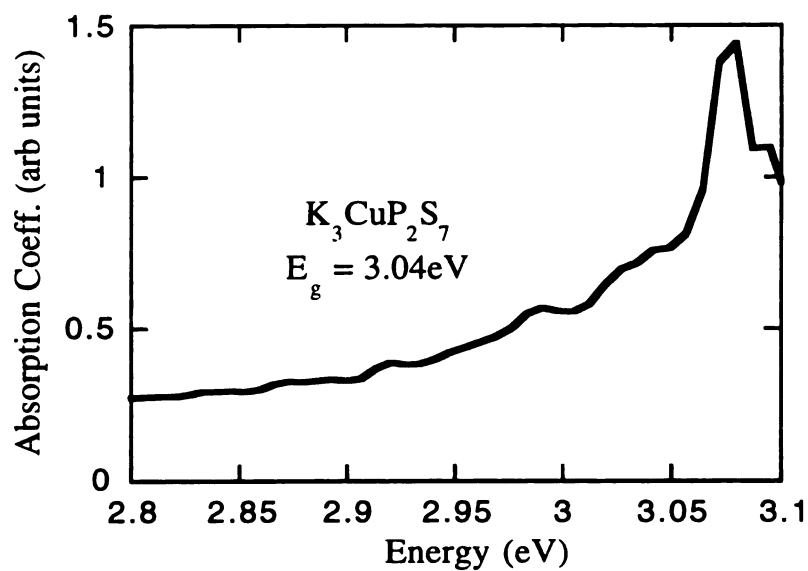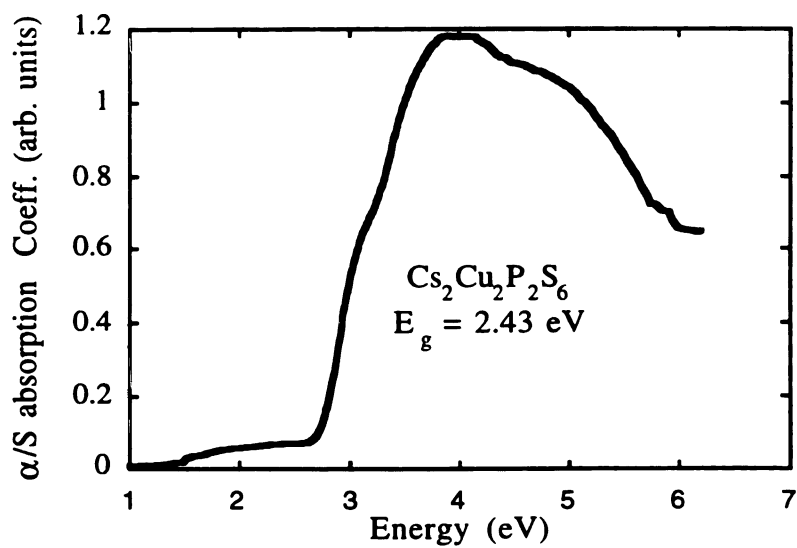
Figure 6-9:   (A) Single crystal optical absorption spectrum of $K_3CuP_2S_7$ (III).
               (B) Solid-state optical absorption spectrum of $Cs_2Cu_2P_2S_6$ (IV).

(A)
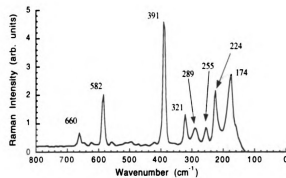
(B)
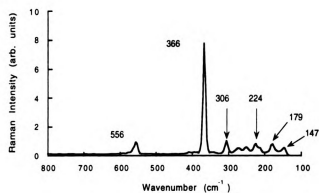
(C)
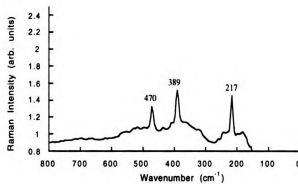
Figure 6-10:   Raman spectra of (A) $K_2CuP_3S_9$ (I), (B) $Cs_2Cu_2P_2S_6$ (III) and (C) $K_3CuP_2S_7$ (IV)
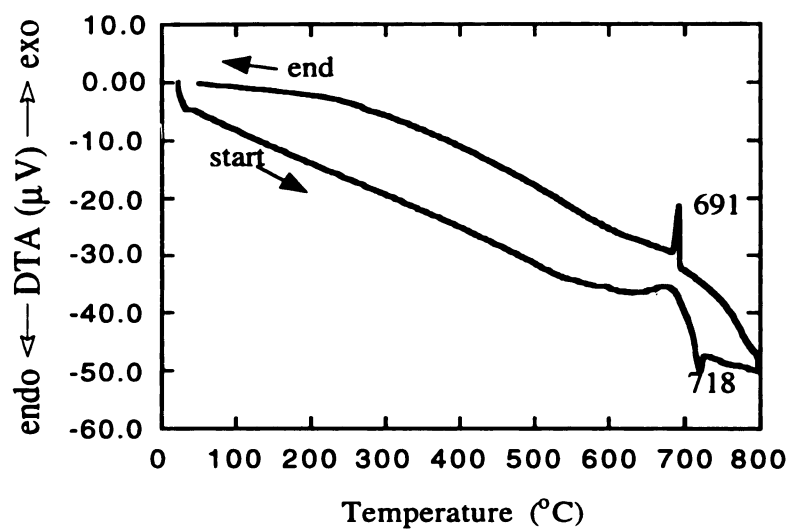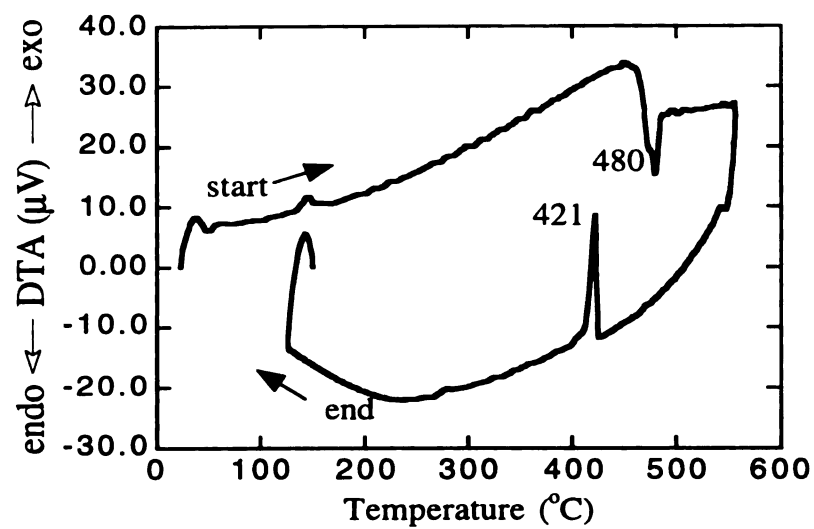
Figure 6-11:   Typical DTA diagrams for $K_2CuP_3S_9$ (I) and $Cs_2Cu_2P_2S_6$ (III).
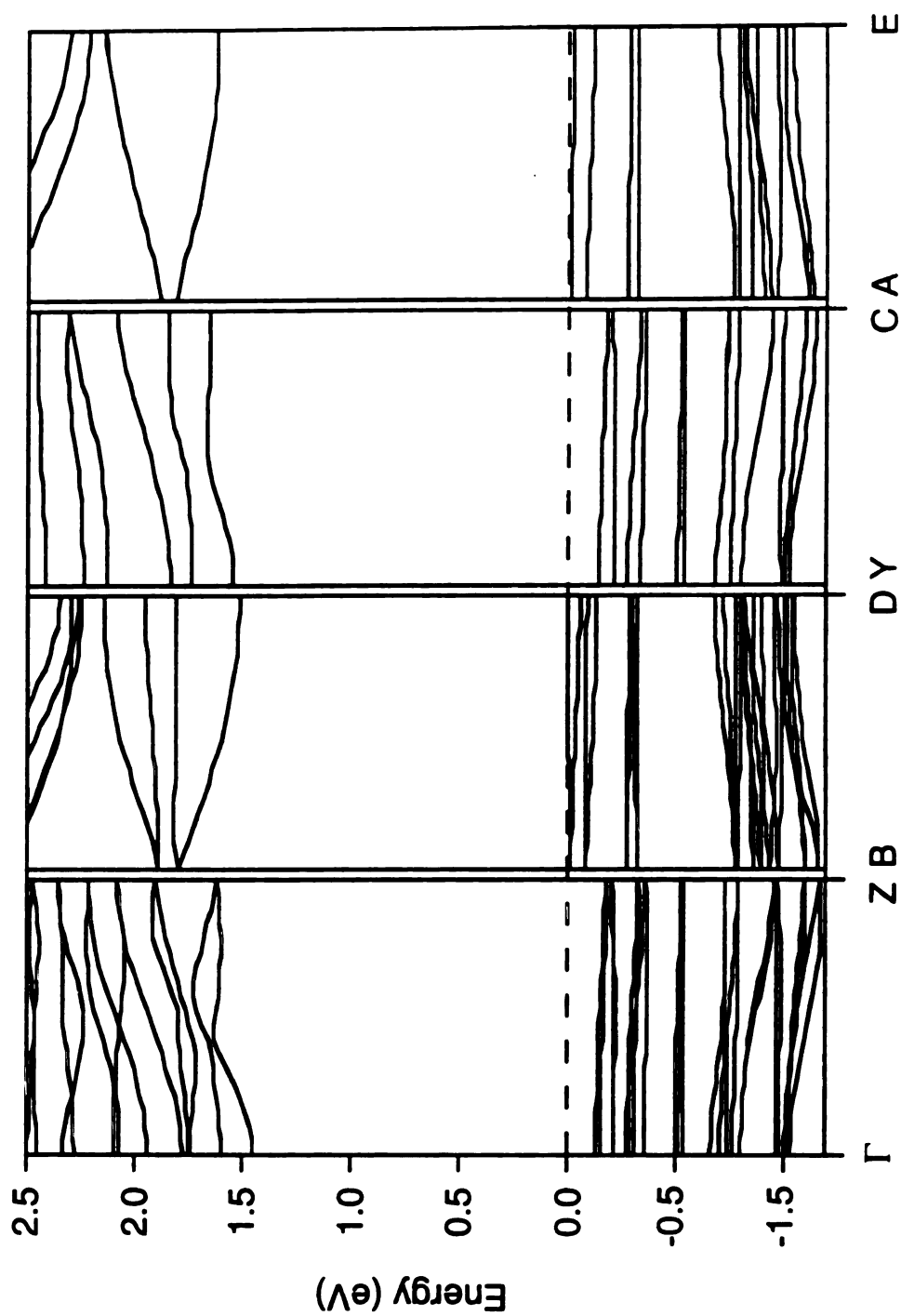
Figure 6-12:   A portion of the electronic band structure in selected directions of reciprocal space. The energy band-gap, which is indirect, if found between the B and Γ points.
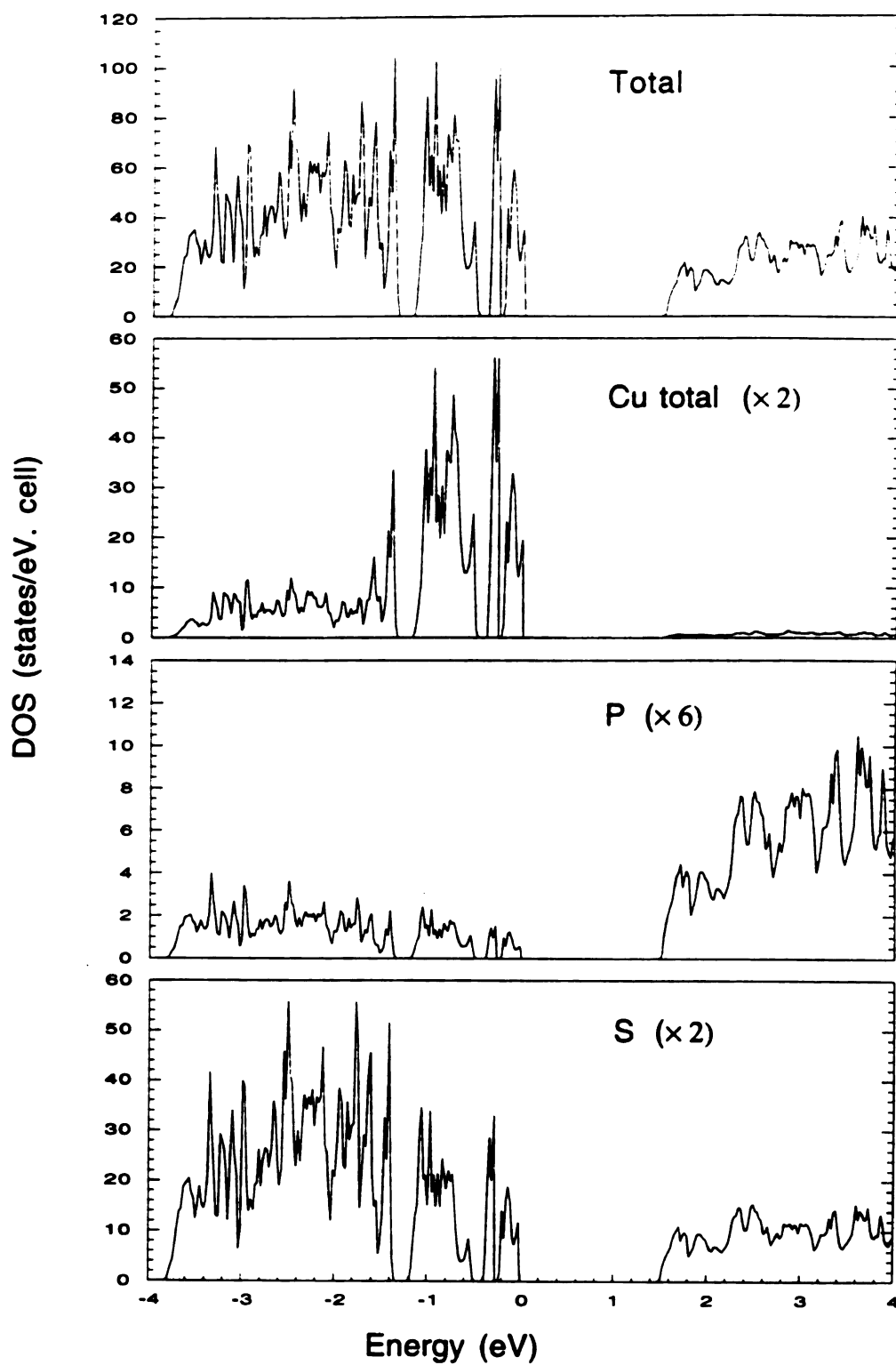
Figure 6-13:　Total density of states and Cu, P, and S projected density of states of $K_2CuP_3S_9$.
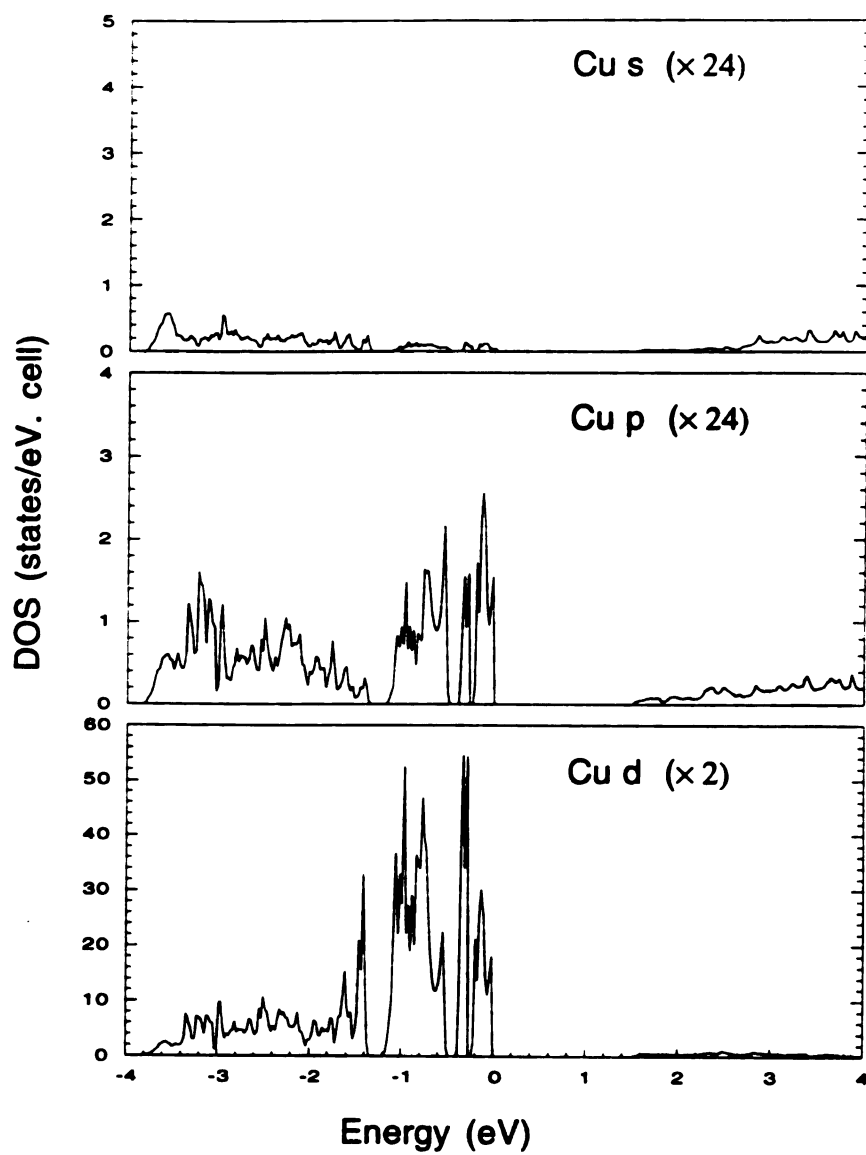
Figure 6-14:   Cu-s, Cu-p and Cu-d projected density of states of $K_2CuP_3S_9$.

(A)
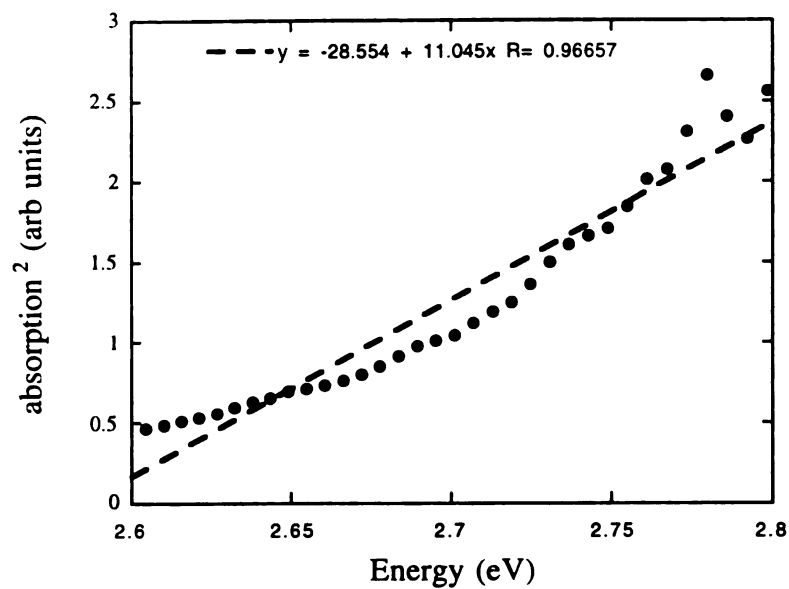
(B)
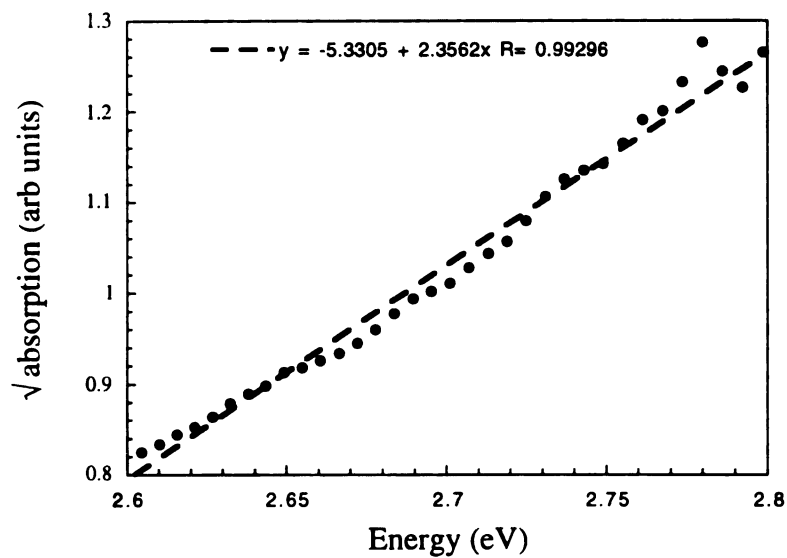
Figure 6-15: Absorption edge of $K_2CuP_3S_9$ plotted as a function of energy: (A) $(abs)^2$ dependence (direct gap) and (B) $\sqrt{abs}$ dependence (indirect gap).

Table 6-11.   IR and Raman Spectroscopic Data for $K_2CuP_3S_9$, $Cs_2Cu_2P_2S_6$, and $K_3CuP_2S_7$

$K_2CuP_3S_9$		$Cs_2Cu_2P_2S_6$		$K_3CuP_2S_7$	
IR	Raman	IR	Raman	IR	Raman
665(s)	660(w)	574(m)	555(m)	578(m)	
647(sh)	582(m)	441(m)		565(m)	470(m)
400(m)	391(s)			463(s)	389(s)
368(m)			367(s)	410(w)	
350(m)				355(w)	
327(w)	321(m)				
303(m)		314(m)	305(m)		
289(w)	289(w)	287(w)		290(w)	
278(m)			272(w)		217(m)
268(w)				263(w)	
253(w)	255(w)				
246(m)		248(w)	250(w)	244(w,b)	
227(s)	224(m)		225(w)	221(w)	
208(w)			179(w)		
202(m)			147(w)		
196(w)					
169(w)	174(m)				

3.4. Band Structure Calculations

Band structure calculations were performed in order to get some insight into the type of band-gap and origin of the yellow color in $K_2CuP_3S_9$. Let us remember that a compound appears yellow because it may be absorbing light in the blue. If color originates from an absorption phenomenon, the energy gap between the two energy levels involved in the absorption process is expected to be about 2.6eV, as it indeed observed experimentally.

The portion of the electronic band structure near the Fermi level is shown in Figure 6-12. The total and partial density of states of $K_2CuP_3S_9$ are depicted in Figures 6-13 and 6-14 in the [-4,4] eV-energy range with the zero energy taken at the last occupied level. From the calculated electronic structure, a semiconductor behavior is predicted with an energy gap of 1.48eV. Such a value is too small compared to the experimentally determined value to explain the yellow color. Nevertheless, this discrepancy indeed originates from the limitation of the TB-LMTO-ASA method (or more exactly the density functional method), which is known to underestimate the energy gap by about 50 - 70%[34]. The indirect nature of the optical band gap is confirmed by the experimental data obtained from single crystals of this compound. Data plots of $(abs)^2$ vs. hv and $\sqrt{abs}$ vs. hv, shown in Figure 6-15, can be used to distinguish between a direct and an indirect gap in semiconductors. This is because in solids the energy dependence of the absorption coefficient is quadratic in materials with direct energy gap while in those with indirect gaps the dependence scales to the square root.[35]

As mentioned above, copper and phosphorus atoms are in a tetrahedral coordination of sulfur. In the corresponding ML_4 tetrahedral isolated molecule, the cation atomic orbitals, engaged in antibonding interactions with chalcogens, are expected to split into d-e and d-t_2 molecular orbitals sets, while s, p orbitals are located at higher energy and are unoccupied for Cu^+ and P^{5+} Hence, the uppermost antibonding levels of the valence band (Figure 6-12a), built on copper d-orbitals as shown on Figure 6-12b, could be associated to Cu-d E and Cu-d T_2 blocks. Moreover, the bottom of the conduction band (Figures 6-

12c), essentially constructed on s, p phosphorus orbitals highly hybridized with sulfur ones, are associated to antibonding sigma P-S interactions. Let us notice that the charge balance $K^+_2Cu^+ P^{5+}_3S^{-2}_9$ is checked from band structure calculation if we assign the conduction band completely to sp orbitals of P^{5+}, and the top of the valence band to the copper d levels. The low contribution of the Cu-s, -p orbitals (Figures 6-13a,b) to the bottom of the conduction band make improbable the occurrence of an intra-site inter-band transfer. The yellow color would rather originate from a charge transfer from S^{2-} to either Cu^+ or P^{5+}. Hence, in the absence of any color center impurities, the color process at work in $K_2CuP_3S_9$ would be a light induced heteronuclear intervalence charge transfer.

4. Conclusions

The difference in electronegativity between sulfur and selenium results in a spectacular difference in the reactivity of the thiophosphate and selenophosphate fluxes. Changing flux conditions (e.g. chalcogenide basicity) results in the formation of various thiophosphate $[P_xS_y]^{n-}$ units. The four compounds reported here support the fact the thiophosphate and selenophosphte systems need to be explored separately. The experimentally observed trend of stabilizing higher nuclearity thiophosphate units, with increased P_2S_5 concentrations endows the system a tremendous amount of flexibility due to the numerous binding modes of the $[P_xS_y]^{n-}$ units. At this stage we have only a sketchy phenomenological understanding of the complex equilibria between the various P^{5+} containing species and any $[P_xS_y]^{n-}$ units based on P^{4+} species. We expect NMR spectroscopy to be of considerable help in elucidating the equilibrium issues in these systems.

List of References

1. (a) Kanatzidis, M.G. *Curr.Opinion Solid State and Mater. Sci.,* **1997**, *2*, 139.

2. (a) Kanatzidis,M. G. Chem. Mater., 2, 353, (1990). (b) Sutorik, A.; Kanatzidis, M.G. *Prog. Inorg. Chem.,* **1995**, *43*, 151.

3. Chondroudis, K.; Hanko, J.A.; Kanatzidis, M.G. *Inorg. Chem.,* **1997**, *36*, 2623.

4. (a) McCarthy, T. J.; Kanatzidis, M.G. *Chem. Mater.,* **1993**, *5*, 1061. (b) McCarthy, T. J.; Kanatzidis, M. G. *J. Chem. Soc. Chem. Commun..,* **1994**, 1089. (c) McCarthy, T. J.; Hogan, T.; Kannewurf, C. R.; Kanatzidis, M. G. *Chem. Mater.,* **1994**, *6*, 1072. (d) McCarthy, T. J.; Kanatzidis, M. G. *J. Alloys Comp.,* **1996**, 236, 70. (e) Chondroudis, K.; McCarthy, T. J.; Kanatzidis, M.G. *Inorg. Chem.,* **1996**, *35* 840. (f) Chondroudis, K.; Kanatzidis, M.G. *J. Chem. Soc. Chem. Commun.,.* **1996**, 1371.

5. (a) McCarthy, T. J.; Kanatzidis, M.G. *Inorg. Chem.,* **1995**, *34*, 1257. (b) Chondroudis, K.; Kanatzidis, M.G. *Inorg. Chem.,* **1995**, *34*, 5401. (c) Chondroudis, K.; McCarthy, T. J.; Kanatzidis, M.G. *Inorg. Chem.,* **1995**, *35*, 3451. (d) Chondroudis, K.; Kanatzidis, M.G., *Angew. Chem.,* **1997**, *36*, 1324. (e) Dorhout, P.K.; Malo, T.M. *Z. Anorg. Allg. Chem.,* **1996**. *622*, 385. (f) Chondroudis, K.; Kanatzidis, M.G. Sumitted for publication.

6. (a) Chondroudis, K.; Kanatzidis, M.G. *C. R. Acad. Sci. Paris, Series B*, **1996**, *322*, 887. (b) Chondroudis, K.; Kanatzidis, M.G. *J. Chem. Soc. Chem.* **1997**, *119*, 2574. (c) Chen, J.H.; Dorhout, P.K. *Inorg. Chem.,* **1995**, *34*, 5705. (d) Chen, J.H.; Dorhout, P.K.; Ostenson, J.E. *Inorg. Chem.,* **1996**, *35*, 5627.

7. (a) Klingen, W.; Eulenberger, G.; Hahn, H. *Z. Anorg. Allg. Chem.,* **1973**, *401*, 97. (b) Toffoli, P.; Khodadad, P.; Rodier, N. *Acta Cryst., Sect. B*, **1978**, *34*, 1779. (c) Klimgen, W.; Ott, R.; Hahn, H. *Z. Anorg. Allg. Chem.,* **1973**, *396*,

271. (d) Jandali, M.Z.; Eulenberger, G.; Hahn, H. *Z. Anorg. Allg. Chem.*, **1978**, *447*, 105.

8. (a) Ouvrard, G.; Brec, R.; Rouxel, J. *Mater. Res. Bull.*, **1985**, *20*, 1181. (b) Lee, S.; Colombet, P.; Ouvrard, G.; Brec, R. *Inorg. Chem.*, **1988**, *27*, 1291. (c) Lee, S.; Colombet, P.; Ouvrard, G.; Brec, R. *Mater. Res. Bull.*, **1986**, *21*, 917. (d) Durand, E.; Ouvrard, G.; Evain, M.; Brec, R. *Inorg. Chem.*, **1990**, *29*, 4916.

9. (a) Odile, J.-P.; Steger, J. J.; Wold, A. *Inorg. Chem.*, **1975**, *14*, 2400. (b) Taylor, B.E.; Steger, J. J.; Wold, A.; Kostiner, E. *Inorg. Chem.*, **1974**, *13*, 2719. (c) Taylor, B.E.; Steger, J. J.; Wold, A. *J. Solid State Chem.*, **1973**, *7*, 461.

10. (a) Lagadic, I.; Leaustic, A.; Clement, R. *J. Chem. Soc.Chem. Commun.*, **1992**, 1396. (b) Clement, R.; Audiere, J.-P.; Renard, J.-P. *Rev. Chim. Miner.*, **1982**, *19*, 560-571. (c) Michalowicz, A.; Clement, R. *Inorg. Chem.*, **1982**, *21*, 3872. (d) Clement, R. *J. Chem. Soc., Chem. Commun.*, **1980**, 647. (e) Joy, P.A.; Vasudevan, S. . *J. Chem. Soc. Chem.*, **1981**, *104*, 7792.

11. Thompson, A.H.; Whittingham, M.S. *U.S. Patent 4,049,879* **1977**. (b) Brec, R.; Le Mehaute'. A. *Fr. Patents 7,704,519* **1977**.

12. Toffoli, P.; Michelet, A.; Khodadad, P.; Rodier, N. *Acta Crystallogr.*, **1982**, *B38*, 706.

13. (a) Pfeiff, R.; Kniep, R. . *J. Alloys Comp.*, **1992**, 186, 111. (b) Evain, M.; Boucher, F.; Brec, R.; Mathey, Y. *J. Solid State Chem.*, **1991**, *90*, 8. (c) Lee, S.; Colombet, P.; Ouvrard, G.; Brec, R. *Mater. Res. Bull.*, **1986**, *21*, 917. (d) Leblanc, A.; Ouili, Z.; Colombet, P. *Mater. Res. Bull.*, **1985**, *20*, 947.

14. (a) Ferrari, A.; Cavalca L. *Gazzetta Chemica Italiana*, **1948**, *78*, 283. (b) Garin, J.; Parthe, E. *Acta Crystallogr.*, **1972**, *B28*, 3672.

15. Loken, S.; Tremel, W., *Eur. J. Inorg. Chem.*, **1998**, *42.*, 283.

16. (a) Yvon, K.; Jeitschko, W.; Parthé, E. *J. Appl. Cryst.*, **1977**, *10*, 73. (b) CERIUS[2], Version 1.6, Molecular Simulations Inc., Cambridge, England, **1994**.

17. McCarthy, T. J.; Ngeyi, S.-P.; Liao J.-H.; DeGroot, D.; Hogan, T.; Kannewurf, C. R.; Kanatzidis, M.G. *Chem. Mater.*, **1993**, *5*, 331.

18. (a) Andersen, O.K. *Phys. Rev. B*, **1975**, *12*, 3060. (b) Andersen, O.K.; Jepsen, O. *Phys. Rev. Letter*, **1984**, *53*, 2571. (c) Jepsen, O.; Z. *Phys.*, **1995**, *97*, 35.

19. Cu, 1.50Å, P(1), 1.15Å, P(2), 1.13Å, P(3), 1.15Å, K(1), 2.43Å, K(1), 2.54Å, S(1), 1.17Å, S(2), 1.15Å, S(3), 1.15Å, S(4), 1.15Å, S(5), 1.14Å, S(6), 1.30Å, S(7), 1.31Å, S(8), 1.30Å, S(9), 1.13Å.

20. (a) Jepsen, O.; Andersen, O.K. *Solid State Comm.*, **1971**, *9*, 1763. (b) Lambrecht, W.R.L.; Andersen, O.K. *Phys. Rev. B*, **1986**, *34*, 2439.

21. (a) Sheldrick,G. M. "SHELXTL[TM] version 5", Siemens Analytical X-Ray Instruments, Inc. Madison, WI. (b) V. Petricek, M. Dusek, "JANA'96 Cristallographic Computing System", Institute of Physics, Academy of Sciences of the Czech Republi c, Praha.

22. van der Lee, A.; Evain, M.; Boucher, F.; Brec, R. *Z. fur Krist..*, **1993**, *203*, 247.

23 Walker, N.; Stuart. D. *Acta. Crystallogr.*, **1983**. *A39*, 158.

24. (a) Sheldrick, G.M. In: *Crystallographic Computing 3*; Sheldrick, G.M., Kruger, C., Goddard R.,Eds.; Oxford University Press: Oxford, England, 1985; p 175. (b) TEXSAN: Single-Crystal Structure Analysis Software, Version 1.7, 1995 Molecular Structure Corp.: 3200 Research Forest Drive, The Woodlands, TX 77381.

25. (a) Liao, J.-H.; Kanatzidis, M.G. *Chem. Mater.*, **1993**, *5*, 1561. (b) Keane, P.M.; Lu, Y.-J.; Ibers, J.A, *Acc. of Chem. Res.*, **1991**, *24*, 223. (c) Lu, Y.-J.; Ibers, J.A, *J. Solid State Chem.*, **1992**, *98*, 312.

26. (A) Grenouilleau, P.; Brec, R.; Evain, M.; Rouxel, *J.Rev. Chim. Miner.*, **1983**, *20*, 628 (b) Bouchetière, M.; Toffoli, P.; Khodadad, P.; Rodier, N. *Acta. Crystallogr.*, **1978**, *B34*, 384.

27. Evain, M.; Brec, R.; Ouvrard, G.; Rouxel, *J. Mat. Res. Bull.*, **1984**, *19*, 41.

28. Queignec, M.; Evain, M.; Brec, R.; Sourisseau, C., *J. Solid State Chem.*, **1986**, *63*, 89.

29. Ondik, H.; *Acta. Crystallogr.*, **1965**, *18*, 226.

30. (a) Menzel, F.; Brockner, W.; Carrillo-Cabrera, W.; von Schnering H.G. *Z. Anorg. Allg. Chem.*, **1994**, *620*, 1081. (b) Carrillo-Cabrera, W.; Sabmannshausen, J.; von Schnering H.G.; Menzel, F.; Brockner, W. *Z. Anorg. Allg. Chem.*, **1994**, *620*, 489.

31. McCarthy, T.J.; Kanatzidis, M.G. *J. Alloys Comp.*, **1996**, *236*, 1089.

32. McCarthy, T.J.; Hogan, T.; Kannewurf, C.R;. Kanatzidis, M. G. *Chem. Mater.*, **1994**, *6*, 1072.

33. Durand, E.; Evain, M.; Brec, R. *J. Solid State Chem.*, **1992**, *102*, 146.

34. Mathey, Y.; Clement, R,; Sourisseau, C.; Lucazeau, G. *Inorg. Chem.*, **1980**, *19*, 2773.

35. Pankove, J.I. in "Optical Processes in Semiconductors." Dover Publications, New York, 1975.

CHAPTER 7

Chemistry of Gold in Molten Alkali Metal Polychalcogeno-phosphate Fluxes. Synthesis and characterization of the low dimensional Compounds A_2AuPS_4 (A = K, Rb, Cs) and $AAuP_2S_7$ (A = K, Rb).

1. Introduction

The polychalcophosphate fluxes provide the best set of experimental conditions for the synthesis of new multinary thiophosphate and selenophosphate compounds.[1] These fluxes form by the *in situ* fusion of $A_2Q/P_2Q_5/Q$ and contain $[P_yQ_z]^{n-}$ (Q=S, Se) units in a molten polychalcogenide solvewnt. These units can coordinate to metal ions utilizing a great variety of binding modes, giving rise to interesting new materials. These materials tend to be structurally and compositionally complex and often cannot be made by standard solid-state methods. After the initial report on $ABiP_2S_7$ (A=K,Rb),[2] the following unusual compounds were reported: $A_3M(PS_4)_2$ (A=Rb, Cs; M=Sb, Bi),[3] $Cs_3Bi_2(PS_4)_3$,[3] $Na_{0.16}Bi_{1.28}P_2S_6$,[3] $A_2MP_2Se_6$ (A=K, Rb; M=Mn, Fe),[1] $A_2M_2P_2Se_6$ (A=K, Cs; M=Cu, Ag),[1] KMP_2Se_6 (M=Sb, Bi),[4] $Cs_8M_4(P_2Se_6)_5$ (M=Sb, Bi),[5] $APbPSe_4$,[6] $A_4M(PSe_4)_2$ (A=Rb, Cs; M=Pb, Eu),[6] $Rb_4Ti_2(P_2Se_9)_2(P_2Se_7)$,[7] $KTiPSe_5$,[7] $A_5Sn(PSe_5)_3$ (A=K, Rb),[8] and $A_6Sn_2Se_4(PSe_5)_2$ (A=Rb, Cs).[8] More recently, $KAu_5P_2Se_8$,[9] $K_2UP_3Se_9$,[10a] $Rb_4U_4P_4Se_{26}$,[10b] and the $K(RE)P_2Se_6$ (RE=Y, La, Ce, Pr, Gd)[11] series of compounds were also reported. Extension of this chemistry to Au looked appealing because no structurally characterized compounds have been reported. The only compound reported is the ternary $AuPS_4$,[12] whose structure remains elusive. Om the basis of vibrational spectroscopy, a polymeric chain consisting of alternating edge-sharing tetrahedral $[PS_4]^{3-}$ and square AuS_4 planes was proposed. Our studies with Au yielded the first structurally characterized gold selenophosphate compound, the mixed-valent $A_6Au^I_{1.5}Au^{III}_{1.5}(P_2Se_6)_3$ (A=K, Rb)[13] which features three different coordination geometries for the Au centers. As an extension of the selenophosphate flux method, the thiophosphate chemistry was

examined in order to investigate the existence of phases isostructural to the expanding list of selenophosphate compounds and to synthesize new structural types.

Here we report the synthesis, structural characterization, optical and thermal properties of the new quaternary gold thiophosphate compounds, A_2AuPS_4 (A=K, Rb, and Cs), and $AAuP_2S_7$ (A=K, and Rb), which represent the first structurally characterized examples of quaternary gold thiophosphates. Access to each phase was achieved by modifying the flux basicity, by means of varying the amount of A_2S and P_2S_5 in the starting composition (see Syntheses).[1, 6-8, 10]

2. Experimental Section

2.1. Reagents

The reagents mentioned in this study were used as obtained unless noted otherwise: (i) Au metal (99.99%) was acquired from Liberty Coins, Lansing MI. (ii) phorphous pentasulfide (P_2S_5) 99.999% purity, Aldrich Chemical Co., Milwaukee, Wi.; (iii) cesium metal, analytical reagent, Johnson Matthey/AESAR Gruop, Seabrook, NH; (iv) rubidum metal, analytical reagent, Johnson Matthey/AESAR Gruop, Seabrook, NH; (v) potassium metal, analytical reagent, Aldrich Chemical Co., Milwaukee, Wi.; (vi) sulfur powder, sublimed, J.T. Baker Chemical Co., Phillipsburg, NJ; (vii) Methanol (MeOH) ACS anhydrous, EM Science, Inc., Gibbstown, NJ.; (viii) diethyl ether, ACS anhydrous, EM Science, Inc., Gibbstown, NJ.

Finely divided Au metal : A Canadian Maple Leaf gold coin, (99.99%, 31.1g) was dissolved in 400 ml of *aqua regia* (300 ml concentrated HCl and 100 ml concentrated HNO_3). The solution was boiled in an acid-resistant fume hood to a volume of approximately 100 ml. The solution was neutralized with ammonium hydroxide and the gold was reduced with excess hydrazine hydrochloride, dissolved in 100 ml of distilled

water. The resulting black suspension was gently heated, with stirring, for one hour to allow particle aggregation. After filtering the suspension, and washing it with copious amounts of distilled water and acetone, the resulting gold powder was heated in air for 2 hours at 200°C to drive off any remaining impurities, yielding 30.9g of Au powder. *Note:* heating too long or at too high a temperature results in impratical grain sizes.

2.2. Syntheses.

A_2S (A = K, Rb, Cs) were prepared by reacting stoichiometric amounts of the elements in liquid ammonia as described elsewhere.[14]

Preparation of K_2AuPS_4 (I). A mixture of Au (0.25 mmole), P_2S_5 (0.50 mmole) , K_2S (0.50 mmole), and (1.5 mmole) S that was sealed under vacuum in a Pyrex tube. The reaction mixture was heated to 500°C for 4 days, followed by cooling to 100°C at a rate of 4°C/hr. The product, which is stable in water and air, was isolated by dissolving the K_2S_x flux with degassed methanol under inert atmosphere to give yellow crystals and chunky yellow crystalline $K_x[P_yS_z]$ flux. The yellow chunks of $K_x[P_yS_z]$ flux were removed by washing with degassed distilled water, followed by methanol and ether to give yellow crystals (75% yield based on Au). The crystals are stable in air and water (signs of decomposition are apparent only after several weeks). Microprobe analysis on single crystals gave an average composition of $K_{1.8}AuP_{1.4}S_{5.6}$.

Preparation of Rb_2AuPS_4 (II): A mixture of Au (0.25 mmole), P_2S_5 (0.50 mmole), Rb_2S (0.50 mmole), and (1.5 mmole) S was sealed under vacuum in a Pyrex tube and heated as in (I). The product, which is stable in air and water, was isolated as in (I) to give yellow crystals (52% yield based on Au). These crystals also show signs of

decomposition after a several week exposure. Microprobe analysis gave an average composition of $Rb_{1.5}AuP_{1.1}S_{5.1}$.

Preparation of Cs_2AuPS_4 (III): A mixture of Au (0.25 mmole), P_2S_5 (0.50 mmole), Cs_2S (0.50 mmole), and (1.5 mmole) S was sealed under vacuum in a Pyrex tube and heated as in (I). The product, which is stable in water and air, was isolated as in (I) to give colorless transparent crystals (63% yield based on Au). Microprobe analysis gave an average composition of $Cs_{2.25}AuP_{3.8}S_{6.1}$.

Preparation of $KAuP_2S_7$ (IV): $KAuP_2S_7$ was synthesized from a more acidic Lewis mixture of Au (0.50 mmole), P_2S_5 (0.75 mmole), K_2S (0.50 mmole), and (1.5 mmole) S that was sealed under vacuum in a Pyrex tube. The reaction mixture was heated to 400°C for 4 days, followed by cooling to 110°C at a rate of 4°C/hr. The product which disintegrates in the presence of water, was isolated with degassed methanol to give dark red crystals (50% yield based on Au). The crystals are soluble in DMF forming an orange-red solution. Microprobe analysis gave an average composition of $K_{1.0}Au_{1.2}P_{2.6}S_{10}$.

Preparation of $RbAuP_2S_7$ (V): $RbAuP_2S_7$ was also synthesized from a more acidic Lewis mixture of Au (0.50 mmole), P_2S_5 (0.75 mmole), K_2S (0.50 mmole), and (1.5 mmole) S that was sealed under vacuum in a Pyrex tube and heated as in (IV). The product, which disintegrates in the presence of water, was isolated as in (IV) to give dark red crystals (50% yield based on Au). These crystals are also soluble in DMF forming an orange-red solution. Microprobe analysis gave an average composition of $Rb_{1.0}Au_{1.2}P_{2.6}S_{9.2}$.

2.3. Physical Measurements

Powder X-ray Diffraction. Analyses were performed using a calibrated Rigaku-Denki/RW400F2 (Rotaflex) rotating anode powder diffractometer controlled by an IBM computer, operating at 45 kV/ 100 mA and with a 1°/min scan rate, employing Ni-filtered Cu radiation in a Bragg-Brentano geometry. Powder patterns were calculated with the CERIUS^2 software.[15] Calculated and observed XRD patterns for (I), (III), and (IV) are given in Tables 7-1 – 7-3, respectively.

Infrared Spectroscopy. Infrared spectra, in the far-IR region (600-50 cm^{-1}), were recorded on a computer controlled Nicolet 750 Magna-IR Series II spectrophotometer equipped with a TGS/PE detector and silicon beam splitter in 4 cm^{-1} resolution. The samples were ground with dry CsI into a fine powder and pressed into translucent pellets.

Raman Spectroscopy. Raman spectra (700 - 100 cm^{-1}) were recorded with a BIO-RAD FT Raman spectrometer with a Spectra-Physics Topaz T10-106c 1.064 nm YAG laser running at 11 to 11.5 amps equipped with a Ge detector. The samples were ground into a fine powder and loaded into glass tubes.

Solid State UV/Vis/Near IR Spectroscopy. Optical diffuse reflectance measurements were performed at room temperature using a Shimadzu UV-3101PC double beam, double monochromator spectrophotometer. The instrument is equipped with integrating sphere and controlled by a personal computer. BaSO$_4$ was used as a 100% reflectance standard for all materials. Samples are prepared by grinding them to a fine powder and spreading them on a compacted surface of the powdered standard material, preloaded into a sample holder. The reflectance versus wavelength data generated can be used to estimate a material's band gap by converting reflectance to absorption data as described earlier.[16]

Single crystal optical transmission spectroscopy. Room temperature single crystal optical transmission spectra were obtained on a Hitachi U-6000 Microscopic FT

Spectrophotometer mounted on an Olympus BH2-UMA metallurgical microscope over a range of 380 to 900 nm. Crystals lying on a glass slide were positioned over the light source and the transmitted light was detected from above.

Differential Thermal Analysis (DTA). DTA experiments were performed on a computer-controlled Shimadzu DTA-50 thermal analyzer. Typically a sample (~ 25 mg) of ground crystalline material was sealed in quartz ampoules under vacuum. A quartz ampoule of equal mass filled with Al_2O_3 was sealed and placed on the reference side of the detector. The sample was heated to the desired temperature at 10 °C/min, then isothermed for 10 minutes and finally cooled to 50 °C at the same rate. Residue of the DTA experiment was examined by X-ray powder diffraction. To evaluate congruent melting we compared the X-ray powder diffraction patterns before and after the DTA experiments. The stability/reproducibility of the samples were monitored by running at multiple cycles.

Semiquantitative microprobe analyses The analyses were performed using a JEOL JSM-6400V scanning electron microscope (SEM) equipped with a TN 5500 EDS detector. This technique was used to confirm the presence of all elements in the compounds, for the compositions are unreliable do to the overestimation or underestimation of certain elements. Data acquisition was performed with an accelerating voltage of 20kV and thirty seconds accumulation time.

Single crystal X-ray Crystallography. Intensity data for (I) and (IV) were collected using a Rigaku AFC6S four-circle automated diffractometer equipped with a graphite crystal monochromator. Intensity data for (III) were collected using a Nicolet (Siemens) four-circle automated diffractometer equipped with a graphite crystal monochromator. Crystal stability was monitored with three standard reflections whose intensities were checked every 150 reflections, and unless noted, no crystal decay was detected in any of the compounds. The space groups were determined from systematic absences and intensity statistics. An empirical absorption correction based on ψ scans was applied to all data during initial stages of refinement. An empirical DIFABS correction[17]

was applied as recommended after full isotropic refinement, after which full anisotropic refinement was performed. The structures were solved by direct methods using SHELXS-86 software[18a] (for all compounds), and full matrix least squares refinement was performed using the TEXSAN software package[18b].

The complete data collection parameters and details of the structure solution and refinement are given in Table 7-4. The coordinates of all atoms, average temperature factors, and their estimated standard deviations are given in Tables 7-5 - 7-7.

Table 7-1.   Calculated and Observed X-ray Powder Patterns for K_2AuPS_4 (I).

hkl	d_{calc}, Å	d_{obsd}, Å	$I/I_{max}(obsd)$
001	9.45	9.49	7
100	6.50	6.52	20
$10\bar{1}$ 011	5.49	5.50	12
101	5.23	5.23	3
002	4.72	4.74	4
$11\bar{2}$	3.92	3.93	6
012	3.87	3.86	8
102	3.73	3.73	71
020	3.37	3.34	2
112 200	3.25	3.25	6
021	3.17	3.17	3
$20\bar{1}$	3.12	3.12	100
201	3.02	3.02	4
120	2.99	2.99	5
$10\bar{3}$	2.89	2.89	3
$12\bar{1}$	2.87	2.87	5
$21\bar{1}$ 121	2.83	2.83	3
103	2.78	2.77	12
$20\bar{2}$	2.748	2.748	3
004	2.363	2.365	5
220	2.342	2.341	4
023	2.303	2.301	2
$10\bar{4}$	2.259	2.260	5
104	2.185	2.185	2
222	2.068	2.068	3
$30\bar{2}$	2.012	2.014	2
024	1.935	1.934	2
$22\bar{3}$	1.914	1.907	2
223	1.847	1.842	2
124	1.834	1.834	3
$32\bar{1}$	1.806	1.804	2

$32\bar{2}$	1.728	1.724	3
$22\bar{4}$	1.695	1.694	2
026	1.649	1.649	3
224	1.633	1.625	2
125	1.582	1.576	4

Table 7-2.   Calculated and Observed X-ray Powder Patterns for Cs_2AuPS_4 (III).

hkl	d_{calc}, Å	d obsd, Å	I/I_{max}(obsd)
020	10.04	10.20	12
100	6.90	6.97	9
110	6.52	6.59	25
021 120	5.69	5.73	10
040	5.02	5.06	16
130	4.80	4.84	17
041	4.08	4.09	32
131	3.96	3.98	27
150	3.47	3.48	21
210	3.40	3.41	100
060	3.34	3.36	15
022	3.31	3.32	15
220	3.26	3.28	31
102	3.13	3.14	16
112	3.09	3.08	26
12$\overline{1}$	2.87	2.87	5
21$\overline{1}$ 121	2.83	2.83	3
103	2.78	2.77	12
20$\overline{2}$	2.748	2.748	3
004	2.363	2.365	5
220	2.342	2.341	4
023	2.303	2.301	2
10$\overline{4}$	2.259	2.260	5
104	2.185	2.185	2
222	2.068	2.068	3
30$\overline{2}$	2.012	2.014	2
024	1.935	1.934	2
22$\overline{3}$	1.914	1.907	2
223	1.847	1.842	2
124	1.834	1.834	3
32$\overline{1}$	1.806	1.804	2

$32\bar{2}$	1.728	1.724	3
$22\bar{4}$	1.695	1.694	2
026	1.649	1.649	3
224	1.633	1.625	2
125	1.582	1.576	4

Table 7-3.   Calculated and Observed X-ray Powder Patterns for $KAuP_2S_7$ (IV).

hkl	d_{calc}, Å	d_{obsd}, Å	$I/I_{max}(obsd)$
002	7.47	7.54	5
110	6.01	6.05	2
11$\bar{1}$	5.62		
111	5.53	5.56	100
020	4.62	4.64	27
021	4.41	4.44	4
022	3.93	3.94	8
113	3.79	3.80	15
20$\bar{2}$	3.54	3.55	3
202	3.45	3.46	6
114	3.14	3.15	3
22$\bar{1}$	2.96	2.95	2
024	2.90	2.91	8
13$\bar{1}$ 22$\bar{2}$	2.82	2.82	8
222	2.76	2.77	16
115	2.65	2.66	2
31$\bar{1}$ 025	2.51	2.51	6
13$\bar{3}$ 006 311	2.49	2.49	7
22$\bar{4}$	2.37	2.36	10
224 040	2.31	2.31	4
13$\bar{4}$ 31$\bar{3}$	2.290	2.291	3
313	2.232	2.234	3
042	2.207	2.208	2
135	2.059	2.061	3
117	1.998	1.998	4
400	1.978	1.979	4
044	1.965	1.966	4
22$\bar{6}$	1.942	1.945	2
24$\bar{2}$	1.936	1.938	2
242	1.920	1.923	3

315	1.906	1.907	2
33$\bar{3}$ 008	1.876	1.877	2
333	1.843	1.846	2
420	1.818	1.820	2
15$\bar{1}$	1.788	1.789	2
42$\bar{2}$ 118 24$\bar{4}$	1.773	1.775	2
422	1.755	1.751	4
404	1.725	1.728	2
13b7	1.723	1.723	2
20$\bar{8}$	1.711	1.708	2
137	1.704	1.703	2
15$\bar{3}$	1.697	1.697	2
153	1.689	1.690	2
31$\bar{7}$	1.659	1.659	2
245	1.647	1.648	3
424	1.616	1.617	2
119	1.591	1.592	2
24$\bar{6}$	1.570	1.573	2
511 246	1.547	1.547	2

Table 7-4. Crystallographic data for K_2AuPS_4, Cs_2AuPS_4 and $KAuP_2S_7$.

	(I)	(III)	(IV)
Formula	K_2AuPS_4	Cs_2AuPS_4	$KAuP_2S_7$
FW	432.25	621.99	522.43
a, Å	6.518(2)	6.904(3)	7.917(3)
b, Å	6.747(2)	20.093(6)	9.247(2)
c, Å	9.468(3)	7.025(5)	14.968(3)
α (deg)	90.00	90.00	90.00
β (deg)	92.98(2)	90.00	91.84(9)
γ (deg)	90.00	90.00	90.00
Z, V(Å^3)	4; 415.8(2)	4, 974.6(8)	4;1095.2(8)
λ (Mo Kα), Å	0.71069	0.71069	0.71069
space group	$P2_1/m$ (#11)	Pbcm (#57)	C2/c (#15)
D_{calc}, g/cm^3	3.469	4.32	3.168
μ, cm^{-1}	196.98	232.71	152.84
2θmax, deg	50	50	50
Temp (°C)	23	-120	23
Final R/R$_w$,[a] %	2.3/3.0	4.7/3.9	1.6/2.2
Octants collected	h, k, ±l	h, k, l	h, k, ±l
Total Data Measured	873	1066	1114
Total Unique Data (ave)	802	1066	1031
$DataF_o^2>3\sigma(F\sigma^2)$	609	769	780
No. of Variables	47	46	54
Abs. ratio (min/max)	0.8679	0.6198	0.7567
Crystal Dimen., mm	0.08x0.08x0.20	0.04x0.040.28	0.08x0.06x0.38

[a]$R = \Sigma(|F_o| - |F_c|)/\Sigma|F_o|$, $R_w = \{\Sigma_w(|F_o| - |F_c|)^2/\Sigma_w|F_o|^2\}^{1/2}$.

Table 7-5.   Positional parameters and B(eq) for K_2AuPS_4 with Estimated Standard Deviations in Parentheses. [a]

Atom	X	Y	Z	B_{eq}[a]$Å^2$
Au1	1.0000	0	0	1.46(2)
K1	1.4551(5)	1/4	-0.1657(3)	2.7(1)
K2	0.7958(4)	1/4	0.4641(3)	1.8(1)
S1	1.5245(5)	1/4	0.1742(3)	2.0(1)
S2	1.3050(5)	1/4	0.4926(3)	1.6(1)
S3	1.0927(3)	-0.0034(3)	0.2370(2)	1.78(8)
P1	1.2650(4)	1/4	0.2804(3)	1.0(1)

[a] B values for anisotropically refined atoms are given in the form of the isotropic equivalent displacement parameter defined as $B_{eq} = (4/3)[a^2B(1, 1) + b^2B(2, 2) + c^2B(3, 3) + ab(\cos\gamma)B(1,2) + ac(\cos\beta)B(1,3) + bc(\cos\alpha)B(2, 3)$

Table 7-6.   Positional parameters and B(eq) for Cs_2AuPS_4 with Estimated Standard
Deviations in Parentheses. [a]

Atom	X	Y	Z	B_{eq}[a]$Å^2$
Au1	0.1130(2)	1/4	0	1.19(5)
Cs1	0.7921(3)	0.4850(1)	1/4	1.26(8)
Cs2	0.3957(3)	0.6646(1)	1/4	2.0(1)
S1	0.529(1)	0.3390(4)	1/4	1.4(3)
S2	0.1137(7)	0.3637(2)	0.0047(9)	1.2(2)
S3	0.297(1)	0.4860(4)	1/4	1.2(3)
P1	0.276(1)	0.3871(4)	1/4	1.0(3)

[a] B values for anisotropically refined atoms are given in the form of the isotropic equivalent displacement parameter defined as $B_{eq} = (4/3)[a^2B(1, 1) + b^2B(2, 2) + c^2B(3, 3) + ab(\cos\gamma)B(1,2) + ac(\cos\beta)B(1,3) + bc(\cos\alpha)B(2, 3)$

Table 7-7.   Positional parameters and B(eq) for KAuP$_2$S$_7$ with Estimated Standard
Deviations in Parentheses. [a]

Atom	X	Y	Z	B$_{eq}$[a]Å^2
Au1	1/4	1/4	0	1.48(1)
K1	1/2	0.2534(3)	1/4	5.1(1)
S1	0.2212(2)	0.4202(2)	0.1153(1)	2.01(6)
S2	-0.0310(2)	0.1920(2)	0.0324(1)	2.06(6)
S3	0	0.1872(2)	1/4	1.83(8)
P1	-0.0133(2)	0.3328(2)	0.1388(1)	1.56(5)

[a] B values for anisotropically refined atoms are given in the form of the isotropic equivalent displacement parameter defined as $B_{eq} = (4/3)[a^2B(1, 1) + b^2B(2, 2) + c^2B(3, 3) + ab(\cos\gamma)B(1,2) + ac(\cos\beta)B(1,3) + bc(\cos\alpha)B(2, 3)$

3. Results and Discussion

3.1 Description of structures.

Structure of K₂AuPS₄ (I) and Rb₂AuPS₄ (II) These two compounds are isostructural. The single-crystal structure determination was performed on the K⁺ salt (I), and so the discussion will refer mainly to this compound. The structure of the $[AuPS_4]_n^{2n-}$ anion is a one-dimensional chain built of alternating $[PS_4]^{3-}$ tetrahedra linked in a corner-sharing fashion to monovalent Au atoms. The chains (Figure 7-1) run along the crystallographic *b*-axis and are separated by alkali metal cations, see Figure 7-2. A view highlighting the semisodial wave nature of a single chain is shown in Figure 7-3. The chains are propagated by a crystallographic screw axis resulting in the terminal sulfides of the $[PS_4]^{3-}$ ligand to appear on opposite sides of the S-Au-S linkage. This structural motif is not observed in the selenophosphates $A_3AuP_2Se_8$[19] (A = K, Rb, Cs) compounds. Remarkably, (I)-(II) are isostructural to the recently reported thioarsenate K_2AuAsS_4 and thiophosphate Tl_2AuPS_4[9]. The S-Au-S angle is constrained by symmetry to be linear. The Au resides on an inversion center with an average Au-S distance of 2.293(2) Å. This compares well with the Au-S distance found in $KAuS_5$,[20] $K_2Au_2SnS_4$,[21] $K_2Au_2Sn_2S_6$,[22] $BaAu_2SnS_4$,[23] and $K_4Au_6S_5$,[24] all featuring linearly coordinated monovalent Au⁺. The $[PS_4]^{3-}$ ligand is a regular tetrahedron with an average P-S bond distance of 2.04(1)Å and mean S-P-S angle of 109(2)°, respectively. The $[PS_4]^{3-}$ tetrahedra are in a staggered arrangement above and below the Au-S linear bond (see Figure 7-3). The Au-Au' distance is 3.598(2), suggesting no significant bonding interactions. Selected bond distances and angles for K₂AuPS₄ are given in Table 7-8. The A⁺ ions are located in two different sites. In K₂AuPS₄, K(1) is coordinated by six S atoms [range of K(1)-S distances, 3.227(4)-3.481(4)Å; av 3.37(3)Å], and K(2) is coordinated by eight S atoms [range of K(2)-S distances, 3.186(4)-3.424(3)Å; av 3.35(4)Å].

Structure of Cs₂AuPS₄ (III): The structure of the $[AuPS_4]_n^{2n-}$ anion is closely related to the selenophosphate compounds, $A_3AuP_2Se_8$ (A= K, Rb,Cs).[19] The $[AuPS_4]_n^{2n-}$ chains run along the crystallographic c -axis and are well separated by cesium cations (Figure 7-4). As view of a fragment of a single $[AuPS_4]_n^{2n-}$ chain is shown in Figure 7.5. The overall anionic structure of the $[AuPS_4]_n^{2n-}$ chains is related to the $[AuP_2Se_8]_n^{3n-}$ macroanion of $A_3AuP_2Se_8$ in that its projection also resembles the letter "C", see Figure 7-6. The difference between the two macroanions is shown Scheme 1.

Scheme 1

[AuP2Se8]n³ⁿ⁻   [AuPS4]n²ⁿ⁻
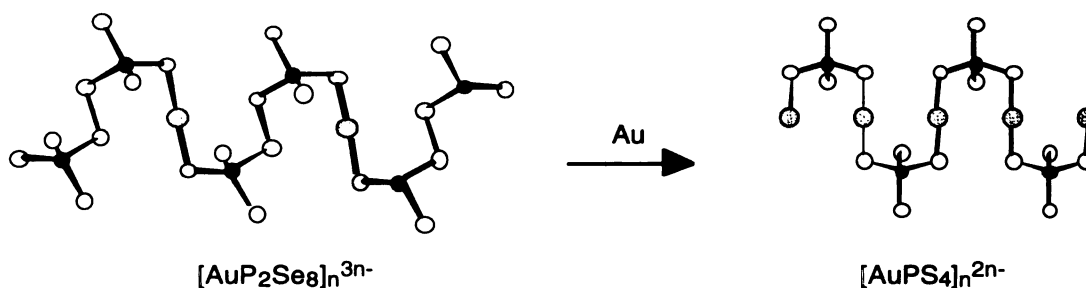
The difference is the reduction of the diselenide bridge of the $[P_2Se_8]^{4-}$ unit is reduced and replaced by a second S-Au-S linkage, creating two $[PS_4]^{3-}$ units. A second difference between the two structures is the packing of the chains. The chains in (III) stack in a centrosymmetric parallel fashion while the $[AuP_2Se_8]_n^{3n-}$ chains pack in an unusual criss-cross packing motiff. These chains run in the [110] and [2$\overline{2}$0] directions and are almost mutually perpendicular to each other, in a criss-cross fashion, an unusual packing for 1-D compounds The ribbons of (III) are isostructural to A_2AuSbS_4 (A = Rb, Cs)[25] and are propagated by a crystallographic glide plane resulting in the ternimal sulfides of the $[PS_4]^{3-}$

ligand to appear on the same side of the essentially linear S-Au-S linkage forming a projection resembling the letter "C". The S-Au-S angle is essentially linear, at $178.9(2)^o$. The Au resides on a 2-fold crystallographic site with Au-S distance of $2.285(2)\text{Å}$. The $[PS_4]^{3-}$ unit binds to two monovalent Au cations leaving the other sulfides terminal. The $[PS_4]^{3-}$ unit is a regular tetrahedron with an average P-S bond distance of 2.05(3) and a mean S-P-S angles of $109(2)^o$. The $[PS_4]^{3-}$ tetrahedra are in a staggered arrangement above and below the S-Au-S linear bond. The Au-Au' distance is $3.667(2)\text{Å}$ indicating no significant bondng interaction. Selected bond distances and angles for Cs_2AuPS_4 are given in Table 7-9. The $[AuPS_4]_n^{2n-}$ chains are separated by Cs^+ ions that are located in two different sites. In Cs_2AuPS_4, Cs(1) is coordinated by nine S atoms [range of Cs(1)–S distances, $3.394(9)-3.51(1)\text{Å}$; av $3.57(3)\text{Å}$], and Cs(2) is coordinted by eight S atoms [range of Cs(2)–S distances, $3.45(1)-3.54(1)\text{Å}$; av $3.75(7)\text{Å}$].

Structure of $KAuP_2S_7$ (IV) and $RbAuP_2S_7$ (V):

These two compounds are isostructural. Therefore the single-crystal structure determination was preformed on the K^+ salt (IV) and so the discussion will refer mainly to this compound. The structure of $[AuP_2S_7]^{n-}$ is a unique one dimensional chain consisting of alternating $[P_2S_7]^{4-}$ units edge sharing fashion to square planar Au^{3+} cations. Having a d^8 electron configuration, the Au^{3+} atom adopts a square planar coordination environment. The chains run along the (101) direction (Figure 7-6) and are separated by alkali cations (Figure 7-7). The Au center resides on an inversion center with Au-S bond distances ranging from 2.352(2) to $2.354(2)\text{Å}$ and P-S distances ranging from 1.952(2) to $2.140(2)\text{Å}$. The Au-Au' distance between chains is $6.068(1)\text{Å}$. Inspection of the S(1)-Au(1)-S(2) angles of 83.49(5) and $96.51(5)^o$, reveals a slight deviation from an ideal square planar geometry, which is due to a strained four-menbered (Au(1)-S(1)-P(1)-S(2)) ring. The pyrothiophsophate $[P_2S_7]^{4-}$ unit consists of two corner sharing $[PS_4]^{3-}$ tetrahedra. Each PS_4 tetrahedron is slightly distorted with S-P-S angles ranging from 98.90(8) to $118.3(1)^o$, respectively. The

smallest angle is associated with the constrained S-P-S-Au four-membered rings and the largest associated with the terminal sulfide. The chains are separated by alkali metal cations residing in a pocket between the terminal sulfide (S(4)) and a bridging sulfide (S(2)) In $KAuP_2S_7$ the potassium caion is coordinated by six sulfur atoms [range of K(1)-S distances 3.324(2) - 3.485(2)Å; av. 3.37(3)Å]. Selected bond distances and angles for $KAuP_2S_7$ are given in Table 7-10.

Table 7-8.   Selected Distances (Å) and Angles (deg) for K$_2$AuPS$_4$ (I) with
Standard Deviations in Parentheses[a].

P(1)-S(1)	2.012(4)	S(1)-P(1)-S(2)	115.5(2)
P(1)-S(2)	2.013(4)	S(1)-P(1)-S(3)	111.2(1)
P(1)-S(3)	2.075(3) x2	S(1)-P(1)-S(3')	111.2(1)
		S(2)-P(1)-S(3)	103.8(1)
Au(1)-S(3)	2.293(2)	S(2)-P(1)-S(3')	103.8(1)
Au(1)-S(3')	2.293(2)	S(3)-P(1)-S(3')	110.9(2)
		S-P-S (mean)	109(1)
Au(1)-Au(1')	3.373(1)		
		S(3)-Au(1)-S(3)	180.00
		Au(1)-S(3)-P(1)	107.3(1)
		K(2)-S(1)	3.186(4)
K(1)-S(1)	3.227(4)	K(2)-S(2)	3.317(4)
K(1)-S(1')	3.377(1) x2	K(2)-S(2')	3.224(4)
K(1)-S(2)	3.331(4)	K(2)-S(2")	3.465(1) x2
K(1)-S(3)	3.481(4) x2	K(2)-S(3)	3.331(3) x2
K(1)-S (mean)	3.37(3)	K(2)-S (mean)	3.33(4)

[a]The estimated standard deviations in the mean bond lengths and the mean bond angles are calculated by the equation $\sigma l = \{\Sigma_n(l_n - l)^2/n(n-1)\}^{1/2}$, where l_n is the length (or angle) of the nth bond, l the mean mength (or angle), and n the number of bonds.

Table 7-9.   Selected Distances (Å) and Angles (deg) for Cs_2AuPS_4 (III) with Standard Deviations in Parentheses[a].

P(1)-S(1)	2.00(1)	Au(1)-S(2)-P(1)	103.6(3)
P(1)-S(2)	2.108(7) x2		
P(1)-S(3)	1.99(1)	S(2)-Au(1)-S(2)	179.8(3)
P(1)-S(mean)	2.05(3)		
		S(1)-P(1)-S(2)	110.9(3) x2
Au(1)-S(2)	2.285(5) x2	S(1)-P(1)-S(3)	114.8(5)
		S(2)-P(1)-S(2')	109.7(4)
Au(1)-Au(1')	3.667(2)	S(2)-P(1)-S(3)	105.1(3) x2
Cs(1)-S(1)	3.45(1)	Cs(2)-S(1)	3.542(9)
Cs(1)-S(3)	3.720(6) x2	Cs(2)-S(1')	3.552(3) x2
Cs(1)-S(3)	3.586(6)	Cs(2)-S(3)	3.986(5) x2
Cs(1)-S(5)	3.420(9)	Cs(2)-S(3')	3.873(6) x2
Cs(1)-S(5)	3.484(9)	Cs(2)-S (mean)	3.75(6)
Cs(1)-S(5)	3.613(3) x2		
Cs(1)-S (mean)	3.57(4)		

[a]The estimated standard deviations in the mean bond lengths and the mean bond angles are calculated by the equation $\sigma l = \{\Sigma_n(l_n - l)^2/n(n-1)\}^{1/2}$, where l_n is the length (or angle) of the nth bond, l the mean mength (or angle), and n the number of bonds.

Table 7-10.   Selected Distances (Å) and Angles (deg) for $KAuP_2S_7$ (IV) with Standard
Deviations in Parentheses[a].

P(1)-S(1)	2.065(2)	S(1)-Au(1)-S(1')	180.00
P(1)-S(2)	2.058(2)	S(1)-Au(1)-S(2)	83.49(5) x2
P(1)-S(3)	2.140(2)	S(1')-Au(1)-S(2')	96.51(5) x2
P(1)-S(4)	1.952(2)	S(2)-Au(1)-S(2')	180.00
P(1')-S(3)	2.140(2)		
		Au(1)-S(1)-P(1)	88.40(7) x2
Au(1)-Au(1')	6.086(1)	Au(1)-S(2)-P(1)	88.52(7) x2
Au(1)-S(1)	2.352(2) x2	S(1)-P(1)-S(2)	98.90(8)
Au(1)-S(2)	2.354(2) x2	S(1)-P(1)-S(3)	110.90(8)
		S(1)-P(1)-S(4)	115.8(1)
K(1)-S(1)	3.321(2) x2	S(2)-P(1)-S(3)	101.79(9)
K(1)-S4	3.485(2) x2	S(2)-P(1)-S(4)	118.3(1)
K(1)-S(4')	3.333(3) x2	S(3)-P(1)-S(4)	109.87(8)
K(1)-S (mean)	3.37(3)	S-P-S (mean)	109(3)
		P(1)-S(3)-P(1')	102.1(1)

[a]The estimated standard deviations in the mean bond lengths and the mean bond angles are calculated by the equation $\sigma l = \{\Sigma_n(l_n - l)^2/n(n-1)\}^{1/2}$, where l_n is the length (or angle) of the nth bond, l the mean mength (or angle), and n the number of bonds.
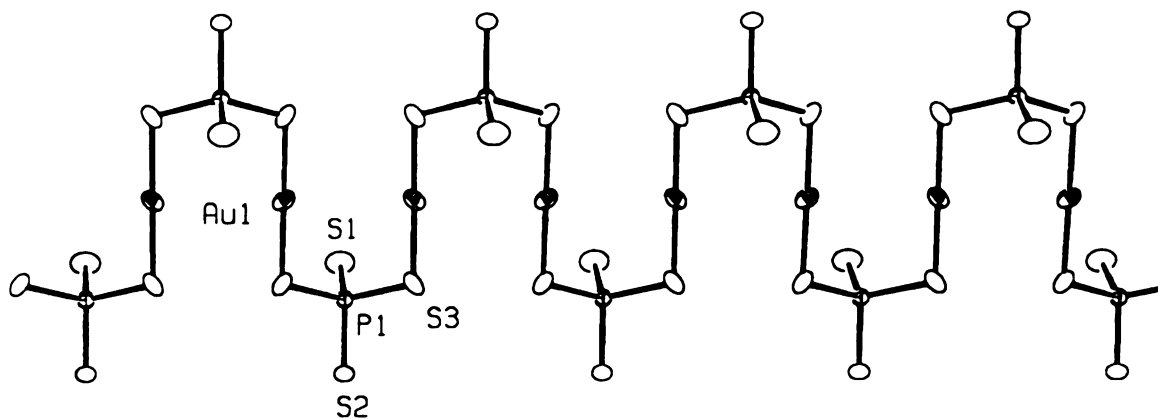
Figure 7-1: View of a single $[AuPS_4]_n^{2n-}$ chain in K_2AuPS_4 (I), with labeling.

Figure 7-2:   ORTEP representation of K$_2$AuPS$_4$ (I) as viewed down the *b* -axis (50% probability elliposids).

Figure 7-3:   ORTEP representation of K2AuPS4 (I) as viewed down the c - axis (50% probability elliposids).

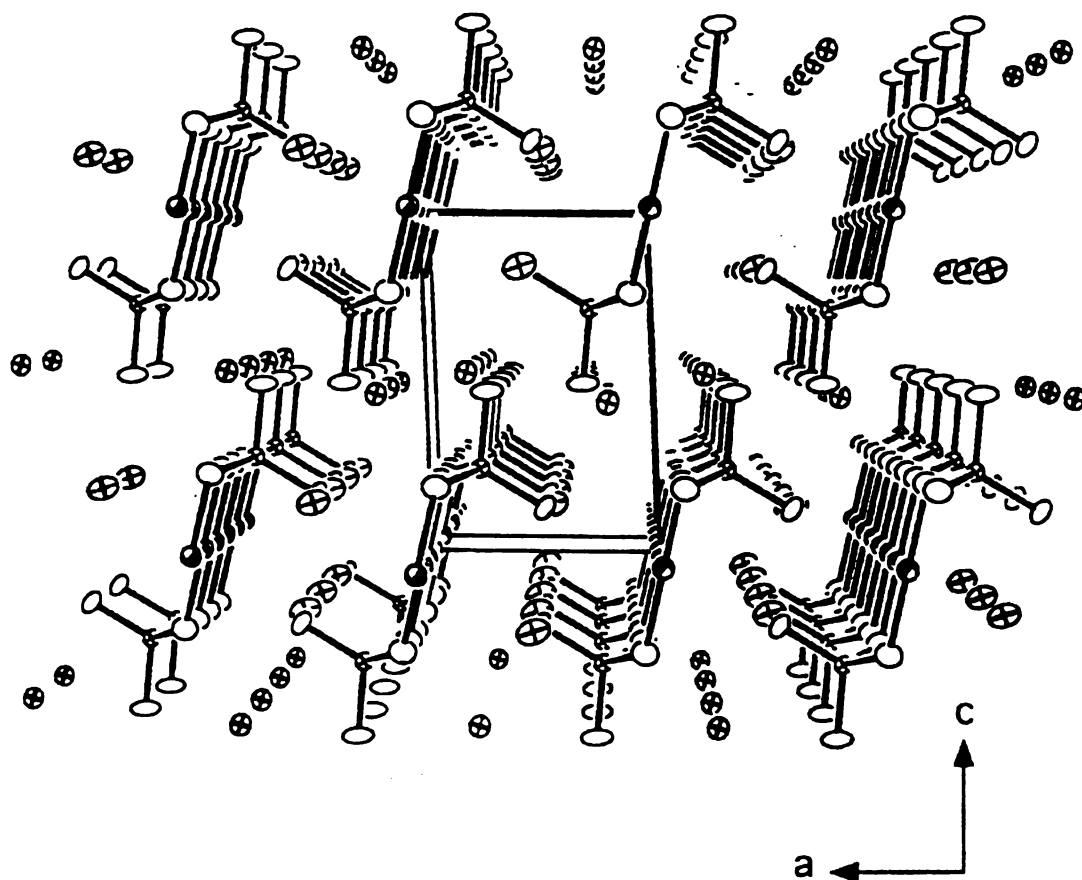Figure 7-4:   View of a single $[AuPS_4]_n^{2n-}$ chain in Cs_2AuPS_4 (III), with labeling.
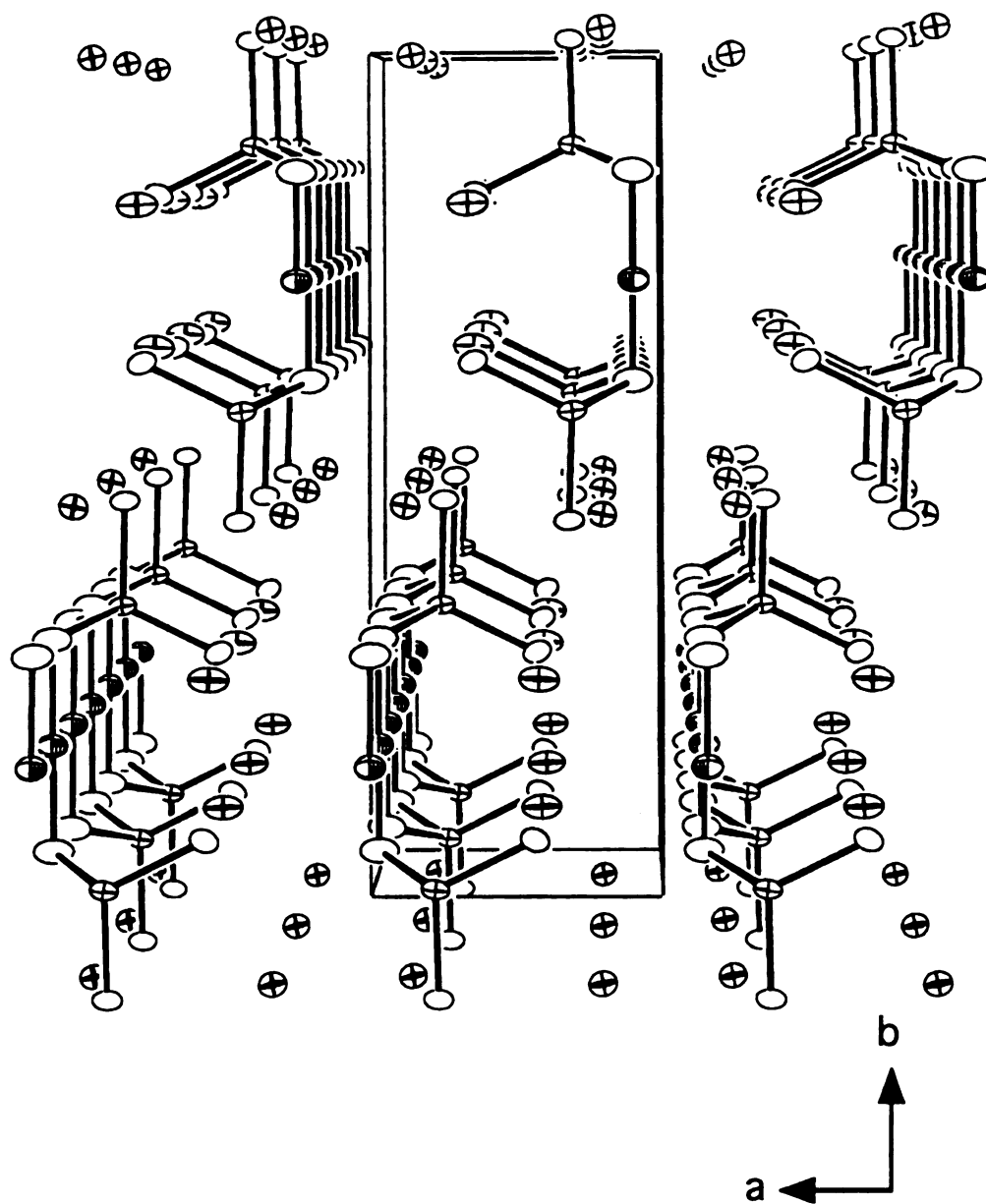
Figure 7-5:   ORTEP representation of Cs₂AuPS₄ (III) as viewed down the c - axis
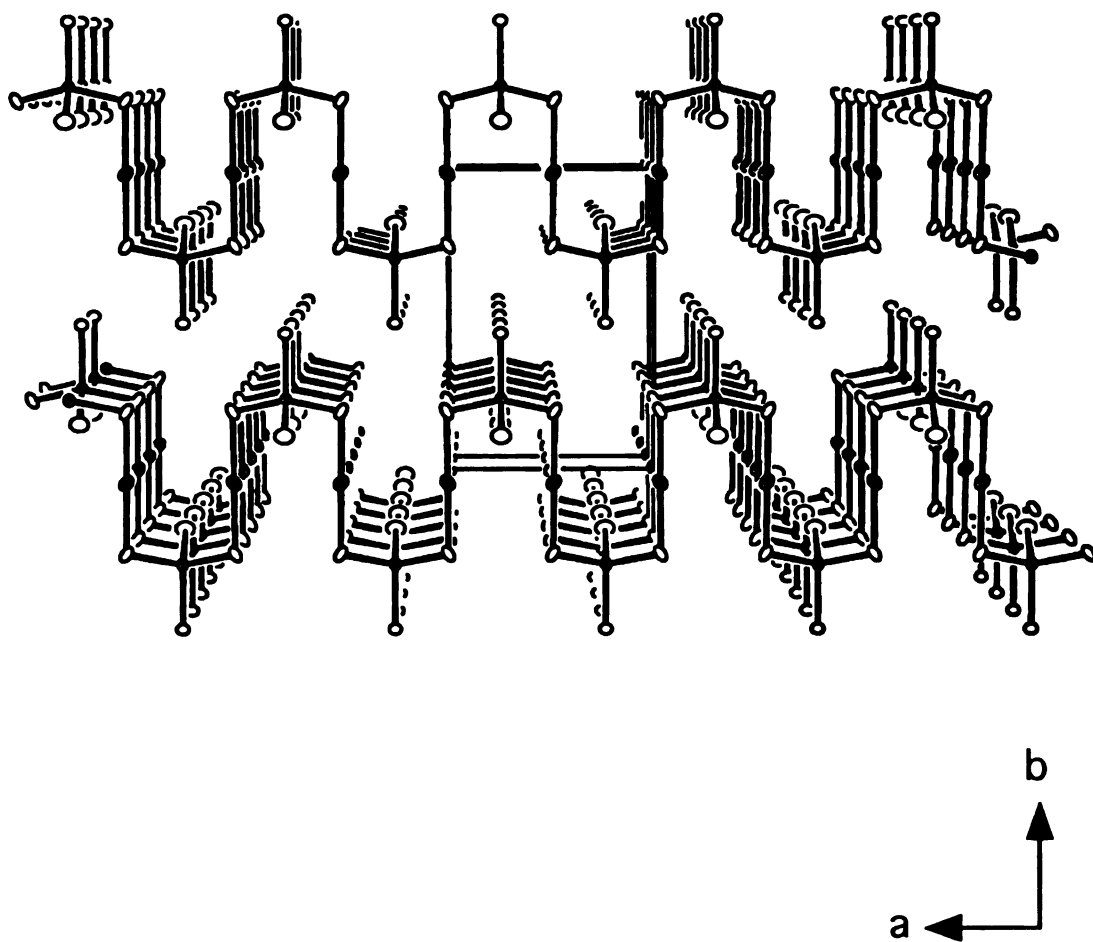(50% probability elliposids).
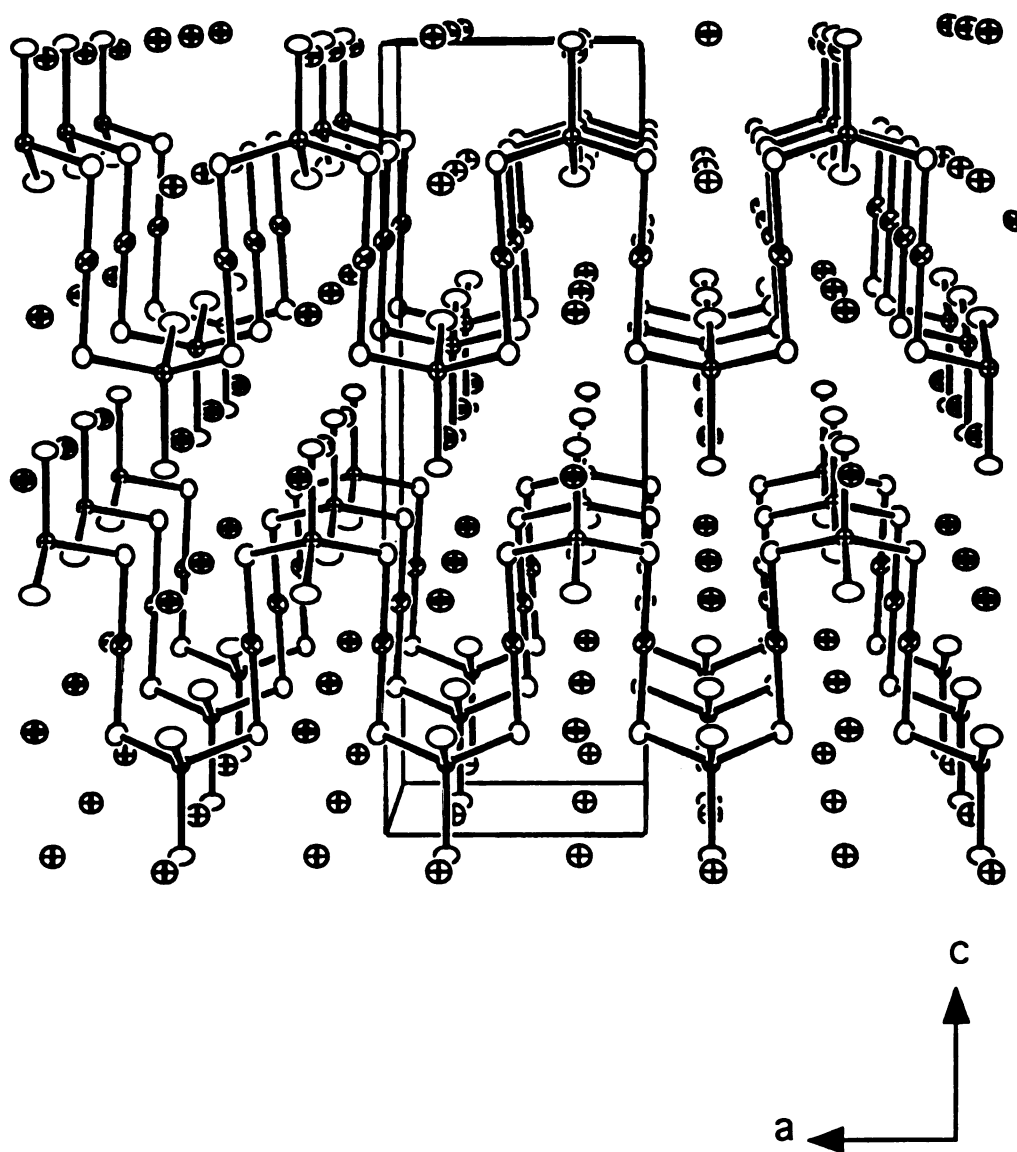
Figure 7-6:   ORTEP representation of Cs$_2$AuSbS$_4$ (III) as viewed down the b - axis
(50% probability elliposids).
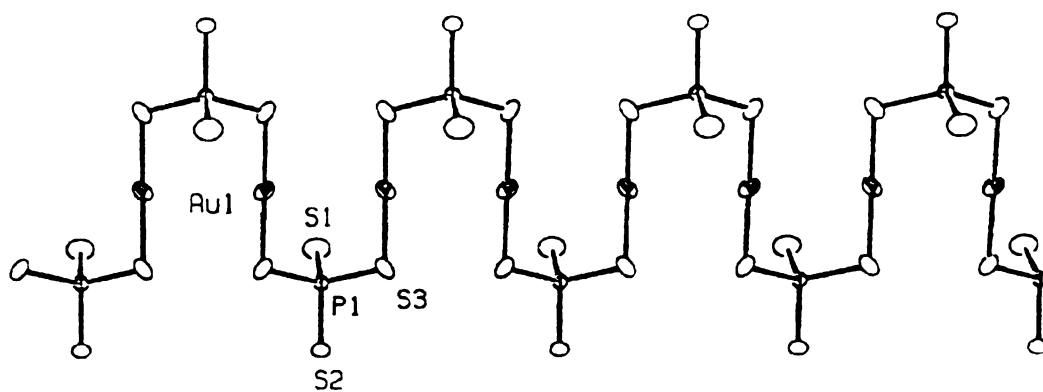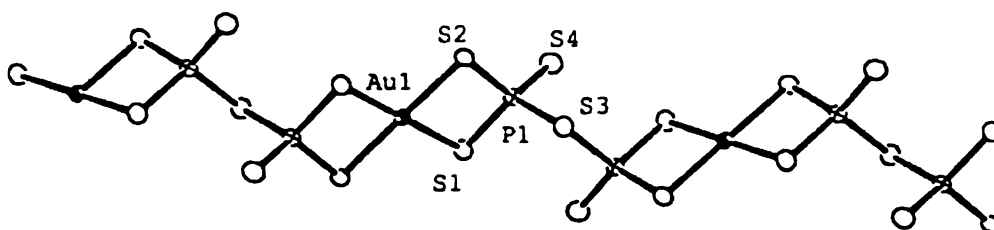
Figure 7-7:   View of a single $[AuP_2S_7]_n^{n-}$ chain in $K_2AuP_2S_7$ (IV), with labeling.

Figure 7-8: ORTEP representation of K$_2$AuP$_2$S$_7$ (IV) as viewed down the *a* - axis (50% probability elliposids). Small octant shaded ellipsoids; Au, principal axis ellipsoids; P, boundary ellipsoids; S, boundary and axis ellipsoids; K.

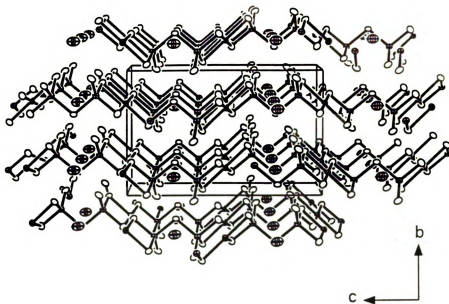Figure 7-9: ORTEP representation of $K_2AuP_2S_7$ (IV) as viewed along the [101] direction (50% probability ellipsoids). small octant shaded elliposids; Au, principal axis ellipsoids; P, boundary ellipsoids; S, boundary and axis ellipsoids; K.
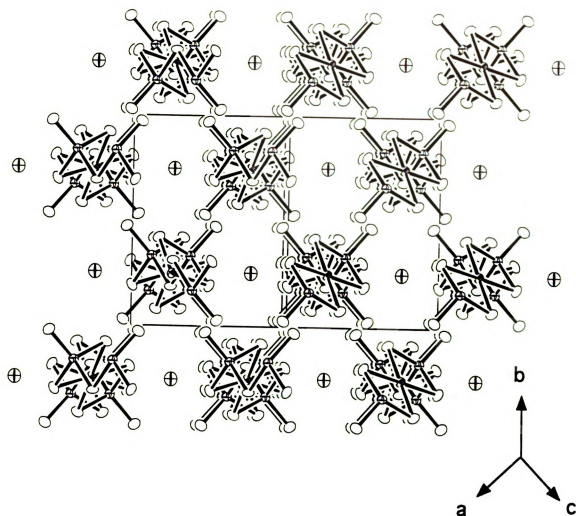
3.2. Synthesis, Spectroscopy and Thermal Analysis

The synthesis were the result of a redox reaction in which the metal is oxidized by polychalcogenide ions in the $A_x[P_yQ_z]$ flux. The Au cation centers are then coordinated by the highly charged $[P_yQ_z]^{n-}$ ligands. The molten polychalcophosphate flux method is very effective for crystal growth in this system. The isolation of pure crystalline products is facilitated by the residual polychalcophosphate fluxes solubility in aqueous and/or organic solvents. The flexibility of this method is demonstrated by the easy manipulation of the fluxes Lewis basicity by varying its starting composition. This results in compounds containing not only different $[P_xQ_y]^{n-}$ units. An additional advantage of this method is its ability to stabilize either P^{5+} or P^{4+} species which results in compounds which form different $[P_xQ_y]^{n-}$ units.

Our studies with quaternary chalcophosphates provide enough examples for the construction of Table 7-11 in which we summarize the conditions under which each species is stabilized. It is evident that there are significant differences between the thiophosphates and the selenophosphates systems and each case we be discuss separately.

For the thiophosphates, a wide range of conditions result in the formation of the P^{5+} species, exclusively. Low P_2S_5 concentrations favors the tetrahedral $[PS_4]^{3-}$ unit while high concentrations of P_2S_5 favors the formation of a higher nuclearity $[P_2S_7]^{4-}$ unit. A review of the literature revealed only a few structurally characterized quaternary alkali compounds featuring the ethane-like $[P_2S_6]^{4-}$ unit. Of these compounds, KMP_2S_6 (M = Mn, Fe)[26] was synthesized by direct combination and only $Na_{0.16}Bi_{1.28}P_2S_6$[3] was produced in a molten thiophosphate flux. In the latter case the use of the less basic Na^+ counterion may be important for the stabilization of a P^{4+} containing $[P_xS_y]^{n-}$ unit. Attempts to increase the amount of gold incorporated into a thiophosphate framework or the breakdown of the

Table 7-11. Synthetic conditions for the different $[P_yQ_z]^{n-}$ units. (M = metal, A_2Q = alkali

chalcogenide).

M / P_2Se_5 / A_2Se / Se	P^{n+} / ligands	References
1 / 1-3 / 1-2 / 10	P^{4+} / $[P_2Se_6]^{4-}$	1, 4, 5, 9, 12, present work
1 / 1.5-2 / 3-4 / 10	P^{5+} / $[PSe_4]^{3-}$, $[PSe_5]^{3-}$, $[P_2Se_8]^{4-}$	6,8, present work
1 / 2-3 / 2 / 10	P^{5+} / $[P_2Se_7]^{4-}$, $[P_2Se_9]^{4-}$	7
M / P_2S_5 / A_2S / S	P^{n+} / ligands	References
1 / 1.5-3 / 2-4 / 4-12	P^{5+} / $[PS_4]^{3-}$, $[P_2S_7]^{4-}$,	2, 3, present work
1 / 3 / 2 / 4	P^{4+} / $[P_2S_6]^{4-}$,	3

$[AuPS_4]_n^{2n-}$ chains into a previously unknown molecular $[Au_2(PS_4)_2]^{4-}$ anion resulted in a mixture of A_2AuPS_4 and unreacted Au metal.

According to the Table 7-11, the most decisive factor to produce P^{5+} or P^{4+} species in the selenophosphates flux is the A_2Se content. Increasing the A_2Se concentrations (raising the Lewis basicity), stabilizes $[P_xSe_y]^{n-}$ units containing P^{5+} species. Decreasing the A_2Se concentration (lowering the basicity), favors the stabilization of a reduced P^{4+} species, and in particular the $[P_2Se_6]^{4-}$ ligand. The only exception is Ti that is found coordinated with $[P_xSe_y]^{n-}$ units containing P^{5+} species,even under low basicity conditions.[7] The highly acidic Ti^{4+} cation may be responsible for this anomaly. Attempts to synthesize the hypothetical $AAuP_2Se_6$ compound, containing a highly oxidized Au^{+3} ions and a reduced P^{+4} species were not succesfull. Instead the mixed valent $A_2AuP_2Se_6$[12] was stabilized, containing both Au^+ and Au^{+3} ions or $A_2Au_2P_2Se_6$, with only Au^+ ions were obtained.

Structurally the thiophosphate and selenophosphate systems possess staggering differences due mainly to the presence of different $[P_xQ_y]^{n-}$ units. Nevertheless, the $[AuPS_4]_n^{2n-}$ macroanion in (III) is similar to the $[AuP_2Se_8]_n^{3n-}$ macroanion in $A_3AuP_2Se_8$[16] in that two oxidatively coupled bridged $[PQ_4]^{3-}$ units give rise to a $[P_2Q_8]^{4-}$ unit. Even in this case, though there are other essential differences such as the metal/phosphorus ratio . When the same ligands and the same countercation are present it is possible to synthesize isostructural compounds. One such example are the isostructural compounds $KTiPSe_5$ [7] and $KTiPS_5$.[27]

The optical absorption properties were evaluated by examining single crystal optical transmission spectra of the materials (see Table 7-12). The spectra confirm the semiconducting nature of the materials by revealing the presence of sharp optical gaps. The band gaps of A_2AuPS_4 (A = K, Rb, and Cs) compounds exhibit steep absorption edges from which the band-gap, E_g, can be assesed at 2.51 (I), 2.59, (II) and 3.04 eV (III), respectively. The band-gaps of $AAuP_2S_7$ are 2.03 (IV), and 2.23 eV (V), respectively .

The energy-gaps for A_2AuPS_4 and $AAuP_2S_7$ (A = K, Rb) increase slightly with a corresponding increase in the cation size. The single crystal absorption specta for (I)-(III) and (IV)-(V) are given in Figures 7-9 and 7-10, respectively.

Table 7-12.   Optical Band Gaps and Melting Point Data for (I)-(V).

Formula	E_g, eV	mp, $^{\circ}C$
K_2AuPS_4	2.50	498
Rb_2AuPS_4	2.59	401
Cs_2AuPS_4	3.04	375*
$KAuP_2S_7$	2.09	398
$RbAuP_2S_7$	2.15	404[i]

* = converts to β - Cs_2AuPS_4 at T = 375°C.

i = incongruent melting.

The far-IR and Raman data were in good agreement and the results are summarized in Table 7-13. The far-IR spectra of A_2AuPS_4 (I)-(III) and $AAuP_2S_7$ (IV)-(V) are quite complex. Absorptions in the 620-400 cm^{-1} range for (I)-(III) are tentatively assigned to the P-S vibrational stretching modes by analogy with the $AuPS_4$,[11] MPS_4 (M = In, Ga, and Ba)[28] and $KNiPS_4$.[29] Absorptions below 400 cm^{-1} are assigned to S-P-S bending modes and Au-S vibrations.[24] By comparison with $KAuS_5$ the absorption at ca. 320 cm^{-1} can be tentatively assigned as Au-S stretching vibration.[30] The Far-IR of (IV)-(V) displays a number of absorptions in the 600-400 cm^{-1} range. The sharp absorption at 458 cm^{-1} represents the characteristic P-S-P stretching vibration while the remaning absorptions are due to the -PS_3 stretching vibrations by analogy to $Ag_4P_2S_7$.[31,32] Absorptions below 400 cm^{-1} are assigned to Au-S stretching vibrations and P-S deformation modes.

The Raman spectra of (I)-(III) displayes absorbencies at ca. 395 cm^{-1}, 217 cm^{-1}, and 181 cm^{-1}, characteristic of the tetrahedral $[PS_4]^{3-}$ unit by comparison with the Raman spectrum of $Na_3PS_4 \cdot 9H_4O$.[27] The characteristic Au-S vibration[12] at ca. 327 cm^{-1} is observed for (I) but not for (III). The Raman spectrum of (IV) display absorptions in the 217-670 cm^{-1} range that are tentatively assigned to P-S and the absorptions below 200cm^{-1} are assigned to Au-S stretching vibrations. The Raman spectra for (I), (III), and (IV) are given in Figure 7-11.

Table 7-13. Infrared and Raman Data (cm⁻¹) for (I), (III) and (IV).

K_2AuPS_4 (I)		Cs_2AuPS_4 (III)		$KAuP_2S_7$ (IV)	
IR	Raman	IR	Raman	IR	Raman
		619			669
	603			576	
552	551			543	
				536	
519		519			
	470		471		
				458	
	419		410		418
400	395	384	398	387	
368		370	363		367
350	355				
327				327	325
303				304	
289				288	286
278			271	280	
268					
253	257			255	256
246	241	241	244	240	
217	217		217	228	
208				209	210
202				203	
196	181		183		
169		161		170	
	152		150		

Differential thermal analysis (DTA) data followed by careful XRD analysis of the residues, show that (I)-(II) melt congruently at 498°C and 401°C, respectively. Typical thermogram for (II) is shown in Figure 7-12A. The DTA of (III) indicates that the compound undergoes a structural transformation above 375°C, forming a mixture of α-Cs_2AuPS_4 and β-Cs_2AuPS_4. The x-ray powder pattern of β-Cs_2AuPS_4 indexed with the powder pattern of (I)-(II), suggesting that α-Cs_2AuPS_4 was a kinetically stable phase. The DTA of (IV) shows that the material melts congruently at 398°C. The DTA of (V) shows that it melts incongruently at 404°C to form a mixture of $RbAuP_2S_7$ and an as yet unknown phase. Typical thermogram for (IV) is shown in Figure 7-12B. Table 7-12 shows the optical and melting point data for all compounds.
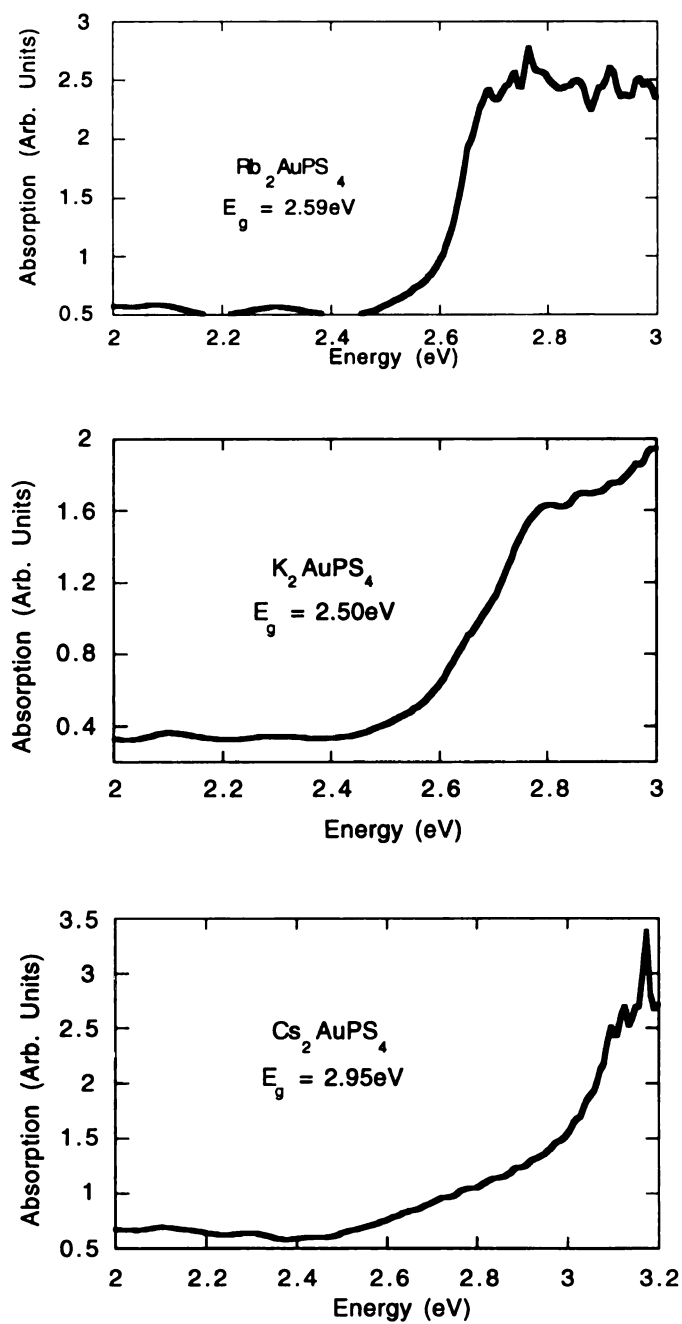
Figure 7-10:   Single crystal optical absorption spectra of (A) K_2AuPS_4 (I), (B) Rb_2AuPS_4 (II) and (C) Cs_2AuPS_4 (III).
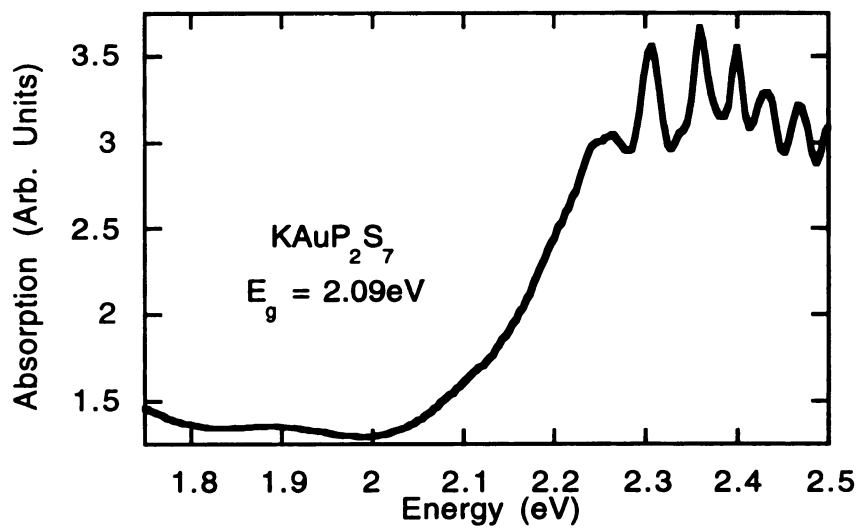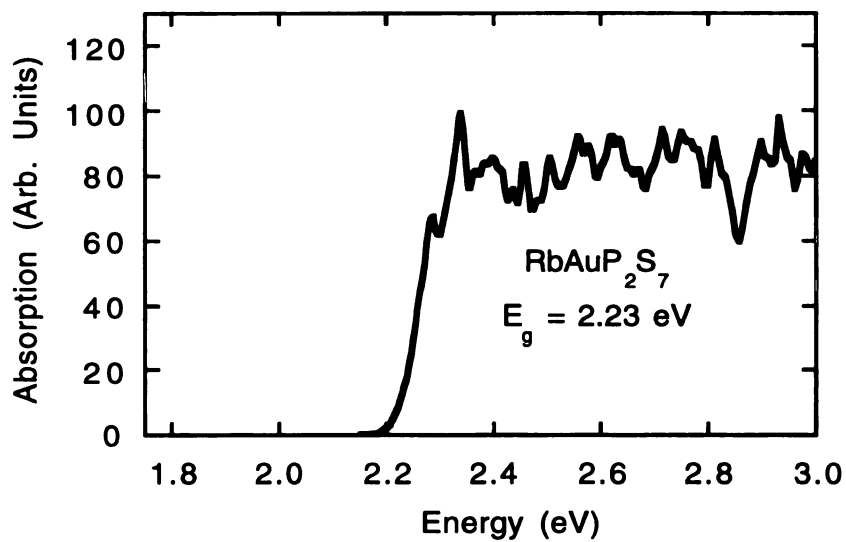
Figure 7-11:   Single crystal optical absorption spectra of (A) KAuP$_2$S$_7$ (IV), and (B) RbAuP$_2$S$_7$ (V).
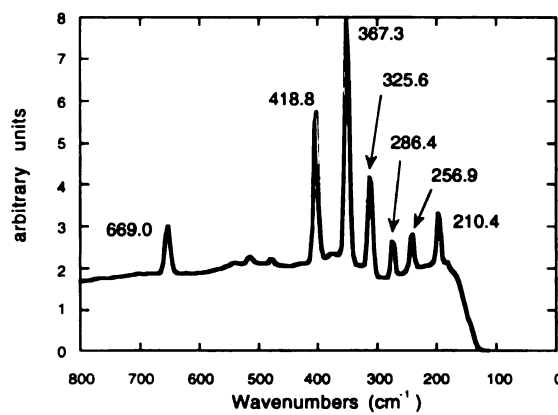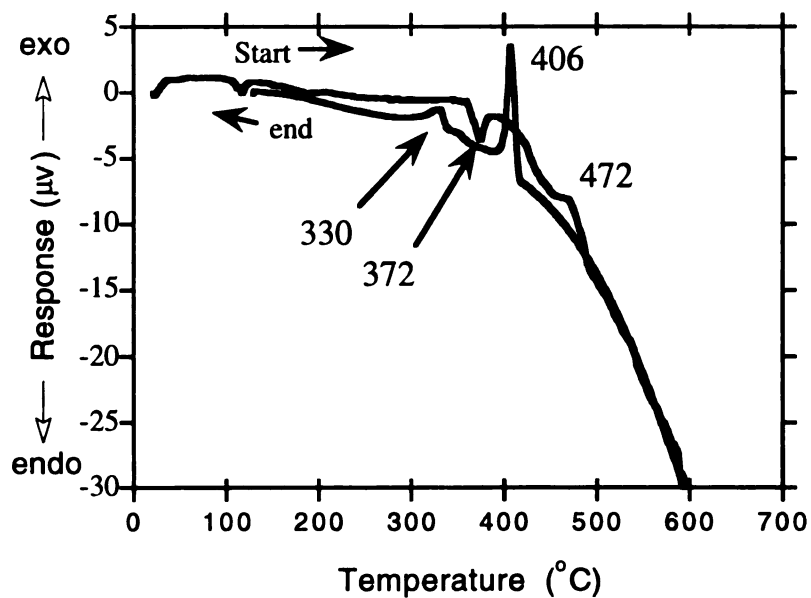
(A)
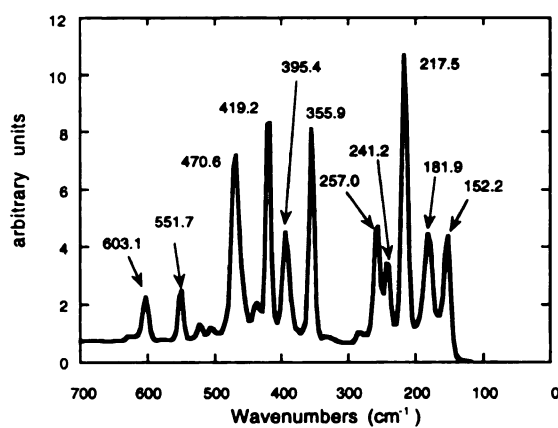
(B)
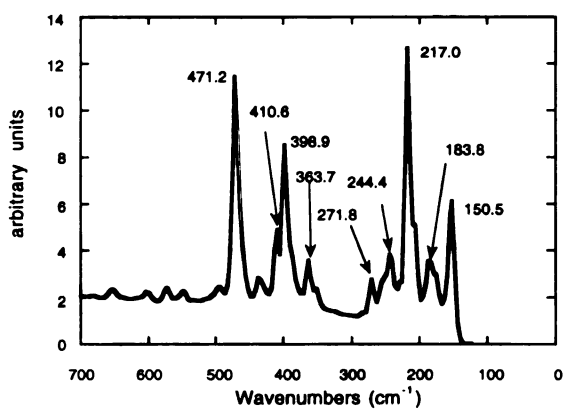
(C)

Figure 7-12:   Raman spectra of (A) K_2AuPS_4, (B) Cs_2AuPS_4, and (C) $KAuP_2S_7$.
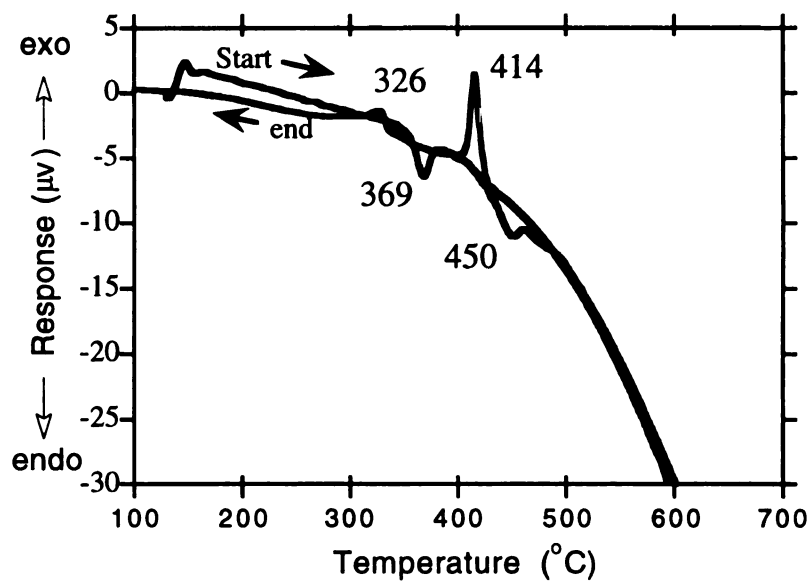
Figure 7-13: (A) DTA diagram for α-Cs$_2$AuPS$_4$ (first cycle).(B) Second DTA cycle of α-Cs$_2$AuPS$_4$, showing two phases.
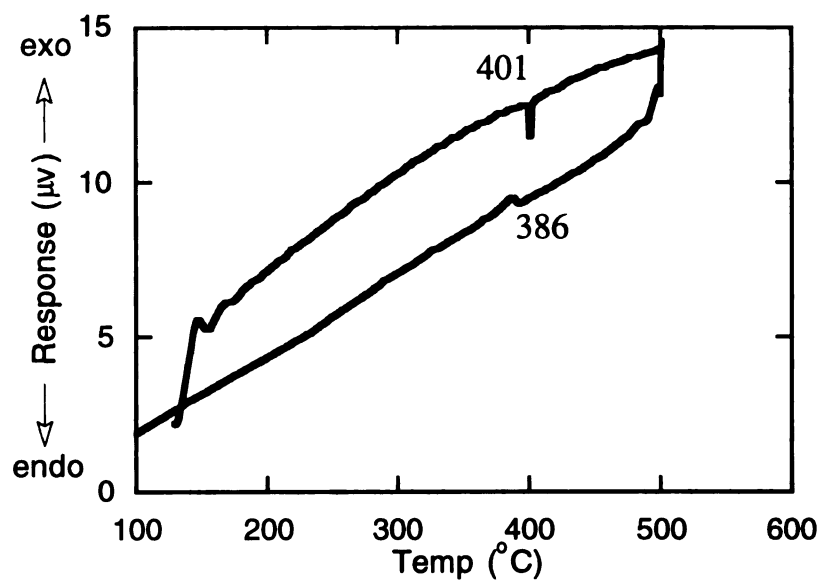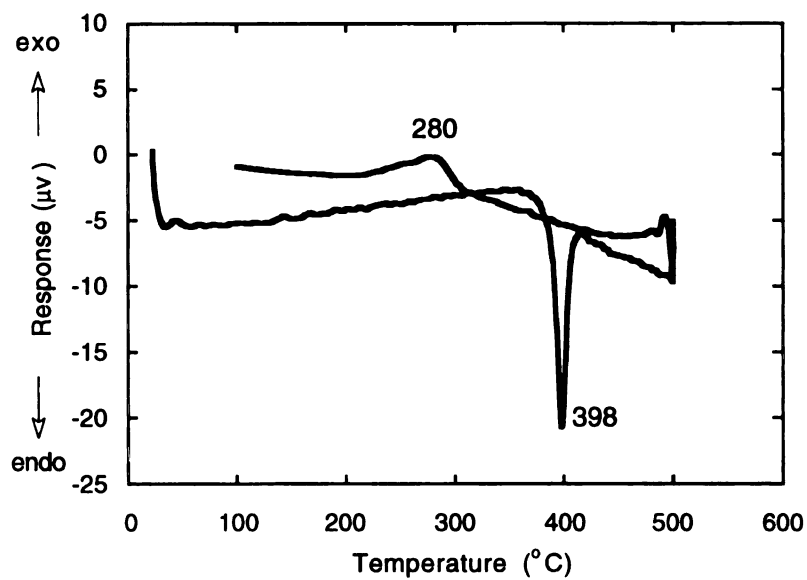
Figure 7-14:   (A) DTA diagram for Rb_2AuPS_4. (B) DTA diagram for $KAuP_2S_7$.

4. Conclusion

In summary, the compounds reported here are the first gold thiophosphate compounds perpared in a molten polythiophosphate flux. The structural diversity displayed is astonishing and is due mainly to the variety of binding modes of the $[P_yQ_z]^{n-}$ units. The fluxes provided a convenient entry into the unknown Au chemistry and preliminary results indicate that the elusive ternary Au/P/Q (Q = S, Se) compounds can also be synthesized and structurally characterized.[34] The use of low temperatures allows the synthesis of thermodynamically unstable compounds. Their metastable nature can be clearly seen in their thermal analysis. Control of the flux composition and basicity is paramount in controling the nature of the $[P_yQ_z]^{n-}$ units stabilized in the resulting materials. This knowledge provides the ability to synthesize compounds with preselected $[P_yQ_z]^{n-}$ units, although the final structure will be almost imposible to predict. This, in addition to, the significant chemical differences between the thiophosphate and selenophosphate systems, suggests that both systems should be explored to fully comprehend the chalcophosphate anion chemistry.

List of References

1. (a) Sutorik, A.; Kanatzidis, M. G. *Progr. Inorg. Chem.,* **1995**, *43*, 151. (b) Kanatzidis, M.G. *Curr. Opinion Solid State and Mater. Sci.,* **1997**, *2*, 139.

2. T. J. McCarthy, T. Hogan, C. R. Kannewurf, M. G. Kanatzidis, *Chem. Mater.,* **1994**, *6*, 1072.

3. McCarthy, T. J.; Kanatzidis, M. G. *J. Alloys Comp.,* **1996**, 236, 70.

4. McCarthy, T. J.; Kanatzidis, M. G. *J. Chem. Soc. Chem. Commun.,* **1994**, 1089.

5. McCarthy, T. J.; Kanatzidis,M. G. *Chem. Mater.,* **1993**, *5*, 1061.

6. Chondroudis, K.; McCarthy, T. J.; Kanatzidis, M.G. *Inorg. Chem.,* **1996**, *35* 840.

7. Chondroudis, K.; Kanatzidis, M.G. *Inorg. Chem.,* **1995**, *34*, 5401.

8. Chondroudis, K.; Kanatzidis, M.G. *J. Chem. Soc. Chem. Commun.,*. **1996**, 1371.

9. Loken, S; Tremel. W., *Eur. J. Inorg. Chem.* , **1998**, 283-.

10. (a) Chondroudis, K.; Kanatzidis, M.G. *C. R. Acad. Sci. Paris, Series B*, **1996**, *322*, 887. (b) Chondroudis, K.; Kanatzidis, M.G. *J. Am. Chem. Soc.,* **1997**, *119*, 2574.

11. (a) Chen, J. H; Dorhout, P. K. *Inorg. Chem.,* **1995**, *34*, 5705. (b) Chen, J. H; Dorhout, P. K. Ostenson, J. E. *Inorg. Chem.* **1996**, *35*, 5627.

12. Pätzmann, U.; Brockner, W.; Cyvin, B. N.; Cyvin, S. J. *Raman Spectroscopy*, **1986**, *17*, 257.

13. Chondroudis, K.; McCarthy, T. J.; Kanatzidis, M.G. *Inorg. Chem.,* **1996**, *35*, 3451.

14. McCarthy, T.J. Kanatzidis, M.G. *Inorg. Chem.,* **1995**, *34*, 1257.

15. CERIUS², Version 1.6, Molecular Simulations Inc., Cambridge, England, 1994.

16. McCarthy, T. J.; Ngeyi, S.-P.; Liao J.-H.; DeGroot, D.; Hogan, T.; Kannewurf, C. R.; Kanatzidis, M.G. *Chem. Mater.,* **1993**, *5*, 331.

17. Walker, N.; Stuart, D. *Acta Cryst.,* **1983**, *A39*, 158.

18. (a) Sheldrick, G. M., in *Crystallographic Computing 3* ; Sheldrick, G. M., Kruger, C., Doddard, R., Eds.; Oxford University Press: Oxford, England, **1985**, p. 175. (b) Gilmore G. J., *Appl. Cryst.* ; **1984**, *17*, 42.

19. Chondroudis, K.; Hanko, J. A.; Kanatzidis, M.G. *Inorg. Chem.,* **1997**, *36*, 2623

18. Brec, R.; Ouvrard, G.; Evain, M.; Grenouilleau, P.; Rouxel, J. *J. Solid State Chem.,* **1983**, *47*, 174.

20. Y. Park, M. G. Kanatzidis, *Angew. Chem. Int. Ed. Engl.* **1990**, *29*, 914.

21. Y. Park, Ph.D. Dissertation, Michigan State University, E. Lansing, MI, **1991**.

22. Liao, J.-H.; Kanatzidis, M.G. *Chem. Mater.,* **1993**, *5*, 1561.

23. Teske, Chr. L. *Z. Anorg. Allg Chem.,* **1978**, *445*, 193-201.

24. Klepp, K.O.; Bronger, W. *J. Less Common Metals.,* **1988**, *137*, 13.

25. Hanko, J.A.; Kanatzidis, M.G. Manuscript in preparation .

26   (a) Menzel, F.; Brockner, W; Carrillo-Cabrera, W.; von Schnering, H.G. *Z. Anorg. Allg Chem.* **1994**, *620* , 1081.   (b) Carrillo-Cabrera, W.; Sabmannshausen, J.; von Schnering, H.G.; Menzel, F.; Brockner, W. *Z. Anorg. Allg Chem.,* **1994**, *620* , 489.

27. Do, J.; Lee, K.; Yun, H. *J. Solid State Chem.,* **1996** *125* , 30.

28. (a) D'ordyai, V.S.; Galagovets, I.V.; Peresh, E. Yu.; Voroshilov, Yu. V.; Gerasimenko, V.S.; Slivka, V. Yu.; *Russ. J. Inorg. Chem,* **1979**, *24*, 1603.

29. Sourisseau, C.; Cavagant, R.; Fouassier, M.; Brec, R.; Elder, S.H.; *Chemical Physics,* **1995**, *195*, 351.

30. Y. Park, Ph.D. Dissertation, Michigan State University, E. Lansing, MI, **1991**.

31. Menzel, F.; Ohse, L.; Bröckner, W.; *Heteroatom Chem.,* **1990**, *1*, 357.

32.   (a) Queigrec, M.; Evain, M.; Brec, R.; Sourisseau, C.; *J. Solid State Chem.*, **1992**, *189*, 209.

33.   Greenwood, N. N.; Earnshaw, A. *Chemistry of the Elements*; Pergamon Press: New York, 1993, p. 1372.

34.   Chondroudis, K.; Hanko, J.A.; Kanatzidis, M.G. Work in progress.

CONCLUSIONS AND OUTLOOK

The chalcophosphate chemistry was the center of a significant amount of research in the 1970's through the 1980's. By using primarily a direct combination approach a number of new ternary chalcophosphate compounds were discovered, many with new structure types. This approach proceeded until almost every element in the periodic table was studied, then the exploratory nature of the research gradually faded and the emphasis shifted to improving the properties of known phases with potential technological interest.

The corresponding chalcoantimonide chemistry was in a similar state of development. Using direct combination and hydrothermal synthesis, a number of new ternary chalcoantimonate compounds covering the spectrum of structural possibilities, from molecular species to three-dimensional frameworks, were observed. The lower reaction temperatures utilized by hydrothermal synthesis allowed the replacement of the alkali cations with larger organic counterions, leading to the formation of more open frameworks that may serve as forerunners to a new class of microporous solids. Even with the extensive research in the chalcophosphate and chalcoantimonate systems, there are still metal systems which have not been studied.

The molten polychalcogenide flux as a new synthetic methodology, particularly the chalcophosphate and chalcoantimonate fluxes, offer a great potential to expand and characterize new classes of compounds in a systematic way. This experimental methodology was first applied to the selenophosphate system, reviving this area of research which had been dormant for several years. The same approach has now been applied to the thiophosphate system to synthesize new quaternary thiophosphate compounds and probe whether the coordination chemistry paralleled that of the selenophosphate system.

This recent activity has uncovered a multitude of new materials with elaborate structure types arising from a variety of new binding modes displayed by the $[P_xQ_y]_n^{n-}$ (Q = S, Se) units. An interesting trend, which became evident in this work, is that the

$[P_xSe_y]_n^{n-}$ species behave very differently than the corresponding $[P_xS_y]_n^{n-}$ species. This trend is manifested in not only in how the $[P_xQ_y]_n^{n-}$ (Q = S, Se) species bind to metal ions but also with respect to their relative stability. For example the tetrahedral $[PQ_4]^{3-}$ (Q = S, Se) unit, typically does not lead to the same structure types when compounds are formed; in fact, they do not give compounds with the same formula. Furthermore, the analogous synthetic conditions which may give rise to a certain $[P_xSe_y]_n^{2-}$ unit tend to give rise to a different $[P_xS_y]_n^{2-}$ unit, the anions often containing the phosphorous atom in a different oxidation state. The latter is a consequence of the difference in the electronegativity between the S and Se atoms. These facts underscore the need for the simultaneous exploration of both the thiophosphate and selenophosphate fluxes for the same metal system, and the continued search for fundamental differences in the chemistry and reactivity.

To further develop the molten polychalcogenide flux as a general synthetic methodology, it was extended to the chalcoantimonate systems, where there are few reported quaternary alkali chalcoantimonate compounds. A comparison of the chalcoantimonate to the chalcophosphate fluxes provides insight into the structural and chemical complexity of the two systems. The chalcoantimonate system follows the experimentally observed trend of the polychalcophosphate system. Basic conditions (increasing A_2Q) favor the tetrahedral $[EQ_4]^{3-}$ unit (E = P, Sb; Q = S, Se). Under these conditions, the $[SbQ_4]^{3-}$ unit is observed as a discrete tetrahedral species, while the $[PSe_4]^{3-}$ unit can participate in complex condensation equilibra, forming higher nuclearity chalcophosphate units such as $[P_2Se_8]^{4-}$, and $[P_2Se_9]^{4-}$. Under acidic conditions (increasing Q or decreasing A_2Q) both P and Sb favor reduced species. In the polythiophosphate system the reduced P^{+4} species is readily observed in the ethane - like $[P_2Q_6]^{4-}$ unit (Q = S, Se). While the antimony analog of the $[P_2Q_6]^{4-}$ unit has yet to be reported, the pyramidal Sb^{3+} species is the only other oxidation state species observed. The pyramidal $[SbQ_3]^{3-}$ unit (Q = S, Se) also participates in a separate yet complex

condensation equilibria, forming higher nuclearity $[Sb_xQ_y]^{n-}$ units. The thiophosphate system does not appear to stabilize a reduced species under acidic conditions, although increasing the P_2S_5 concentration favors a complex condensation equilibra, forming higher nuclearity chalcophosphate units such as $[P_2S_7]^{4-}$, and $[P_3S_9]^{3-}$.

Although the ability to synthesize new materials with preselected ligands imparts a large degree of synthetic control, a number of important parameters are still unknown. In particular, the nature of the thiophosphate and chalcoantimonate systems in the molten state can only be speculated, based on the $[P_xQ_y]^{n-}$ and $[Sb_xQ_y]^{n-}$ units found in the resulting compounds. Further elucidation of the kind of $[P_xQ_y]^{n-}$ and $[Sb_xQ_y]^{n-}$ units, existence of intermediates, equlibria resulting in the formation of higher nuclearity units, and the interaction with the metal need to be examined. The need for *in situ* experiments, such as Raman spectroscopy and X-ray or neutron diffraction experiments, may be the best approach to gain this information. In addition, NMR spectroscopy should be of considerable help in elucidating the equilibrium issues in these systems.

APPENDIX 1

Thiophosphate Flux Synthesis of $Cs_2CuP_3S_9$: An Unusual Chrial Compound with One-Dimensional Screw Helices.

Thiophosphate Flux Synthesis of $Cs_2CuP_3S_9$: An Unusual Chrial Compound with One-Dimensional Screw Helices.

Jason A. Hanko and Mercouri G. Kanatzidis[*]

Department of Chemistry, and Center for Fundamental Materials Research, Michigan State University, East Lansing, Michigan 48824.

Abstract

The reaction of Cu with a molten mixture of Cs_2S/P_2S_5 produces the quaternary compound $Cs_2CuP_3S_9$ (I). The bright yellow crystals of $Cs_2CuP_3S_9$ are stable in air and water for over a month. The compound crystallizes in the acentric, hexagonal space group $P6_5$ (no. 170) and at 23°C: $a = 15.874(2)$Å; $c = 35.100(7)$Å; $V = 7660(3)$Å^3; $Z = 22$. The $[CuP_3S_9]_n^{2n-}$ chains are comprised of an alternating arrangement of tetrahedral Cu^+ ions and cyclic $[P_3S_9]^{3-}$ units. The structure contains two unique $[CuP_3S_9]_n^{2n-}$ chains that pack in a helical fashion along the c-axis. The $[P_3S_9]^{3-}$ unit is related to the molecular adamantine $[P_4S_{10}]$ unit with one $[PS]^{3+}$ vertices removed and replaced by a Cu^+ ion. The title compound was characterized by Differential Thermal Analysis (DTA), Far-IR and Raman, and single crystal optical transmission spectroscopy. The preliminary investigations into the non-linear properties of (I) will be reported.

Introduction

During the past several years, we have demonstrated that the chalcophosphate fluxes are an excellent choice for the synthesis of new multinary chalcophosphate compounds.[1] These fluxes are commonly formed by the *in situ* fusion of $A_2Q/P_2Q_5/Q$ (A = alkali metal; Q = S, Se), forming a variety of $[P_yQ_z]^{n-}$ units in a molten polychalcogenide solvent. Under these conditions the coinage metals (Cu, Ag, Au) are readily oxidized by the polychalcogenide ligands from the flux and then coordinated by the various $[P_yQ_z]^{n-}$ (Q = S, Se) units, building up extended frameworks, stabilized by alkali cations. The exploration of the coordination chemistry of the coinage metals with these fluxes produced several unusual compounds, examples include: $Cs_2M_2P_2Se_6$ (M = Cu, Ag),[2] $K_3M_3P_3Se_9$ (M = Cu,[3a] Ag,[3b]), $ALa(P_2Se_6)$,[4] the mixed-valent $A_6Au^I_{1.5}Au^{III}_{1.5}(P_2Se_6)_3$ (A= K, Rb),[5] $A_3AuP_2Se_8$ (A = K, Rb, Cs),[6] $A_2Au_2P_2Se_6$ (A = K, Rb),[6] A_2AuPS_4 (A = K, Rb, Cs),[6] and $AAuP_2S_7$ (A = K, Rb),[6] $K_3CuP_2S_7$,[7] and $K_2Cu_2P_4Se_{10}$.[8] An unexplored area of the chalcophosphate chemistry is the phosphorous-rich thiophosphate fluxes, which can be achieved by the removal of the elemental sulfur. As previously reported,[6] a $[P_2S_5]$ rich flux favors the formation of the higher nuclearity $[P_2S_7]^{4-}$ unit. With the removal of the elemental sulfur delutant, the phosphorous concentration is further increased, stabilizing even higher nuclearity $[P_yS_z]^{n-}$ units. Preliminary investigations with these phosphorous-rich fluxes produced the quaternary compounds $A_2CuP_3S_9$ (A = K, Rb) containing the cyclic $[P_3S_9]^{3-}$ unit and $Cs_2Cu_2P_2S_6$[7], containing the ethane-like $[P_2S_6]^{4-}$ unit. Continuing our investigation of the coordination chemistry of these higher nuclearity $[P_xS_y]^{n-}$ units with coinage metals, we report on the synthesis, and physicochemical characterization of $Cs_2CuP_3S_9$,[9] a novel one-dimensional compound with an acentric structure. The $[CuP_3S_9]_n^{2n-}$ macroanion in (I) are very similar to the $[CuP_3S_9]_n^{2n-}$ chains previously reported in $A_2CuP_3S_9$ (A = K, Rb),[7] but with a completely different packing arrangement. In the previous structure, the $[CuP_3S_9]_n^{2n-}$ chains pack in an alternating

centrosymmetric fashion, but in $Cs_2CuP_3S_9$ the $[CuP_3S_9]_n^{2n-}$ macroanions pack in a helical screw-like arrangement.

The structure of $Cs_2CuP_3S_9$[10] contains two different $[CuP_3S_9]_n^{2n-}$ chains of alternating cyclic $[P_3S_9]^{3-}$ units chelating in a tridendate fashion to Cu^+ ions, see Figure 1. Figure 2a shows a $[CuP_3S_9]_n^{2n-}$ chain, highlighting the helical packing along the polar c-axis. Figure 2c shows a view of a $[CuP_3S_9]_n^{2n-}$ chain down the polar c-axis. A view of the $[CuP_3S_9]_n^{2n-}$ chain containing Cu(1) is shown in Figure 2c.

As viewed in Figure 2c, the basal plane of the $[CuS_4]$ tetrahedrons is defined by the tridendate chelation of three of the sulfurs from the cyclic $[P_3S_9]^{3-}$ units to the Cu^+ ions while the apical site of the copper tetrahedra is filled by a sulfur atom from a second neighboring $[P_3S_9]^{3-}$ unit. The average Cu-S distance of the three $[CuS_4]$ tetrahedrons is 2.306(9)Å, 2.307(9)Å, and 2.316(7)Å for Cu(1), Cu(2), and Cu(3), respectively. The S-Cu-S angles display a slight distortion from the tetrahedral geometry, with an average S-Cu-S angle of 109(2)°, 109(1)°, and 109(2)° for Cu(1), Cu(2), and Cu(3), respectively.

The two $[CuP_3S_9]_n^{2n-}$ chains contain three different $[P_3S_9]^{3-}$ units, with P-S bond distance and S-P-S angles that are well within the expected range reported for $A_2CuP_3S_9$ (A = K, Rb).[7] The P-S distances and S-P-S angles of $[P_3S_9]^{3-}$ unit in the $[CuP_3S_9]_n^{2n-}$ chain containing the Cu(1) ion are representative of the other two $[P_3S_9]^{3-}$ units. The P-S distances are in the range from 1.954(4)Å to 2.139(3)Å with an average P-S distances of 2.04(3)Å, 2.05(3)Å and 2.04(3) for P(1), P(2) and P(3), respectively. The S-P-S angles reveal only a slight distortions from the tetrahedral coordination geometry, with average S-P-S angle of 109(2)° for P(1), P(2), and P(3), respectively. The $[P_3S_9]^{3-}$ unit contains a $[P_3S_3]$ ring chair-shaped a almost-equilateral triangle with a mean P-P-P angle of 60.00(5)° and a mean P-P distance of 3.483(3)Å. Selected bond distances and angles are given in Table 1.

As described in the structure of $A_2CuP_3S_9$ (A = K, Rb),[7] there are two types of P-S distances in the three different cyclic $[P_3S_9]^{3-}$ units, the longer P-S distances within the

P_3S_3 ring and shorter P-S distances for the terminal sulfides. The average ring P-S distances were 2.11(5)Å, 2.11(4)Å and 2.12(4) for P(1), P(2), and P(3), respectively. The average terminal P-S distances were much shorter at 1.97(1)Å, for P(1), P(2), and P(3), respectively. Other $[P_xS_y]^{n-}$ units such as the bi-tetrahedral $[P_2S_6]^{2-}$ (2.111(1)Å versus 1.993(1)Å) and quadri-tetrahedral $[P_4S_{12}]^{4-}$ units (2.113(3)Å versus 1.989(2)Å), display a similar discrepancies in the $[P_3S_3]$ ring P-S bond distances and the terminal P-S bond distances. In oxides, this segregation is more pronounced. Examination of the corresponding phosphates $Na_3P_3O_9$ and the monohydrate $Na_3P_3O_9,H_2O$,[12] show that the average P-O bond distance in the P_3O_3 ring is 1.615Å, while the average terminal P-O bind distance is 1.484Å.

The $[CuP_3S_9]^{2-}$ chains are separated by Cs^+ ions that are located in six different sites. In $Cs_2CuP_3S_9$ Cs(1) is in ninefold coordination to sulfur atoms [range of Cs(1)-S distances, 3.501(3)Å to 4.107(3)Å ; average 3.73(6)Å], Cs(2) is in eightfold coordination to sulfur atoms [range of Cs(2)-S distances, 3.515(3)Å to 3.911(3)Å; average 3.70(4)Å], Cs(3) is in tenfold coordination to sulfur atoms [range of Cs(3)-S distances, 3.512(3)Å to 4.082(3)Å; average 3.83(6)Å], Cs(4) is in tenfold coordination to sulfur atoms [range of Cs(4)-S distances, 3.575(3)Å to 4.185(3)Å; average 3.83(7)Å], Cs(5) is in ninefold coordination to sulfur atoms [range of Cs(5)-S distances, 3.530(3)Å to 4.143(3)Å ; average 3.74(8)Å], and Cs(6) is in ninefold coordination to sulfur atoms [range of Cs(6)-S distances, 3.552(3)Å to 4.085(3)Å ; average 3.73(5)Å].

The optical absorption properties were evaluated by examining the single crystal optical transmission spectrum of $Cs_2CuP_3S_9$, see Figure 3. The sharp optical gap in the spectrum suggest that the compound is a wide bandgap semiconductor with a band gap (E_g) of 2.61 eV.

The far-IR[12a] spectrum of $Cs_2CuP_3S_9$ displays several absorptions in the 600-400 cm^{-1} range. The sharp absorption at 400 cm^{-1} and 463 cm^{-1} are characteristic of the P-S-P stretching vibrations in the cyclic $[P_3S_9]^{4-}$ unit. The doubly bridging bonding motif of the

tetrahedral $[PS_4]^{3-}$ units lowers the energy of the S-P-S vibrations. The remaining absorptions are tentatively assigned to the $-PS_2$ stretching vibrations by analogy to $AAuP_2S_7$ (A = K, Rb)[3]. Absorptions below 400 cm^{-1} are assigned to Cu-S stretching vibrations.

The Raman spectrum[12b] of $Cs_2CuP_3S_9$ displays absorptions in the 250-600 cm^{-1} range that are tentatively assigned to P-S and absorptions below 250 cm^{-1} are assigned to Cu-S stretching vibrations. The stretching vibrations at *ca.* 386 cm^{-1} and 294 cm^{-1} are assigned to the $[PS_4]^{3-}$ by analogy to A_2AuPS_4, $AAuP_2S_7$ (A = K, Rb)[3], and $A_2P_2S_6$ (A = K, Cs)[13]. The Raman spectrum of $Cs_2CuP_3S_9$ is shown in Figure 4.

Differential thermal analysis (DTA) data followed by careful XRD analysis of the residues, revealed that the title compound melts incongruently at ~477°C forming a mixture of $Cs_2CuP_3S_9$ and $Cs_2P_2S_6$[14].

The non - linear optical properties were examined using a preliminary screening test developed in our lab.[15] The sample displayed a weak second harmonic generation (SHG) signal. Although a weak SHG signal is observed, the test is not conclusive because the sample cannot be examined in all possible orientations.

The synthesis of $Cs_2CuP_3S_9$ further validates the chemical diversity of the thiophosphate system and further underscores the chemical difference between the selenophosphate system. The acentric structure of $Cs_2CuP_3S_9$ is very unusual and could not have been predicted before the compound was synthesized. The highly acentric arrangement makes it a potential candidate for a number of applications. While the preliminary investigations of the non-linear optical properties of the title compound were encouraging, further testing is necessary. The dramatic structural change introduced by the slight modifications of the thiophosphate flux shows that we are still at the mercy of serendipity. For at this stage, we only have a rough idea of the complex equlibra between stabilization of these higher nuclearity $[P_xS_y]^{n-}$ units.

List of References

1. (a) Kanatzidis, M.G. *Curr.Opinion Solid State and Mater. Sci.* **1997**, *2*, 139. (b) Sutorik, A.; Kanatzidis, M.G. Prog. Inorg. Chem., **1995**, *43*, 151.

2. McCarthy, T. J.; M. G. Kanatzidis, *Inorg. Chem.* **1995**, *34*, 1257.

3. Dorhout, P.K.; Malo, T.M. *Z. Anorg. Allg. Chem.* **1996**. *622*, 385.

4. Chen, J.H.; Dorhout, P.K. *Inorg. Chem.* **1995**, *34*, 5705. (b) Chen, J.H.; Dorhout, P.K.; Ostenson, J.E. *Inorg. Chem.* **1996**, *35*, 5627.

5. Chondroudis, K.; McCarthy, T. J.; Kanatzidis, M.G. *Inorg. Chem.* **1996**, *35*, 3451.

6. Chondroudis, K.; Hanko, J.A.; Kanatzidis, M.G. *Inorg. Chem.* **1997**, *36*, 2632.

7. Hanko, J.H.; Kanatzidis, M.G. Submitted for Publication.

8. Chondroudis, K.; Kanatzidis, M.G. Submitted for Publication.

9. (a) $Cs_2CuP_3S_9$ was synthesized from a mixture of 0.032g (0.50 mmole) Cu, 0.220g (1 mmole) P_2S_5 and 0.149g (0.50 mmole) Cs_2S which was sealed under vacuum in a Pyrex tube and heated to 500°C for 4 d followed by cooling to 100°C at 4°C h^{-1}. The excess $Cs_x[P_yS_z]$ flux was removed by washing with degassed methanol under inert atmosphere to reveal irregular bright yellow crystals (75% yield based on Cu). Microprobe analysis gave an average composition of $Cs_{2.25}CuP_{3.8}S_{6.1}$.

10. A Siemens SMART Platform CCD diffractometer from a crystal of 0.200 x 0.200 x 0.120 mm dimensions and Mo Ka (1 = 0.71073 Å) radiation. An empirical absorption correction.was applied to the data during data processing. Crystal data at 23°C: a = 15.874(2)Å; b = 15.874(2)Å; c = 35.100(7)Å; a = 90.00; b = 90.00; g = 120.00; V = 7660(3)Å^3; Z = 22; D_C = 2.767 g/cm^{-3}; space group $P6_5$ (no. 141); m = 6.804 cm $^{-1}$ index ranges -19 = h = 21, -20 = k = 21, -22 = l = 47 ; total data 48681; unique data 9745; (R_{int} = 0.0944); data with $F_o^2 > 2s(F_o^2)$ 4056; no. of variables, 406; final R/Rw 0.030/0.069; GOF 0.335; largest diff. peak and hole

0.882/-0.767e Å⁻³. (b) SHELXL: Version 5.03, 1994. Sheldrick, G.M. Siemens Analytical X-ray Instruments, Inc., Madison, WI 53719.

11. Ondik, H.; *Acta. Crystallogr,* **1965**, *18*, 226.

12. (a) Far-IR (CsI matrix) gave absorptions at 619(w), 519(w), 384(s), 370(s,sh), 241(w), and 161(w)cm⁻¹. (B) The Raman spectrum, in the same region, gave absorptions at 653(w,b), 586(m), 555(w), 486(w,b), 386(s), 325(m), 294(w), 254(w), 221(s), 175(m), and 150(w)

13. Brockner, W.; Becker, R.; Eisenmann, B.; Schaefer, H. *Z. Anorg. Allge. Chem.* **1985**, *520*, 51.

14. Sala, O.; Temperini, M.L.A. *Chem. Phys. Lett.* 1975, *36*, 625.

15. Marking, G.A.; Liao, J.-H.; Kanatzidis, M.G. manuscript in preparation. (b) Liao, J.-H.; Ph. D. dissertation, Michigan State University, 1993. (c) Kanatzidis, M.G.; Liao, J.-H.; Marking, G.A., United States Patent 5,618,471. (d) Kanatzidis, M.G.; Liao, J.-H.; Marking, G.A., United States Patent 5,614,128.

Table 1. Selected bond distances (Å) and angles (°) for $Cs_2CuP_3S_9$.

Cu(1)-S(12)	2.286(3)	P(1)-S(1)	1.977(3)
Cu(1)-S(23)	2.300(3)	P(1)-S(17)	2.121(3)
Cu(1)-S(14)	2.305(3)	P(1)-S(6)	1.991(3)
Cu(1)-S(01)	2.333(3)	P(1)-S(18)	2.124(3)
Cu(1)-S (mean)	2.306(9)		
		P(2)-S(10)	2.139(3)
Cu(2)-S(11)	2.281(3)	P(2)-S(15)	1.958(4)
Cu(2)-S(09)	2.301(3)	P(2)-S(24)	1.983(4)
Cu(2)-S(25)	2.323(3)	P(2)-S(26)	2.121(4)
Cu(2)-S(07)	2.325(3)		
Cu(2)-S (mean)	2.307(9)	P(3)-S(2)	1.954(4)
		P(3)-S(3)	2.131(4)
Cu(3)-S(05)	2.293(3)	P(3)-S(14)	1.981(4)
Cu(3)-S(06)	2.315(3)	P(3)-S(18)	2.116(4)
Cu(3)-S(19)	2.322(3)		
Cu(3)-S(24)	2.337(3)	P(4)-S(26)	2.135(4)
Cu(3)-S (mean)	2.316(7)	P(4)-S(04)	2.117(4)
		P(4)-S(5)	1.985(4)
S(11)-Cu(2)-S(09)	116.34(10)	P(4)-S(13)	1.955(4)
S(11)-Cu(2)-S(25)	112.60(12)		
S(09)-Cu(2)-S(25)	105.21(11)	P(5)-S(3)	2.122(4)
S(11)-Cu(2)-S(07)	108.83(12)	P(5)-S(8)	1.955(4)
S(09)-Cu(2)-S(07)	104.64(11)	P(5)-S(12)	1.988(4)
S(25)-Cu(2)-S(07)	108.75(11)	P(5)-S(17)	2.134(4)

S(21)-P(7)-S(07)	115.6(2)	P(6)-S(7)	1.977(4)
S(21)-P(7)-S(22)	103.9(2)	P(6)-S(16)	2.120(4)
S(07)-P(7)-S(22)	113.3(2)	P(6)-S(21)	1.963(4)
S(21)-P(7)-S(16)	102.7(2)	P(6)-S(22)	2.113(4)
S(07)-P(7)-S(16)	115.3(2)		
S(22)-P(7)-S(16)	104.6(2)	P(7)-S(4)	2.125(3)
		P(7)-S(10)	2.101(3)
S(25)-P(8)-S(09)	112.4(2)	P(7)-S(19)	1.977(3)
S(25)-P(8)-S(27)	114.3(2)	P(7)-S(23)	1.985(3)
S(09)-P(8)-S(27)	105.7(2)		
S(25)-P(8)-S(22)	114.5(2)	P(8)-S(22)	2.119(3)
S(09)-P(8)-S(22)	103.0(2)	P(8)-S(25)	1.976(3)
S(27)-P(8)-S(22)	105.98(14)	P(8)-S(27)	2.117(4)
		P(8)-S(9)	1.983(3)
S(20)-P(9)-S(11)	114.7(2)		
S(20)-P(9)-S(16)	105.1(2)	P(9)-S(11)	1.988(4)
S(11)-P(9)-S(16)	113.6(2)	P(9)-S(16)	2.120(4)
S(20)-P(9)-S(27)	103.4(2)	P(9)-S(27)	2.122(4)
S(11)-P(9)-S(27)	113.6(2)	P(9)-S(20)	1.959(4)
S(16)-P(9)-S(27)	105.3(2)		

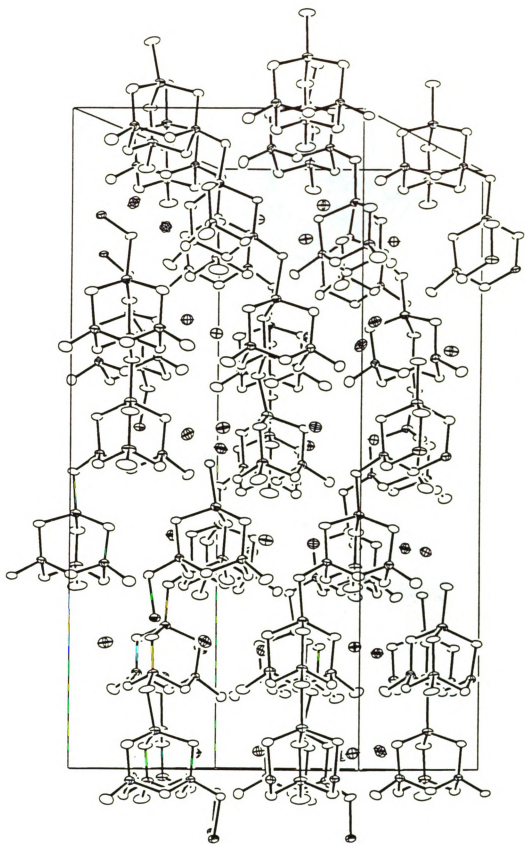# Figure Captions
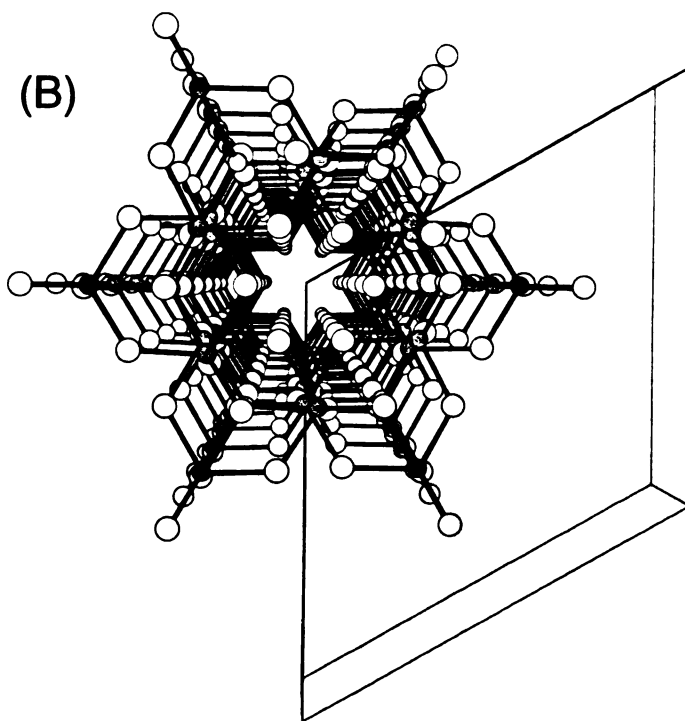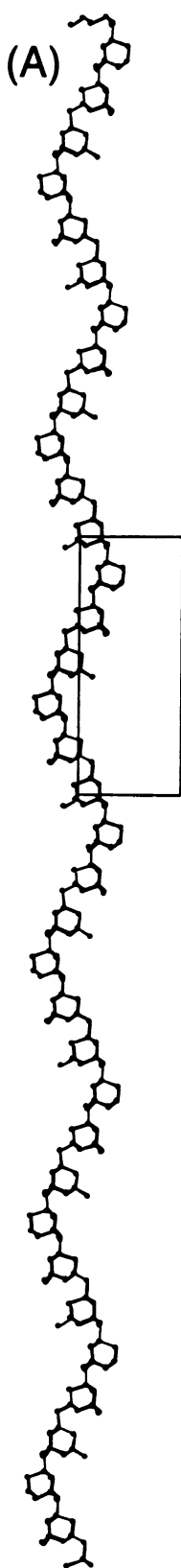
Figure 1: ORTEP representation of $Cs_2CuP_3S_9$ as viewed down perpendicular to the c - axis (50% probability ellipsoids). ellipsoids with octant shading; Cu, boundary and axis ellipsoids; P atoms, boundary ellipsoids; S, and principal and axis ellipsoids; Cs.

Figure 2: (A) View of the $[CuP_3S_9]^{2-}$, chain containing Cu(1), prepindicular to the c - axis, highlighting the helical arrangemt of the chain. (B) View of the same chain, viewed down the c - axis. (C) View of a fragment of a $[CuP_3S_9]^{2-}$ chain containing Cu(1), with a labeling scheme.

Figure 3: Single-crystal optical absorption spectrum of $Cs_2CuP_3S_9$. The sharp features at high absorbance are noise and due to the very low transmission of light at those energies.

Figure 4. Raman spectra of $Cs_2CuP_3S_9$.

Cs$_2$CuP$_3$S$_9$
Eg = 2.61eV